

ulm university universität

uulm

Nanoscale magnetic spectroscopy with colour centres in diamond

Dissertation

zur Erlangung des Doktorgrades

Dr. rer. nat.

der Fakultät für Naturwissenschaften

der Universität Ulm

vorgelegt von

Simon Christian Schmitt

aus Offenbach am Main

2020

Amtierender Dekan: Prof. Dr. Thorsten Bernhardt

Betreuendes Institut: Institut für Quantenoptik, Universität Ulm

Gutachter:
1. Prof. Dr. Fedor Jelezko
2. PD Dr. Boris Naydenov

Tag der Promotion: 23. Februar 2021

version of 8th August 2021

© 2021 Simon Christian Schmitt

Abstract

Quantum technologies are expected to significantly change our world in the next decades and the possible applications are diverse – ranging from quantum computation and encryption to metrology with unprecedented sensitivity. This thesis focuses on quantum sensing and imaging based on single nitrogen-vacancy (NV) centres in diamond to measure magnetic fields. Its electronic spin qualifies this point defect as a highly sensitive quantum sensor and its atomic size offers nanoscale spatial resolution. The simple optical initialisation and readout, together with the relatively long coherence time at ambient conditions, make NV centres promising candidates for biological applications and in particular for nuclear magnetic resonance (NMR) on the nanoscale. Recording the spectral information on the nanoscale allows to determine the structure of single or just a few molecules. However, the current main problems and challenges include insufficient spectral resolution, artificial signals and overall poor performance. In this thesis new spectroscopic techniques which tackle these issues are presented.

First, it is shown that by randomisation of control pulse phases spurious harmonic signals can be suppressed, which otherwise complicate spectrum interpretation and can lead to false signal identification. At the same time the effects of pulse imperfections are mitigated.

Furthermore, a protocol allowing to measure with a coherence independent spectral resolution is presented. It is demonstrated that linewidths below 1 mHz are possible, which is an improvement of more than seven orders of magnitude compared to traditional methods. Due to its simple implementation, the protocol is relevant for many applications. Initially developed to measure signals oscillating up to several megahertz, it is further shown that modifications allow to extend the frequency range into the gigahertz domain.

Finally, quantum frequency discrimination with the task to differentiate between two frequency distributions using a quantum sensor is analysed. An optimised protocol is introduced and the influences of different readout strategies are discussed with respect to the probability to make an incorrect decision. These findings are useful for diagnostic tests in NMR.

Contents

1 Introduction **1**

2 Quantum sensing and spectroscopy **7**

2.1 The quantum bit 7
2.2 Initialisation of a quantum system 10
2.3 Readout of a quantum system 10
2.4 Interaction between a quantum system and a physical quantity 13
2.5 Coherent control of the quantum state 13
2.6 Steps of a quantum measurement 18

3 The nitrogen-vacancy centre in diamond **21**

3.1 The nitrogen-vacancy centre as a qubit 22
3.1.1 Quantum systems in solid states 22
3.1.2 Diamond as a host material 23
3.1.3 The nitrogen-vacancy centre 25
3.1.4 The ground state Hamiltonian of the nitrogen-vacancy centre 27
3.2 Initialisation of the nitrogen-vacancy centre 32
3.3 Readout of the nitrogen-vacancy centre 34
3.3.1 Readout via spin-dependent fluorescence 34
3.3.2 Signal-to-noise ratio 36
3.3.3 Improvement of the traditional optical readout 38
3.4 Couplings of the nitrogen-vacancy centre 41
3.5 Coherent control of the nitrogen-vacancy centre 42

4 Spectroscopy with the nitrogen-vacancy centre **45**

4.1 Optically detected magnetic resonance 45
4.2 Ramsey interferometry 48
4.3 Dynamical decoupling spectroscopy 50
4.3.1 Dynamical decoupling Hamiltonian 50
4.3.2 Dynamical decoupling filter 52
4.3.3 The XY8-sequence 55

4.4 Relaxometry . . . 56
4.5 Precision, sensitivity and limits of quantum spectroscopy . . . 57
4.5.1 The quantum Fisher information . . . 57
4.5.2 Sensitivity for quantum projection noise limited measurements . . . 58
4.5.3 Sensitivity for photon shot noise limited measurements . . . 59
4.5.4 Relaxation of the quantum state . . . 60

5 Nanoscale nuclear magnetic resonance 67
5.1 Principles of NMR . . . 69
5.1.1 Interpreting the NMR spectrum . . . 70
5.1.2 Sample magnetisation in classical NMR . . . 72
5.2 Principles of nanoscale NMR . . . 73
5.2.1 Sample magnetisation in nanoscale NMR . . . 73
5.2.2 Experimental realisation . . . 74
5.3 Limitations up to date . . . 78

6 Quantum spectroscopy using randomisation of pulse phases 81
6.1 Spurious responses under dynamical decoupling . . . 81
6.2 The randomisation protocol . . . 85
6.3 Experimental realisation of the randomisation protocol . . . 86
6.4 Robustness enhancement by randomisation . . . 90
6.5 Conclusion . . . 94

7 Quantum heterodyne detection 95
7.1 Principle of quantum heterodyne detection . . . 96
7.1.1 The idea . . . 96
7.1.2 The working principle . . . 97
7.1.3 Experimental realisation with nitrogen-vacancy centres . . . 99
7.2 Quantum heterodyne detection based on dynamical decoupling . . . 101
7.2.1 Derivation of the population formula . . . 101
7.2.2 Proof of principle . . . 102
7.2.3 In depth analysis of Qdyne . . . 103
7.2.4 Multiple frequency fields . . . 108
7.2.5 Bandwidth of Qdyne spectroscopy . . . 109
7.2.6 Nanoscale NMR with Qdyne . . . 110
7.2.7 Conclusion . . . 113

8 Quantum frequency discrimination 115
8.1 Theoretical derivation . . . 116
8.2 Experimental demonstration . . . 119
8.3 Quantum discrimination for complex frequency distributions . . . 121
8.4 Discussion of different readout strategies . . . 122
8.4.1 Strategy 1 – Ensemble averaging . . . 123
8.4.2 Strategy 2 – Single-shot readout . . . 127
8.4.3 Performance for quantum frequency discrimination . . . 132
8.5 Conclusion . . . 136

9 Quantum spectrum analysis 137
9.1 Measurement sequence and theoretical analysis . . . 138
9.1.1 Derivation of the population formula . . . 139
9.1.2 Illustrative explanation . . . 140
9.1.3 Non-negligible frequency detuning . . . 142
9.2 Experimental demonstration of the principle . . . 142
9.2.1 Population as a function of the signal phase . . . 142
9.2.2 Frequency spectrum . . . 143
9.2.3 Signals with multiple spectral components . . . 144
9.2.4 Interactions during initialisation and readout . . . 145
9.3 Signal reconstruction . . . 148
9.4 Improving the sensitivity . . . 150
9.4.1 Qdyne spectroscopy using single-shot readout . . . 151
9.4.2 Enhanced sensitivity through decoupling . . . 153
9.5 Bandwidth of the quantum spectrum analyser . . . 156
9.5.1 Dynamic bandwidth . . . 156
9.5.2 Spectral bandwidth . . . 157
9.6 Conclusion . . . 160

10 Conclusion and Outlook 161
10.1 Conclusion . . . 161
10.2 Outlook . . . 162

A Appendix 167
A.1 Setup . . . 167
A.1.1 Microwave setup . . . 167
A.1.2 Confocal microscope . . . 168
A.1.3 Photon counting . . . 171

A.1.4 Control PC and measurement software 171
A.1.5 Overview of examined diamond samples 172
A.1.6 Magnetic field alignment 173
A.2 Diamond synthesis and nitrogen-vacancy centre creation 177
A.3 Mathematical derivations 180
A.3.1 Time evolution and rotating reference frame 180
A.3.2 Fisher information for binomial and Poisson distributions 184
A.3.3 Sensitivity of ODMR spectroscopy 185
A.3.4 Precision and dynamic range for Ramsey interferometry 186
A.3.5 Derivation of the spectral filter for dynamical decoupling 189
A.3.6 Additional information concerning Qdyne 190
A.3.7 Charge state of the nitrogen-vacancy centre 191

Abbreviations and Symbols **195**

List of Figures **201**

List of Tables **205**

Bibliography **207**

Acknowledgements **245**

List of Publications **247**

Curriculum Vitae **253**

Erklärung **255**

1 Introduction

Sensors are an indispensable part of our daily life. They appear in a variety of forms, a wide range of dimensions, have different functions and, especially in the last ten years, their number has increased dramatically. This proliferation is mainly due to the improved accuracy, reliability, safety, efficiency and productivity of applications that utilise sensors. For example, in a modern car there are about $60 - 100$ different sensors [1], ranging from simple thermometers to more advanced laser and radar systems, which help for instance with parking or braking. This number is rapidly growing with the emergence of autonomous driving [2]. Beyond daily life, better sensors are important for the discovery and understanding of new physics. An important recent example is the detection of gravitational waves by the Laser Interferometer Gravitational-Wave Observatory [3].

Quantum sensors are based on quantum systems, quantum properties and quantum phenomena and have the potential to perform certain tasks much better than classical sensors [4]. For example, they can be used for neuroimaging applications through detecting the intensity and direction of firing neurons in a scalable and non-invasive way [5]. This promises a better understanding of neuron activities and consciousness and could enable medical examinations with portable devices insensitive to environmental magnetic fields.

A particular area where sensors have found broad application is spectral analysis. Spectra reveal the frequency and amplitude components of time-varying signals and are relevant in all fields of natural science and medicine, since there is a wide range of practical applications including development of time and frequency standards [6, 7], medical diagnosis [8–10], chemical identification [11], imaging and microscopy [12, 13], radar detection [14] and quantum state tomography [15]. The accuracy with which spectral information can be obtained is given by physical laws. Ultimately, quantum mechanics determines the limits and therefore only quantum mechanical detectors, which operate in accordance to these laws, can perform quantum spectroscopy at the limits of sensitivity, resolution and still be non-invasive.

This thesis focuses on one application of spectroscopy in particular – nuclear magnetic resonance (NMR) spectroscopy, which currently is the gold standard for molecular analysis and structural determination [11]. However, the low sensitivity of classical inductive coils, mainly used as detectors, requires a macroscopic sample to induce a sufficiently large

current. Alternative state-of-the-art techniques with chemical sensitivity and atomic resolution are invasive or even destructive, require cryogenic temperatures and/or vacuum conditions (e.g. electron microscopy [16, 17] and atomic force microscopy [18]) or crystallised samples (X-ray diffraction [19]). Therefore, NMR spectroscopy is an important application, where the usage of quantum sensors has the potential to significantly improve the current state-of-the-art. By reducing the sample size, microscopy of single molecules and examination of dynamics and properties on the nanoscale come within reach. Furthermore, it is possible to perform experiments without large magnetic bias fields, which are accompanied by bulky and expensive setups.

One highly promising quantum sensor is the nitrogen-vacancy (NV) centre in diamond. Its electronic spin and atomic size provide high sensitivity for magnetic fields and nanoscale spatial resolution. The principle of NV magnetic field sensing is similar to that of optical magnetometry, where a magnetic field shifts the energy of the spin levels proportionally to the magnitude of the applied field [20,21]. By recording the magnetic field originating from nuclear spins contained in molecules on the surface of diamond, these sensors have allowed for NMR spectroscopy at the limits of single molecules and nuclei to be performed [22–26].

Although extremely impressive sensitivities on the order of few spins/$\sqrt{\text{Hz}}$ have been demonstrated [24], there are a number of issues, which currently present an inherent obstacle to the widespread adoption and commercialisation of the techniques and reduce their investigative power. For example, due to either sensor decoherence or intrinsic sample properties [22, 27], the spectral resolution limits the precision of frequency estimation, obscures frequency information encoded in couplings and prevents chemical identification or structural characterisation. Since frequency precision translates directly into spatial resolution and chemical sensitivity, a high spectral resolution is paramount to imaging performance. Furthermore, the need to acquire an entire spectrum point-by-point means that signal acquisition times on the order of several minutes to hours are required in order to obtain sufficient signal-to-noise ratio. In a typical NMR experiment, where 1 Hz resolution is desired across a 100 kHz frequency range, which spans chemical shifts of a few parts per million, the spectrum contains 10^5 frequency components. These long signal averaging times severely hinder studies of molecular dynamics and are unsuitable for practical applications. Beyond that, the protocols, which are typically used to record NMR spectra with NV centres, lead to unwanted spurious responses, which cause additional signals and complicate spectrum interpretation [28]. This is especially relevant for NMR since the gyromagnetic ratios of two of the most important nuclear spin isotopes, ^{1}H and ^{13}C, are almost multiple of each other and thus their discrimination can be problematic. Furthermore, these techniques are usually limited to frequencies of just a few tens of megahertz and so they are unsuitable in combination with high magnetic bias fields, for

which the resolution of chemical shifts is simpler. Moreover, for many specific problems the optimal measurement strategies are still not explored. By addressing these limitations, this thesis aims to transform the state-of-the-art for nanoscale NMR spectroscopy with NV centres.

In an introducing theoretical section the basics and requirements for quantum sensing (chapter 2) are shortly outlined, a deeper insight into the physical properties of the NV centre is given (chapter 3) and the basics for spectroscopy with NV centres are explained (chapter 4).

Thereafter, the principles and problems of nanoscale NMR are discussed in chapter 5. It is shown in chapter 6 that through pulse phase randomisation spurious signals can be efficiently suppressed. Using the same technique, the effect of pulse imperfections is also reduced, allowing improved and more faithful spectra to be obtained.

Furthermore, techniques, which were developed to improve the spectral resolution of NV based spectroscopy by several orders of magnitude, are introduced in this thesis. Since all spectral components in a given bandwidth are recorded simultaneously, the same technique provides a significant speed-up in measurement time and has further consequences, which are discussed in chapter 7.

NMR diagnosis tests can be especially useful for medical applications, for example by revealing the presence of a certain molecule or indicating if a specific chemical reaction has occurred. Such a discrimination problem, where the task is to find the present spectral distribution out of two possible options using a single quantum sensor, is discussed in chapter 8. We show that it is possible to achieve perfect frequency discrimination within a single coherent interaction period if classical readout noise can be neglected.

In chapter 9, the possibility to use a single quantum sensor for spectrum analysis is discussed. The introduced protocol extends the range of accessible frequencies into the gigahertz regime.

After a short conclusion and an outlook in chapter 10, the principles of the experimental setup, including the confocal microscope and the used diamond samples, are described. Also, mathematical derivations, which are omitted in the main part for reasons of readability, can be found in appendix A.

Theoretical Background

2 Quantum sensing and spectroscopy

Quantum systems have to fulfill certain requirements in order to be suitable for sensing applications. These criteria are very similar to the DiVincenzo's criteria for quantum computation [29]. For quantum sensors the list of necessary condition is [4]:

1. The quantum system has discrete and resolvable energy levels.
2. It is possible to initialise the quantum system.
3. The state of the quantum system is readable.
4. There is an interaction between quantum system and the physical quantity of interest.
5. The system can be coherently controlled.

In the following, these criteria are discussed in more detail.

2.1 The quantum bit

The first criterion for a system to qualify as a quantum sensor is the accessibility to at least two discrete and resolvable energy levels. Here, discrete and resolvable means that these states may not overlap due to intrinsic or thermal broadening and are decoupled from all other existing levels. For more advanced applications three or more states might be necessary, but for simplicity the following concentrates on two energy levels, which represent a so called quantum bit (qubit). Like a classical bit, a qubit has two eigenstates, from here on called $|0\rangle$ and $|1\rangle$, with a transition energy E_0 (see figure 2.1(a)). While a classical bit can only be in exactly one of its states similar to a switch, which can be either "On" or "Off", a pure qubit state $|\Psi\rangle$ can be an arbitrary superposition of both eigenstates:

$$|\Psi\rangle = \alpha\,|0\rangle + \beta\,|1\rangle\,, \tag{2.1}$$

where $\alpha = a\mathrm{e}^{i\phi_\alpha}$ and $\beta = b\mathrm{e}^{i\phi_\beta}$ are complex numbers. Since the global phase of the wave function is physically unimportant, the qubit state can be simplified to:

$$|\Psi\rangle = a\,|0\rangle + b\mathrm{e}^{i\phi}\,|1\rangle\,, \tag{2.2}$$

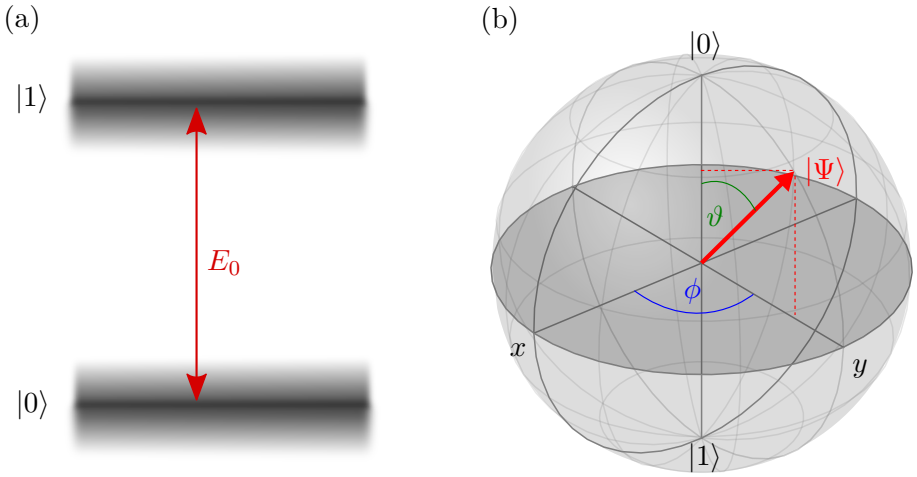

Figure 2.1: Qubit as two-level system and presented in the Bloch sphere. (a) A qubit is a discrete and resolvable two-level system. It is important that the energy difference E_0 between the two states is larger than the intrinsic and thermal broadening. (b) Representation of the qubit state $|\Psi\rangle$ as a vector (red arrow), which can be described by the two angles ϑ and ϕ, on the Bloch sphere.

where $\phi = \phi_\beta - \phi_\alpha$. The probability to find the qubit in one of its eigenstates is given by the squares of the absolute values $|\alpha|^2$ and $|\beta|^2$ and it follows:

$$|a|^2 + |b|^2 = 1. \tag{2.3}$$

Bloch sphere representation

A convenient tool to graphically represent the state of a single qubit is the so called Bloch sphere, illustrated in figure 2.1(b) (all Bloch spheres in this thesis are prepared using the QuTiP software [30, 31]). The idea is to assign every pure qubit state to a point on the surface of this sphere. By rewriting $a = \cos(\vartheta/2)$ and $b = \sin(\vartheta/2)$, the quantum system is described by the two angles ϑ and ϕ, which makes the use of spherical coordinates convenient and is in accordance to equation (2.3). The qubit state then reads:

$$|\Psi\rangle = \cos\left(\frac{\vartheta}{2}\right)|0\rangle + \mathrm{e}^{i\phi}\sin\left(\frac{\vartheta}{2}\right)|1\rangle\,. \tag{2.4}$$

Due to this definition the two poles are assigned to the $|0\rangle$ and $|1\rangle$ states. The projection of the vector describing $|\Psi\rangle$ onto the z-axis correlates to the probability to find the qubit in $|0\rangle$ or $|1\rangle$. For example for $|0\rangle$ the probability is:

$$P_0 = \frac{1}{2} + \frac{1}{2}\cos(\vartheta) = \left(\cos\left(\frac{\vartheta}{2}\right)\right)^2. \tag{2.5}$$

For many sensing purposes and protocols the superposition states which are lying on the equatorial plane (dark grey area in figure 2.1(b)), are especially interesting:

$$|\Psi\rangle = \frac{1}{\sqrt{2}}(|0\rangle + \mathrm{e}^{i\phi}\,|1\rangle). \tag{2.6}$$

From here on, $\phi = \pi/2$ represents the y-axis and $\phi = 0$ the x-axis.

Hamiltonian and temporal evolution of a qubit

The Hamiltonian of a two-level system without external perturbation can be written as:

$$\mathcal{H}_0 = \frac{E_0}{2}\,|0\rangle\langle 0| - \frac{E_0}{2}\,|1\rangle\langle 1| = \frac{E_0}{2}\hat{\sigma}_z, \tag{2.7}$$

where $\hat{\sigma}_z$ in one of the Pauli matrices:

$$\hat{\sigma}_x = \begin{pmatrix} 0 & 1 \\ 1 & 0 \end{pmatrix},\ \hat{\sigma}_y = \begin{pmatrix} 0 & -i \\ i & 0 \end{pmatrix},\ \hat{\sigma}_z = \begin{pmatrix} 1 & 0 \\ 0 & -1 \end{pmatrix}. \tag{2.8}$$

The state of a quantum system, which is described by a Hamiltonian $\mathcal{H}(t)$, may evolve between the times t_0 and t_1:

$$|\Psi(t_0)\rangle \xrightarrow{\mathcal{H}(t)} |\Psi(t_1)\rangle\,, \tag{2.9}$$

and this temporal evolution is described by the time-dependent Schrödinger equation:

$$i\hbar\frac{\partial}{\partial t}\,|\Psi(t)\rangle = \mathcal{H}(t)\,|\Psi(t)\rangle\,, \tag{2.10}$$

where $\mathcal{H}$ is the system Hamiltonian and $\hbar$ is the reduced Planck constant. The idea for defining the so called time-evolution operator $\mathcal{U}(t_1, t_0)$:

$$|\Psi(t_1)\rangle = \mathcal{U}(t_1, t_0)\,|\Psi(t_0)\rangle\,, \tag{2.11}$$

is that all information about the dynamics of the system is contained in $\mathcal{U}(t_1, t_0)$ and the final state $|\Psi(t_1)\rangle$ can be obtained by applying $\mathcal{U}(t_1, t_0)$ to the initial state $|\Psi(t_0)\rangle$. As derived in more details in appendix A.3.1, for time-independent Hamiltonians or if the operators $\mathcal{H}$ which correspond to different moments of time commute, $\mathcal{U}(t_1, t_0)$ is given by:

$$\mathcal{U}(t_1, t_0) = \exp\left(-\frac{i}{\hbar}\int_{t_0}^{t_1}\mathcal{H}(t')\mathrm{d}t'\right). \tag{2.12}$$

2.2 Initialisation of a quantum system

Quantum sensing is based on the interaction of a quantum system with a field of interest, which alters the quantum state. In order to detect this change the final state has to be compared with the initial one, which thus has to be known. Since multiple repetitions of the same experiment are usually required to gather sufficient statistics, it is convenient to initialise the system into a specific state.

A standard way to initialise the state of a qubit is to measure it. Through the readout, a quantum state is projected onto one of its eigenstates, which is then usually also known. This state can further be manipulated by coherent control if necessary (see section 2.5). Also, different initialisation channels, if available, can be utilised, as it is shown for the NV centre in section 3.2.

An important parameter is the initialisation fidelity $\mathcal{F}$ – the probability to bring the qubit into the desired state. In practice, perfect initialisation is almost impossible and $\mathcal{F}$ could for example be limited due to imperfect readout, spontaneous changes of the quantum state or imperfect manipulation. This initialisation fidelity is even more relevant, if multiple qubits need to be initialised. Further consequences of an imperfect initialisation are discussed in chapter 8.

2.3 Readout of a quantum system

For quantum sensing applications, it is essential to readout the sensor state, which provides the measurement information. The principles differ fundamentally from classical readout. In classical physics an observer with complete information about an isolated system can always exactly determine and even predict the value of any parameter of interest. If an experiment is repeated under identical conditions, the outcome stays unchanged. In quantum mechanics, a pure state can be described by a wavefunction $|\Psi\rangle$, which is a superposition of eigenstates $|\psi_n\rangle$:

$$|\Psi\rangle = \sum_n \xi_n |\psi_n\rangle . \tag{2.13}$$

In order to obtain the state of a quantum system the respective amplitudes ξ_n have to be found. It is, however, not possible to measure this superposition state directly. Due to interactions during the readout, $|\Psi\rangle$ is projected to one of its eigenstates and consequently, the measurement result corresponds to this eigenstate. The exact process is still under debate, even after over a century of discussion, and possible explanations range from

collapse of the wave function to decoherence and pointer states [32]. The probability to find a certain eigenstate $|\psi_n\rangle$ is given by:

$$P_n = |\langle\Psi|\psi_n\rangle|^2 = |\xi_n|^2. \tag{2.14}$$

Thus, it is not possible to make deterministic predictions in quantum mechanics, but only probabilistic statements. Since after a measurement, the quantum system is in the measured state and any further readouts would result in the same state, the only option to estimate all amplitudes ξ_n is to repeat the experiment multiple times.

The above discussion simplifies for qubits, since there are only two possible measurement outcomes, namely the eigenstates $|0\rangle$ and $|1\rangle$. If the state before readout is $|\Psi\rangle = \alpha|0\rangle + \beta|1\rangle$, the respective probabilities are:

$$P_0 = |\langle\Psi|0\rangle|^2 = |\alpha|^2 \tag{2.15}$$

to find $|0\rangle$ and

$$P_1 = |\langle\Psi|1\rangle|^2 = |\beta|^2 \tag{2.16}$$

to measure $|1\rangle$. Since both probabilities are correlated due to $P_0 = 1 - P_1$, it is sufficient to consider only one of them.

Quantum projection noise

Due to this probabilistic nature of the readout the fidelity of a measurement outcome is limited. The problem is analogous to a coin flip, where the coin might be biased and the task is to find the probability that a flip results in heads or tails.

In order to experimentally obtain P_0, a set of measurements has to be recorded. The theoretical probability to find n times the measurement result $|0\rangle$ in N repetitions is described by the binomial distribution:

$$\mathcal{B}(n, N, P_0) = \binom{N}{n} P_0^n (1 - P_0)^{N-n}. \tag{2.17}$$

The dependency of this function on n is plotted for $P_0 = 0.4$ and $N = 10, 30, 100$ in figure 2.2(a). In order to improve the comparability the y-axis is normalised by multiplying with N. The maximum for all distributions, so the most probable outcome, is the closest integer number to the expectation value $P_0 \cdot N$. Due to that, the estimate with the highest likelihood is:

$$P_0 = \frac{n}{N}. \tag{2.18}$$

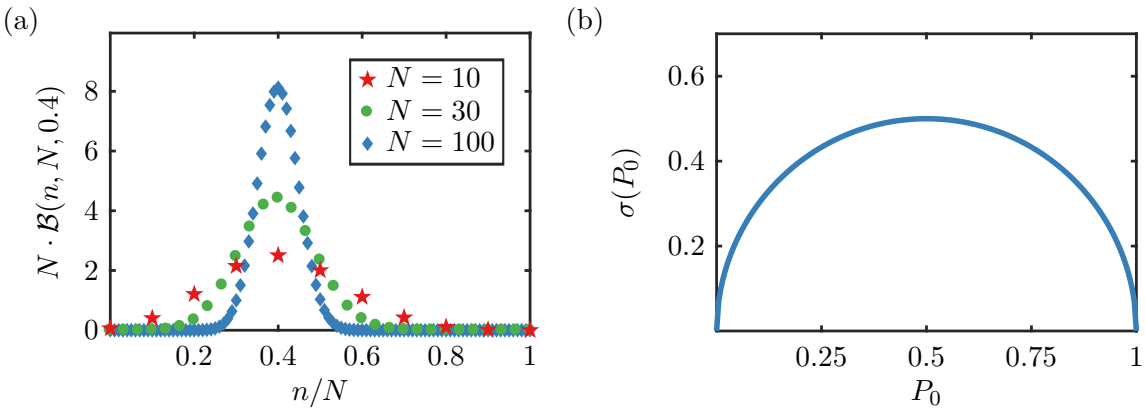

Figure 2.2: Binomial distribution and standard deviation. (a) Normalised binomial distributions $\mathcal{B}(n, N, P_0 = 0.4)$ as a function of n/N for $N \in \{10, 30, 100\}$. In order to improve the comparability the y-axis is multiplied by N. All maxima are at the expectation value $n/N = P_0$ and the full width at half maximum decreases as $\sqrt{N}$. (b) The standard deviation $\sigma(P_0)$ of the binomial distribution as a function of P_0 for $N = 1$ is maximal for $P_0 = 0.5$ and vanishes for $P_0 = 0$ and $P_0 = 1$.

The uncertainty for estimating P_0 is referred to as quantum projection noise (QPN). It presents a fundamental limit for quantum measurements [33] and corresponds to the standard deviation of the binomial distribution:

$$\sigma(P_0) = \sqrt{NP_0(1 - P_0)}. \tag{2.19}$$

Interestingly, $\sigma(P_0)$ is a function of P_0, which is plotted for $N = 1$ in figure 2.2(b). The closer P_0 is to zero or one, the smaller is $\sigma(P_0)$ and the standard deviation completely vanishes for $P_0 = 0$ and $P_0 = 1$. Experiments, which take advantage of this behaviour, are discussed in chapter 8.

Since the signal improves linearly with N, and the standard deviation increases as $\sqrt{N}$, the estimation uncertainty ΔP_0 reduces as $\sqrt{N}$ with the number of measurements N. This can also be observed in the reduced relative width of the binomial distributions with increasing N in figure 2.2(a).

In real-world experiments, the quantum state needs to be readout by detecting a measurable quantity, for example photons or electrons. Thus, additional noise sources can influence the uncertainty of an experiment. If the readout is performed optically for example, photon shot noise has to be taken into account. These additional noise sources can reduce the distinctness between the $|0\rangle$ or $|1\rangle$ states, which for the NV centre is in more detail discussed in section 3.3 and chapter 8.

2.4 Interaction between a quantum system and a physical quantity

Quantum sensing is based on an interaction between a quantum system acting as a probe and a field of interest which influences the evolution of the system's state. By detecting this change an estimate of the field parameters can be obtained. It is optimal if the sensor response to the field of interest is large while at the same time the sensor is only minimal affected by unwanted signals and other noise sources. The stronger this coupling, the more sensitive is the sensor and the more precise measurements can be performed.

The sensor response can usually be quantified by a coupling tensor or parameter γ_c and the resulting Hamiltonian for a qubit interacting with a field described by the vector $\vec{A}$ is:

$$\mathcal{H} = \frac{E_0}{2}\hat{\sigma}_z + h\vec{A}^{\mathrm{T}}\gamma_c\vec{\sigma}, \tag{2.20}$$

where $\vec{\sigma} = (\hat{\sigma}_x\ \hat{\sigma}_y\ \hat{\sigma}_z)^{\mathrm{T}}$ is the vector of the Pauli matrices. For the NV centre the most important couplings are summarised in section 3.4.

2.5 Coherent control of the quantum state

Operations which can manipulate the quantum state via an external control are important for all quantum technologies. For example in quantum sensing and spectroscopy, application of a suitable control sequence can highly improve the measurement performance, which is in more detail discussed in chapter 4. For this purpose, control fields with frequencies close to the transition frequency ($\omega_0 = E_0/\hbar$) of the qubit are required. As it is shown in the following, these interactions can be illustrated as rotations on the Bloch sphere. As long as the control Hamiltonian is chosen correctly and the system is closed, every starting point on the Bloch sphere can be transferred into any arbitrary final point.

Rotating reference frame

If a two-level quantum system interacts with a near-resonant field with frequency ω_1 the Hamiltonian in the laboratory reference frame reads:

$$\mathcal{H} = \underbrace{\frac{\hbar\omega_0}{2}\hat{\sigma}_z}_{\mathcal{H}_0} + \underbrace{\hbar\Omega\cos(\omega_1 t + \theta_1)\hat{\sigma}_x}_{\mathcal{H}_1}, \tag{2.21}$$

where ω_0 is the transition frequency of the system, Ω is the coupling constant and θ_1 is the signal phase. So, even if $\mathcal{H}_1 = 0$, the quantum system is not stationary in this reference

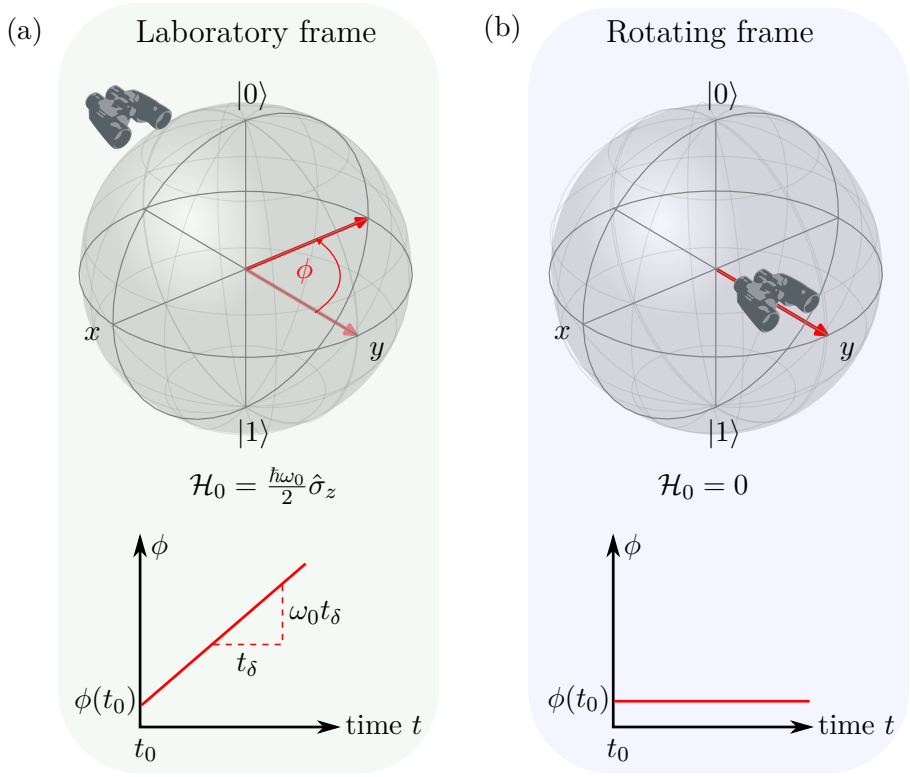

Figure 2.3: Laboratory and rotating frame. (a) In the laboratory frame, the qubit state is usually not stationary from the perspective of an external observer and a relative phase $\phi(t) = \omega_0 \cdot t + \phi(t_0)$ is accumulated. (b) In the rotating frame of the quantum system, the state is time-independent in the absence of any external perturbation.

frame, since $\mathcal{H}_0$ involves a rotation around the z-axis, which is sketched in figure 2.3(a) and more closely discussed in appendix A.3.1.

The physical description as well as the mathematical formalism can often be simplified by changing the reference frame to the rotating frame of the quantum system (figure 2.3(b)). An intuitive analogy is the rotation of the surface of the earth. From the point of view of an extraterrestrial observer, we perform our everyday measurements in the rotating frame of the earth.

In order to transfer a quantum system into a different interaction picture, both its Hamiltonian $\mathcal{H}(t)$ as well as its state $|\Psi\rangle$ have to be adapted. The mathematical formalism is in more detail discussed in appendix A.3.1. If in addition, the rotating wave approximation (for mathematical description and visual illustration see appendix A.3.1) is applied, equation (2.21) yields for a resonant field ($\omega_1 = \omega_0$):

$$\mathcal{H}_{\text{int}} = \frac{\hbar\Omega}{2}\left[\cos(\theta_1)\hat{\sigma}_x + \sin(\theta_1)\hat{\sigma}_y\right]. \tag{2.22}$$

This resonant case is especially important, since all quantum control relevant for this thesis should optimally be resonant.

Temporal evolution of the quantum system under a resonant field

The time evolution operator $\mathcal{U}(t, t_0)$, which describes the evolution of the quantum system, reads (compare equation (2.12)):

$$\mathcal{U}(t) \equiv \mathcal{U}(t, t_0 = 0) = \exp\left(-i\frac{\Omega t}{2}\left[\cos(\theta_1)\hat{\sigma}_x + \sin(\theta_1)\hat{\sigma}_y\right]\right), \tag{2.23}$$

and describes a rotation on the Bloch sphere. First concentrating on the rotation angle Θ by setting $\theta_1 = \pi$, $\mathcal{U}(t)$ reads in the matrix representation:

$$\mathcal{U}(t) = \begin{pmatrix} \cos\left(\frac{\Omega t}{2}\right) & i\sin\left(\frac{\Omega t}{2}\right) \\ i\sin\left(\frac{\Omega t}{2}\right) & \cos\left(\frac{\Omega t}{2}\right) \end{pmatrix}. \tag{2.24}$$

Applying $\mathcal{U}(t)$ to an arbitrary initial state $|\Psi(t=0)\rangle = (a \;\; b)^{\mathrm{T}}$, it follows:

$$|\Psi(t)\rangle = \mathcal{U}(t)\begin{pmatrix} a \\ b \end{pmatrix} = \begin{pmatrix} a\cos\left(\frac{\Omega t}{2}\right) + ib\sin\left(\frac{\Omega t}{2}\right) \\ b\cos\left(\frac{\Omega t}{2}\right) + ia\sin\left(\frac{\Omega t}{2}\right) \end{pmatrix}, \tag{2.25}$$

and the temporal evolution of the population $P_0(t) = |\langle 0|\Psi(t)\rangle|^2$ in the $|0\rangle$ state reads:

$$\begin{aligned} P_0(t) &= |a|^2\cos^2\left(\frac{\Omega t}{2}\right) + |b|^2\sin^2\left(\frac{\Omega t}{2}\right) \\ &= \frac{1}{2} + \frac{|a|^2 - |b|^2}{2}\cos(\Omega t). \end{aligned} \tag{2.26}$$

Thus, P_0 is a sinusoidal function with frequency Ω and the resulting oscillations are often referred to as Rabi oscillations [34]. The amplitude depends on the initial state and as an example the temporal evolution for $|\Psi(t_0 = 0)\rangle = (1 \;\; 0)^{\mathrm{T}}$ is illustrated in figure 2.4. In this case equation (2.26) simplifies to:

$$P_0(t) = \cos^2\left(\frac{\Omega t}{2}\right) = \frac{1}{2} + \frac{1}{2}\cos(\Omega t), \tag{2.27}$$

and by changing either the interaction time t or the coupling strength Ω, the rotation angle $\Theta = \Omega \cdot t$ can be controlled.

An important gate in quantum science is the $\pi/2$-pulse, also called Hadamard gate. As the name implies, it rotates the state on the Bloch sphere by a $\pi/2$-angle and can be realised by applying a resonant field for a duration of $t_{\pi/2} = \pi/(2\Omega)$. These operations are

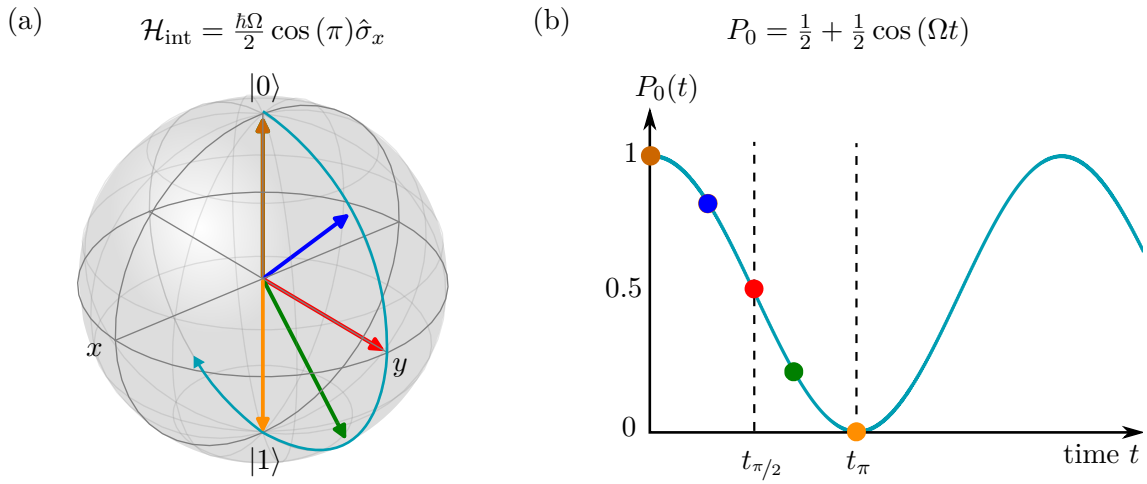

Figure 2.4: Coherent control of a qubit. (a) Resonant fields initiate rotations on the Bloch sphere. (b) The resulting probability P_0 to measure $|0\rangle$ oscillates with the frequency Ω.

especially relevant for initialisation and readout of the quantum system. For example, a $\pi/2$-pulse allows to map the quantum state from an eigenstate into an equally populated superposition state, which is advantageous for many sensing protocols.

Hereby, the final position on the equator is determined by the rotation axis. If the initial state is $|\Psi(t_0 = 0)\rangle = (1 \;\; 0)^{\mathrm{T}}$ and $t = \pi/(2\Omega)$, the final state reads using equation (2.23):

$$|\Psi(t = \frac{\pi}{2\Omega})\rangle = \frac{1}{\sqrt{2}}\left(|0\rangle - ie^{i\theta_1}|1\rangle\right). \tag{2.28}$$

Thus, the rotation axis is determined by the phase of the control signal θ_1 and an illustrative example is sketched in figure 2.5.

Also very relevant for many applications are so called π-pulses. Inserting $t_\pi = \pi/\Omega$ into equation (2.26), the final population reads:

$$P_0(t) = |b|^2. \tag{2.29}$$

Thus, a π-pulse inverts the populations of the eigenstates.

Non-resonant fields

Optimally, the frequency of the driving field ω_1 is resonant to the transition frequency ω_0 of the system. However, in experimental scenarios there are always small deviations, for example due to fluctuations in the environment or limited estimation accuracy of ω_0. As shown in appendix A.3.1, the Hamiltonian (equation (2.21)) then remains time-dependent – even in the reference frame of the qubit – and finding the time evolution operator is

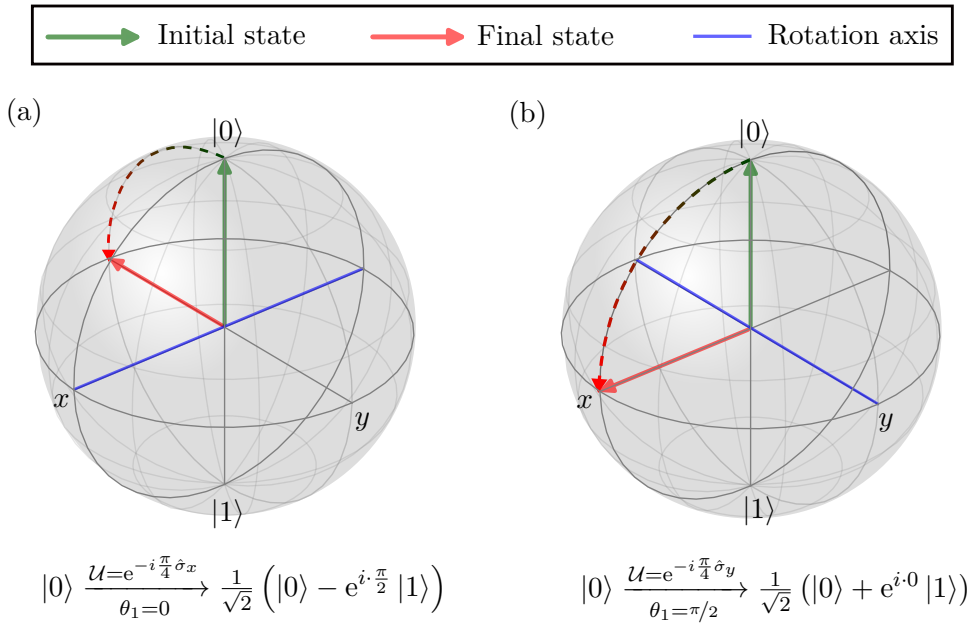

Figure 2.5: Application of $\pi/2$-pulses around different axes. The initial state (green arrow) is rotated around (in blue) (a) the x-axis ($\theta_1 = 0$) and (b) the y-axis ($\theta_1 = \pi/2$). Although the rotation angle is the same, the final states (red arrows) occupy different positions on the Bloch sphere.

usually not trivial in this case. Nevertheless, it is possible to find an analytical solution and, if initialised into $|\Psi(t_0 = 0)\rangle = (1\ \ 0)^{\mathrm{T}}$, the population in the $|0\rangle$ state as a function of the interaction time t reads [35]:

$$P_0 = 1 - \frac{\Omega^2}{\Omega_{\mathrm{R}}^2} \cdot \sin^2\left(\frac{\Omega_{\mathrm{R}} \cdot t}{2}\right) = 1 - \frac{\Omega^2}{2\Omega_{\mathrm{R}}^2} \cdot \left(1 - \cos\left(\Omega_{\mathrm{R}} \cdot t\right)\right), \tag{2.30}$$

where $\omega_\Delta = \omega_1 - \omega_0$ is the frequency detuning and Ω_{R} is the so-called generalised Rabi frequency:

$$\Omega_{\mathrm{R}} = \sqrt{\Omega^2 + (\omega_\Delta)^2}. \tag{2.31}$$

Thus, the effective frequency is increased, but the contrast reduces. A few consequences are more closely discussed in chapters 6 and 9.

Rotations about the z-axis

Rotations about the z-axis can be realised by using a time-independent field or by altering the reference frame. As in more detail shown in appendix A.3.1, the reference frame can be changed using the following rotation operator:

$$\mathcal{R} = \exp\left(-i\Delta\phi\hat{\sigma}_z/2\right). \tag{2.32}$$

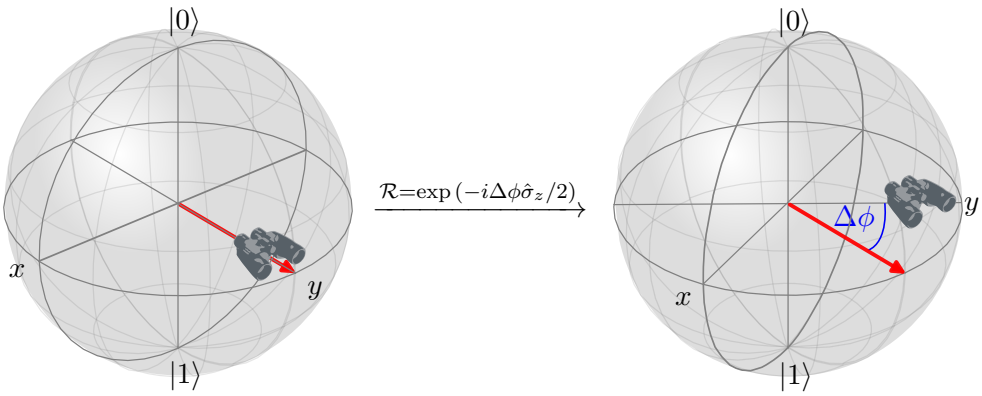

Figure 2.6: Rotation about the z-axis. A rotation about the z-axis can be realised by changing the reference frame using the rotation operator $\mathcal{R}$. This operation is equivalent to rotating the Bloch sphere by $\Delta\phi$.

If $\mathcal{R}$ is applied onto some arbitrary initial state $|\Psi\rangle = a\,|0\rangle + b\mathrm{e}^{i\phi}\,|1\rangle$, it follows:

$$|\Psi\rangle \xrightarrow{\mathcal{R}} a\mathrm{e}^{-i\Delta\phi/2}\,|0\rangle + b\mathrm{e}^{i(\phi+\Delta\phi)/2}\,|1\rangle \Leftrightarrow a\,|0\rangle + b\mathrm{e}^{i(\phi+\Delta\phi)}\,|1\rangle\,. \tag{2.33}$$

Thus, the relative phase changes by $\Delta\phi$, which corresponds to a rotation around the z-axis in the Bloch sphere representation, as sketched in figure 2.6. Experimentally this can be realised by adapting the readout basis and the phases of the control pulses. The second option, namely applying a time-independent magnetic field orientated along the z-axis, yields the following Hamiltonian:

$$\mathcal{H}_{\mathrm{DC}} = \hbar\Omega_0\frac{\sigma_z}{2}, \tag{2.34}$$

where Ω_0 includes the field strength and the coupling to the qubit. The corresponding time evolution operator reads:

$$\mathcal{U}_{\mathrm{DC}} = \exp\left(-i\frac{\Omega_0 t}{2}\sigma_z\right), \tag{2.35}$$

which is the same as $\mathcal{R}$ if $\Delta\phi = \Omega_0 \cdot t$ and thus, by controlling Ω_0 and t the rotation angle can be adjusted.

2.6 Steps of a quantum measurement

A typical quantum sensing experiment is a sequence of the operations discussed in the previous sections. A measurement usually can be divided into three parts, which are sketched in figure 2.7 and have to be repeated many times in order to gather enough stat-

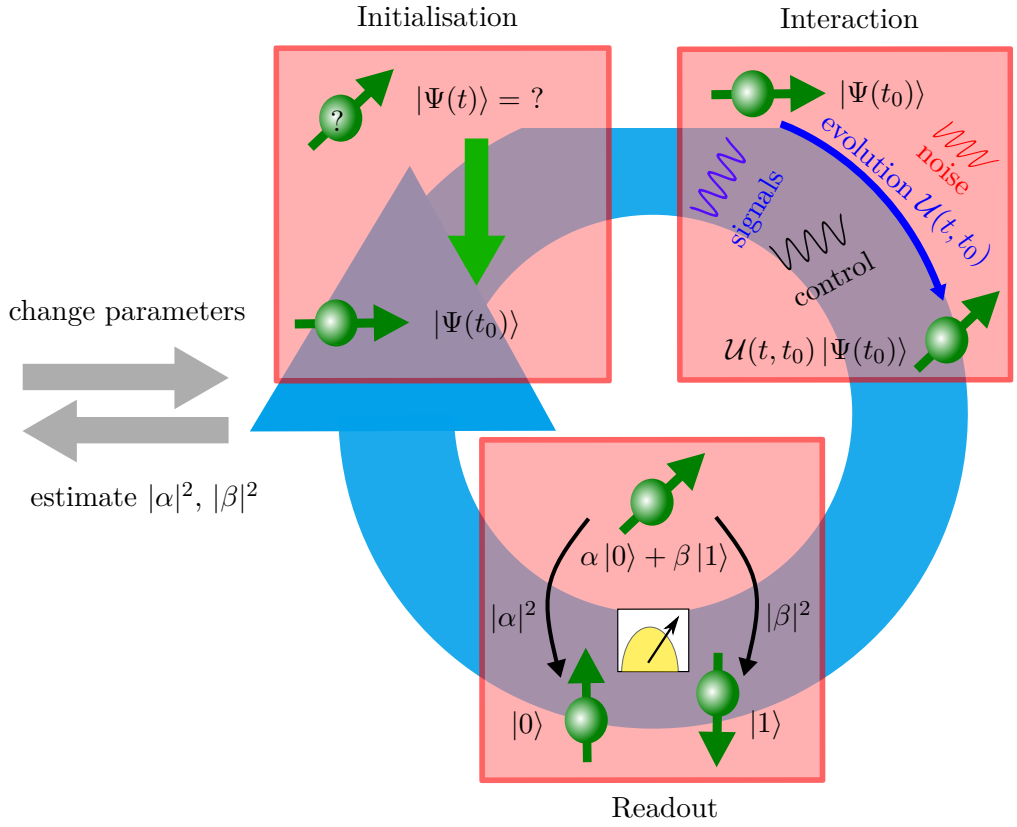

Figure 2.7: Steps in a typical quantum sensing measurement. First, the qubit is initialised into a specific state $|\Psi(t_0)\rangle$, from where it interacts with signals of interests, control fields or noise sources. Thereby, the quantum state evolves and the measurement information is encoded in $|\Psi(t)\rangle$. During the readout the qubit is projected to one of its eigenstates and by estimating the probabilities $|\alpha|^2$ and $|\beta|^2$, the measurement information can be extracted.

istics. First, the quantum system needs to be initialised into a known state $|\Psi(t_0)\rangle$, which is usually a superposition state. Thereafter, the sensor interacts with signals, noise sources as well as optionally applied control fields and evolves according to the corresponding time evolution operator $\mathcal{U}(t, t_0)$. The sensor state is readout to retrieve the encoded information and after repeating these steps many times, the probability P_0 to detect state $|0\rangle$ can be estimated. From P_0 relevant parameters of the signal can be extracted. Afterwards, one or more measurement variables can be changed, for example to probe a different frequency component for spectroscopy.

3 The nitrogen-vacancy centre in diamond

A highly promising quantum system which has the potential to find use as quantum sensor is the nitrogen-vacancy (NV) centre in diamond, the centrepiece of this work. As point defects consisting of a nitrogen atom and an adjacent vacancy, NV centres can be considered as atoms trapped in the diamond lattice. While they have many atom like properties, no trapping fields or high vacuum conditions are required. Their possible use at ambient conditions is essential for biological samples and lifescience.

First identified in 1976 [36], it took almost 30 years to realise the high potential of these defects. The many useful properties, as optical readout [37,38] and coherent manipulation of the electronic spin [39], its relatively low relaxation rates [40] and high stability, made NV centres to a very relevant research topic. As figure 3.1 shows, the interest in NV centres has been growing almost exponentially over the last 20 years and there has been a more than fivefold increase of scientific publications in the last decade.

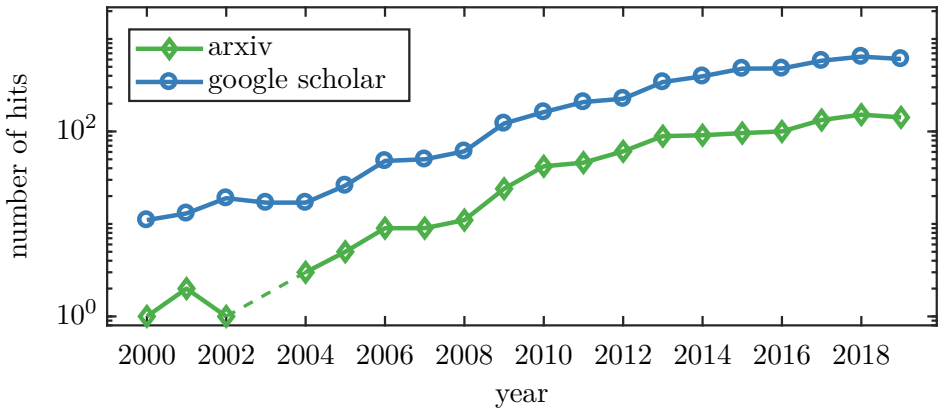

Figure 3.1: Publications relating to NV centres. Number of hits per year when searching for nitrogen-vacancy centres on arXiv and Google scholar[1]. Although these findings do not correspond to the exact number of scientific publications, the trend is representative.

[1]For arXiv: term: "nitrogen vacancy cent??" in "All fields", date of search: 15th Nov, 2019
For Google scholar: term: "nitrogen vacancy center" AND "nitrogen vacancy centre", date of search: 15th Nov, 2019

To the present day, detection of magnetic fields [41, 42], electric fields [43–45], temperature [46–48], pH values [49] or pressure and force [50–52] has been experimentally demonstrated. Due to this wide range of applications, NV centres are highly interesting for medicine, geophysics, biophysics or navigation. For example, the high sensitivity and spatial resolution make them very promising candidates for nuclear magnetic resonance (NMR) on the nanoscale [53–55]. The first successful experimental realisations were published in 2013 [22, 23]. In these experiments, the detection volume, that means the voxel from which most of the signal originates, was estimated to be on the order of $100\,\mathrm{nm}^3$. Furthermore, it was shown, that the sensitivity is sufficient to detect a single nuclear spin [24] – the absolute sensitivity limit for NMR.

3.1 The nitrogen-vacancy centre as a qubit

In this section, the NV centre is introduced and its most important properties that qualify it as a qubit are discussed.

3.1.1 Quantum systems in solid states

Discrete and resolvable energy levels exist in many types of materials [56], as for instance free atoms or condensed matter systems, and in principle every pair of levels qualifies as a qubit. The advantages of solid state systems are far reaching. Nowadays, most electronic devices and technologies are mainly based on solid state components. Thus, there is hope that solid state quantum systems are compatible with the current micro- and nanoelectronics and combining these systems with available technologies is feasible. Moreover, solid state systems are usually very compact and robust. Both attributes are especially important to have potential application in our daily life. Well developed fabrication techniques promise good preparation, accurate localisation and good scalability.

A large disadvantage of quantum systems in solids is that they are embedded in an environment which they interact strongly with, for example via phonons. These interactions lead to unwanted relaxation, often within time scales too short for a meaningful operation. Special conditions as cryogenic temperatures require a complex setup and are not compatible in combination with most biological samples.

Besides superconducting devices [57], especially defects in semiconductors have recently attracted a lot of attention [4, 58–62]. The idea is to add additional energy levels inside the band gap of these materials, for example by introducing lattice defects or impurities. Since those energy levels are very well isolated and the defects are very efficiently spatially localised by the inflexible lattice, they qualify as building blocks for qubits. As sketched in figure 3.2, individual levels close to the conduction or valence band as well as multiple

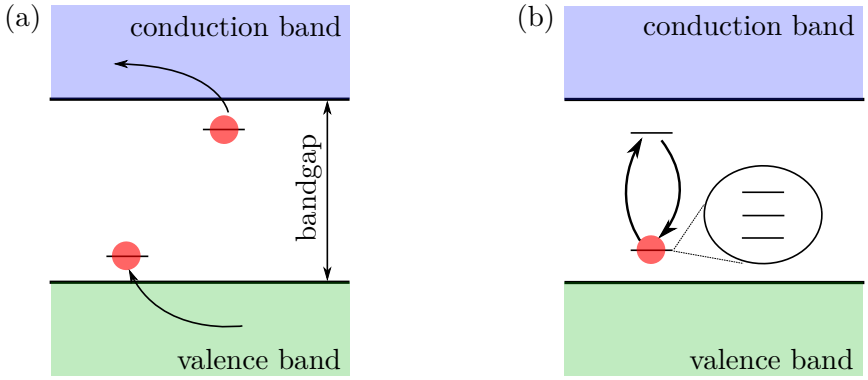

Figure 3.2: Discrete energy levels in solid state systems. Additional levels inside the bandgap of a semiconductor can be introduced by lattice defects or impurities. (a) Both, individual levels close to the valence or conduction band and (b) multiple isolated energy states are possible. These levels can further split up due to fine or hyperfine interactions.

isolated defect levels are possible. These levels can further split up, for example due to fine or hyperfine interactions. Especially diamond with its large band gap, its very stiff lattice and further extraordinary properties, which are in more detail discussed in the next section, is a very promising candidate as host material for solid state quantum systems.

3.1.2 Diamond as a host material

Diamond is an exceptional material with widespread applications. Due to its overwhelming beauty, it is famous as the probably most popular gemstone in the jewellery industry. However, diamond also plays an important role in other areas of industry and science due to its extraordinary properties, for example its extreme hardness, which is the highest known under the natural materials. This is a result of the tight packing of carbon atoms, and the strong bonds between them make diamond an ideal material for cutting and abrasive tools. Diamond also has the highest known thermal conductivity at room temperature of about 2000 W/(Km) and phonons provide the main mechanism for spreading the heat. For high purity diamond and temperatures around 100 K, this number can increase to 41 000 W/(Km) [63]. In diamond each sp^3-hybridised carbon atom is covalently bound to four neighbouring carbon atoms with a distance of 1.54 Å. The resulting unit cell is face-centred cubic with a lattice constant of 3.57 Å at ambient conditions [64] and a two-atomic basis [(0, 0, 0), (1/4, 1/4, 1/4)]. Although, diamond is not the stable allotrope of carbon at ambient conditions, the conversion to graphite is rather slow due to the high activation barrier between $728 - 1159$ kJ/mol, depending on the diamond surface [65].

Probably most relevant for quantum applications is that diamond is a semi-conductor with a large indirect band gap of 5.47 eV [66].

Table 3.1: Types of diamond. Diamonds can be categorised by their nitrogen (N) and boron content. Most naturally generated diamonds are of type Ia. More interesting for scientific applications are low-defect diamonds of type IIa (values taken from [68]).

type	description	N content in ppm
Ia	natural diamond with aggregates of nitrogen	500 - 3000
Ib	single substitutional N	40 - 100
IIa	very low N content	< 1
IIb	boron impurities (p-type doping)	< 1

Defects in diamond

Defects inside the band gap of diamond are of great interest for quantum applications. Some of them can potentially be used for qubits, but on the other hand, they also represent possible sources of noise. Although the diamond lattice is very stiff, there are a variety of possible defects and up to date more than 500 optically active defects are known [67]. The simplest defect is a vacancy, so a missing carbon atom in the lattice, but also impurity atoms can be found in diamond. Since boron and nitrogen are the direct neighbours of carbon in the periodic table, they have similar sizes and are thus predestined to replace a carbon atom in the diamond lattice. Due to that, boron and nitrogen are the most prevalent impurities and their content can be used to categorise diamonds as shown in table 3.1.

Defects can influence the physical properties of the host diamond, as for example the colour. While pure diamond is transparent for visible light (due to the large band gap), additional energy levels generated by defects and impurities can absorb and emit light in the visible range and give the diamond a colour, as shown in figure 3.3. For that reason these defects are referred to as *colour centres*. Due to their high nitrogen content most natural diamonds are of type Ia. Since both stable isotopes of nitrogen also form other optically active defects with electronic and nuclear spins, which represent a source of optical and magnetic noise, samples with a very high nitrogen concentration are usually unsuited for certain scientific purposes. In contrast, diamonds of type II with a very low nitrogen content are more interesting and all results presented in this work are obtained using type IIa diamonds. A more detailed description of the relevant diamonds can be found in appendix A.1.5. Since type II diamonds are usually not found naturally, it is essential to artificially synthesise them. Manufacturing of diamond has the additional advantage that further properties, as the type and density of impurities, can be controlled to a certain degree. The most prominent techniques are the chemical vapour deposition (CVD) process and the high pressure high temperature (HPHT) method, and they are discussed in more detail in appendix A.2.

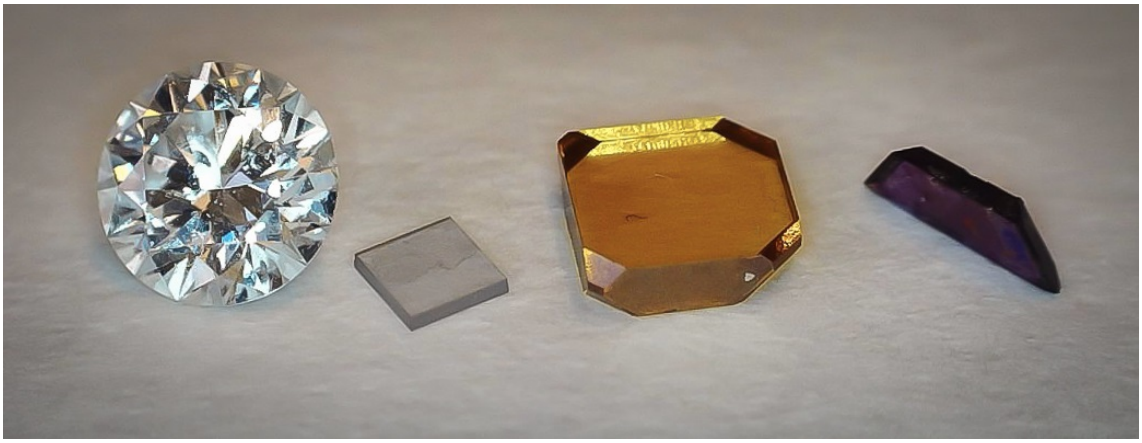

Figure 3.3: Photography of different types of diamond. Pure diamonds do not absorb visible light due to their big band gap and are thus transparent. In the jewellery industry, diamonds are often polished into a specific shape (left). For research purposes a flat surface is usually more convenient since scattering of light is reduced (second from left). Impurities can introduce additional levels in the band gap, which might absorb light and give the diamond a colour. Nitrogen atoms lead to a yellow colouration (second from right). In combination with vacancies, they form NV centres which are of high interest for quantum sensing. Diamonds with high concentration of NV centres have a violet colour (right). The photography was taken by Jochen Scheuer.

Out of the variety of possible defects in diamond, a few have attracted increased interest as building blocks for possible quantum applications. For example, the silicon-vacancy centre has, due to its high Debye-Waller factor, properties which makes it interesting as a source for single indistinguishable photons [69–72]. These are relevant for applications requiring entanglement, as quantum repeaters. The recent discovery and examination of the germanium-vacancy shows that there is still on-going research to find new candidates [73, 74]. Theoretical calculations can help to predict and find defects with suitable properties as the recently prepared tin-vacancy centre demonstrates [75].

3.1.3 The nitrogen-vacancy centre

The probably most famous and examined defect in diamond is the nitrogen-vacancy (NV) centre – the quantum system of interest in this work. As sketched in figure 3.4(a), the NV centre is a point defect, which consists of a nitrogen atom substituting a carbon atom and an adjacent vacancy. It has C_{3v} symmetry and the symmetry axis coincides with the imaginary connecting line between the nitrogen atom and the vacancy. Due to that, the NV centre can be found in four different crystallographic orientations, as shown in figure 3.4(b).

NV centres have a variety of extraordinary properties, which make them very interesting candidates for applications in quantum technologies. For example, they are optically

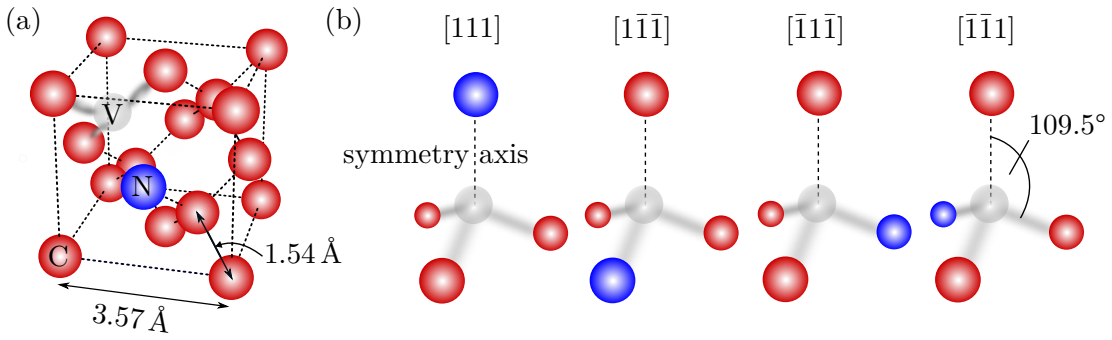

Figure 3.4: The nitrogen-vacancy centre in diamond. (a) Sketch of the NV centre in diamond. It consists of a nitrogen atom (blue) replacing a carbon atom (red) and an adjacent vacancy (grey). (b) The four possible orientations of NV centres in diamond. The bonding angle is about 109.5°.

stable under illumination. Furthermore, NV centres are vigorously confined in the stiff diamond lattice, which results in an in principle unlimited lifetime – without the need of special conditions. One consequence is, that they are stable up to temperatures of about 1700 °C [76]. Compared to other defects in diamond, NV centres stand-out due to their relatively long relaxations times for the electron spin (see section 4.5.4) – even at ambient conditions. Another advantage is the optical access, which allows initialisation (see section 3.2) and readout (see section 3.3) of the spin state.

For applications as a quantum sensor two attributes are essential. First, the NV centre introduces discrete energy levels into the band gap of diamond. As sketched in figure 3.5(b), both the ground and the first excited state are located in this band gap. In principle, these two states form a qubit, however the lifetime in the excited state is very short ($\approx 10\,\mathrm{ns}$), which would prevent a high sensitivity. Second, there are two unpaired electrons forming a spin $S = 1$ system, as shown in figure 3.5(a). In total six electrons contribute to the electronic structure – two unbounded electrons from the nitrogen, three unbounded electrons from the carbon atoms next to the vacancy and one electron from a donor in the lattice. Calculations indicate that these electrons fill the ground and excited a_1 states [77]. The remaining two electrons are unpaired in the e_x and e_y levels, generating a spin triplet $^3A_2$ state [78]. Spatially, these electronic states are located close to the carbon atoms and the vacancy, while the spin density on the nitrogen atom is nearly negligible [79]. Without an external magnetic field the $m_s = +1$ and $m_s = -1$ sub-levels are degenerate, while the $m_s = 0$ sub-level has a down-shifted energy (about $11.9\,\mu\mathrm{eV} = h \cdot 2.87\,\mathrm{GHz}$). Any combination of two out of these three spin-levels can be used as an effective qubit, as exemplified for the $m_s = 0$ and $m_s = -1$ states in figure 3.5(b). As spin systems are very sensitive to magnetic fields, they are excellent magnetic field sensors.

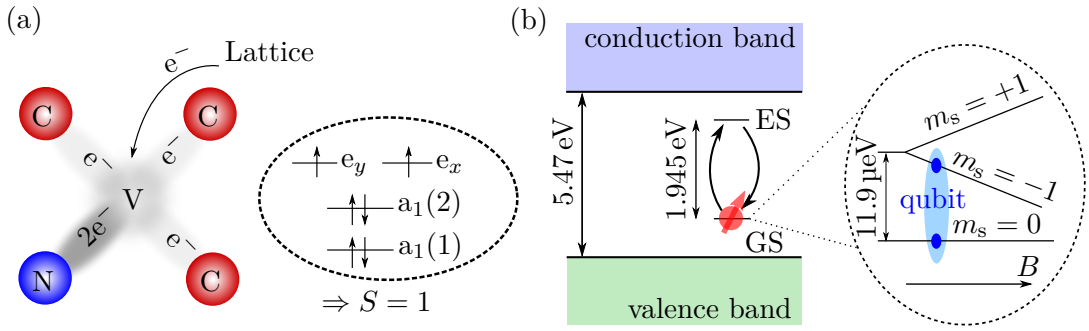

Figure 3.5: The nitrogen-vacancy centre as a spin qubit. (a) The NV centre as electron spin. The electronic structure consists of one electron from the lattice and five electrons, which are contributed by unbound electrons from the next neighbour nitrogen and carbon atoms. Four of these electrons fill the ground $a_1(1)$ and excited $a_1(2)$ states. The remaining two unpaired electrons in the e_x and e_y states form a spin $S = 1$ system. (b) The NV centre as qubit. Both, the ground state (GS) as well as the excited state (ES) lie in the band gap of diamond. Two spin states of the ground state can be used as an effective qubit, as indicated with the $m_s = 0$ and $m_s = -1$ levels. By applying an external magnetic field B, the $m_s = +1$ and $m_s = -1$ states split up due to the Zeeman effect.

However, this electronic configuration is not always present and the NV centre can occur in different charge states. If the above discussed negatively charged NV centre loses one electron, for example due to optical ionisation, it becomes the neutrally charged NV^0 centre [80, 81]. Recently, the stabilisation of the positively charged NV^+ centre has been observed experimentally [82]. From here on the abbreviation NV explicitly refers to the negatively charge state unless specified otherwise.

Due to the high nitrogen and vacancy content, NV centres usually exist in every diamond. However, for scientific purposes it is desirable to have control over certain properties as position or density. In appendix A.2, techniques to create artificial NV centre are discussed.

3.1.4 The ground state Hamiltonian of the nitrogen-vacancy centre

For defects in diamond with an electronic spin, the ground state spin Hamiltonian can usually be classified into four terms [83]. The first term $\mathcal{H}_{ZF}$ describes the interaction between the unpaired electrons. The coupling of the electron spin to an external magnetic field due to the Zeeman effect is captured by $\mathcal{H}_Z$. $\mathcal{H}_{hf}$ accounts for the hyperfine interactions between the electron spin and coupled nuclear spins and the quadrupole interaction is described by $\mathcal{H}_Q$. The full Hamiltonian then reads:

$$\mathcal{H}_{NV} = \mathcal{H}_{ZF} + \mathcal{H}_Z + \mathcal{H}_{hf} + \mathcal{H}_Q. \tag{3.1}$$

An overview of all individual terms is sketched in figure 3.6 and a compilation of the relevant coupling constants can be found in table 3.2. Further small couplings, as the nonsecular Zeeman, nonsecular hyperfine and nuclear Zeeman interaction, are neglected here [84]. Since the excited state is only important during the optical pumping cycle for initialisation and readout (compare sections 3.2 and 3.3), but is irrelevant during the sensing period, it is also not discussed here and the interested reader is referred to [85–87].

Zero-field splitting

Due to dipole-dipole interactions between the two unpaired electrons of the NV centre, the $m_\mathrm{s} = 0$ spin state is energetically more favourable and the $m_\mathrm{s} = 0$ and the $m_\mathrm{s} = \pm 1$ sublevels are not degenerate. The corresponding zero-field Hamiltonian $\mathcal{H}_\mathrm{ZF}$ is given by:

$$\mathcal{H}_\mathrm{ZF}/h = \vec{S}^\mathrm{T} \hat{D} \vec{S}, \tag{3.2}$$

where $\hat{D}$ is the zero-field tensor and $\vec{S} = (\hat{S}_x, \hat{S}_y, \hat{S}_z)^\mathrm{T}$ is the spin vector with the spin matrices:

$$\hat{S}_x = \frac{1}{\sqrt{2}} \begin{pmatrix} 0 & 1 & 0 \\ 1 & 0 & 1 \\ 0 & 1 & 0 \end{pmatrix}, \; \hat{S}_y = \frac{1}{\sqrt{2}} \begin{pmatrix} 0 & -i & 0 \\ i & 0 & -i \\ 0 & i & 0 \end{pmatrix}, \; \hat{S}_z = \begin{pmatrix} 1 & 0 & 0 \\ 0 & 0 & 0 \\ 0 & 0 & -1 \end{pmatrix}. \tag{3.3}$$

In the eigenvalue framework, $\hat{D}$ is diagonal and can be written as:

$$\hat{D} = \begin{pmatrix} D_x & 0 & 0 \\ 0 & D_y & 0 \\ 0 & 0 & D_z \end{pmatrix} = \begin{pmatrix} \frac{1}{3}D + E & 0 & 0 \\ 0 & -\frac{1}{3}D - E & 0 \\ 0 & 0 & \frac{2}{3}D \end{pmatrix}, \tag{3.4}$$

where $D = \frac{3}{2}D_z$ and $E = \frac{D_x - D_y}{2}$ is used. Then, $\mathcal{H}_\mathrm{ZF}$ simplifies to [83]:

$$\mathcal{H}_\mathrm{ZF}/h = D\left(\hat{S}_z^2 - \frac{S(S+1)}{3}\mathbb{1}\right) + E(\hat{S}_x^2 - \hat{S}_y^2), \tag{3.5}$$

where $D = 2.87\,\mathrm{GHz}$ is the axial dipole-dipole interaction. Here, E is only non-zero if the C_{3v} symmetry is broken, for example due to an electric field or strain [88] and is usually in the range of several MHz, thus much smaller than D. Since the term $S(S+1)/3 \cdot \mathbb{1}$ is just a constant offset, it can also be omitted. Since dipole-dipole interactions depend on the distance r between the electrons as [83]:

$$D \sim \langle r^{-3} \rangle, \tag{3.6}$$

where the average is over all possible locations of the two electron spins, all parameters which change the crystal structure have an influence on D. Important examples are pressure p ($\mathrm{d}D/\mathrm{d}p = 1.46\,\mathrm{kHz/bar}$ [51]) and temperature T ($\mathrm{d}D/\mathrm{d}T = -74.2\,\mathrm{kHz/K}$ [89]).

Electron Zeeman Interaction

The interaction of the NV centre with a magnetic field is described by the electron Zeeman part $\mathcal{H}_\mathrm{Z}$:

$$\mathcal{H}_\mathrm{Z}/h = \gamma_\mathrm{NV}\vec{B}^\mathrm{T}\vec{S}, \tag{3.7}$$

where $\vec{B}$ is the vector of the magnetic field, which describes its strength and direction and $\gamma_\mathrm{NV} \approx 28\,\mathrm{GHz/T}$ is the gyromagnetic ratio of the electronic spin, which has approximately identical axial and non-axial components [90]. If the magnetic field is orientated parallel to the symmetry axis of the NV centre, $\mathcal{H}_\mathrm{Z}$ reads:

$$\mathcal{H}_\mathrm{Z}/h = \gamma_\mathrm{NV}B_z\hat{S}_z. \tag{3.8}$$

While the $m_\mathrm{s} = 0$ spin state is insensitive to magnetic fields, the $m_\mathrm{s} = \pm 1$ levels are shifted equally, but with a different sign and thus their degeneracy is lifted. Magnetic signals further shift these energy levels and detecting these changes is the measurement principle of magnetometry with the NV centre.

Hyperfine interaction

The interactions between the electron spin of the NV centre and coupled nuclear spins, as for example the inherent nitrogen spin, is described by the hyperfine Hamiltonian:

$$\mathcal{H}_\mathrm{hf}/h = \sum_n \vec{S}^T\hat{A}_n\vec{I}_n, \tag{3.9}$$

where the $\hat{A}_n$ are the hyperfine coupling tensors, $\vec{I}_n = (\hat{I}_{n,x}, \hat{I}_{n,y}, \hat{I}_{n,z})^\mathrm{T}$ are the nuclear spin vectors and the sum goes over all coupled nuclear spins. $\mathcal{H}_\mathrm{hf}$ combines the effects due to isotropic Fermi contact interactions and anisotropic dipole interactions [83, 91]. The tensors $\hat{A}_n$ are axially symmetric due to the 3-fold rotational symmetry of the NV centre and can be written as [90]:

$$\hat{A}_n = \begin{pmatrix} A_{n,\perp} & 0 & 0 \\ 0 & A_{n,\perp} & 0 \\ 0 & 0 & A_{n,\parallel} \end{pmatrix}, \tag{3.10}$$

Table 3.2: Coupling constants for the NV centre. The main contributions to the ground state Hamiltonian are usually the zero-field splitting parameter D and the Zeeman interaction with coupling γ_{NV}. Nitrogen isotope specific constants are the parallel ($A_{||}$) and perpendicular ($A_{\perp}$) hyperfine couplings and the quadrupole parameter P. Values taken from [94].

isotope	D (GHz)	γ_{NV} (GHz/T)	$A_{\|\|}$ (MHz)	$A_{\perp}$ (MHz)	P (MHz)
^{14}N	2.87	28.0	−2.14	−2.79	−5.01
^{15}N			3.03	3.65	–

where $A_{n,\parallel}$ and $A_{n,\perp}$ are the parallel and perpendicular hyperfine coupling parameters. For the ^{14}N and ^{15}N isotopes, the respective values can be found in table 3.2. For other nuclei these parameters depend on the relative positions [91, 92]. Assuming only one coupled nuclear spin, the hyperfine interaction Hamiltonian reads:

$$\mathcal{H}_{\mathrm{hf}}/h = A_{\parallel}\hat{S}_z\hat{I}_z + A_{\perp}(\hat{S}_x\hat{I}_x + \hat{S}_y\hat{I}_y). \tag{3.11}$$

The first term in the equation above commutes with $\mathcal{H}_{\mathrm{ZF}}$ and thus shifts the individual spin levels. The second term, which includes $A_{\perp}$, does not commute with $\mathcal{H}_{\mathrm{ZF}}$, and thus shifts the energy levels only in second order [84, 93]. Most prominent among other nuclear spins in the vicinity are ^{13}C spins in the diamond lattice.

Quadrupole interaction

All nuclear isotopes with a spin larger than $I > 1/2$, as for example the ^{14}N nucleus, have a quadrupole moment. The corresponding Hamiltonian can be written as [78]:

$$\mathcal{H}_{\mathrm{Q}}/h = P\left(\hat{I}_z^{\,2} - \frac{I(I+1)}{3}\mathbb{1}\right), \tag{3.12}$$

where P is the quadrupole moment [94] and $I(I+1)/3 \cdot \mathbb{1}$ is just an omittable offset. As a consequence, there is only a contribution if the nuclear spin is in one of the $m_{\mathrm{I}} \neq 0$ states.

The nitrogen-vacancy centre as a qubit

Due to the three spin levels, the NV centre is not a classical qubit. In addition, couplings to nearby nuclei further complicate the level structure. Just taking the inherent nitrogen spin into account, there are seven (five) split levels for ^{14}N (^{15}N), as shown in figure 3.6.

However, since magnetic fields in the microwave regime are used to drive transitions between different states in this thesis (compare section 3.5), there are some restrictions. For example, when microwave photons are absorbed, the electron spin quantum number may change only by $|\Delta m_s| = 1$, while the nuclear spin state is unaffected (red arrows

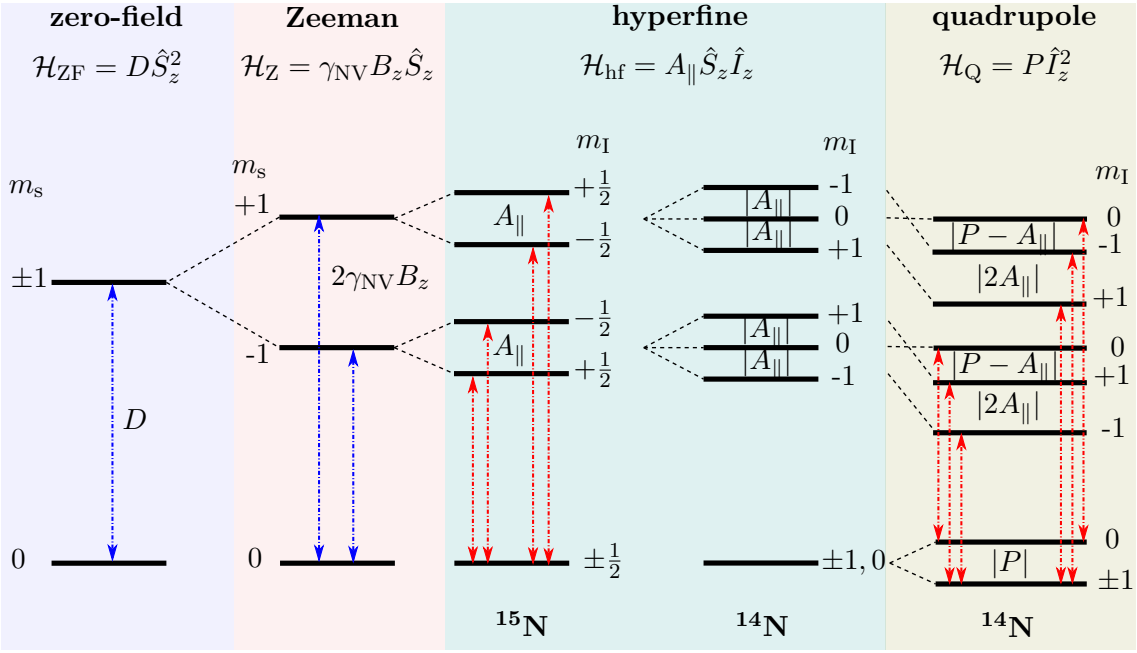

Figure 3.6: Level scheme of the NV centre's electronic spin in the ground state. The four main interactions are the zero-field splitting (blue), the electron Zeeman interaction (red), the hyperfine interaction (green) and in the case of coupled $I > 1/2$ nuclei the quadrupole interaction (yellow). By using resonant microwaves, the red and blue dotted line are allowed transitions. Electromagnetic fields in the radiofrequency range can be used to change the nuclear spin state (not shown). Values for the coupling terms can be found in table 3.2. Not considered contributions are the nonsecular Zeeman, the nonsecular hyperfine and the nuclear Zeeman interactions. For reasons of overview the Planck constant h is omitted in the equations.

in figure 3.6). Furthermore, the frequency ω of the microwave needs to be resonant to the energy difference of two levels ($\hbar\omega_0$), which allows to address only one transition and thus to isolate a qubit. The transition amplitude depends on the frequency detuning ω_Δ and the driving strength Ω of the microwave field (compare section 2.5). For example, all transitions with a frequency much smaller than Ω are driven simultaneously. As a consequence, if Ω is much larger than the respective hyperfine splittings, the energy scheme simplifies to the three electron spin levels and two possible transitions (blue arrows in figure 3.6). This is especially convenient, since the coupled nuclear spins do not have to be initialised.

On the contrary, all levels for which ω_Δ is much larger than Ω have a negligible transition amplitude and can be ignored. Due to the large ZFS and Zeeman terms, the resonance frequencies for the $m_s = 0 \Leftrightarrow m_s = -1$ and $m_s = 0 \Leftrightarrow m_s = +1$ transitions are usually very different. Thus, by conveniently choosing the microwave frequency and driving strength, the NV centre represents an effective qubit.

3.2 Initialisation of the nitrogen-vacancy centre

One of the exquisite features of the NV centre is that its electron spin can be transferred into the $m_s = 0$ state by optical pumping. As depicted in figure 3.7(a), optical excitation from the orbital-singlet, spin-triplet $^3A_2$ ground state [78] into vibronic levels above the first excited state can be achieved by non-resonant laser illumination. Although the excited ^3E state is orbital-doublet and spin-triplet, it can be modelled as an effective spin-triplet system [87, 95] with a zero-field splitting of 1.42 GHz [85, 96] above temperatures of about $20 - 25$ K, where the spin-orbit coupling is averaged out. Non-radiative decay into the lowest vibrational band happens on a very short timescale of about $0.05 - 4$ ps [97, 98].

For the relaxation back to the ground state there are two possible paths, which are sketched in figure 3.7(b). The direct decay under emission of a photon is spin-conserving (red arrows) and happens mainly into one of the vibronic levels of the ground state. The second decay path involves a non-radiative intersystem crossing (ISC) to intermediate states, which are energetically located between the ground and excited states. They consist of an orbital-singlet, spin-singlet state $^1A_1$ and an orbital-doublet, single spin $^1E_{1,2}$ state [95], which are coupled by an optical transition with a ZPL of 1042 nm [99]. The ISC from the excited state to the $^1A_1$ state is mainly mediated by spin-orbit coupling and strongly spin-dependent [95]. While for the $m_s = 0$ spin state this transition is very weak, it is about four times more probable for the $m_s = \pm 1$ spin states [100, 101]. After a fast decay to the ^1E state, the transition to the ground state shows only a small spin-dependency, as recent studies report [100, 101].

As a consequence, the probability for a change of the spin state after one optical cycle is about 8 % when starting in the $m_s = 0$ state, and roughly 35 %, if the initial state was $m_s = \pm 1$ [100]. Thus, on average the $m_s = \pm 1$ spin states get depopulated in favour of the $m_s = 0$ state. Since there is a small chance for both, a ISC from the excited $m_s = 0$ state into the intermediate $^1A_1$ state and a transition from the ^1E state to the $m_s = \pm 1$ levels in the ground state, unity initialisation fidelity cannot be observed and an equilibrium is reached. It is reported to be about 80 % for ensembles [102] of NV centres and about $84 - 92$ % for single defects [103–105].

This principle works up to temperatures of at least 500 K [20]. Initialisation into any other qubit state is possible by combining the above described optical pumping into the $m_s = 0$ state and subsequent coherent control (see section 3.5). After turning off the optical illumination, it can not be excluded that the NV centre is in the intermediate states. Therefore, an additional waiting time of at least 1 µs for relaxation should be included before starting further experiments. The duration to reach the above described

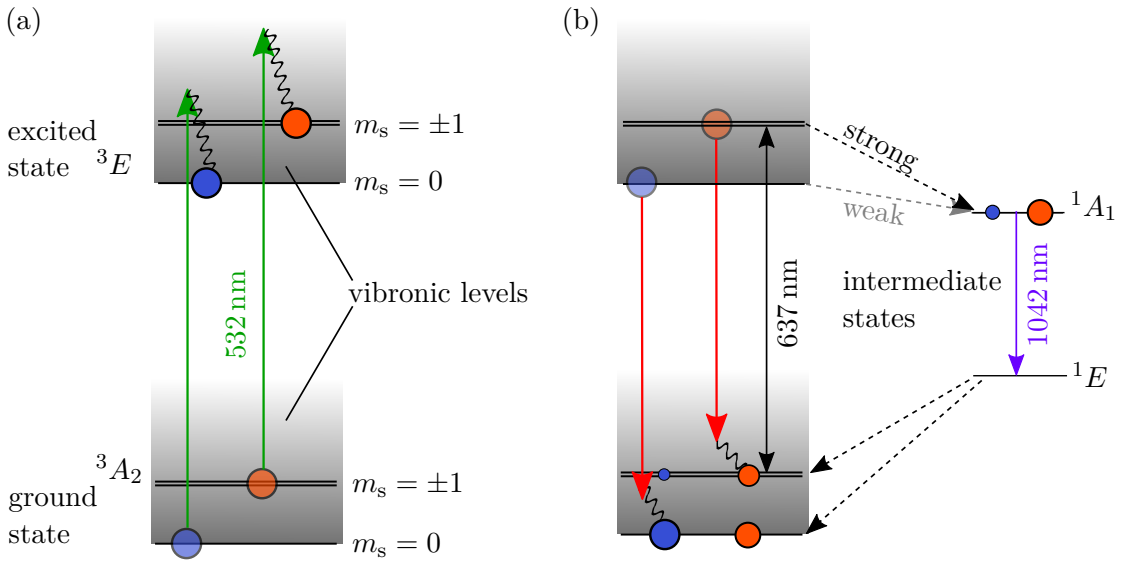

Figure 3.7: Initialisation of the NV centre's electronic spin by optical pumping. (a) Off-resonant excitation from the $^3A_2$ ground state into vibronic levels above the ^3E excited states preserves the spin state. (b) For the relaxation back to the ground state, there are two relevant paths. The direct decay into vibronic levels of the ground state is also spin-conserving. The emitted photons are red-shifted compared to the zero phonon line at 637 nm. The second decay path involves a spin-dependent intersystem crossing to intermediate $^1A_1$ and ^1E states. This transition is stronger for the $m_s = \pm 1$ spin states. The decay from the ^1E into the $m_s = 0$ ground state is slightly more probable. As a consequence, an optical cycle increases the probability to be in the $m_s = 0$ spin state.

equilibrium depends on the excitation power since it determines the excitation rate from the ground into the excited state.

Dynamical nuclear polarisation

This spin polarisation can also be used to initialise other coupled qubits. A very promising application is dynamical nuclear polarisation. In conventional nuclear magnetic resonance and magnetic resonance imaging experiments, the signal originates from the thermal polarisation of the target nuclear spins, which is very low at ambient conditions (see section 5.1 for more information). Improving the polarisation by enhancing the magnetic bias field requires complex as well as expensive instruments and the actual gain is marginal. Also, using traditional methods to transfer the much higher thermal polarisation of electron spins needs cryogenic temperatures and thus an elaborated as well as expensive setup and is time-consuming [106, 107].

In contrast, the electron spin of the NV centre can be initialised optically within a few microseconds at ambient conditions. The idea is to polarise a very high number of NV centres located just a few nanometres below the surface of the diamond and use their

coupling to the nuclear spins, positioned on the top of the diamond, to transfer their spin polarisation. For this purpose, nanodiamonds are very interesting since the average NV-sample distance is smaller. In the last years, the first proof-of-principle experiments have shown polarisation of external nuclear spins [108, 109].

3.3 Readout of the nitrogen-vacancy centre

A number of different techniques to measure the electron spin of NV centres have been reported recently. For example, one commonly used readout is based on the detection of the spin-dependent photoluminescence (PL). The charge dynamics under illumination facilitate spin-to-charge conversion techniques. The different charge states can be either discriminated optically [105, 110, 111] or by electrically detecting the freed charge carriers [112–114]. At cryogenic temperatures spin-selective excitation yields fluorescence only from one of the states and allows the readout with a very high contrast [115–117]. Furthermore, infra-red absorption techniques can also be used [118]. The following concentrates on the readout techniques relevant for this thesis and a more complete overview of all currently known detection methods can be found in [119].

3.3.1 Readout via spin-dependent fluorescence

The probably simplest way to measure the spin state of NV centres is to record the spin-dependent fluorescence. Although spin-selective excitation is not possible at room temperature, since the optical transitions are not narrow enough, spin-conserving excitation from the ground into the excited state can be achieved by illumination with laser light. The lifetime in the excited state is about 7 ns for the $m_s = \pm 1$ spin states and around 13 ns for the $m_s = 0$ spin state [100], as indicated in figure 3.8(a). Other studies reported similar values [101, 120]. As discussed in section 3.2, there are two possible decay paths.

The spin-conserving direct relaxation back into the ground state is mainly into vibronic levels and thus, most of the emitted photons are red-shifted compared to the zero phonon line (ZPL) at 637 nm. A typical background corrected spectrum, recorded at ambient conditions, is shown in figure 3.8(b). Even at cryogenic temperatures only around 4 % of the total fluorescence is included in the ZPL [69, 121] and the spectrum is dominated by the large phonon sideband with a maximum around 680 nm. Optical excitation can also cause unavoidable back and forth conversion into the neutral charge state of the NV centre [80, 81, 105]. The altered electronic structure with a zero phonon line around 575 nm results in photons with a shorter wavelength. Thus, only the fluorescence above 637 nm is usually recorded (red shading) and higher energetic photons are filtered out (blue shading).

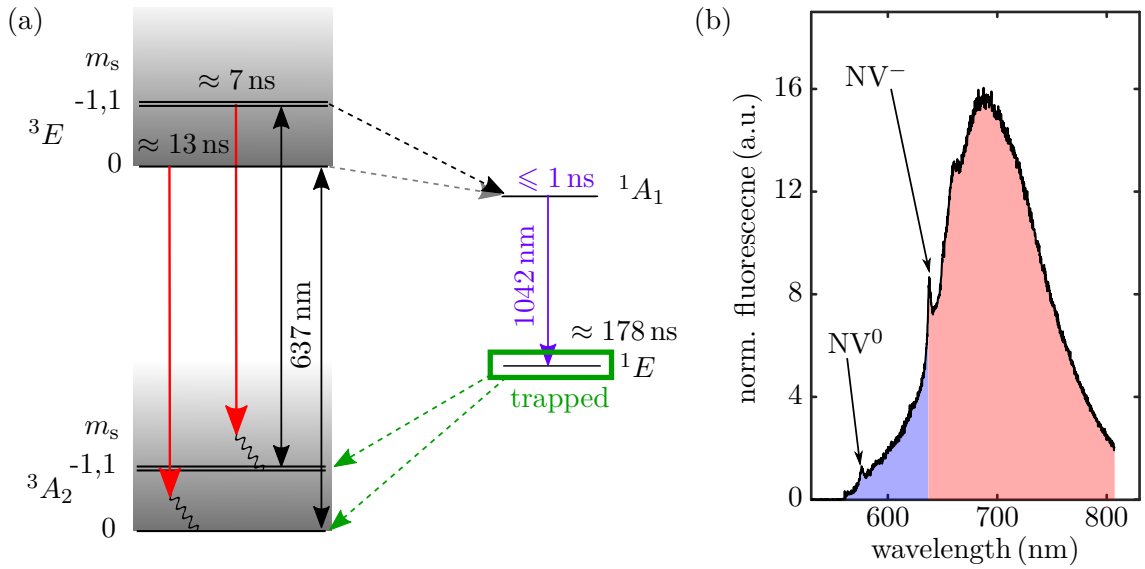

Figure 3.8: Relaxation dynamics and fluorescence properties of the NV centre. (a) While under the direct relaxation path (red arrows), visible photons are emitted, there is an infra-red transition during the decay via the ISC. The ^1E state is relatively long-living and interrupts the optical cycling. Because the ISC is much more probable for the $m_s = \pm 1$ spin states, on average less visible photons are emitted for theses states. Values are taken from [89, 100]. (b) Background corrected fluorescence spectrum of an NV centre. Most of the PL is included in the large phonon sideband. Fluorescence from the NV^0 charge state, which is due to unavoidable charge state cycling under illumination, can be partially removed by filtering out low-wavelength photons (blue shading) and only recording lower energetic PL (red shading).

The second decay path involves an ISC. After the crossing, there is a quick decay via an infrared transition (about 1042 nm [89]), whereas the ^1E state is rather long-living compared to the other involved lifetimes.

There are two reasons, why the fluorescence depends on the spin state. First, the decay via the ISC is much more probable for the $m_s = \pm 1$ states, as depicted in figure 3.8(a). Thus, the probability that a photon is emitted during one optical cycle is lower for these spin states. Second, the low relaxation rate from the ^1E state to the ground state is an efficient trap and prevents further optical excitation. The lifetime of this level is temperature dependent and values between 178 ns and 300 ns at room temperature have been reported [89,99,115]. At the same time, lots of cycles under the direct decay can take place and thereby many photons are emitted. This results in higher PL for the $m_s = 0$ spin state on average.

Time-resolved fluorescence traces are shown in figure 3.9(a). The data is an average of the PL recorded during multiple 3 µs laser pulses (532 nm). There is a clear difference between the fluorescence in the different spin states during the first 1 µs (red shading). For this example, the deviation is maximal around 130 ns and then slowly declines, as shown

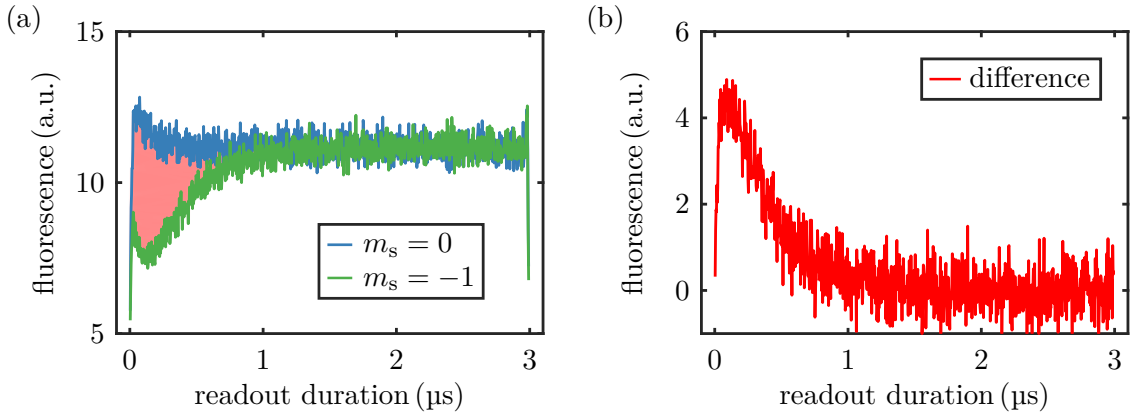

Figure 3.9: Fluorescence for different spin states as a function of time. (a) During the first 1 µs the number of recorded photons is lower if the spin state was $m_s = -1$ before the readout. (b) This difference decreases since the $m_s = 0$ state is populated during the optical cycling.

in figure 3.9(b). Even if the system is initially in the $m_s = -1$ spin state, the $m_s = 0$ state is populated during cycling through the optical transitions. The longer the readout is performed the higher is the probability that the quantum spin number is $m_s = 0$ and the optical contrast diminishes. Interestingly, the fluorescence of the $m_s = 0$ state also slightly reduces. This is due to the increasing probability that the NV centre is trapped in the ^1E states after a certain time. In order to ensure that relaxation into the ground state takes place before further measurements, a short idle time of at least 1 µs should be applied after illumination.

3.3.2 Signal-to-noise ratio

Finding the optimal readout duration requires maximising the signal-to-noise ratio (SNR), which is discussed in more detail in the following.

Measurement contrast

For the above described readout, PL photons are the measurement quantity and the typical strategy is to sum up all photons detected within a certain time window t_w. Since t_w is limited to about 1 µs and the detection efficiency is very low, on average only about $0.05 - 0.15$ photons are recorded for single NV centres within every individual readout. This is not enough for a trustworthy discrimination between the different spin states.

Therefore, an experiment is usually repeated many times and all photons recorded over these iterations are summed up. In this way it is possible to obtain the probability P_0 to

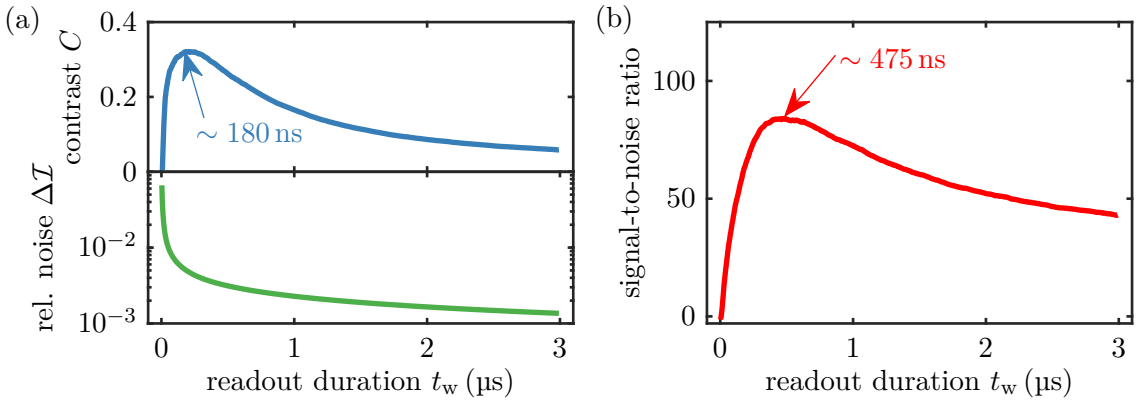

Figure 3.10: Optimal readout duration for NV centres. (a) The readout signal is the sum of the recorded photons up to t_w. Upper panel: The contrast C (compare equation (3.13)) is optimal if all photons up to around 180 ns are taken into account. Lower panel: Longer readout durations could be nevertheless beneficial, since the relative noise $\Delta\mathcal{I}$ further reduces. (b) Maximising the SNR yields an optimal compromise (here for $t_w \sim 475$ ns).

find the system in the $m_s = 0$ state, as the averaged number of detected photons $\mathcal{N}(t_w)$ is given by:

$$\mathcal{N}(t_w) = \mathcal{I}_0(t_w)P_0 + \mathcal{I}_1(t_w)(1 - P_0), \tag{3.13}$$

where $\mathcal{I}_n(t_w) = Nc_n(t_w)$, N is the number of measurement repetitions and $c_0(t_w)$ and $c_1(t_w)$ are the number of photons expected to record during t_w for $|0\rangle$ and $|1\rangle$ in a single readout, respectively. The relative contrast is here defined as:

$$C(t_w) = \frac{c_0(t_w) - c_1(t_w))}{c_0(t_w)}. \tag{3.14}$$

In the upper panel of figure 3.10(a), C is plotted as a function of the readout duration t_w, for the laser pulses in figure 3.9. The contrast first steeply increases (up to about 180 ns) where it reaches almost 32 %. Beyond that the difference between c_0 and c_1 reduces and C decreases.

Photon shot noise

Due to their quantum nature, photons can only exist in integer numbers. If the counting of the fluorescence photons can be considered as independent events, the number of detected photons varies between every measurement – even if it is performed under exactly the same conditions. These random fluctuations are referred to as photon shot noise (PSN). For this

type of statistics, the probability to detect a certain number of photons N_{ph} depending on the expected number of photons $\mathcal{N}$ is described by the Poisson distribution:

$$\mathcal{P}(\mathcal{N}, N_{\mathrm{ph}}) = \frac{\mathcal{N}^{N_{\mathrm{ph}}}}{N_{\mathrm{ph}}!} \mathrm{e}^{-\mathcal{N}}. \tag{3.15}$$

Since the standard deviation is $\sqrt{\mathcal{N}}$ and the expected number of photons increases linearly with N, the relative noise reduces as the reciprocal square root of the number of readouts. The signal is given by the difference between $\mathcal{I}_0$ and $\mathcal{I}_1$ and the variance reads:

$$\sigma^2_{\mathcal{I}_0-\mathcal{I}_1} = \mathcal{I}_0 + \mathcal{I}_1. \tag{3.16}$$

Using the standard deviation $\sqrt{\sigma^2_{\mathcal{I}_0-\mathcal{I}_1}}$ the relative noise can be defined as:

$$\Delta\mathcal{I}(t_{\mathrm{w}}) = \left(\frac{\sqrt{\mathcal{I}_0(t_{\mathrm{w}}) + \mathcal{I}_1(t_{\mathrm{w}})}}{\mathcal{I}_0(t_{\mathrm{w}})} \right). \tag{3.17}$$

For the same laser pulses, $\Delta\mathcal{I}(t_{\mathrm{w}})$ is plotted as a function of t_{w} in the lower panel of figure 3.10(a). It reduces monotonically since more and more photons are collected.

In general, the total readout noise is a combination of PSN and quantum projection noise (QPN). However, for the traditional readout, the number of detected photons during each individual readout is very low. As a consequence, the overall noise is dominated by PSN and QPN can be neglected, as it is in more detail discussed in chapter 8.

Optimal readout duration

The optimal readout window t_{w} is a compromise between contrast and measurement noise. Since both usually contribute linearly to the SNR of a quantum sensing experiment, it is:

$$\mathrm{SNR} = \frac{C}{\Delta\mathcal{I}} = \frac{\mathcal{I}_0 - \mathcal{I}_1}{\sqrt{\mathcal{I}_0 + \mathcal{I}_1}}. \tag{3.18}$$

As shown in figure 3.10(b), the optimal readout duration for this example is about 475 ns. In general, this time depends on the experimental conditions, especially on the excitation laser power, and can deviate from the value obtained here.

3.3.3 Improvement of the traditional optical readout

From a quantum mechanical point of view the above described optical readout is far from perfect. First, all spin states fluoresce and thus their discriminability is limited since the contrast is lower than one. Recording for an arbitrary duration is not possible since the

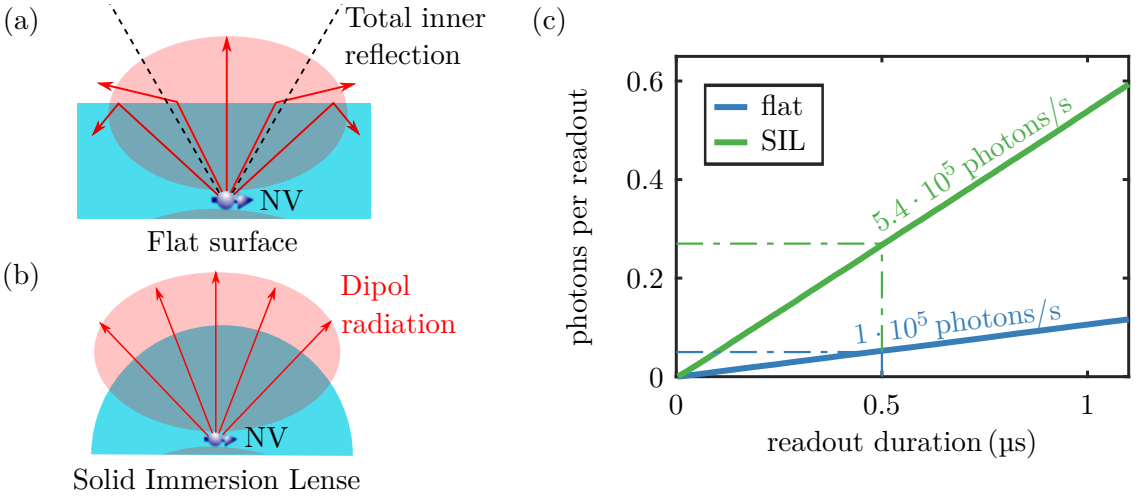

Figure 3.11: Fluorescence for differently shaped diamonds. (a) Total internal reflection is a big problem for diamonds with a flat surface due to the large refractive index of diamond. (b) Working principle of a SIL. Due to its hemisperical shape, the propagation direction of the photons is perpendicular to the diamond surface preventing total internal reflection. (c) Experimentally recorded number of photons as a function of the readout duration. Summing up all photons recorded in the relevant first 500 ns yields about 0.05 photons for the diamond with flat surface and about 0.27 photons per readout for the SIL sample (for the $m_s = 0$ state).

spin is populated into the $m_s = 0$ state during illumination. Furthermore, the photon-detection efficiency – so the ratio of detected and emitted photons – is very low.

One big problem is the high refractive index of diamond of about 2.42 [66] and the resulting small critical angle for total internal reflection, as sketched in figure 3.11(a). For a diamond-air interface this angle is just around 24.4° and even for commonly used immersion oil, this angle is still very small (refractive index of 1.5 corresponds to 38.3°). Furthermore, fluorescence is basically emitted in all spatial directions and the detection apparatus can usually cover only a small fraction of the full space. Additionally, optical absorption and emission is not optimal for NV centres in the most widely used diamonds with (100) surface, since the optical dipoles, orientated perpendicular to the symmetry axes, are not aligned with the diamond surface. So only a small fraction of the emitted photons leave the diamond and from those only a small part is detected. The total efficiency is on the order of $1 - 3\,\%$ [122, 123] and as a consequence, far less than one photon is on average collected during the first 500 ns of the readout, which is exemplified in figure 3.11(c). While the limited state discriminability and readout durations are intrinsic to NV centres, the detection efficiency can be improved.

For example photonic structures, as nanopillars, nanowires, waveguides and cavities can help to overcome the high refractive index mismatch [122–128]. Especially grinding the diamond into a hemispherical solid immersion lens (SIL) can help to improve the collection

efficiency by an order of magnitude [129–131]. The idea is sketched in figure 3.11(b). While for a flat diamond total internal reflection is a big problem, a large part of the photons can penetrate the diamond surface of a SIL due to the hemispherical shape. A quantitative experimental comparison of the fluorescence recorded from a single NV centre inside a diamond with flat surface and a NV centre inside a SIL sample is given in figure 3.11(c). For approximately the same excitation power, the number of photons detected with the SIL sample is about 5.4 times higher, which results in an improvement of the SNR by about 2.3. In literature, improvements up to a factor of 10 are reported [129]. As a nice side effect, the point spread function of the confocal microscope is improved since the excitation beam can be focused to a smaller volume, which reduces background fluorescence [129].

However, this is still by far not enough to obtain sufficient information about the spin state of the NV centre after a single measurement. Furthermore, designing optimised structures remains a big challenge up to date due to the difficulties associated with nanofabrication of diamond.

Nuclear assisted readout

For a high-fidelity discrimination of the different spin states, the measurement signal would need to be larger than the associated noise. Assuming photon-shot noise dominates, a simple estimate for the numbers of required photons for $\mathcal{I}_0$ and $\mathcal{I}_1$ is (compare equation (3.16)):

$$\underbrace{\sqrt{\mathcal{I}_0 + \mathcal{I}_1}}_{\text{noise}} < \underbrace{\mathcal{I}_0 - \mathcal{I}_1}_{\text{signal}}. \tag{3.19}$$

For a typical contrast of $C = (\mathcal{I}_0 - \mathcal{I}_1)/\mathcal{I}_0 \approx 0.25$, it follows:

$$\mathcal{I}_0 > 28 \quad \text{and} \quad \mathcal{I}_1 > 21. \tag{3.20}$$

So, at least 30 photons would be required for a single-shot readout (SSR) of the NV centre's electron spin state. Assuming, that only around 0.05 photons are recorded per readout, this is equivalent to around 600 repetitions.

One option to achieve such a high number is the usage of an additional long-living memory qubit. The method is described in more detail in chapter 8 and in the following, only the idea is shortly outlined.

Before the readout, the NV centre's electron spin can be entangled with the memory qubit. After being projected during the first readout, the state of this memory qubit can be repetitively probed using the NV centre. For a convenient choice of the memory qubit, its state is long-living enough for several thousand repetitions, which results in collecting enough photons for a SSR.

3.4 Couplings of the nitrogen-vacancy centre

The NV centre couples to a variety of physical quantities and in the following the most important ones are listed.

Magnetic field sensing

The principle of the coupling to magnetic fields is the linear Zeeman effect, which shifts the energies of the spin states with non-zero spin quantum number m_s in an external magnetic field $\vec{B}$. The corresponding Hamiltonian reads (compare equation (3.7)):

$$\mathcal{H}_\mathrm{Z} = h\gamma_\mathrm{NV}\vec{B}^\mathrm{T}\vec{S} = h\gamma_\mathrm{NV}(B_x\hat{S}_x + B_y\hat{S}_y + B_z\hat{S}_z), \tag{3.21}$$

where $\vec{S}$ is the spin vector, γ_NV is the gyromagnetic ratio:

$$\gamma_\mathrm{NV} = \frac{g_\mathrm{NV}\cdot\mu_\mathrm{B}}{h} \approx 28.03\,\mathrm{GHz/T}, \tag{3.22}$$

μ_B is the Bohr magneton and $g_\mathrm{NV} \approx 2.0028$ is the g-factor of the NV centre's electron spin [78, 83].

For small fields, the terms containing B_x and B_y are efficiently suppressed due to the much larger ZFS parameter and only the B_z component can be detected [53]. Only if B_x and B_y have frequency components resonant to the splitting of two spin states, they can drive transitions, as it is shown in the sections 2.5 and 3.5 and thus be sensed (compare also chapter 9). In order to perform vector magnetometry, NV centres with different crystal orientations can be probed [132].

Electric field and strain sensing

The NV centre couples to electric fields via the linear Stark effect [43, 133, 134]. The physical principle is the spin orbit coupling between the ground and the excited triplet states and the relevant Hamiltonian reads [43]:

$$\mathcal{H}_\mathrm{el}/h = d_\parallel E_z\hat{S}_z - d_\perp E_x(\hat{S}_x\hat{S}_y + \hat{S}_y\hat{S}_x) + d_\perp E_y(\hat{S}_x^2 - \hat{S}_y^2), \tag{3.23}$$

where $\vec{E} = (E_x\ E_y\ E_z)^\mathrm{T}$ is a combination of the electric field and strain. The relevant coupling constants are:

$$d_\parallel = 0.0035\,\mathrm{HzV^{-1}m} \text{ and } d_\perp = 0.17\,\mathrm{HzV^{-1}m}. \tag{3.24}$$

Nanoscale electric field sensors are of great importance since many particles, as for example free electrons, generate strong electric fields but only weak magnetic fields. For example, a single charge in 150 nm distance can be detected, after averaging for only one second and an overall AC electric-field sensitivity of $2.02\,\mathrm{Vm^{-1}Hz^{-1/2}}$ can be reached [43]. Other possible applications of the NV centre as an electric field sensor are proposed in [135, 136].

Pressure and temperature sensing

Since the NV centre is a $S = 1$ spin system, it has a ZFS, which depends on the distance of the two unpaired electrons (compare equation (3.6)). Thus, all external parameters that influence this distance may change the ZFS parameter D. Important examples are pressure p ($\mathrm{d}D/\mathrm{d}p = 1.46\,\mathrm{kHz/bar}$ [51]) and temperature T ($\mathrm{d}D/\mathrm{d}T = -74.2\,\mathrm{kHz/K}$ [89]), and thus NV centres might also find applications as nanoscale temperature [46–48] or pressure sensors [51].

Rotation sensing

The measurement of a rotation frequency is based on the accumulation of a geometric phase, the so called Berry phase [137]. If a diamond sample is rotated around the symmetry axis of the NV centre, the corresponding Hamiltonian reads [138–140]:

$$\mathcal{H}_{\mathrm{rot}} = h\nu_{\mathrm{rot}}\hat{S}_z, \tag{3.25}$$

where ν_{rot} is the rotation frequency, which linearly changes the splitting of the spin levels. Since $\mathcal{H}_{\mathrm{rot}}$ is independent of the gyromagnetic ratio, nuclear spins, which have longer relaxation times, can be used without losing sensitivity [139]. Inertial sensors find application in many areas and are especially relevant in navigation systems. Due to their small dimensions and high robustness, NV centres represent interesting option for gyroscopic applications.

3.5 Coherent control of the nitrogen-vacancy centre

For NV centres, coherent control of the spin state is possible by using resonant magnetic fields (compare section 2.5). If only two states are considered, for example between the $m_{\mathrm{s}} = 0$ and $m_{\mathrm{s}} = -1$ states, the corresponding interaction Hamiltonian in the laboratory frame reads:

$$\mathcal{H}_1 = \hbar\Omega\cos(\omega t + \theta)\hat{\sigma}_x, \tag{3.26}$$

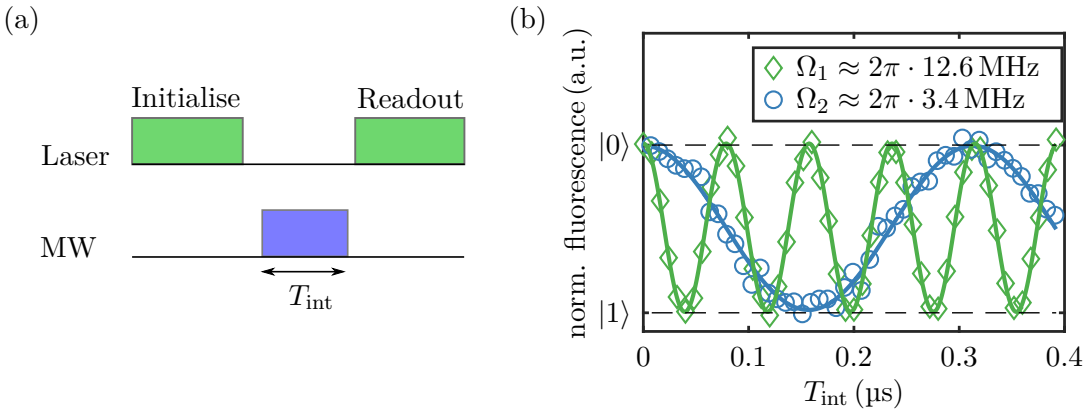

Figure 3.12: Coherent control of the NV centre. (a) Pulse sequence to probe the coupling between resonant microwave (MW) field and NV centre. Between optical initialisation and readout, microwaves are applied for a variable duration T_{int}. (b) The frequency of the resulting Rabi oscillations depend on the coupling strength (Ω_1 or Ω_2) of the applied microwave. Solid lines correspond to sinusoidal fits to the data.

where Ω is the coupling parameter, $\hat{\sigma}_x$ is the corresponding Pauli matrix, ω is the frequency and θ the phase of the control field. As derived in section 2.5, the angle of rotation depends linearly on the coupling Ω and the interaction time T_{int}. This is experimentally demonstrated with the sequence shown in figure 3.12(a). After initialisation of the spin state into $|0\rangle$ by using green laser light, a resonant microwave field is applied for a variable duration T_{int}. The resulting sensor state is measured optically. As the experimental data in figure 3.12(b) shows for two different field amplitudes, which correspond to $\Omega_1 \approx 2\pi \cdot 12.6\,\mathrm{MHz}$ and $\Omega_2 \approx 2\pi \cdot 3.4\,\mathrm{MHz}$, P_0 undergoes sinusoidal Rabi oscillations [141]. These Rabi oscillations can be used to calibrate for example the durations of $\pi/2$- or π-pulses (compare section 2.5).

4 Spectroscopy with the nitrogen-vacancy centre

NV centres can be used to detect and characterise magnetic signals. For this purpose, there are a variety of different measurement sequences and their applicability and performance depend on the form of the magnetic field. In the following, the most common techniques are described.

4.1 Optically detected magnetic resonance

Magnetic resonance is a very useful and widespread technique and is based on the absorption (and/or emission) of electromagnetic radiation by paramagnetic particles [142]. As spins possess a magnetic moment, electromagnetic fields, resonant to a transition between two spin levels, can be absorbed. Thus, an unknown frequency can be found by varying the energy difference between the spin levels and detecting the absorption. Based on the same principle, the transition frequency of a qubit can be determined by sweeping the frequency of an external control signal.

Since the fluorescence of the NV centre is spin-dependent, optically detected magnetic resonance (ODMR) is a simple but powerful technique for spectroscopy [21]. The principle is sketched in figure 4.1(a). The NV centre is continuously irradiated with light and simultaneously subject to microwave radiation. While the laser light constantly populates the $m_\mathrm{s} = 0$ state, the microwaves drive spin transitions if the frequency is resonant to one of them. If the frequency does not match with the energy splitting between the $m_\mathrm{s} = 0$ and $m_\mathrm{s} = -1$ or $m_\mathrm{s} = +1$ spin states, the recorded fluorescence is high. If the microwave, however, is absorbed, the spin state can change and the fluorescence reduces. Since the NV centre is illuminated continuously, an equilibrium, which depends on the excitation power of the laser and the driving amplitude of the microwave field, is established between these two opposing mechanisms. Without an external magnetic field the $m_\mathrm{s} = -1$ and $m_\mathrm{s} = +1$ spin states are degenerate and shifted by $D = 2.87\,\mathrm{GHz}$ compared to the $m_\mathrm{s} = 0$ level. Due to the Zeeman interactions both states with non-zero spin quantum number split and

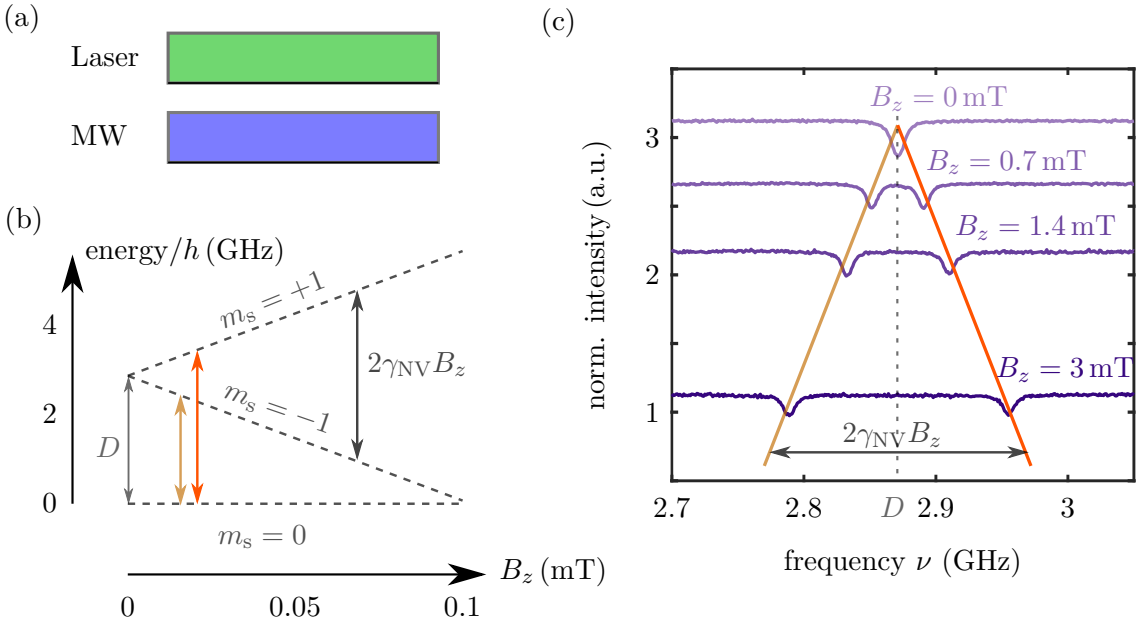

Figure 4.1: Principle of the ODMR technique. (a) The NV centre is constantly illuminated and simultaneously subject to a microwave field. (b) If the frequency of the microwave is resonant to either the $m_s = 0 \Leftrightarrow m_s = -1$ (beige arrow) or the $m_s = 0 \Leftrightarrow m_s = +1$ transition (brown arrow), it can be absorbed. Due to selection rules, the $m_s = -1 \Leftrightarrow m_s = +1$ transition is forbidden. (c) ODMR spectra for different magnetic fields. The resonance line split symmetrically with increasing bias field.

transitions with the $m_s = 0$ can be selectively addressed, as sketched in figure 4.1(b). This splitting ν_Δ in units of frequency is given by:

$$\nu_\Delta = m_{s,\Delta}\gamma_{NV}B_z \approx 2 \cdot 28\,\mathrm{GHz/T} \cdot B_z, \tag{4.1}$$

where $m_{s,\Delta} = 2$ is the difference of the spin quantum numbers, γ_{NV} is the gyromagnetic ratio of the NV centre's electron spin and B_z is the projection of the magnetic field onto the symmetry axis of the NV centre. Since the spin quantum number can just change by one due to the selection rules, only the $m_s = 0 \leftrightarrow m_s = -1$ and $m_s = 0 \leftrightarrow m_s = +1$ can be driven directly. Taking the zero-field splitting D into account, the resonance frequencies read:

$$\nu_{res} = D \pm \gamma_{NV}B_z = 2.87\,\mathrm{GHz} \pm 28\,\mathrm{GHz/T} \cdot B_z. \tag{4.2}$$

In figure 4.1(c), ODMR spectra for different magnetic bias fields B_z are shown. For this purpose, the fluorescence was recorded while changing the frequency ν of an artificial microwave field. For $B_z = 0$, only one dip can be observed at $\nu = D$. With increasing magnetic field two lines, corresponding to the beige and brown arrows in figure 4.1(b) can be detected. As a consequence, the strength of an unknown magnetic field can be directly

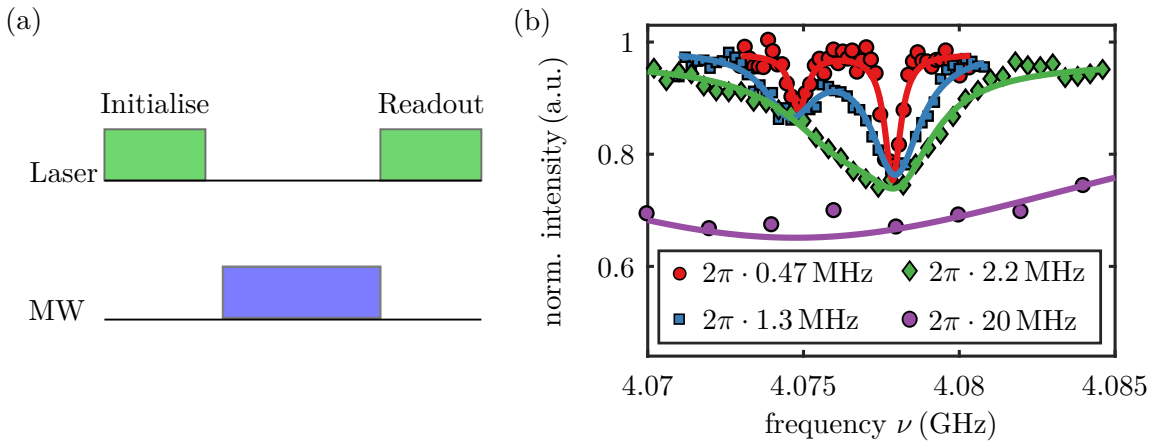

Figure 4.2: Principle of pulsed ODMR. (a) A laser pulse is used to initialise the NV centre in the $m_s = 0$ spin state. The change of the spin state due to the applied microwave field is readout by recording the spin-dependent fluorescence. (b) Pulsed ODMR spectra for different MW driving strengths Ω (shown in legend, pulse durations adjusted). The linewidth reduces inversely proportional to Ω. The hyperfine coupling with the inherent ^{15}N nuclear spin of 3.03 MHz can only be fully resolved for the red and blue data. The uneven height of the hyperfine peaks is due to polarisation of the nuclear spin, which results from interactions with the NV centre's electron spin. The solid lines are two-peak Lorentzian fits to the data.

obtained by detecting these dips. Based on the same principle, an oscillating field with unknown frequency can be recorded by sweeping a well-known bias field.

The sensitivity of an ODMR measurement is in more detail discussed in appendix A.3.3.

Pulsed ODMR

The working principles of the continuous-wave ODMR and pulsed ODMR techniques are essentially the same. The main difference is, that for the latter the microwave and the light radiation are separated in time. A sketch of the pulsed ODMR sequence is shown in figure 4.2(a).

A laser pulse is used to initialise the electron spin into $m_s = 0$ state, before the microwave field is applied and the final state is read out by detecting the spin-dependent fluorescence. The advantage is, that the polarisation into the $m_s = 0$ spin state due to the optical cycling and the spin transfer due to the microwave absorption are not competing. Therefore, it is possible to use very low Ω and a broadening of the line in the spectrum is suppressed. The linewidth depends inverse on the driving strength Ω (compare equation (2.30)) and is eventually limited by inherent dephasing and decoherence effects (compare section 4.5.4). The highest precision can be achieved when the combination of duration and amplitude of the microwave field corresponds to a π-pulse, because the readout contrast is maximal in this case.

In figure 4.2(b) pulsed ODMR spectra, recorded using different driving strengths Ω are shown. As expected, the width of the resonance line reduces with decreasing Ω. For $\Omega \approx 2\pi \cdot 1.3\,\mathrm{MHz}$ and $\Omega \approx 2\pi \cdot 0.47\,\mathrm{MHz}$, the hyperfine splitting with the intrinsic ^{15}N nuclear spin can be resolved. However, for a reduced microwave field amplitude the interaction duration has to be increased in order to obtain the same contrast.

4.2 Ramsey interferometry

Another way to measure a time-independent or only slowly varying field is Ramsey interferometry, often also called free induction decay (FID) [143, 144]. The Hamiltonian of a time-independent field B_z, orientated parallel to the NV symmetry axis, in the rotating frame can be written as:

$$\mathcal{H} = \frac{\hbar\tilde{\gamma}_{\mathrm{NV}}}{2} B_z \hat{\sigma}_z. \tag{4.3}$$

where $\tilde{\gamma}_{\mathrm{NV}} = 2\pi \cdot \gamma_{\mathrm{NV}}$. The corresponding time evolution operator is (see equation (2.12)):

$$\mathcal{U}(T_{\mathrm{int}}, 0) = \exp\left(-\frac{i}{2}\int_0^{T_{\mathrm{int}}} \tilde{\gamma}_{\mathrm{NV}} B_z \hat{\sigma}_z \mathrm{d}t\right), \tag{4.4}$$

where T_{int} is the interaction time. If a qubit is initialised into a coherent superposition state:

$$|\Psi\rangle = \frac{1}{\sqrt{2}}\left(|0\rangle + \mathrm{e}^{i\phi_0}|1\rangle\right), \tag{4.5}$$

where $\phi_0 = \phi(T_{\mathrm{int}} = 0)$ is the initial relative phase between both states, the temporal evolution of the relative phase $\phi(T_{\mathrm{int}})$ is when following equation (4.4):

$$\phi(T_{\mathrm{int}}) = \phi_0 + \tilde{\gamma}_{\mathrm{NV}} \int_0^{T_{\mathrm{int}}} B_z \mathrm{d}t = \phi_0 + \tilde{\gamma}_{\mathrm{NV}} B_z T_{\mathrm{int}}. \tag{4.6}$$

The measurement principle is sketched in figure 4.3(a). An initial laser pulse prepares the electron spin in the $|0\rangle$ state and a $\pi/2$-pulse creates a coherent superposition. After a variable time T_{int}, the relative phase ϕ is retrieved by a second $\pi/2$-pulse with the aim to obtain a population difference in the readout-basis. If this final $\pi/2$-rotation is applied around the same axis in the rotating frame as the first one, the probability to find the quantum system in the $|0\rangle$ reads:

$$P_0(T_{\mathrm{int}}) = \frac{1}{2} - \frac{1}{2}\cos(\phi) = \frac{1}{2} - \frac{1}{2}\cos(\tilde{\gamma}_{\mathrm{NV}} B_z T_{\mathrm{int}}) \tag{4.7}$$

Thus, P_0 is a sinusoidal function of B_z and the interaction time T_{int}. In figure 4.3(b) example measurements are shown. For these experiments, a bias field of around 50 mT

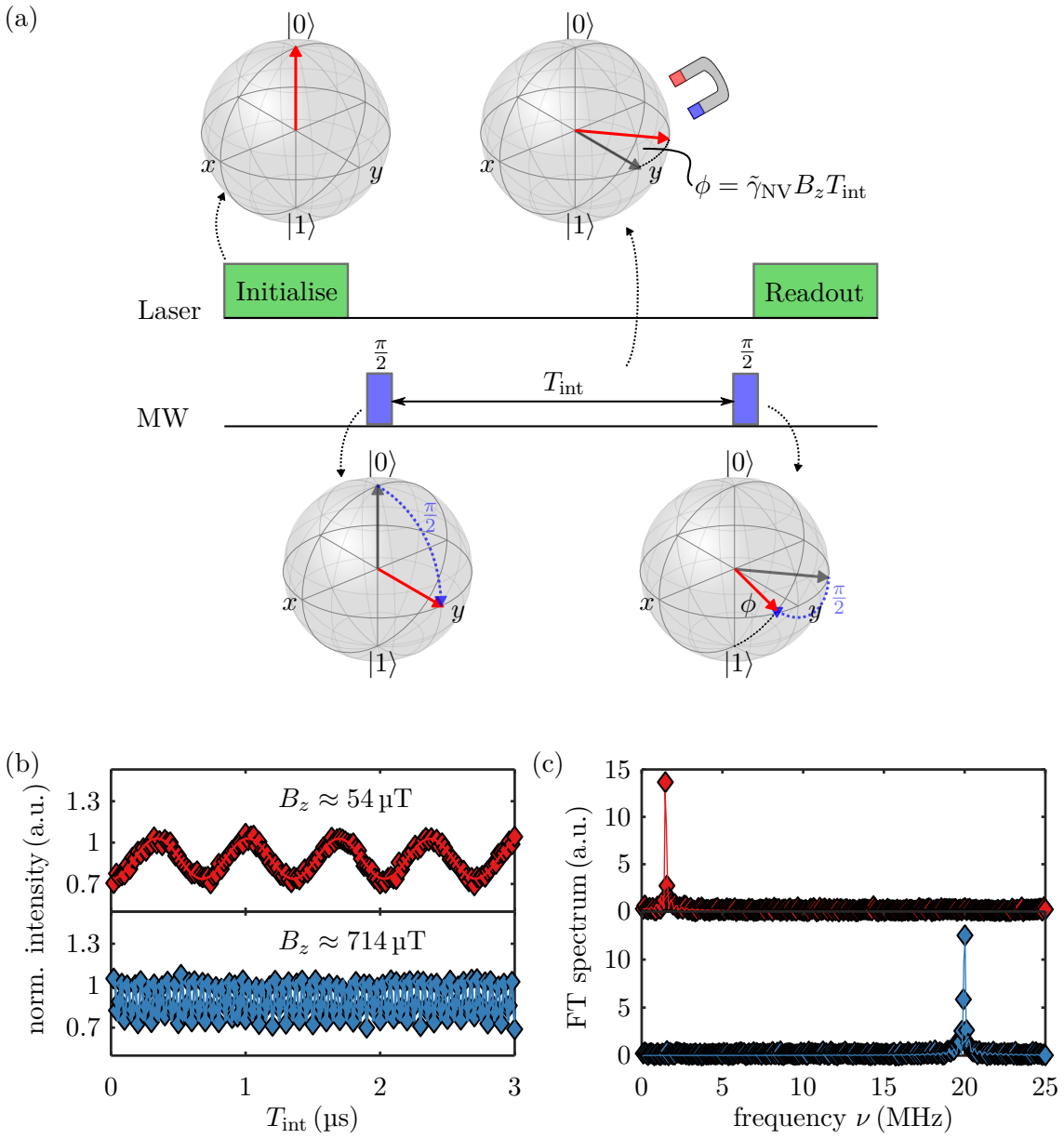

Figure 4.3: Scheme and experimental examples for Ramsey interferometry. (a) After initialisation with a laser pulse into $|0\rangle$, a $\pi/2$-pulse creates a coherent superposition state. During the interaction time T_{int}, a phase ϕ is accumulated on the equator of the Bloch sphere due to interaction with magnetic fields. Before readout, ϕ is transferred to a population difference by a second $\pi/2$-pulse. (b) Measurement outcomes for two different magnetic field strengths B_z. The frequency of the oscillations is directly proportional to the magnetic field: $\nu = \gamma_{\mathrm{NV}} \cdot B_z$. Solid lines correspond to sinusoidal fits to the data. (c) Fourier transforms (FT) of the curves in (b).

was aligned parallel to the symmetry axis of the NV centre in order to polarise the inherent nitrogen nuclear spin [145]. By finding the frequency of the observed oscillation $\nu_{\mathrm{FID}} = \gamma_{\mathrm{NV}} \cdot B_z$, for example via Fourier transform as illustrated in figure 4.3(c), the magnetic field strength can be obtained as $|B_z| = \nu_{\mathrm{FID}}/\gamma_{\mathrm{NV}}$, where $\gamma_{\mathrm{NV}} = \tilde{\gamma}_{\mathrm{NV}}/2\pi$ and the sign of B_z is ambiguous. The achievable precision and the dynamic range are in more detail discussed in appendix A.3.4.

Ramsey interferometry can also be used to measure the frequency ω_1 of a near-resonant field of interest, if it is possible to use this field to perform the $\pi/2$-pulses and turn off the interaction in between. Then, in the rotating frame with respect to ω_1, the sensor accumulates a phase and it follows:

$$P_0(T_{\mathrm{int}}) = \frac{1}{2} - \frac{1}{2}\cos\left(\omega_\Delta T_{\mathrm{int}}\right), \tag{4.8}$$

where $|\omega_\Delta| = |\tilde{\gamma}_{\mathrm{NV}} B_z - \omega_1|$. If B_z and the sign of ω_Δ are known, ω_1 can be obtained.

4.3 Dynamical decoupling spectroscopy

Dynamical decoupling (DD) [146] is a quantum control technique that finds application in quantum information [147–149], spin resonance experiments and quantum spectroscopy [4]. Especially for NV centres, DD is the key procedure for sensing time-dependent magnetic fields, for example needed for nanoscale nuclear magnetic resonance (NMR) or magnetic resonance imaging (MRI) experiments [22, 150–156]. Further applications are detection, identification and control of single or ensembles of nuclear spins [24, 157–166].

While in quantum information and processing the main purpose is to protect the quantum system from noise by decoupling it from environmental influences [167–172], the idea in spectroscopy is to create a tunable spectral filter. The principle is discussed in the following.

4.3.1 Dynamical decoupling Hamiltonian

As sketched in figure 4.4, a pulsed DD sequence in the most general case consists of a series of equidistant and ideally instantaneous π-pulses. The DD Hamiltonian is given by:

$$\mathcal{H}_{\mathrm{DD}} = \sum_{n=1}^{N_\pi} \mathcal{H}_\pi(t_n), \tag{4.9}$$

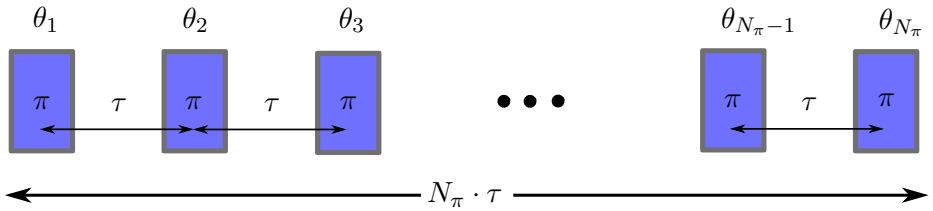

Figure 4.4: Principle of a pulsed DD sequence. A DD sequence consists of a train of N_π π-pulses, which are usually equidistantly spaced. The pulse phase θ determines the rotation axis and the total interaction time T_{int} is given by $N_\pi \cdot \tau$.

where $\mathcal{H}_\pi(t_n)$ is the Hamiltonian of a single π-pulse applied at time t_n. This Hamiltonian can be used to detect an oscillating field $H(t)$ described by:

$$\mathcal{H}_{\text{signal}} = \frac{\hbar H(t)}{2}\hat{\sigma}_z, \tag{4.10}$$

and the complete Hamiltonian reads:

$$\mathcal{H} = \mathcal{H}_0 + \mathcal{H}_{\text{signal}} + \mathcal{H}_{\text{DD}}, \tag{4.11}$$

where $\mathcal{H}_0 = \frac{\hbar\omega_0}{2}\hat{\sigma}_z$ describes the energy gap between the two levels of the quantum system. By moving into the interaction picture with respect to $\mathcal{H}_0$, applying the rotating wave approximation (assuming all relevant frequencies are much smaller than ω_0), and moving into the interaction picture of the DD control, it follows:

$$\mathcal{H}_I/\hbar = \frac{F(t)H(t)}{2}\hat{\sigma}_z, \tag{4.12}$$

where $F(t)$ is a square wave function for instantaneous π-pulses:

$$F(t) = (-1)^{k(t)}, \tag{4.13}$$

and $k(t)$ is the number of control pulses applied up to the moment t. The form of $F(t)$ represents a spectral filter, since the temporal evolution of the sensor phase ϕ in a coherent superposition reads:

$$\phi(t) = \int_{t_0}^{t_0+T_{\text{int}}} F(t)H(t)\mathrm{d}t, \tag{4.14}$$

where t_0 is the starting time and T_{int} is the interaction period. Although there are also a few DD sequences, which have a non-periodic spacing or are continuous [173–179], the following concentrates on DD techniques, for which a train of equidistantly spaced π-pulses with spacing τ is used.

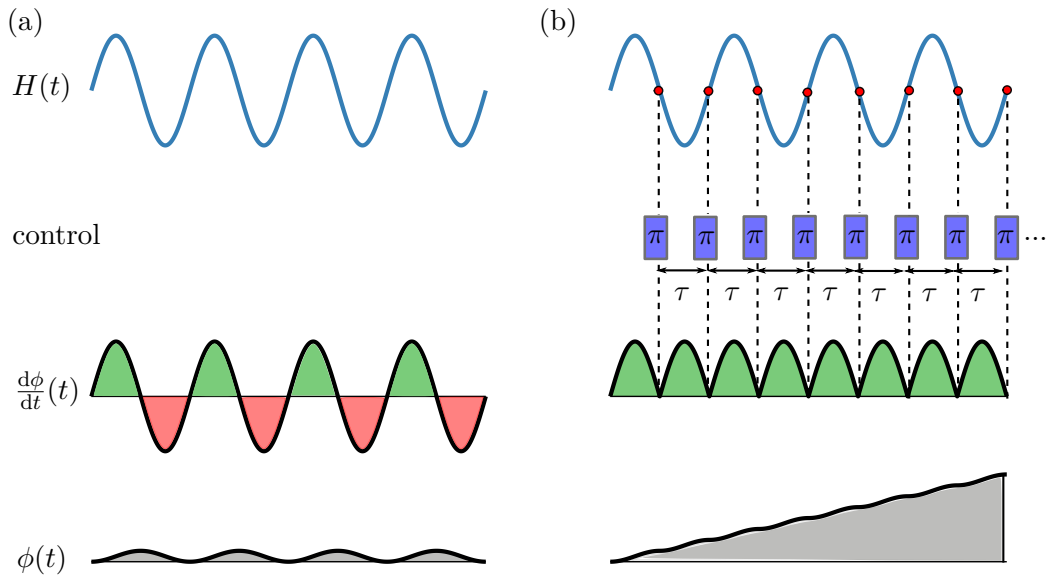

Figure 4.5: Principle of sensing AC fields using DD. (a) Without additional control, all phase, which the sensor accumulates during the first half of a signal period (green shading), is cancelled during the second half (red shading) and over a full period no phase is acquired. (b) By applying a control in form of π-pulses, whenever the signal changes sign ($\tau = \pi/\omega$), all parts in between the control pulses are added up.

4.3.2 Dynamical decoupling filter

For spectroscopic purposes it is usually more interesting, how this filter $F(t)$ looks in terms of frequencies. For this purpose, $F(t)$ can be Fourier transformed (compare appendix A.3.5):

$$\mathcal{F}(\omega) = \int_{-\infty}^{\infty} F(t')\mathrm{e}^{i\omega t'}\mathrm{d}t' \approx \frac{2}{i\omega}\left[\sum_{n=0}^{N_\pi}(-1)^n\mathrm{e}^{i\omega n\tau}\right]. \tag{4.15}$$

If ω is an uneven multiple of (π/τ):

$$\mathrm{e}^{i\omega n\tau} = (-1)^n, \tag{4.16}$$

and $|\mathcal{F}(\omega)|$ becomes large. For a simple sinusoidal signal, an illustrative explanation is sketched in figure 4.5. If the oscillating field $H(t)$ is recorded without any control, the sign of sensor phase accumulation $\mathrm{d}\phi/\mathrm{d}t$ changes, whenever the sign of $H(t)$ changes and over a full period $\phi = 0$. On the contrary, π-pulses with a resonant spacing result in a monotonically growing $\phi(t)$, as sketched in figure 4.5(b). If ω is an even multiple of (π/τ):

$$\mathrm{e}^{i\omega n\tau} = 1, \tag{4.17}$$

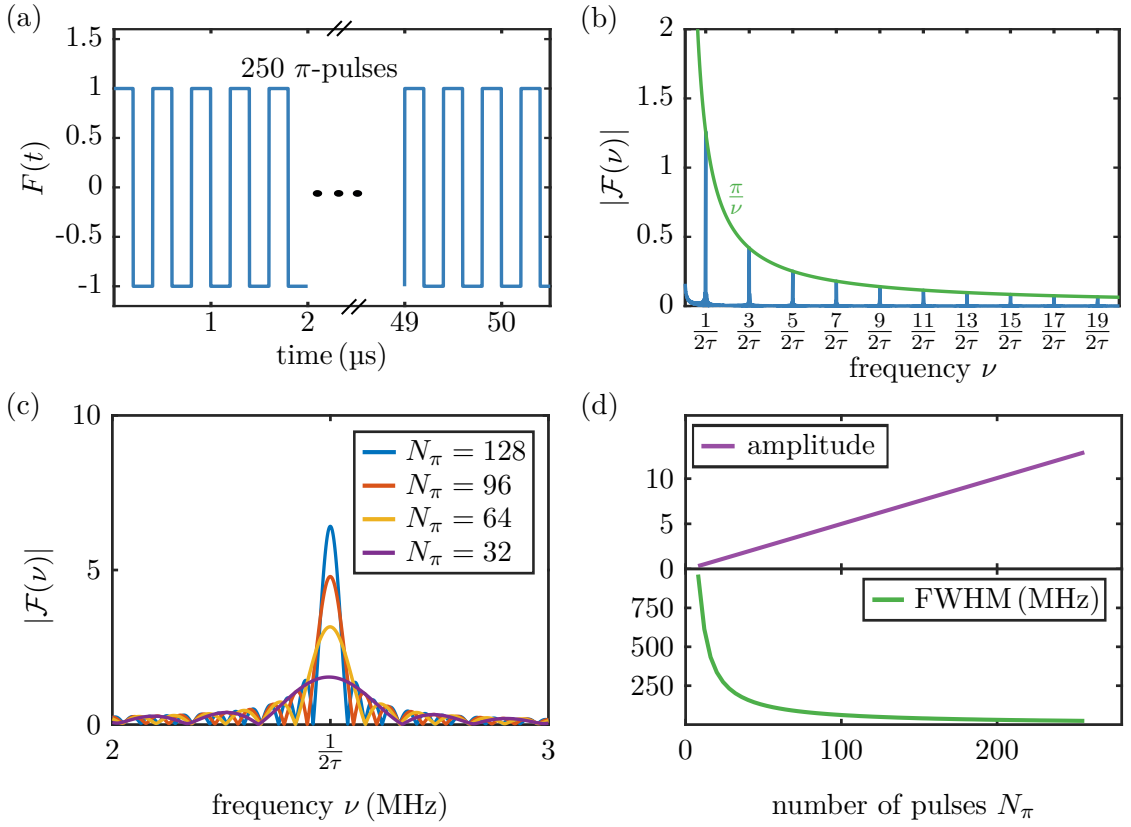

Figure 4.6: DD control in time and frequency space. (a) In time space, the function $F(t)$, describing the DD control, has a step-wise form and changes sign whenever a π-pulse is applied. (b) In frequency space, $|\mathcal{F}(\nu)|$ shows, that DD represents an adjustable spectral filter. (c) $|\mathcal{F}(\nu)|$ in dependence of the number of applied π-pulses N_π. (d) While the amplitude increases linearly with N_π, the FWHM reduces as N_π^{-1}.

and $|\mathcal{F}(\omega)| \approx 0$. As an example, the Fourier transformation of $F(t)$, which describes 250 π-pulses with spacing $\tau = 200\,\text{ns}$ (shown in figure 4.6(a)), is computed numerically. The result is displayed in figure 4.6(b). $|\mathcal{F}(\omega)|$ and is a series of sharp equidistant peaks, which can be found for:

$$\nu = \frac{\omega}{2\pi} = \frac{(2m-1)}{2\tau}, \tag{4.18}$$

where m is an integer number and the peak amplitudes decrease as $1/(2m-1)$. For example for $m = 2$, the spacing between two pulses corresponds to one and a half periods of the signal. Since one period averages out, only the remaining half of the period and thus, only one third of the total interaction time contributes to the signal. For sequences with equally spaced π-pulses, $|\mathcal{F}(\omega)|$ can be written as [170, 180]:

$$|\mathcal{F}(\omega, N_\pi, \tau)|^2 = \frac{2}{\omega^2} \cdot 8 \frac{\sin^4\left(\frac{\omega\tau}{4N_\pi}\right) \sin^2\left(\frac{\omega\tau}{2}\right)}{\cos^2\left(\frac{\omega\tau}{2N_\pi}\right)}. \tag{4.19}$$

In figure 4.6(c), the peak at $\nu = (1/2\tau)$ is plotted in a higher resolution for different number of applied π-pulses N_π. The height increases linearly with N_π and as a consequence, a higher sensitivity can be achieved. On the other side, the FWHM decreases as N_π^{-1}, as shown in figure 4.6(d). Thus, the precision of frequency estimation increases and it is also possible to differentiate between signals with a smaller frequency difference.

An illustrative explanation is sketched in figure 4.7(a). If τ is not exactly resonant, the π-pulse do not coincide with the signal nodes and the deviations increase with the number of pulses (growing area of the red shadings). The maximal number for N_π is eventually limited by the coherence time of the qubit (compare section 4.5.4).

By tailoring the inter-pulse spacing τ of a DD sequence, the sensor can be made sensitive only for signals in a specific frequency range. Thus, by probing different values of τ, DD can be used for spectroscopy. The accumulated sensor phase ϕ reads (compare 4.14):

$$\phi(\omega) = \int_{-\infty}^{\infty} \mathcal{J}(\omega')\mathcal{F}(\omega')\mathrm{d}\omega', \tag{4.20}$$

where $\mathcal{J}(\omega)$ is the Fourier transformation of the signal:

$$\mathcal{J}(\omega) = \frac{1}{2\pi}\int_{-\infty}^{\infty} H(t')\mathrm{e}^{i\omega t'}\mathrm{d}t'. \tag{4.21}$$

Up to now, the phase of the signal θ has been neglected. However, it is important for the measurement outcome, as figure 4.7(b) sketches. If the signal nodes do not match with the π-pulses, the overall sensor phase is reduced, even for a resonant pulse spacing. If the signal of interest can be described by a single sinusoidal function with frequency ω_{sig}:

$$H(t) = \Omega \sin\left(\omega_{\mathrm{sig}} t + \theta\right), \tag{4.22}$$

the accumulated sensor phase $\phi(t)$, given a measurement period between t_0 and $t_0 + T_{\mathrm{int}}$, reads [153]:

$$\phi = \frac{2\Omega}{\pi\omega_\Delta}\left(\cos\left(\omega_\Delta t_0 + \theta\right) - \cos\left(\omega_\Delta\left(t_0 + T_{\mathrm{int}}\right) + \theta\right)\right), \tag{4.23}$$

and is a function of the coupling strength Ω, the frequency difference $\omega_\Delta = \omega_{\mathrm{sig}} - \pi/\tau$ and the signal phase θ. The dependency of ϕ on θ plays an important role for the experimental results in the chapters 7 to 8 and is discussed there in more detail.

The performance of a DD sequence depends on the quality of the π-pulses. Furthermore, the repetition rate is limited, since the spacing between two π-pulses can not be smaller than the pulse duration (usually between 10 ns and 100 ns in experiments for this thesis). The influences of non-instantaneous control and other pulse imperfections is in more detail discussed in chapter 6.

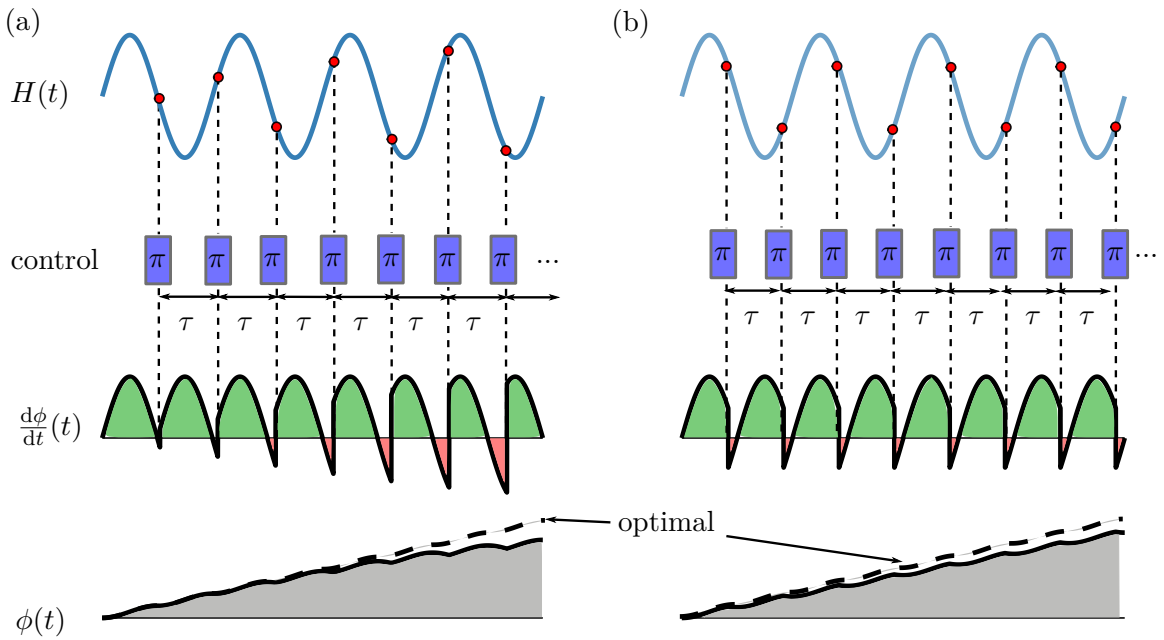

Figure 4.7: Performance of DD as a function of pulse spacing and signal phase. (a) If the inter-pulse spacing does not match the resonant condition, the overall sensor phase is reduced. The more π-pulses are applied, the more sensible is the measurement outcome in this case. (b) If the phase of the signal can not be controlled, it is not possible to match the control pulses with the signal nodes. Then, the overall sensor phase is reduced, even for a resonant pulse spacing.

4.3.3 The XY8-sequence

Besides compensated pulses [146] or optimal control and calibration techniques [181, 182], one well-established option to mitigate the influences of pulse errors and imperfections is to apply the π-pulses around different axes. When designed carefully, the error of each pulse is then partially compensated by other pulses of the cycle [183]. A famous example is the XY8 sequence [184], which uses π-pulses about the x- and the y-axis, as sketched in figure 4.8. The basic unit of the XY8-sequence consists of eight equidistantly spaced π-pulses with the ordering $\pi_x - \pi_y - \pi_x - \pi_y - \pi_y - \pi_x - \pi_y - \pi_x$ and this symmetric shape makes the XY8-sequence only sensitive to second order pulse errors [185]. The effectiveness has been demonstrated theoretically and experimentally [168, 185–187].

The interaction time can be increased by repeating this basic unit and, if in total M repetitions are performed, the notation, chosen from here on, is XY8-M. Recently, it was reported, that more complicated DD protocols, which are based on rotations around further axes, as the KDD sequences, or on concatenation, even further improve the robustness [183, 187, 188]. However, due to its good performance and the relative simple implementation, all DD protocols, used in this thesis, are based on the XY8-sequence.

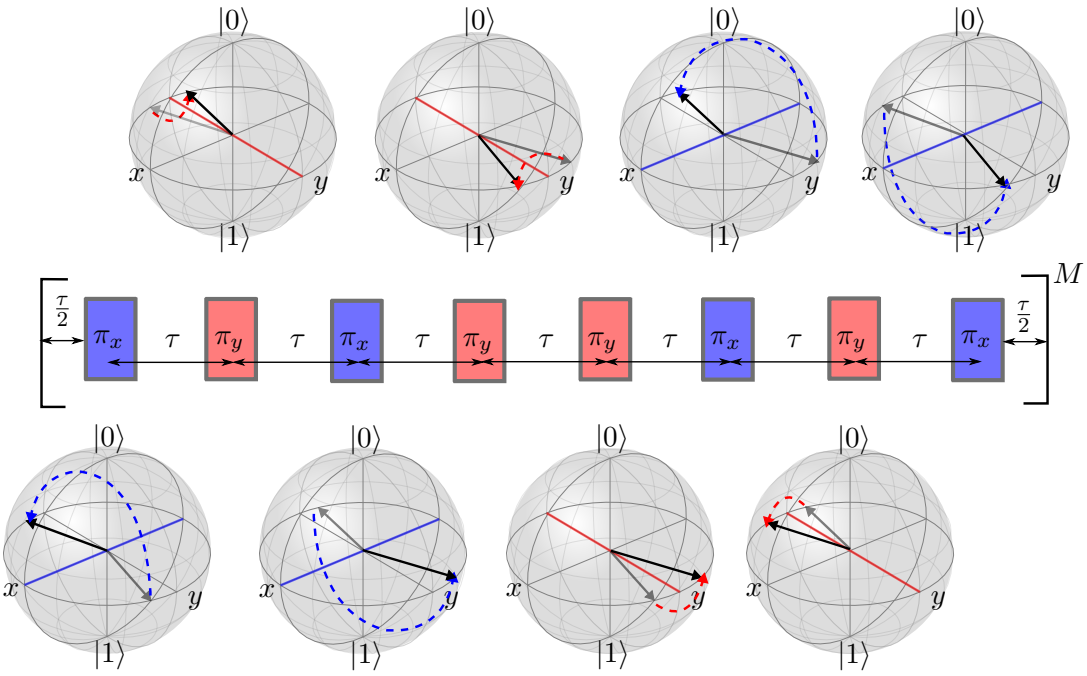

Figure 4.8: Principle of the XY8-sequence. The XY8-sequence consists of a train of equidistantly spaced π-pulses around the x- and the y-axis (solid blue and red lines). Its symmetrical structure ensures that without any further interactions the qubit state (black arrows) is preserved. Due to the rotation around different axis pulse imperfections can be efficiently mitigated.

One of its major drawbacks is, that spurious responses due to the finite width of the π-pulses can complicate a spectrum and lead to false signal identification [28]. However, it is possible to mitigate these effects and simultaneously improve the robustness with a small modification, which is discussed in chapter 6.

4.4 Relaxometry

Many important biological and condensed matter systems generate magnetic noise with a mean value close to zero [189]. Interaction with noise relaxes the quantum state and both the rate and the shape of the decay contain information about the type, strength and variance of the interacting noise sources.

The idea of relaxometry is to prepare the quantum sensor into a certain state, let it interact with the environment for a variable time and record the relaxation into its equilibrium state. The relevant relaxation mechanisms are described in more detail in section 4.5.4. Spectroscopy can be performed by tailoring the frequency range, which the sensor is sensitive for. As instance, for T_1-relaxation, where noise with a frequency, close to the transition frequency of the sensor qubit, dominates the relaxation, spectroscopy can be

performed by adjusting the energy difference between the qubit states. As a consequence, different frequency components, typically in the MHz and GHz range, can be sampled. Noise spectroscopy based on DD is relevant for nanoscale NMR and the principles are discussed in more detail in section 5.2. For more general information about noise sensing and applications, the interested reader is referred to [189–195].

4.5 Precision, sensitivity and limits of quantum spectroscopy

The task of a sensor is to gather information about its environment. Since measurement time is usually a limiting resource, the more information that can be obtained about a field or parameter of interest in a given duration, the better. This rate is given by the sensitivity, which can be used to characterise a sensor. In the following, the precision and sensitivity of a quantum sensor are discussed in more detail. Thereafter, the relaxation mechanisms, which limit the interaction time are addressed more explicitly.

4.5.1 The quantum Fisher information

In quantum metrology, the task is to determine a single parameter or a set of parameters as precisely as possible [196]. The measurement quantity is the state of the sensor – or in other words, the probability P_0 to find the quantum system in a certain eigenstate (for example $|0\rangle$) after measuring it. Thus, the precision of parameter estimation depends on the accuracy of determining P_0. Since quantum measurements are probabilistic, a set of recorded data is required for an estimate of P_0. A concept from mathematical statistics, which determines the amount of information contained in a measurement result about a parameter A, is the Fisher information (FI) $I(A)$. If x are the potential outcomes, $\mathcal{X}$ is the set of all possible outcomes and $f(x|P_0)$ is a discrete distribution that models the probability for measuring x given a certain P_0, the Fisher information is defined as [197–199]:

$$I(A) = \sum_{x\in\mathcal{X}} \left[\left(\frac{\mathrm{d}}{\mathrm{d}A} \log f(x|P_0) \right)^2 f(x|P_0) \right]. \tag{4.24}$$

Without going deeper into detail, the derivative $\frac{\mathrm{d}}{\mathrm{d}A} \log f(x|P_0)$ is the so called score function and describes how sensitive the model is to changes in A. Since not all outcomes have the same probability, the second term $f(x|P_0)$ weights with respect to the chance to find x. Due to the established Cramér-Rao bound [200, 201]:

$$(\Delta A)^2 \geq \frac{1}{I(A)}, \tag{4.25}$$

determining $I(A)$ yields the minimal uncertainty ΔA.

In the context of quantum measurements, a Hamiltonian $\mathcal{H}$ can in principle be probed using a variety of different measurement techniques in order to estimate a parameter (or a set of parameters) of interest. The final sensor population P_0 depends on this used protocol because it consists of a distinct combination of initial state, control sequence and readout basis. In order to obtain the quantum Fisher information, $I(A)$ needs to be maximised over all possible measurement protocols. It was recently shown in [202] that the upper bound of the quantum FI $I_{\mathrm{Q}}(A)$ can be expressed as:

$$I_{\mathrm{Q}}(A) = \left[\int_0^{T_{\mathrm{int}}} (\lambda_{\max} - \lambda_{\min})\ \mathrm{d}t\right]^2 . \tag{4.26}$$

where $\lambda_{\max}$ and $\lambda_{\min}$ are the maximal and minimal eigenvalues of $\partial\mathcal{H}/\partial A$ and T_{int} is the interaction time. For more-parameter problems and more specific literature the interested reader is referred to [203, 204].

4.5.2 Sensitivity for quantum projection noise limited measurements

The absolute limit in quantum mechanics is given by quantum projection noise (QPN) (compare section 2.3). Here, a perfect measurement is defined as a measurement, which only relies on this uncertainty and excludes all other sources of noise. For quantum applications, which are based on a qubit as a probe, there are only two possible outcomes, namely the two eigenstates of the system. Such a quantum sensing experiment is a Bernoulli trial and the probability for measuring n times $|0\rangle$ in N tries is given by the binomial distribution:

$$\mathcal{B}(n|P_0) = \binom{N}{n} P_0^n (1-P_0)^{N-n}. \tag{4.27}$$

The corresponding FI reads (full derivation in appendix A.3.2):

$$I(A) = \frac{N}{P_0(1-P_0)} \left(\frac{\partial P_0}{\partial A}\right)^2 , \tag{4.28}$$

and the minimal uncertainty is:

$$\Delta A = \min\left(\sqrt{\frac{P_0(1-P_0)}{N}} \left|\frac{\partial P_0}{\partial A}\right|^{-1}\right), \tag{4.29}$$

where the minimum is over all possible protocols. This equation can be more illustrative explained by evaluating the individual terms separately. The factor $\partial P_0/\partial A$ corresponds

to the response of the sensor on a variation of the parameter of interest A. The term $\sqrt{P_0(1-P_0)}$ represent the measurement noise of a single measurement, which reduces relatively with the number of tries as $\sqrt{N}$.

The uncertainty ΔA depends on the number of individual measurements N and thus on the total recording time T. Since ΔA improves as $\sqrt{N}$, the precision can not quantify the performance of a sensor or a sensing protocol and it is convenient to introduce the sensitivity as:

$$\eta = \Delta A \sqrt{T}. \tag{4.30}$$

The idea is to have a measure for how much information can be obtained per unit time. By replacing $N = T/T_{\text{sin}}$ in equation (4.29), the sensitivity is given by:

$$\eta = \min \left(\sqrt{P_0(1-P_0) \cdot T_{\text{sin}}} \left| \frac{\partial P_0}{\partial A} \right|^{-1} \right), \tag{4.31}$$

where T_{sin} is the duration of a single measurement, which includes all temporal overheads, for example due to initialisation and readout. It is important to note that $\partial P_0/\partial A$ often also depends on the interaction time, and thus increasing T_{sin} usually does not worsen the sensitivity.

4.5.3 Sensitivity for photon shot noise limited measurements

For NV centres, when the readout is performed optically, photon shot noise (PSN) is usually dominant. According to equation (4.24), the Fisher information reads (derivation in appendix A.3.2):

$$I(A) = \frac{1}{\mathcal{N}} \left(\frac{\partial \mathcal{N}}{\partial A} \right)^2, \tag{4.32}$$

where $\mathcal{N}$ is defined in equation (3.13). The optimal precision then reads:

$$\Delta A = \min \left(\sqrt{\mathcal{N}} \left| \frac{\partial \mathcal{N}}{\partial A} \right|^{-1} \right). \tag{4.33}$$

Inserting $\mathcal{N}$, the sensitivity reads:

$$\eta = \min \left(\frac{\sqrt{((c_0 - c_1)P_0 + c_1)}}{(c_0 - c_1)} \sqrt{T_{\text{sin}}} \left(\frac{\partial P_0}{\partial A} \right)^{-1} \right), \tag{4.34}$$

where c_0 and c_1 are again the number of photons expected to record within a single readout for the $|0\rangle$ and $|1\rangle$ states. Readout of an ensembles of N quasi identical NV centres yields the same sensitivity as probing a single NV centre N times.

4.5.4 Relaxation of the quantum state

Environmental fluctuations may influence the evolution of the quantum state and in particular noise sources, which are of the same type as the target signals, can have a strong impact on the measurement result. These unwanted interactions usually lead to an irreversible relaxation of the quantum system into its thermal equilibrium. Thereby, one differentiates between longitudinal and transverse relaxation.

Transverse Relaxation – Dephasing

Many quantum sensing techniques are based on the accumulation of a relative phase ϕ in a coherent superposition state. After mapping ϕ into a population difference, the readout population P_0 for these kinds of experiments is usually given by:

$$P_0(\phi) = \frac{1}{2} + \frac{1}{2}\cos(\phi). \tag{4.35}$$

Due to the probabilistic nature of quantum measurements, every experiment has to be repeated multiple times. If additional influences can be neglected, the final $\phi = \phi_0$ is the same for every iteration. However, environmental noise sources may impact the sensor evolution and $\phi_n = \phi_0 + \phi_n^{\text{noise}}$ may vary with every repetition. The average over all N iterations is then:

$$\langle P_0 \rangle = \frac{1}{N}\sum_{n=1}^{N} P_0(\phi_n). \tag{4.36}$$

Assuming the noise can be described by a normal distribution with variance σ_ϕ^2 and zero mean $\langle \phi_{\text{noise}} \rangle = 0$, it is for $\phi_0 = 0$:

$$\langle P_0 \rangle = \frac{1}{2} + \frac{1}{2}\exp\left(-\frac{\sigma_\phi^2}{2}\right). \tag{4.37}$$

Thus, $\langle P_0 \rangle$ decays to a mixed state and the relevant time scale is given by the variance σ_ϕ^2. The form and the time-dependence of σ_ϕ^2 depend on the relevant noise sources, which is in more detail discussed in [189]. Rewriting equation (4.37) yields:

$$\langle P_0 \rangle = \frac{1}{2} + \frac{1}{2}\exp\left(-(\frac{\tau}{T_2^*})^\varepsilon\right), \tag{4.38}$$

where the relevant decay time is often referred to as free induction decay time or T_2^*-time and ε depends on the type of noise.

The Ramsey sequence, sketched in figure 4.9(a), is usually used to experimentally determine the T_2^*-time. The idea is to prepare the quantum system in a superposition state

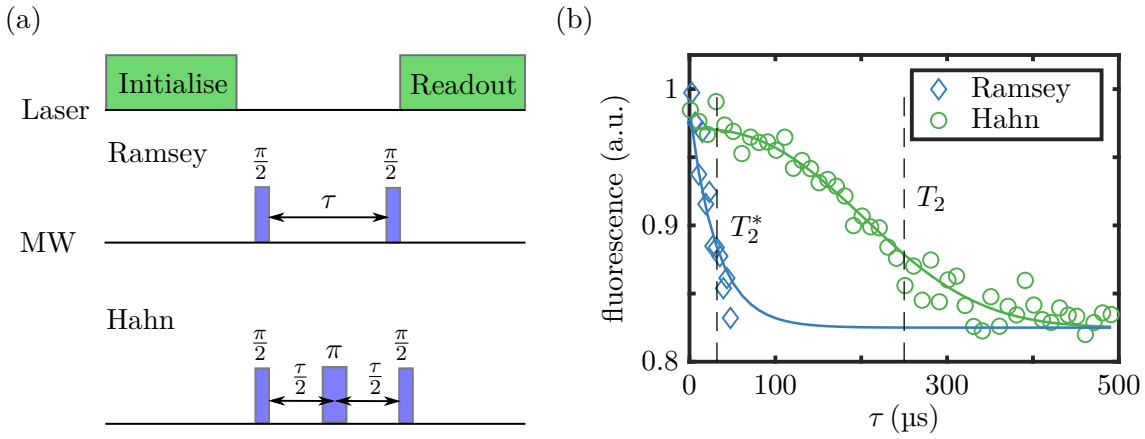

Figure 4.9: Experimental determination of the T_2^*- and T_2-times for a NV centre. (a) The T_2^*-time can be probed by bringing the quantum system into a superposition state and measuring the sensor phase after different idle times τ. The Hahn sequence corresponds to the Ramsey sequence, but includes an additional π-pulse in the middle of the interaction time. (b) This refocusing pulse extends the coherence of the NV centre. The solid lines are fits to the data following equation (4.38).

with known relative phase ϕ. In the absence of a signal, ϕ is measured after different idle times τ.

For NV centres, magnetic and electric noise originating from the lattice or the surface of the diamond are the main sources of the dephasing process [205–207]. As a consequence, diamonds which are enriched with the spin-free isotope ^{12}C usually have much longer T_2^* times (up to 100 µs [42]) compared to diamonds with a natural abundance of ^{13}C (on the order of 1 µs). But also slow drifts, for example of the temperature, or temporal and spatial inhomogeneities of the bias field can contribute to a shortening of T_2^*.

Transverse Relaxation – Decoherence

In order to reduce dephasing, a π-pulse can be applied in the middle of the interaction, and the final sensor phase ϕ then reads:

$$\phi = \int_{\tau/2}^{\tau} H(t)\mathrm{d}t - \int_{0}^{\tau/2} H(t)\mathrm{d}t, \tag{4.39}$$

where $H(t)$ includes the signal as well as possible noise sources. If $H(t)$ does not change during the interaction, the relative phase acquired during the first half is cancelled during the second half of the interaction period and ϕ reduces to zero. As a consequence, all noise which varies with a rate slower than the interaction time τ is efficiently filtered out and thus, the π-pulse acts as a filter for low frequency noise. As a consequence, the variance σ_ϕ^2 reduces and the resulting extended characteristic time is called coherence time, T_2-time

or spin-spin relaxation time. The measurement principle is usually referred to as Hahn echo sequence, which is sketched in figure 4.9(a). The interaction time can be increased by about an order of magnitude, as shown in figure 4.9(b).

As the edge of the frequency filter is shifted towards higher frequencies if τ becomes smaller, the idea to further enhance the interaction time is to apply a number of π-pulses instead of a single one. This principle is referred to as dynamical decoupling, which is in more detail discussed in section 4.3. Thereby, the decoherence time increases as $N_\pi^{2/3}$ with the number of π-pulses N_π, if noise with a Lorentzian shape and a very long coherence time can be assumed [180].

For ^{12}C enriched diamonds, the T_2-times of single NV centres can reach up to few milliseconds at room temperature [42] and up to a second at 77 K [208].

Longitudinal Relaxation

Longitudinal relaxation is the irreversible evolution of a quantum system into its thermal equilibrium. The released energy is absorbed by the environment, called the 'lattice', and the typical time constant is usually referred to as 'spin-lattice-relaxation' or T_1-time. If the thermal equilibrium state is a completely mixed state, the decay reads:

$$P_0(\tau) = \frac{1}{2} + \frac{1}{2}\mathrm{e}^{-\tau/T_1}. \tag{4.40}$$

As shown in figure 4.10(a), T_1-times can be experimentally obtained by initialising the quantum system into an eigenstate and recording the decay into the thermal equilibrium. For NV centres, mainly interactions with phonons are responsible for this type of relaxation at ambient conditions, whereas, at low temperatures, relaxation is mainly due to cross relaxation with neighbouring spins [209]. Due to the high Debye temperature of diamond, which limits the appearance of optical phonons, and the large zero-field splitting, which detunes the NV centre spin from other electronic spins, T_1-times can be very long. At cryogenic temperatures, relaxation times up to several hundreds seconds have been observed [102, 209]. At ambient conditions, T_1-times are typically on the order of a few milliseconds [209, 210], as exemplified in figure 4.10(b). More detailed literature about T_1-relaxation can be found in [20, 102, 209–212].

Since the T_1-time describes the relaxation into the thermal equilibrium, it is an absolute limit for all quantum operations and protocols using NV centres. The characteristic time scales usually behave as:

$$T_2^* < T_2 < T_1. \tag{4.41}$$

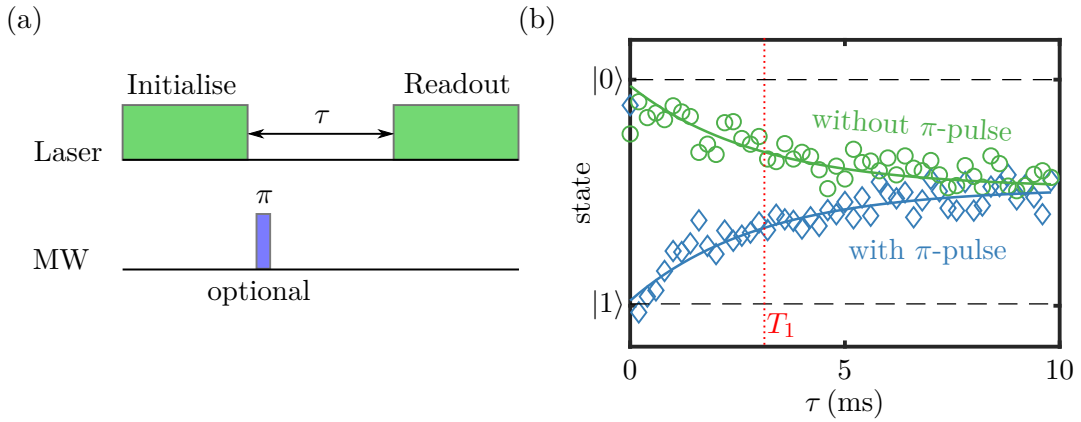

Figure 4.10: Experimental determination of the T_1-time for a NV centre. (a) A laser pulse is used to initialise the spin state into $|0\rangle$ or optionally into $|1\rangle$ using an additional π-pulse. After a variable time τ the probability to remain in the initial state is recorded optically. (b) This probability decays typically exponentially with the characteristic time scale T_1. The solid lines are fits to the data following equation (4.40).

There is another typical time constant which describes the relaxation in the rotation frame at the presence of an external resonant driving field. It is usually referred to as spin locking or $T_{1\rho}$ time. For more information, the interested reader is referred to [142].

Experiments

5 Nanoscale nuclear magnetic resonance

Nuclear magnetic resonance (NMR) is one of the most powerful scientific tools and finds application in all areas of natural science as well as in medicine [213, 214]. It is based on the detection of electromagnetic fields generated by precessing nuclear spins and the oscillation frequency depends on the external bias field, the nuclear isotopes and their chemical environment.

The dependency on the external bias field can be used for imaging. The idea is to put a sample into well known magnetic field gradients. By recording the resonance frequency for various magnetic field orientations and gradients, the location of the target spins can be assigned. Imaging contrast can be obtained by using relaxation rates, which depend on the chemical environment [215]. For example, the T_2-time of hydrogen spins close to a tumor is usually longer than in muscular tissue. This technique is known as magnetic resonance imaging (MRI) and is frequently used in medicine, especially for imaging human organs and tissues, due to its high resolution, non-invasiveness and insensitivity for hard structures as bones.

On the other side, the dependency of the frequency on the nuclear isotope and the chemical environment can be used to reveal information about the sample composition and the electrical and nuclear environment of the target spins. This turns out to be very useful for determining the structure of a molecule of interest. Also, NMR spectra represent unique fingerprints and thus can be used for sample identification. For their work on this topic, Bloch and Purcell received the Noble prize in physics 1952 [216, 217].

Despite all the usefulness and achievements there is one problem. The electromagnetic fields generated by the precessing nuclear spins are rather weak, and classical sensors, usually detection coils, have limited sensitivities. Therefore, a high number of spins (typically about 10^{15}) and thus large samples sizes ($>\mu m^3$) are required to record an NMR signal, as sketched in figure 5.1 [218, 219].

Furthermore, the dimension of a coil is not arbitrarily reducible and thus, the spatial resolution is too poor to examine processes on the nanoscale. Studying these processes would be highly interesting for research and medical applications – especially, since in many cases, the properties and behaviour of materials on the nanoscale are completely different from the macroscopic characteristics. Because a lot of quantum and thermal effects are not

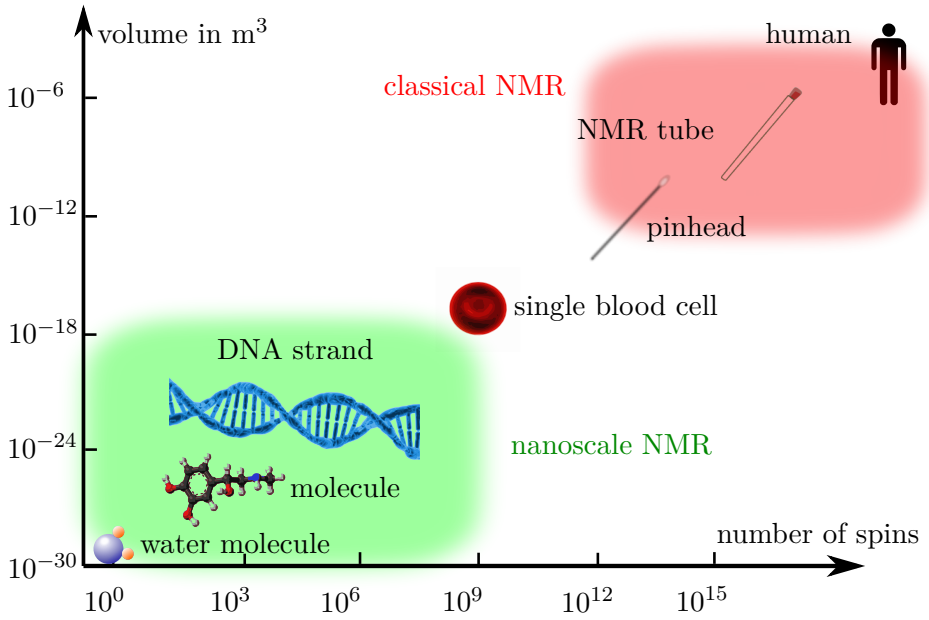

Figure 5.1: Size comparison between classical and nanoscale NMR. Classical detectors require a large number of nuclear spins and thus macroscopic sample sizes. Using the NV centre in diamond it is possible to perform NMR on the nanoscale, which might lead to new insights and discoveries.

observable in large systems, many areas including nanoscience, nanotechnology, surface sciences and semiconductor physics would highly benefit from NMR on the nanometer length scale. Monitoring phenomena and dynamics on the nanoscale or precise structure determination of proteins or cells could also help our understanding of biological processes and aid detection and treatment of diseases.

In the following, the NV centre is presented as a possible sensor to record NMR fields of a nanoscale sample. Due to its excellent sensitivity and nanoscale resolution, it represents a promising detector for nanoscale NMR and MRI. Using dynamical decoupling (see section 4.3) the NV centre can be made sensitive to AC magnetic fields generated by the precessing spins [220]. The variety of recent publications highlight the great potential of this technique [22, 150–156, 221].

In the next sections, first, the physical principles of NMR are introduced. After that, the ideas for realising nanoscale NMR using single NV centres in diamond are explained and experimental results are shown. Finally, problems and limitations are discussed.

5.1 Principles of NMR

Nuclear magnetic resonance is the analogue to electron paramagnetic resonance (EPR) for nuclear spins. Thus, the principles are essentially identical and the biggest difference is the highly reduced gyromagnetic ratios (about $10^3 - 10^4$ times smaller), mainly due to the higher masses of the nuclear spin isotopes. Whether or not a nuclear isotope possesses a spin depends on the number of protons and neutrons it contains. A selection of the most important isotopes with a nuclear spin is listed in table 5.1.

Table 5.1: List of some of the most important nuclear isotopes with a spin. The values for the gyromagnetic ratios γ_n, the spin angular momenta and natural abundances are taken from [222].

isotope	γ_n in MHz/T	spin	natural abundance
^{1}H	42.58	1/2	99.9 %
^{2}H	6.54	1	0.01 %
^{13}C	10.71	1/2	1.1 %
^{14}N	3.08	1	99.6 %
^{15}N	-4.32	1/2	0.4 %
^{19}F	40.08	1/2	100.0 %
^{29}Si	-8.47	1/2	4.67 %

If the spin is $I = 1/2$, there are two eigenstates, namely $|\uparrow\rangle$ ($m_\mathrm{I} = 1/2$ state) and $|\downarrow\rangle$ ($m_\mathrm{I} = -1/2$ state). Without external influences these two states are energetically degenerate and as in EPR this degeneracy can be lifted by applying a magnetic bias field. The energy difference E_Δ is given by:

$$E_\Delta = h\nu_L = h\gamma_n|\vec{B}| = h\gamma_n(|\vec{B}_0 + \vec{B}_\mathrm{env}|), \tag{5.1}$$

where h is Planck's constant, ν_L is the Larmor frequency, γ_n is the gyromagnetic ratio of the nucleus and the magnetic field vector $\vec{B}$ is composed of the external bias field $\vec{B}_0$ and the magnetic field generated by the environment $\vec{B}_\mathrm{env}$. The nucleus can absorb electromagnetic radiation with a frequency ν_L and thereby change its spin state.

Every nuclear spin has a magnetic moment and thus the whole sample usually possesses a net magnetisation $\vec{M}$, which is the sum of all the individual nuclear spin contributions. If $\vec{M}$ has a component $M_\perp$ perpendicular to the external magnetic field $\vec{B}$, the magnetisation precesses around $\vec{B}$ and electromagnetic radiation is emitted with a frequency equal to ν_L and an amplitude proportional to $M_\perp$. This radiation represents the NMR signal.

If the net magnetisation $\vec{M}$ is parallel to $\vec{B}$, a radio-frequency pulse can be used to perform a $\pi/2$-rotation to align the magnetisation into the perpendicular direction (same principles as described in section 2.5).

5.1.1 Interpreting the NMR spectrum

In the centre of figure 5.2, a typical one-dimensional ^{1}H-NMR spectrum is displayed (here 1,1,2-trichloroethane) [223]. In the following, the information contained in this spectrum is analysed step-by-step. For more advanced purposes higher dimensional NMR spectroscopy can help to further improve resolution and peak assignments.

Chemical shift - Electronic environment

Although both main lines in the spectrum origin from hydrogen spins, they are separated by a relative frequency difference of about 2 ppm. The reason is that the Larmor frequency of each spin also depends on its chemical environment – especially on the surrounding electron density – and this phenomena is called chemical shift. The principle is sketched in the top box of figure 5.2. In an external magnetic field $\vec{B}_0$ electrons circulate and generate an additional magnetic field $\vec{B}_{\mathrm{env}}$ opposing the external field $\vec{B}_0$. The reduced effective field at the nucleus is thus $\vec{B}_0 + \vec{B}_{\mathrm{env}}$. The higher the surrounding electron density, the larger is this shielding effect and the lower is the effective field felt by the nucleus. For the example above, chlorine has a larger electronegativity compared to hydrogen and carbon. Therefore, the hydrogen ($\mathrm{H_b}$) bound to the carbon joined to two chlorine atoms has a slightly lower surrounding electron density and its Larmor frequency is higher. The other two hydrogen atoms ($\mathrm{H_a}$) have an equivalent configuration and thus the same frequency. Since chemical shifts δ_{cs} depend on the bias field, spectra are usually plotted in terms of relative frequency rather than in terms of absolute frequency:

$$\delta_{\mathrm{cs}} = \frac{\nu - \nu_{\mathrm{ref}}}{\nu_{\mathrm{ref}}}, \tag{5.2}$$

with units of parts-per-million, relative to some standard ν_{ref} (usually tetramethylsilane is taken for protons).

Splitting - Coupling to neighbours

By taking a close look at the spectrum, it can be seen, that the two main peaks are split into two and three sub-peaks, respectively. This splitting occurs when the neighbouring atoms also have a magnetic moment, for example a nuclear spin. For this spin-spin coupling (or J-coupling) the orientations of the magnetic moments are relevant, since they represent an additional magnetic field, which further influences the effective field of NMR active nuclei. In the spectrum above, the $\mathrm{H_a}$-protons experience the spin of $\mathrm{H_b}$, which can have two orientations – parallel or anti-parallel to the external bias field. Thus, the peak splits into two sub-peaks, which are centred around the original position and are called

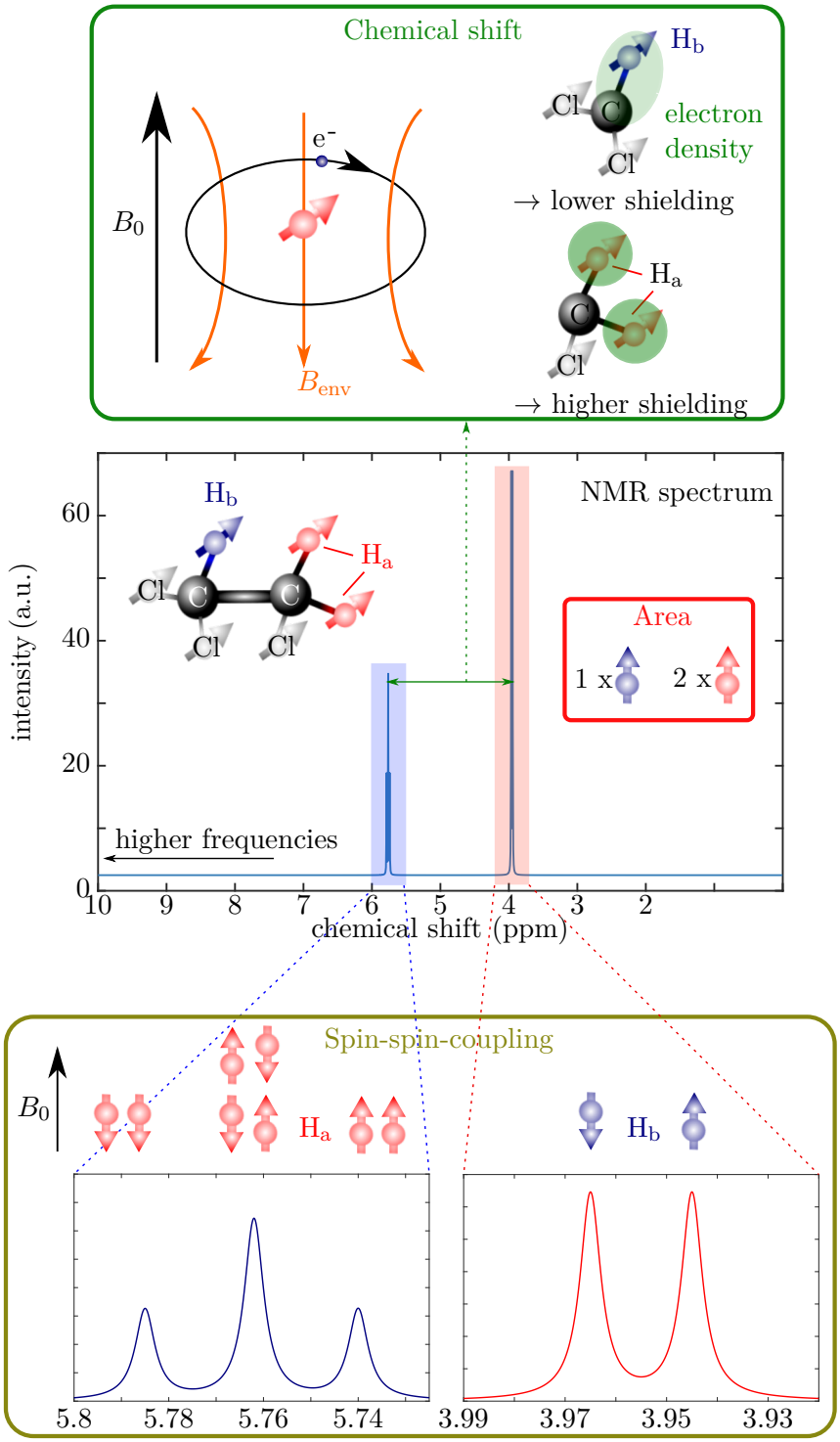

Figure 5.2: Interpretation of an NMR spectrum. The signal peaks in a typical NMR spectrum contain information about the composition and environment of a sample (here 1,1,2-trichloroethane, data taken from [223]). A more detailed discussion is in the text.

a doublet. The two spins of the H_a-protons can align into four configurations and the two configurations where the spins are orientated anti-parallel are equivalent and generate no additional field. For this reason, the peak splits into a triplet and the central peak is unshifted and has twice the amplitude. In general, the number of lines depends on the number of neighbouring atoms with a magnetic moment. The magnitude and the sign of the splitting depends on the coupling strength and therefore contains information about connectivity of chemical bonds and relative bond distances and angles. This type of coupling is independent of magnitude of the external magnetic field and about 6 Hz in the above example.

Peak area - Spin density/number

The peak area is proportional to the number of spins contributing to this peak. The more spins oscillate with the same frequency, the larger is the generated magnetic field. For the example above, the signals of two H_a spins per molecule add to the right peak and its area is twice the area of the left peak, for which only a single H_b spin per molecule contributes.

5.1.2 Sample magnetisation in classical NMR

In classical NMR the magnetisation of the sample depends on the thermal polarisation. If the whole sample contains N spins, a number of spins $N_\uparrow$ aligns parallel to the external magnetic field while the rest $N_\downarrow = N - N_\uparrow$ arranges anti-parallel. Since the contribution of a single spin to the NMR signal is cancelled by another spin with opposing orientation, the net magnetisation depends only on the difference $N_\uparrow - N_\downarrow$. Although the parallel orientation is energetically more favourable, thermal motion populates both states and the ratio is given according to Boltzmann statistics:

$$\frac{N_\downarrow}{N_\uparrow} = \mathrm{e}^{-E_\Delta/k_B T} \approx 1 - \frac{h\gamma_n B}{k_B T}, \tag{5.3}$$

where $k_B = 1.38 \cdot 10^{-23}\,\mathrm{J/K}$ is the Boltzmann constant. The magnetisation depends on the ratio of magnetic energy $E_\Delta = h\gamma_n B$ and thermal energy $E_{\mathrm{therm}} = k_B T$. Unfortunately, at ambient conditions and even for high magnetic fields, E_{therm} is much larger than E_Δ. As an example, for $T \approx 300\,\mathrm{K}$, $\gamma_{^1\mathrm{H}} = 42.58\,\mathrm{MHz/T}$ and $B = 15\,\mathrm{T}$, $E_\Delta/E_{\mathrm{therm}} \approx 10^{-4}$ and thus $N_\downarrow/N_\uparrow \approx 0.9999$, which corresponds to about 1 spin out of 10^4. Improving the polarisation by reducing the temperature is incompatible with most biologic samples and further increasing B requires expensive and elaborated setups. Thus, alternative techniques to increase $N_\downarrow/N_\uparrow$ are of very high interest in research and industry.

The low polarisation at ambient conditions is also one main reason why one needs a high number of spins and thus macroscopic sample sizes for classical NMR. In order to perform NMR experiments with nanoscale samples, the magnetisation has to be detected in a non-inductive way.

5.2 Principles of nanoscale NMR

The idea presented here is based on the direct detection of oscillating NMR magnetic fields. For this purpose, a magnetic field sensor with a very high sensitivity and spatial resolution is required. Although there are a few promising candidates, including magnetic force resonance microscopes [219, 224, 225], the following concentrates on the detection with single NV centres in diamond. The first realisation were reported recently [22, 23] and the principle is sketched in figure 5.3.

A single NV centre located just a few nanometres below the surface of the diamond is used to sense the magnetic field generated by the nuclear spins placed directly on top of the surface. The examined sample size is on the order of $100\,\mathrm{nm}^3$. Furthermore, the sensitivity is in principle sufficient to detect and characterise a single spin [24].

5.2.1 Sample magnetisation in nanoscale NMR

In contrast to classical NMR, the sample magnetisation in nanoscale NMR is dominated by statistical effects rather than thermal polarisation [216]. The numbers of spins aligned parallel and anti-parallel to the external field $N_\uparrow$ and $N_\downarrow$ can usually be very well approximated by binomial distributions [219]. For a large number of total spins N, the relative standard deviation ($\sim 1/\sqrt{N}$) is very small. However, when reducing the sample size, statistical effects become more and more important. For example, when considering in total only 10 spins the probability that $N_\uparrow = 6$ and $N_\downarrow = 4$ is about 21 % and thus not negligible. In this case $N_\downarrow/N_\uparrow = 2/3$, while according to equation (5.3) and the same parameters as above $N_\downarrow/N_\uparrow \approx 0.9999$ for the thermal polarisation. Thus, the so called statistical polarisation clearly exceeds the thermal polarisation [216, 219, 225]. The critical numbers for the transition between both regimes vary, depending on temperature and magnetic bias field, between 10^9 and 10^{15} nuclear spins. Since in a volume of $1\,\mathrm{nm}^3$ there are usually less than 100 spins, statistical polarisation clearly dominates on the nanoscale.

In contrast to the thermal polarisation, the statistical polarisation is time-dependent. Statistical nuclear spin flips due to interactions with the environment change the magnetisation in the detection volume. Furthermore the dipole-dipole interactions between the electron spin of the NV centre and the nuclear spins depend strongly on the distances and thus diffusion in liquid samples becomes important.

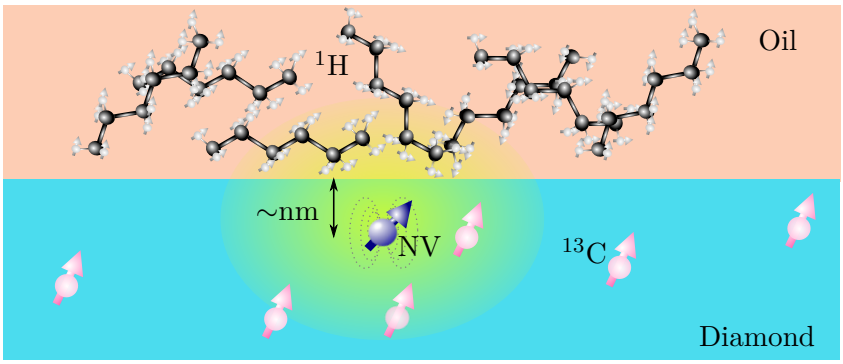

Figure 5.3: Nanoscale nuclear magnetic resonance setup. A shallow NV centre located just a few nanometre below the diamond surface interacts with nuclear spins in the sample. The corresponding detection volume (yellow shading) is in the $100\,\mathrm{nm}^3$-range.

A simulation of a typical nanoscale NMR signal is shown in figure 5.4 (see [226] for details about the method). The magnetic field oscillates with the nuclear Larmor frequency (here 0.1 MHz), but its amplitude and phase vary with time. Thereby, the relevant time scale is often referred to as the correlation time τ_{corr}. The Fourier transform of this signal is a peak centred around the Larmor frequency. The width, however, is limited by the inverse of τ_{corr}.

5.2.2 Experimental realisation

In order to record the NMR signal, the NV centre has to be made sensitive to frequencies close to the Larmor frequency of the target spins. As extensively discussed in section 4.3, dynamical decoupling (DD) uses a series of N_π π-pulses to generate a controllable frequency filter. The representation of the DD sequence in frequency space $\mathcal{F}(\omega, N_\pi, \tau)$ determines the sensitivity of a sensor for a certain frequency $\omega(= 2\pi\nu)$ as a function of the pulse spacing τ. A more detailed description of $\mathcal{F}(\omega, N_\pi, \tau)$ can be found in section 4.3. Due to the interaction with the NMR field and the DD control the NV sensor accumulates a quantum phase ϕ, which represents the measurement quantity (compare equation (4.20) and [156]):

$$\phi_i(\omega, N_\pi, \tau) = \tilde{\gamma}_{\mathrm{NV}} \int_{-\infty}^{\infty} \tilde{B}_i(\omega)\mathcal{F}(\omega, N_\pi, \tau)\mathrm{d}\omega, \tag{5.4}$$

where $\tilde{\gamma}_{\mathrm{NV}} = 2\pi \cdot \gamma_{\mathrm{NV}} \approx 1.76 \cdot 10^{11}\,\mathrm{rad/(sT)}$ is the gyromagnetic ratio of the NV centre's electron spin and $\tilde{B}_i(\omega)$ is the Fourier transform of the magnetic field during the interaction period. As shown above, the amplitude and phase of the signal vary over time and thus the accumulated phase $\phi_i(\omega, N_\pi, \tau)$ varies for every measurement repetition. The final result

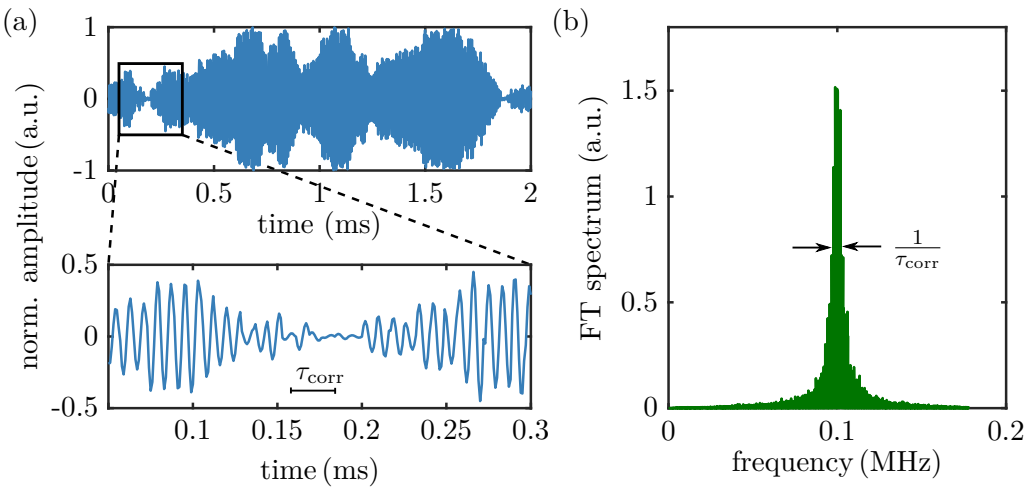

Figure 5.4: Simulated nanoscale NMR signal. (a) Due to the time-dependent statistical polarisation, the signal amplitude and phase vary with time, while the oscillation frequency is fixed. (b) The Fourier transform (FT) yields a peak centred around this frequency, albeit with a finite width which depends inversely on the correlation time τ_{corr}.

is a weighted average over all possible values for $\phi_i(\omega, N_\pi, \tau)$ and the weighting function depends on the distributions of amplitudes and phases. Excluding additional relaxation mechanisms and assuming the distribution for ϕ follows a normal distribution with variance $\langle\phi^2\rangle$ and zero mean, the averaged probability function can be written as [156]:

$$\langle P_0\rangle = \frac{1}{2}(1 - \langle\cos\phi\rangle) = \frac{1}{2}\left(1 - \mathrm{e}^{\frac{-\langle\phi^2\rangle}{2}}\right) = \frac{1}{2}\left(1 - \mathrm{e}^{-\chi}\right), \tag{5.5}$$

where the decoherence function $\chi = \langle\phi^2\rangle/2$ represents a convolution of power spectral density $\mathcal{S}(\omega)$ and $|\mathcal{F}(\omega, N_\pi, \tau)|^2$ [24, 156]:

$$\chi = \frac{\tilde{\gamma}_{\mathrm{NV}}^2}{4\pi}\int_{-\infty}^{\infty}\mathcal{S}(\omega)\,|\mathcal{F}(\omega, N_\pi, \tau)|^2\,\mathrm{d}\omega. \tag{5.6}$$

The power spectral density of the NMR signal is given by:

$$\mathcal{S}(\omega) = |\tilde{B}(\omega)|^2 = \int_{-\infty}^{\infty}\langle B(t)B(0)\rangle\,\mathrm{e}^{i\omega t}\mathrm{d}t, \tag{5.7}$$

and for N_π equally spaced π-pulses, $|\mathcal{F}(\omega, N_\pi, \tau)|^2$ can be written as [170, 180]:

$$|\mathcal{F}(\omega, N_\pi, \tau)|^2 = \frac{2}{\omega^2}\cdot F(\omega\tau) = \frac{2}{\omega^2}\cdot 8\frac{\sin^4\left(\frac{\omega\tau}{4N_\pi}\right)\sin^2\left(\frac{\omega\tau}{2}\right)}{\cos^2\left(\frac{\omega\tau}{2N_\pi}\right)}, \tag{5.8}$$

where $F(\omega\tau)$ is often referred to as filter function in literature.

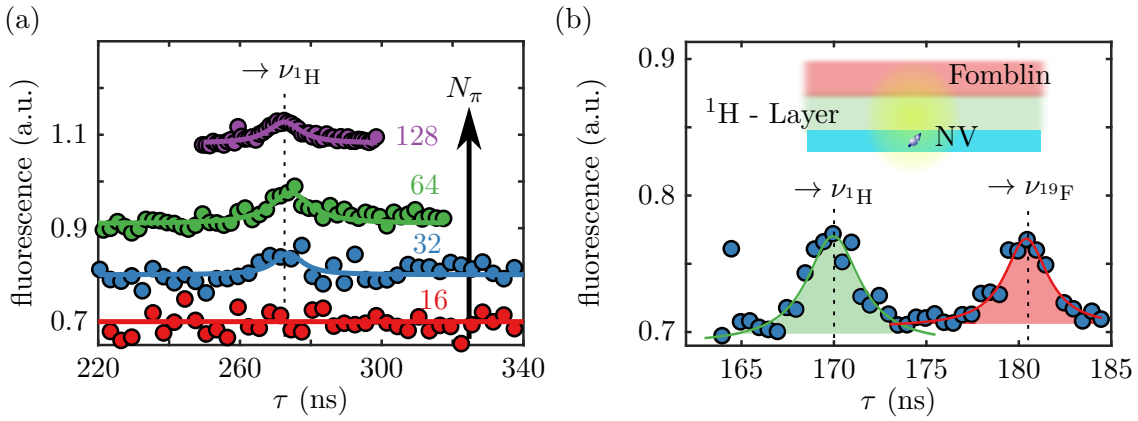

Figure 5.5: Experimental nanoscale NMR. (a) ^{1}H NMR spectra recorded using different number of applied pulses N_π with the same NV centre. The signal height increases with N_π until decoherence limits the contrast. The data was partially offset for reasons of overview. (b) Nanoscale NMR experiment showing nuclear isotope discrimination. For an arrangement, as sketched in the inset, the signal of both ^{1}H- and ^{19}F-spins were recorded simultaneously.

Nanoscale ^{1}H-NMR measurements recorded with different N_π are shown in figure 5.5(a). The spectra were measured with a single NV centre located $(4.1 \pm 0.3)\,\mathrm{nm}$ below the surface of the diamond (determination see below) in a setup as sketched as in figure 5.3. The target ^{1}H-spins are located inside an immersion oil (Fluka Analytical 10976) with a density of $\rho \approx 50\,\mathrm{nm}^{-3}$. The time τ separating the N_π π-pulses of the used XY8 sequence was adapted successively and the corresponding final sensor state was measured. The magnetic bias field of 43.2 mT corresponds to a ^{1}H Larmor frequency of about $\nu_{1\mathrm{H}} \approx 1.84\,\mathrm{MHz}$ and thus the resonant pulse spacing should be $\tau = 272\,\mathrm{ns}$ (compare equation (4.18)). For $N_\pi = 16$, the interaction time is too short to detect a signal within the chosen recording time. By increasing the number of pulses a clear signal becomes visible. Although the signal height should in principle further increase with N_π, relaxation processes interfere with the measurement and reduce the contrast. The interaction duration for DD spectroscopy is limited by the T_2-time.

In figure 5.5(b), it is shown, that it is possible to discriminate different nuclear spin isotopes. For this experiment, a different, about $(6.5 \pm 1.0)\,\mathrm{nm}$ deep, NV centre was used and the idea was to measure the ^{19}F spins of the Fomblin molecule, which is hydrogen free. At a bias field of about 69 mT, XY8-16 sequences (so $N_\pi = 128$) were used. Surprisingly, there are two peaks in the resulting spectrum – one corresponding to the ^{19}F Larmor frequency ($\tau = 180.8\,\mathrm{ns}$) and one to the ^{1}H Larmor frequency ($\tau = 170.2\,\mathrm{ns}$). A possible interpretation is that an adsorptive thin layer containing hydrogen atoms forms during sample preparation, resulting in a setup as sketched in the inset of figure 5.5(b).

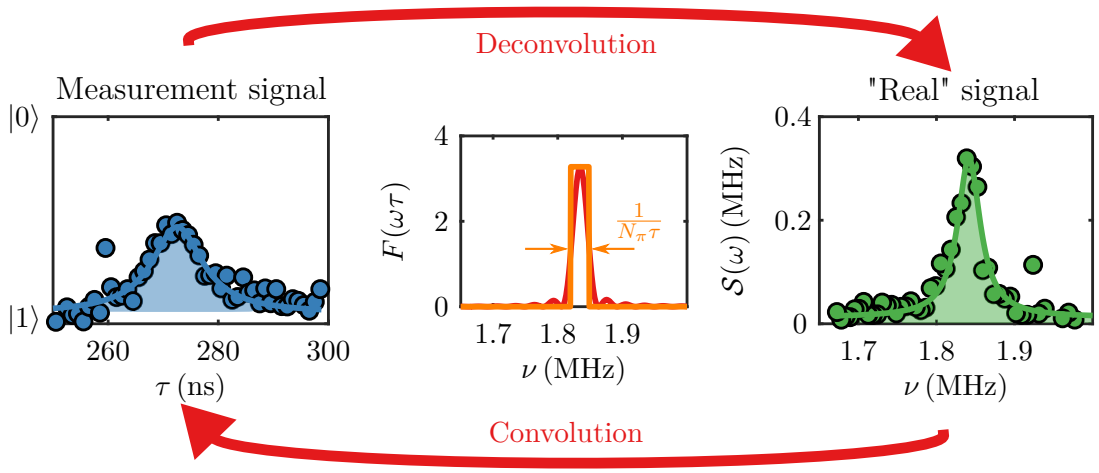

Figure 5.6: Deconvolution of the measurement signal. The recorded data is a convolution of the magnetic signal $S(\omega)$ and the filter generated by the used DD protocol. In order to extract $\mathcal{S}(\omega)$, a deconvolution has to be performed. Since an exact computation is not possible, $F(\omega\tau)$ is approximated as an rectangular function.

For further analysis, $\mathcal{S}(\omega)$ needs to be extracted from the recorded data. Due to the limited number of experimental data points compared to the infinite number of unknown power spectral density amplitudes, computing an exact deconvolution is impossible. A well established approach is to approximate $F(\omega\tau)$ as a rectangular function, centred around the maximum position $\omega = \pi/\tau$ ($\leftrightarrow \nu = 1/(2\tau)$), with width $\omega_\Delta = 2\pi/(N_\pi\tau)$ ($\leftrightarrow \nu_\Delta = 1/(N_\pi\tau)$) [22]:

$$F(\omega\tau) = A \cdot \left[\Theta_\mathrm{H}\left(\omega - \frac{\pi}{\tau} + \frac{\pi}{N_\pi\tau}\right) - \Theta_\mathrm{H}\left(\omega\tau - \frac{\pi}{\tau} - \frac{\pi}{N_\pi\tau}\right)\right], \tag{5.9}$$

where $\Theta_\mathrm{H}(x)$ is the Heaviside step function. A comparison is sketched in figure 5.6 which shows that this is a reasonable approximation. For large number of pulses the height A increases as $2N_\pi^2$ since the sensor phase increases linearly with the number of pulses N_π, but the result depends on the variance $\langle\phi^2\rangle$ which scales quadratically. The width is chosen as the full width at half maximum of the filter function. Then equation (5.6) simplifies to [24]:

$$\chi = \frac{4\tilde{\gamma}_\mathrm{NV}^2}{\pi^2}\mathcal{S}(\omega)N_\pi\tau, \tag{5.10}$$

with $\omega = \pi/\tau$ and solving for $\mathcal{S}(\omega)$ yields:

$$\mathcal{S}(\omega = \frac{\pi}{\tau}) = \frac{\pi^2}{4\tilde{\gamma}_\mathrm{NV}^2 N_\pi\tau}\chi. \tag{5.11}$$

Both the shape and the area of $\mathcal{S}(\omega)$ contain valuable information. The profile, for example, depends on the nanoscale dynamics of the target spins [227]. The width can provide information about diffusion and nuclear relaxation mechanism [22, 27, 228]. The area is a measure of the strength of the magnetic field fluctuations (neglecting the influences of diffusion and dipolar coupling onto the measurement result) [24]:

$$\langle \Delta B^2 \rangle = \frac{1}{2\pi} \int_{-\infty}^{\infty} S(\omega) d\omega, \tag{5.12}$$

which can for example be used to determine the depth d of the NV centre if the proton density ρ_N is known or vice versa [24, 156]:

$$d = \left[\frac{5}{1536\pi \langle \Delta B^2 \rangle} \mu_0^2 h^2 \gamma_n^2 \rho_N \right]^{1/3}, \tag{5.13}$$

where $\mu_0 = 4\pi \cdot 10^{-7}\,\mathrm{N/A^2}$ is the vacuum permeability.

5.3 Limitations up to date

Although single NV centres are capable of measuring NMR signals from a nanoscale sample volume and are in principle sensitive enough to detect a single external nuclear spin, the quality of the spectra is usually clearly worse compared to the ones known from classical NMR.

One of the most important drawbacks is the limited spectral resolution. Using conventional dynamical decoupling, the obtainable linewidth is limited by the T_2 coherence time of the sensor. Especially for shallow NV centres, the T_2 time is typically in the range of just a few microseconds, which corresponds to a spectral resolution of several tens or hundreds of kilohertz. This is far from sufficient to resolve the small shifts and splittings caused by the chemical environment, which contain an enormous amount of information and made NMR spectroscopy so important. Great effort has been made to solve this issue and the ideas reach from improving the properties of the NV centres by material science to new analysis methods [229] and utilising more advanced techniques including correlation spectroscopy [27, 228, 230]. The quantum heterodyne technique [153], which represents another possible approach, is introduced in chapter 7 of this thesis.

The same protocol helps with reducing the recording time, which for DD spectroscopy is rather long since every frequency component has to be sampled individually and thus, a lot of time has to be spent for a spectrum with high signal-to-noise ratio and many data points.

Another problem is the time-dependence of the statistical magnetisation, which leads to broadening of the NMR lines. Due to the strong distance dependence of dipolar couplings, one of the main issues is diffusion. Ideas to reduce the influence of diffusing nuclear spins include increasing the sample volume by using deeper NV centres improving the signal coherence time quadratically with depth [230] or to use polymers which slow down diffusion.

Furthermore, the used π-pulses can lead to signal distortion and artificial peaks in spectra. The origin of this problem and a solution are discussed in chapter 6.

Another issue is that optimal strategies for certain tasks are not known yet, for example when recording a full spectrum is excessive. The solution for such a specific problem is discussed in chapter 8.

Finally, the appearance of spurious harmonics due to the finite duration of the π-pulses in the XY8-sequence complicates the spectrum and may lead to false signal identification [28]. A possibility to overcome this problem is discussed in detail in chapter 6 and the findings are confirmed by experimental data.

6 Quantum spectroscopy using randomisation of pulse phases

Pulse errors are unavoidable in experiments and limit their performance. This is especially critical when larger numbers of pulses, which suffer from amplitude and/or frequency detuning errors, are applied. Therefore, robust dynamical decoupling (DD) sequences that include several pulse phases [146,167,179,184,231] were developed and they compensate for those errors to a certain degree. However, they have the disadvantage to produce spurious harmonic responses [28], which distort the measurement outcome. Possible consequences are incorrect signal identification and inaccurate result interpretation.

The idea to suppress spurious responses, that is introduced in the following, is based on adapting the phases of the used π-pulse randomly. Furthermore, it is shown that signal distortions due to π-pulse imperfections can be mitigated when using this randomisation technique. The performance is experimentally shown for nanoscale nuclear spin sensing and magnetometry of classical AC fields. Although single NV centres in diamond are used as a sensor, the method is applicable to any qubit sensor and can be combined with existing multi-pulse quantum sensing sequences to enhance their performance. Adapted with permission from [232]. Copyright 2019 by the American Physical Society.

6.1 Spurious responses under dynamical decoupling

In quantum sensing the aim is to detect a target field $B(t)$, for instance originating from a single nuclear spin or a weak magnetic signal. DD can be used to control the quantum sensor by applying π-pulses that create a spectral filter and make the sensor sensitive to only a specific frequency range, while it is decoupled from noise of different spectral regions. By adapting the spacing between individual pulses, various frequency components can be sampled and thus it is possible to do spectroscopy (see also section 4.3).

The sequence of π-pulses is usually arranged as a periodic repetition of a basic pulse unit. In order to improve the robustness, those π-pulses often have specific phases θ_i, as shown in figure 6.1(a). A famous example is the routinely used XY8 sequence, sketched in figure 6.1(b), whose basic unit consists of eight equidistant π-pulses with phase differ-

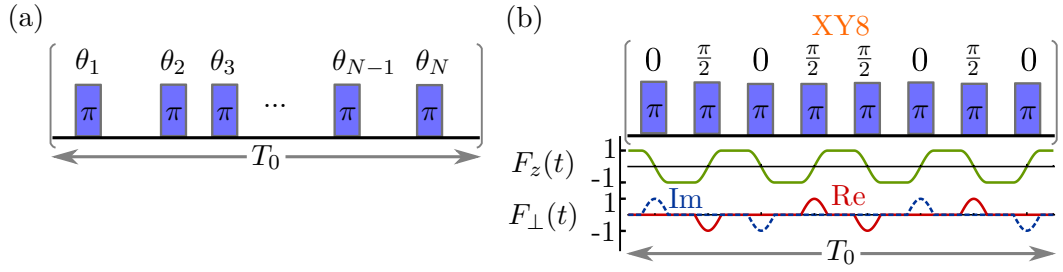

Figure 6.1: Basic unit for pulsed dynamical decoupling. (a) The phases θ_i and the timing of the π-pulses define the basic unit of a DD pulse sequence. (b) The basic unit of the XY8 sequence consists of eight equidistant π-pulses with phases alternating between 0 and $\pi/2$. The corresponding $F_z(t)$ and $F_\perp(t)$ are plotted below the sequence (see equations 6.2 and 6.3). Due to the finite length of the π-pulses, $F_\perp(t)$ does not vanish completely. Adapted with permission from [232]. Copyright 2019 by the American Physical Society.

ences of $\pi/2$, arranged in a way to mitigate pulse errors and imperfections [184] (also see section 4.3.3).

As shown in figure 6.2(a), the basic DD unit may be repeated M times, which increases the total signal accumulation time $T_{\text{total}} = MT_0$ and thereby enhances the acquired contrast [165]. Furthermore, the frequency resolution is improved to $\sim 1/T_{\text{total}}$ and M is eventually limited by the coherence time of the sensor.

In theory the shape of a π-pulse is often assumed δ-like. In realistic situations, however, the π-pulses can not be instantaneous because of limited control power due to hardware specifications or heat stability of the used equipment. Taking finite pulse length into account, the Hamiltonian of the DD protocol and the target field $B(t)$ reads [232]:

$$\mathcal{H}(t) = \frac{1}{2}F_z(t)B(t)\hat{\sigma}_z + \frac{1}{2}[F_\perp(t)\hat{\sigma}_- + \text{H.c.}]B(t), \tag{6.1}$$

where $\hat{\sigma}_- = |0\rangle\langle 1|$. $F_z(t)$ is the modified stepped modulation function (compared to equation (4.13)) of the DD control [232]:

$$F_z(t) = (-1)^{m-1}\cos(\kappa(t)), \tag{6.2}$$

where m is the number of π-pulses applied up to time t and $\kappa(t)$ is the angle of rotation. Between the pulses, $\kappa(t) = 0$ and thus $F_z(t)$ remains unaltered. For instantaneous π-pulses, $F_z(t)$ directly changes sign. For finite length pulses, $\kappa(t) = \Omega t$, where Ω is the Rabi frequency, and $F_z(t)$ takes different values during the application of the pulses as sketched in figure 6.1(b).

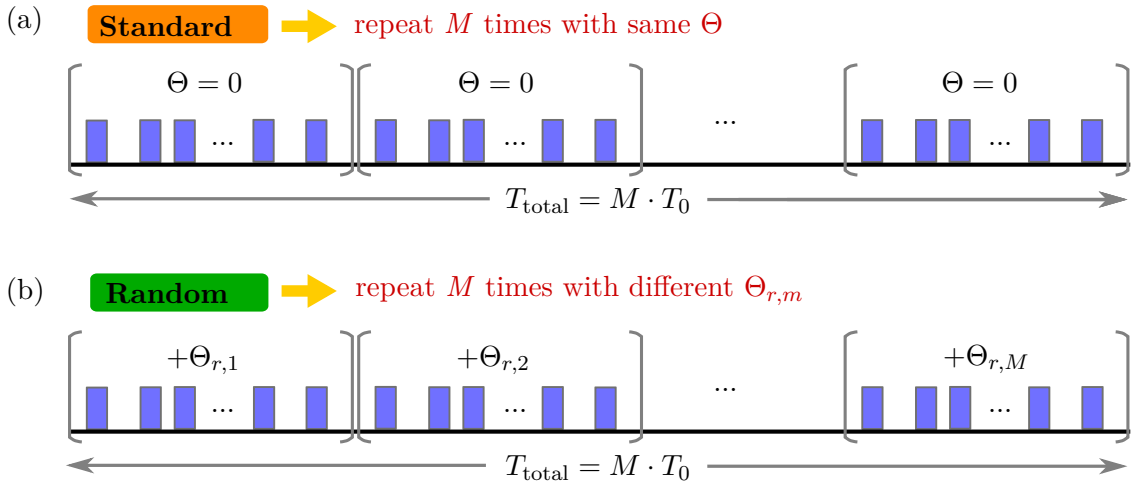

Figure 6.2: Principle of phase randomisation for dynamical decoupling. (a) In order to increase the sequence duration usually the same basic pulse unit is repeated multiple times (here M times). (b) For the randomisation protocol the same randomly determined phase $\Theta_{r,m}$ is added to all pulse phases within each unit, and there is a different independent random phase for every unit. The set of random phases $\{\Theta_{r,1}, \Theta_{r,2}, \ldots, \Theta_{r,M}\}$ can be renewed for different iterations of the sensing experiment. Adapted with permission from [232]. Copyright 2019 by the American Physical Society.

The perpendicular modulation function $F_\perp(t)$ takes the form [232]:

$$F_\perp(t) = i(-1)^{m-1} \exp\left\{-i[2\sum_{l=1}^{m-1}(-1)^l\theta_l + (-1)^m\theta_m]\right\} \sin\left(\kappa(t)\right), \tag{6.3}$$

and vanishes between pulses due to $\kappa(t) = 0$. The same applies for instantaneous control, where $\kappa(t)$ immediately changes from 0 to π and back. During a π-pulse, however, $F_\perp(t)$ has a non-zero value as indicated in figure 6.1(b) for the XY8 sequence. Although pulse shaping techniques [233] can eliminate the effect of deviations in $F_z(t)$, a non-zero $F_\perp(t)$ can influence the measurement outcome. For a frequency component, being the kth multiple of $1/T_{\text{total}}$, a spurious response will be created whenever the Fourier amplitude [232, 234]:

$$f_k^\perp = \frac{1}{T_{\text{total}}} \int_0^{T_{\text{total}}} F_\perp(t) \exp\left(-i\frac{2\pi kt}{T_{\text{total}}}\right) \mathrm{d}t = c_{k,M}\tilde{f}_{k/M}^\perp, \tag{6.4}$$

is non-zero, where

$$\tilde{f}_{k/M}^\perp \equiv \frac{1}{T_0} \int_0^{T_0} F_\perp(t) \exp\left(-i\frac{2\pi kt}{MT_0}\right) \mathrm{d}t, \tag{6.5}$$

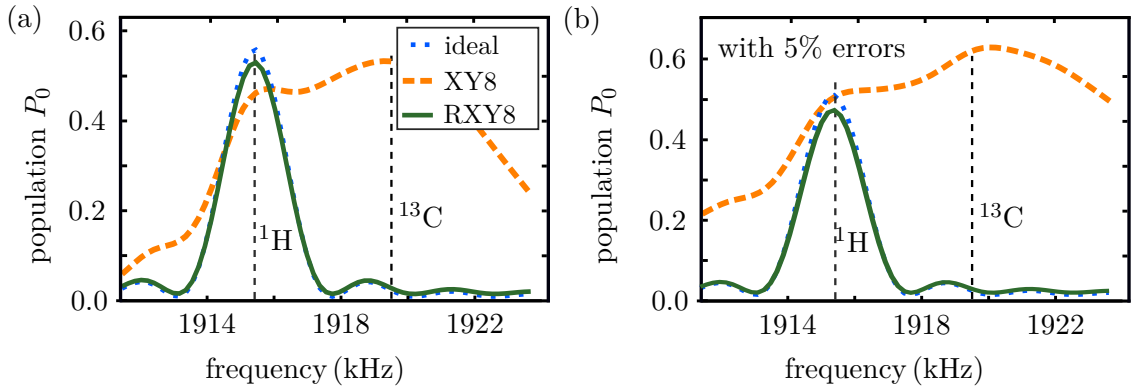

Figure 6.3: Simulated quantum spectroscopy with the XY8 sequence. (a) Spectra computed for a single NV centre coupled to one ^{1}H and one ^{13}C spin, respectively (for parameters see text). For the ideal XY8 sequence (blue dotted line) with instantaneous and error-free π-pulses, only a signal due to the ^{1}H spin is present in the shown frequency range. For π-pulses taking 200 ns, an additional peak due to the ^{13}C complicates the spectrum (orange dashed line). Using randomisation of the pulses phases the ^{13}C spin signal can be efficiently removed (green solid line). (b) Same as in (a), but including additional 5 % pulse errors in frequency detuning and driving amplitude, with respect to the ideal Rabi frequency, for the simulations of the π-pulses. Adapted with permission from [232]. Copyright 2019 by the American Physical Society.

is the Fourier component defined over a single period T_0 and [232]

$$c_{k,M} = \frac{1}{M} \sum_{m=1}^{M} \exp\left(-i \frac{2\pi k(m-1)}{M}\right). \tag{6.6}$$

The product $M c_{k,M}$ is a sum over roots of unity and cancels to zero, unless k/M is an integer and equation (6.6) yields $c_{k,M} = 1$ [232]. For standard repetitions of a basic pulse unit, the Fourier amplitudes are [232]:

$$f_k^{\perp} = \begin{cases} \tilde{f}^{\perp}_{k/M} & \text{if } k/M \in \mathbb{Z}, \\ 0 & \text{otherwise.} \end{cases} \tag{6.7}$$

This spurious response can cause false signal identification, which is especially critical for NMR experiments since the gyromagnetic ratios of two of the most relevant nuclei in NMR (^{1}H and ^{13}C) are almost a multiple of each other ($\gamma_{^1\mathrm{H}} \approx 4\gamma_{^{13}\mathrm{C}}$) [28]. In order to exemplify this, the results of simulated quantum spectroscopy experiments are shown in figure 6.3. A single NV centre is assumed to interact with one ^{1}H spin via the hyperfine field with components $A_\perp = 2\pi \cdot 2\,\mathrm{kHz}$ and $A_\parallel = 2\pi \cdot 1\,\mathrm{kHz}$. Furthermore, a single ^{13}C spin (hyperfine components $A_\perp = 2\pi \cdot 5\,\mathrm{kHz}$ and $A_\parallel = 2\pi \cdot 50\,\mathrm{kHz}$) is included [232]. XY8 sequences with $M = 200$ are used to compute spectra between 1910 kHz and 1925 kHz.

First, an ideal XY8 protocol with instantaneous π-pulses and no imperfections is used (blue dotted line). As expected for a magnetic bias field of about 45 mT, only the ^{1}H spin produces a signal in this frequency range. Taking finite π-pulse length (here 200 ns) into account, the simulated spectrum (orange dashed line) shows a high side-peak due to the carbon spin, which interferes with the ideal spectrum. If additional pulse errors are added to the π-pulses in form of frequency detuning and non-optimal driving amplitude (5 % deviation respectively), the performance gets even worse as shown in figure 6.3(b).

6.2 The randomisation protocol

In order to mitigate all spurious signals, the idea is to randomly modify the π-pulse phase in the following way [232]. Within one basic unit the phases of all π-pulses are incremented by the same random phase $\Theta_{r,m} \in [0, 2\pi[$. For each other repetition this additional phase is randomly and independently changed. The principle is sketched in figure 6.2(b). By setting all the random phases equal to zero, the standard DD version is recovered. Since the internal structure of the individual basic units is not altered, the robustness and the working principle are preserved.

This modification does not influence $F_z(t)$, but changes $F_\perp(t) \to F_\perp(t)e^{i\Theta_{r,m}}$ and it follows [232]:

$$\begin{aligned} f_k^\perp &= \frac{1}{MT_0}\int_0^{MT_0} F_\perp(t)\exp\left(-i\frac{2\pi kt}{MT_0}\right)\mathrm{d}t \\ &= \frac{1}{MT_0}\sum_{m=1}^{M}\int_{(m-1)T_0}^{mT_0} F_\perp(t)e^{-i\Theta_{r,m}}\exp\left(-i\frac{2\pi kt}{MT_0}\right)\mathrm{d}t \\ &= Z_{r,M}\tilde{f}_{k/M}^\perp, \end{aligned} \tag{6.8}$$

where [232]

$$Z_{r,M} = \frac{1}{M}\sum_{m=1}^{M} e^{i[\Theta_{r,m}-2\pi k(m-1)/M]}. \tag{6.9}$$

Using that $\Theta_{r,m}$ and thus $\Theta_{r,m} - 2\pi k(m-1)/M$ are random, $Z_{r,M}$ can be simplified to:

$$Z_{r,M} = \frac{1}{M}\sum_{m=1}^{M}\exp(i\Theta_{r,m}), \tag{6.10}$$

and thus represents a sum of random complex phases. Since the average of independent random phases is zero, both the expectation value $\langle|Z_{r,M}|^2\rangle$ [232]:

$$\langle|Z_{r,M}|^2\rangle = 1/M, \tag{6.11}$$

and the variance reduce with M [232]:

$$\langle(|Z_{r,M}|^2 - \langle|Z_{r,M}|^2\rangle)^2\rangle = (M-1)/M^3. \tag{6.12}$$

Averaging over K independent measurements, each recorded with a different set of random phase, further reduces $\langle|Z_{r,M}|^2\rangle$ by a factor of $1/K$ [232]. In contrast to a specific set of phases $\Theta_{r,m}$, which could only minimise $f_k^{\perp}$ for certain k, the randomisation method suppresses all spurious peaks produced by any DD sequence [232].

The simulations described above were repeated for the randomised version of the XY8 protocol, keeping all other parameters identical. As shown in both subfigures of figure 6.3, the unwanted disturbance of the ^{13}C spin is cancelled completely and the spectra are almost identical to the ideal ones.

6.3 Experimental realisation of the randomisation protocol

To experimentally benchmark the performance, different signal types were measured using DD spectroscopy. For the results shown in the following, exclusively the XY8 protocol was used and the performance of the standard and the randomisation versions are compared. However, the findings in principle apply to any other DD protocol (for example YY8 [235] or UR8 [231]). For the randomisation protocol, a random phase was added to all π-pulses as described above and in figure 6.2(b). In order to generate these random phases, the Python package *random* was used.

Experimental details

For all experiments the QuDi software suite was utilised (appendix A.1.4 and [236]). Single NV centres were used as sensing qubits (with states $|0\rangle$ and $|1\rangle$) through lifting the degeneracy of their $m_s = -1$ and $m_s = +1$ spin states by applying magnetic bias fields between 40 mT and 50 mT. Resonant microwave pulses then allow to selective address the $m_s = 0 \leftrightarrow m_s = -1$ transition. By using a $\pi/2$-pulse before applying the DD protocols, the NV centre is brought into a coherent superposition. After the interaction period the readout is performed in the same basis by mapping the acquired sensor phase to a population difference with a second $\pi/2$-pulse. These two $\pi/2$-pulses were without any intentional errors, also for section 6.4 where pulse errors to the π-pulses were introduced on purpose.

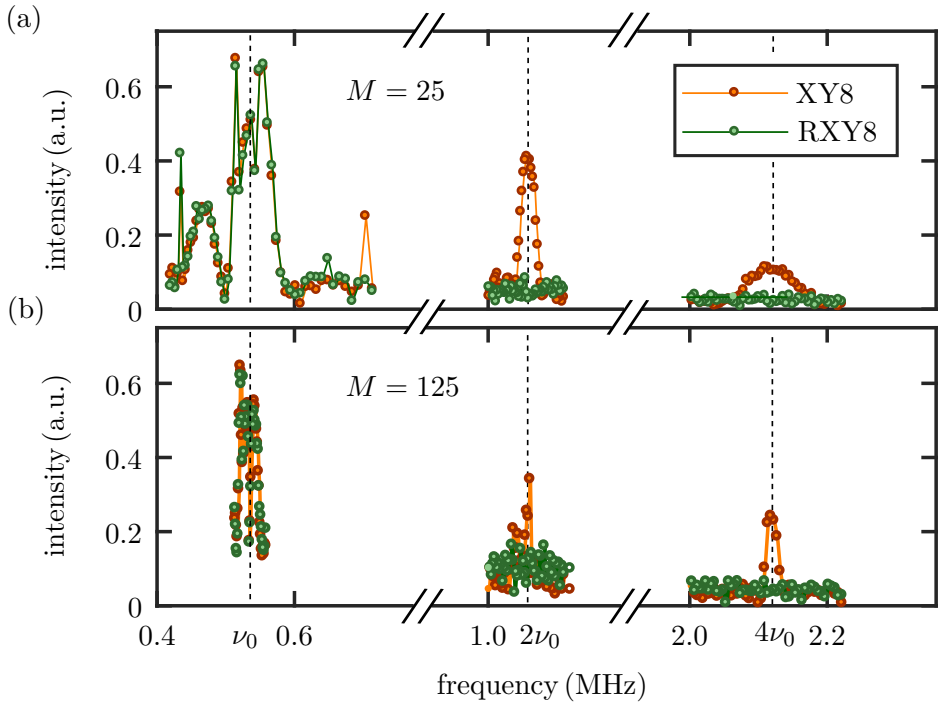

Figure 6.4: Experimental suppression of spurious harmonics by phase randomisation. An artificial AC magnetic field with frequency $\nu_0 = 530\,\mathrm{kHz}$ was measured using the XY8 sequence. The non-instantaneous π-pulses (Rabi frequency: $\Omega \approx 2\pi \cdot 5\,\mathrm{MHz}$) produce spurious peaks at the frequencies $2\nu_0$ and $4\nu_0$ in the spectrum of the standard version (orange). For the same signal and pulse durations the XY8 sequence with phase randomisation (green) efficiently suppresses all the spurious peaks while the desired signal, which is centred around ν_0, is preserved. For the experiments in (a) $M = 25$ repetitions were used and in (b), for a much weaker AC field, $M = 125$ repetitions. Adapted with permission from [232]. Copyright 2019 by the American Physical Society.

Nanoscale AC magnetometry

First, an artificial AC magnetic field with a frequency of $\nu_0 = 530\,\mathrm{kHz}$ was recorded. It was generated by a Gigatronics 2520B signal generator and a $20\,\mu\mathrm{m}$ thin copper wire acting as antenna. The spectra obtained with $M = 25$ individual XY8 units (thus 200 π-pulses in total) are shown in figure 6.4(a). In the spectrum of the standard version (orange points), there is a large signal at the expected position around ν_0. However, there are also significant peaks at $2\nu_0$ and $4\nu_0$. These additional signals originate from the spurious response during the finite-length π-pulses (here about 100 ns). In contrast, for the randomised XY8-version (green points), where all 25 individual units had additional random phases, there is no detectable signal around $2\nu_0$ and $4\nu_0$. The provided data is an average of $K = 10$ realisations differing in the set of random phases $\{\Theta_{r,1}, \Theta_{r,2}, \ldots, \Theta_{r,M}\}$. The same result and conclusion can be obtained when recording a much weaker signal

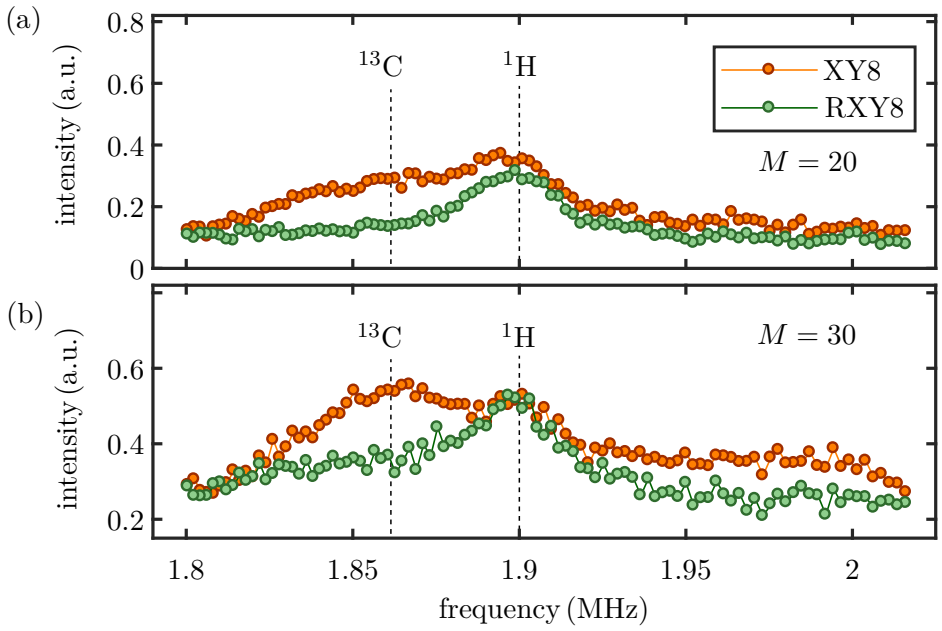

Figure 6.5: Experimental detection of proton spins using the randomised XY8 sequence. The standard protocol produces strong and wide spurious peaks, which originate from coupled ^{13}C nuclear spins naturally occurring in diamond. This complicates the detection of ^{1}H spins on the diamond surface. For both $M = 20$ in (a) and $M = 30$ in (b), these additional ^{13}C peak can be efficiently suppressed using the randomisation protocol. Then just the ^{1}H signal centred around 1.9 MHz remains. Adapted with permission from [232]. Copyright 2019 by the American Physical Society.

for which a larger number of π-pulses ($M = 125$) was used as shown with the spectra in figure 6.4(b).

Nanoscale NMR

Nanoscale NMR and MRI experiments are based on the detection of nuclear spin ensembles. These nuclear spins generate magnetic fields oscillating with their Larmor frequencies, which can be detected with the NV centre (compare chapter 5). The spectra (for $M = 20$ and $M = 30$) in figure 6.5 were measured using a single shallow NV centre in a natural abundance ^{13}C diamond (1.1 %, description of diamond in appendix A.1.5), which interacts with both: ^{1}H spins in oil molecules on top of the diamond surface and coupled ^{13}C spins inside the diamond (compare figure 5.3). Since both spin isotopes have gyromagnetic ratios differing by about a factor of four ($\gamma_{^1\mathrm{H}} \approx 4\gamma_{^{13}\mathrm{C}}$) it should be easy to distinguish their spectral contributions. The 44.6 mT bias field corresponds to the frequencies $\nu_{^1\mathrm{H}} = 1.899$ kHz for the ^{1}H spins and $\nu_{^{13}\mathrm{C}} = 0.4774$ kHz for the ^{13}C spins. Although the spectra in figure 6.5 only show a narrow range around $\nu_{^1\mathrm{H}}$, a signal due to ^{13}C spins

can be found for the standard XY8 protocol (orange data, Rabi frequency of the π-pulses: $\Omega \approx 2\pi \cdot 11\,\mathrm{MHz}$). Due to that, NMR experiments with NV centres usually require highly ^{12}C isotopically purified diamonds in order to reduce the effects of spurious harmonics from intrinsic ^{13}C spins. In contrast, all the spurious ^{13}C background noise is absent in the spectra recorded with the randomised XY8 sequence and only the ^{1}H signal is present (green data). Removing the spurious responses also improves the accuracy and reliability of further analyses. For example, the spectrum can be used to determine the distance of an NV centre to the diamond surface as shown in section 5.2.2 (also compare [156]). For this analysis the peak area needs to be extracted and theses areas are clearly different for the standard and randomised spectra. For the standard XY8 sequence the calculated depth is about $(5.88 \pm 0.52)\,\mathrm{nm}$, whereas for the randomised XY8 sequence $(7.62 \pm 0.29)\,\mathrm{nm}$ is obtained – a deviation of about 30 % [232]. These results make the usage of hard to manufacture and thus expensive highly isotopically purified diamonds for nanoscale NMR experiment less important – without the need to create new and complicated measurement and analysis protocols.

Spectroscopy of quantum signals

Very important for the characterisation of quantum systems is the detection of single building blocks, as individual spins, and the identification of their hyperfine fields. These hyperfine fields shift the resonance frequencies, which can be detected using the same DD techniques as described above. Here, in particular, spectroscopy using a single NV centre is performed with the aim to measure its ^{13}C spin environment. First, the standard XY8 principle is used ($M = 2$) and the results are display in figure 6.6 (orange data). At the carbon Larmor frequency at about $\nu_0 = 0.45\,\mathrm{MHz}$ for the 42.5 mT bias field (left dotted line) there is a large signal. In addition, at a slightly higher frequency another peak which is probably due to at least one strongly coupled ^{13}C spin is detected (further discussion in [232]). When performing spectroscopy around $2 \cdot \nu_0$ and $4 \cdot \nu_0$ there are again spurious harmonic signals (M was increased to $M = 60$ and $M = 100$ respectively). Subsequently, the same measurements were repeated using the randomisation principle (green data). Both signal peaks around the bare Larmor frequency match the data recorded with the standard XY8 technique. In contrast, the randomisation protocol efficiently suppresses the spurious harmonics at $2 \cdot \nu_0$ and $4 \cdot \nu_0$ from both, bath the single spins.

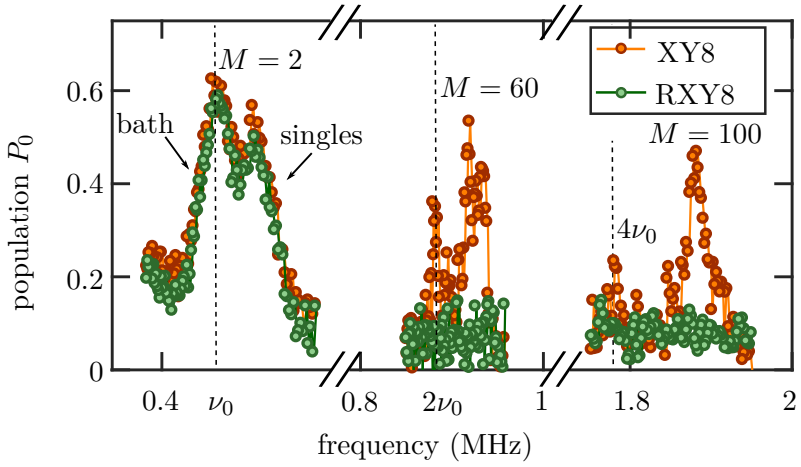

Figure 6.6: Quantum spectroscopy with the randomised XY8 sequence. Spectra recorded with a NV centre coupled to single ^{13}C spins and a ^{13}C spin bath. The randomised XY8 sequence suppresses any higher harmonics. Adapted with permission from [232]. Copyright 2019 by the American Physical Society.

6.4 Robustness enhancement by randomisation

Since the central component of DD sequences are the π-pulses, the performance of experiments based on DD is limited by errors in these control pulses, which are unavoidable in experiments. In order to manipulate the spin state of the NV sensor usually microwave fields are used. These fields have a frequency, an amplitude, a phase and in the case of pulses a duration. In the Bloch sphere representation the pulses describe rotations (for more details see section 2.5). The frequency should be resonant to the energy splitting between the sensor levels. The product of amplitude and duration determines the rotation angle and should correspond to a π-rotation for a π-pulse. Finally the phase of the microwave field, in this section also referred to as the phase of the π-pulse, determines the angle of rotation.

Since all these parameters can not be measured or, due to hardware constraints, adjusted with arbitrary accuracy, there are always some deviations in experiments. Furthermore, instabilities of the hardware, for example noise of the microwave amplifier, or drifts of the background magnetic field cause further fluctuations. Therefore, it is desirable to use DD protocols whose performance is minimally affected by these deviations, called pulses errors.

If the influence from the environment can be neglected, the expected behaviour of DD is to maintain the qubit state. For example, if the initial state is $|0\rangle$, the state after the

DD sequence should also be $|0\rangle$. For a single basic unit, static control imperfections cause error transition with the amplitude [231]:

$$\langle 0|\mathcal{U}_{\text{unit}}|1\rangle = V\epsilon + O(\epsilon^2), \tag{6.13}$$

where $\mathcal{U}_{\text{unit}}$ is the time evolution operator of a single DD block and V is the factor of the leading order error ϵ. Using the standard protocol, for which the basic unit is repeated M times, the error accumulates [232]:

$$\langle 0|(\mathcal{U}_{\text{unit}})^M|1\rangle = MV\epsilon + O(\epsilon^2). \tag{6.14}$$

Similar to the mitigation of the spurious harmonics, this accumulation is suppressed by the factor $Z_{r,M}$ (see equation (6.10)) [232]:

$$\langle 0|\mathcal{U}_r|1\rangle = Z_{r,M}MV\epsilon + O(\epsilon^2), \tag{6.15}$$

where $\mathcal{U}_r$ is the time evolution operator of the randomisation protocol.

Frequency and amplitude errors

The enhanced robustness is shown in figure 6.7 with both, simulations and experimental data. The performance of the XY8 sequence with in total 200 π-pulses ($M = 25$) and an interpulse spacing of $\tau = 200\,\text{ns}$ was examined for different pulse imperfections. Both, the amplitude errors and the frequency detunings were calibrated with respect to the experimental Rabi frequencies (about $\Omega_{\text{ideal}} = 2\pi \cdot 33\,\text{MHz}$ for these experiments). For example, a Rabi error of 10 % corresponds to deviation in the driving strength of about $2\pi \cdot 3.3\,\text{MHz}$. The initialisation and the readout were performed as described in section 6.3. The population remaining after the error-prone DD is measured and colour-coded. The experimental data was recorded with a resolution of 10×10 pixel and is post-processed by resizing (factor 5) and interpolating (weighted average of pixels in the nearest 4-by-4 neighbourhood). The results for the standard version (XY8) and the randomisation protocol (RXY8) are shown in figure 6.7(a) and (b), respectively.

The simulations and experiments demonstrate robustness improvement when applying phase randomisation. For example, for a Rabi error of 10 % and about 10 % MW detuning, we find 96 % remaining population for the randomised version and below 90 % population for the standard protocol.

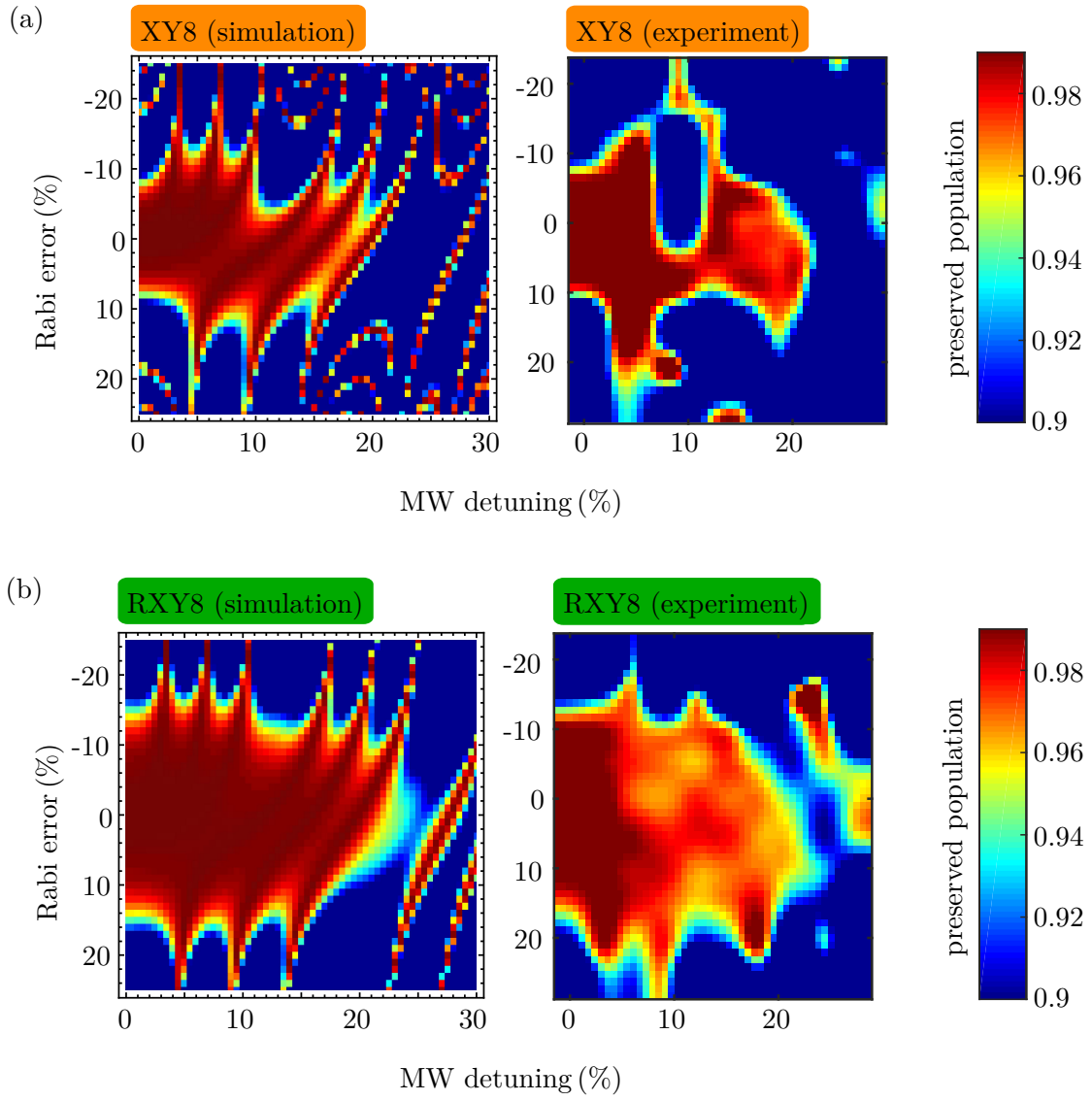

Figure 6.7: Enhancement of robustness with phase randomisation. The population preserved after an error-prone XY8 sequence is examined via simulations and experiments for (a) the standard XY8 sequences and (b) the randomisation version of XY8 (RXY8). The detuning and Rabi frequency errors are calibrated in terms of the ideal Rabi frequency of $\Omega = 2\pi \cdot 32.8\,\mathrm{MHz}$. The sequences have a pulse spacing of $200\,\mathrm{ns}$ and $M = 25$ XY8 units. With RXY8 an enhanced robustness for a wider range of parameters can be observed. The experimental data in (a) and (b) were recorded with a resolution of 10×10 pixels and were resized as well as interpolated. Adapted with permission from [232]. Copyright 2019 by the American Physical Society.

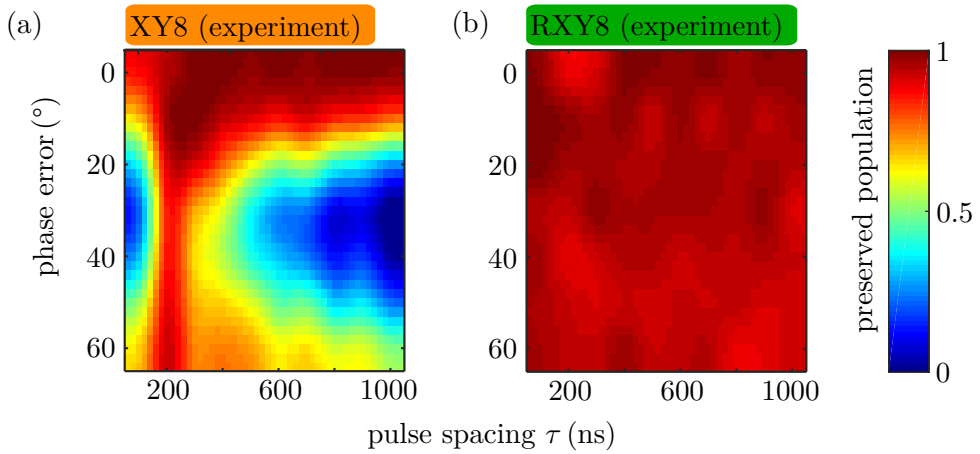

Figure 6.8: Enhanced phase robustness with the randomisation protocol. The phase relation between the X ($\theta = 0°$) and Y (should be $\theta = 90°$) pulses of the XY8 sequence is distorted and the preserved population as a function of the pulse spacing τ is measured for (a) the standard XY8 sequences and (b) the randomised protocol. For both experiments 96 ($M = 12$) resonant microwave π-pulses are used with a Rabi frequency of $\Omega_{\text{ideal}} = 2\pi \cdot 66.6\,\text{MHz}$. The recorded data ($7 \times 10$ pixel resolution) is rescaled and interpolated. Adapted with permission from [232]. Copyright 2019 by the American Physical Society.

Phase errors

Robust DD protocols, as the XY8 sequence, usually use rotations about different axes. Thereby it is important that the relations between the individual phases are adjusted accurately. When using a digital pulsing device, pulses with different phases are usually generated by splitting up the microwaves from the source and shifting the phase in one arm by suitable equipment. However, different cable lengths in both arms or the limited working accuracy of the used devices can sum to relative phase errors. In figure 6.8 the improvement of phase robustness for the randomised XY8 sequences ($M = 12$) using otherwise error-free microwaves is shown. For this purpose the 90° phase difference between the X ($\theta = 0°$) and Y (should be $\theta = 90°$) π-pulses in the XY8 protocol was distorted intentionally. As an example, for a phase error of 10°, the phase of the Y pulse was changed to 100° and the population remaining after application of the respective XY8 sequence was measured as described in section 6.3. The data was recorded with a resolution of 7×10 pixel and post-processed by resizing (factor 5) and interpolating (weighted average of pixels in the nearest 4-by-4 neighbourhood). The performance of the conventional XY8 sequence (figure 6.8(a)) drops drastically under phase-errors, especially with growing spacing τ between individual π-pulses. On the contrary, the application of the randomisation protocol provides a strong suppression of the phase-error, as shown in figure 6.8(b). It is

very likely that for a larger number of control pulses the difference in performance further increases.

6.5 Conclusion

It is theoretically derived and experimentally shown that phase randomisation retains the expected signal, while efficiently and universally suppressing spurious responses for DD sequences. The protocol is equally well applicable for quantum and classical signals, and can be used for facilitating clear and unambiguous AC field and nuclear spin detection [232]. Especially relevant for magnetometry with NV centres is that the presented method decreases the dependency on ^{13}C purified diamond. In addition, the robustness against pulse imperfections is further enhanced. The technique is simple to implement, is valid for all DD protocols and is in general applicable to all quantum platforms where DD sequences are used [232].

7 Quantum heterodyne detection

NV centres in diamond have shown extraordinary sensitivity and spatial resolution for non-invasive magnetic field detection and characterisation [42]. However, the spectral resolution remains poor when using the standard protocols, which are usually based on dynamical decoupling (DD). By applying a train of π-pulses onto the sensor qubit, a spectral filter is generated, which can be used to sample different frequency components (compare section 4.3). The width of this spectral filter is given by the inverse of the interaction time between sensor and signal. Thus, the finite T_2 coherence time of quantum probes sets a limit to the performance. Although additional measurements up to time T can further reduce noise by averaging and thereby improve the accuracy of frequency estimation, usually as $\sqrt{T}$, the resolution remains unamended. This becomes especially relevant for NMR, since frequency shifts due to environmental influences, which contain useful information, are very small and thus sensors with a very good resolution are necessary (compare chapter 5). An example is sketched in figure 7.1, where the $T_2 = 0.1\,\mathrm{ms}$ coherence time is not sufficient to resolve the small differences between the ^{13}C-NMR-spectra of acetic acid (blue lines) and methyl formate (green lines) due to the different chemical environment of their ^{13}C-spins.

Another disadvantage is that all spectral components need to be sampled individually. If in a fixed time the number of data points in a spectrum should be increased, less time can be spent for every frequency component and thus the relative individual noise raises. Recently, the first realisations to perform spectroscopy beyond the T_2-limit were reported. For example by transferring the quantum phase to a state population, the usually longer T_1-relaxation time can be used [27, 228]. If an additional long-living qubit is available, it can be used as a memory [155, 230, 237–239]. The idea is to correlate the quantum phase acquired in the beginning of the sensing period and transferred to the memory qubit with the quantum phase accumulated after a variable idle time. Then, the T_2-limit of the quantum system is effectively replaced by the lifetime of the long-living qubit. Although the frequency resolution is improved this way, the overall sensitivity might be reduced, since a large part of the time is not used to acquire a signal. Repeating the measurement results in the standard $T^{-1/2}$-scaling for the uncertainty in frequency estimation.

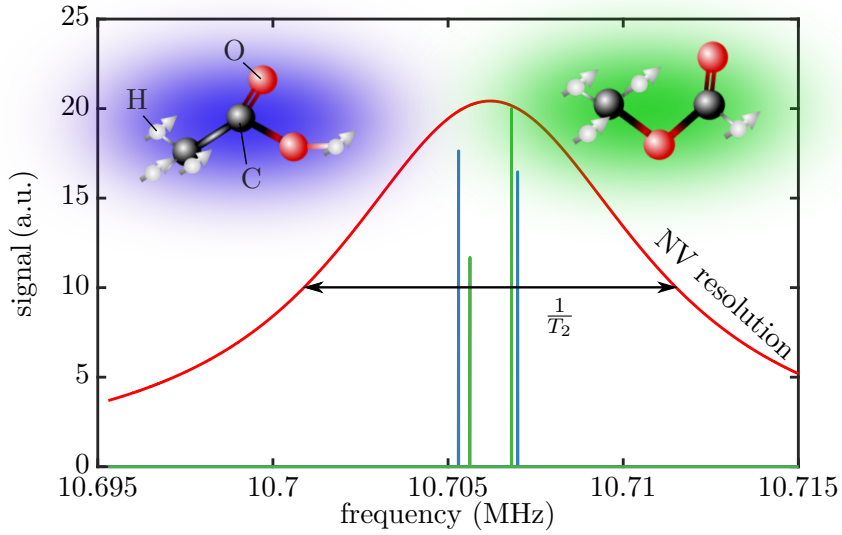

Figure 7.1: Limited resolution of dynamical decoupling spectroscopy. The ^{13}C-NMR spectra of acetic acid (blue lines) and methyl formate (green lines) differ only by a few Hertz, even at a relative high magnetic field of 1 T (NMR data from [223]). The limited coherence times of quantum sensors (here $T_2 = 0.1\,\mathrm{ms}$) are usually not sufficient to discriminate the small influences due to different environments of the ^{13}C-spins in both molecules with conventional coherence limited techniques.

In the following the principle of the quantum heterodyne (Qdyne) detection scheme [153], which allows coherence independent frequency resolution with an enhanced precision scaling of $T^{-3/2}$ is introduced (section 7.1) and experimentally realised using DD (section 7.2). For the experiments in this work the NV centre is used as a quantum sensor, but the idea of Qdyne is general and in principle can be transferred to all other qubit based sensors.

7.1 Principle of quantum heterodyne detection

In the following the idea, the working principle and the experimental realisation of Qdyne with NV centres are discussed.

7.1.1 The idea

Heterodyne detection is a principle known since the beginning of the 20th century and is for example used in optics and image processing. The idea is to measure a signal with unknown frequency ν by non-linear mixing with a reference frequency ν_{LO} from a local oscillator. The frequencies of the mixed signal depend on the difference and sum of ν and ν_{LO}. Classically, the primary benefit is that the lower frequency signal can

be easier detected and processed. For quantum spectroscopy another advantage can be more important: The spectral resolution is limited by the stability of the local oscillator. Quantum heterodyne (Qdyne) detection can be realised by using a quantum probe as the non-linear mixing element that brings in the measurement information and utilising a highly stable classical clock as the local oscillator. This hybrid classical-quantum approach combines the advantages of the high spatial resolution and sensitivity of the quantum sensor and the high stability of the local oscillator.

7.1.2 The working principle

Although the principle works for arbitrary frequency distributions, for simplicity, the following for the moment concentrates on signals with a single frequency. An oscillating field of interest $H(t)$ can then be described by its amplitude H_0, its frequency ν and its initial phase $\theta_0 = \theta(t = 0)$:

$$H(t) = H_0 \cdot \sin\left(\theta(t)\right), \tag{7.1}$$

where

$$\theta(t) = 2\pi\nu t + \theta_0. \tag{7.2}$$

If it is possible to measure $\theta(t)$ at any time, the frequency ν can be estimated by recording at different moments in time $\{t_0, t_1, ..., t_n\}$, where $\{\}$ corresponds to a set. The precision and spectral range of the estimate depend on the choice of $\{t_0, t_1, ..., t_n\}$ in correspondence to the Nyquist-Shannon theorem, but also on how accurate these interrogation times can be adjusted experimentally.

Qdyne uses this principle to enable high resolution spectroscopy. For this purpose, it is essential that the response of the quantum probe to a field of interest $H(t)$ depends on its phase $\theta(t)$. This can usually be realised by applying a suitable control on the sensor and two possible options are introduced in this thesis (see section 7.2 and chapter 9). In order to adjust the set of interrogation times a very stable clock can be used. If the $\{t_0, t_1, ..., t_n\}$ are equidistantly spaced ($t_n = n \cdot t_\Delta$), the sampling rate is $1/t_\Delta$. Since multiple signal periods might be within t_Δ (for $t_\Delta > 1/\nu$), the local oscillator frequency is here defined as:

$$\nu_{\mathrm{LO}} = m/t_\Delta, \tag{7.3}$$

where m is the integer number, which minimises $|t_\Delta - m/\nu|$ and is a measure for the number of elapsed signal periods per t_Δ. Although, it seems that this definition of ν_{LO} is ambiguous since m can only be determined exactly if ν is known, quantum control can usually be used to make the probe sensitive to only a specific frequency range (see section 7.2.5). In addition, further measurements can be performed with slightly modified

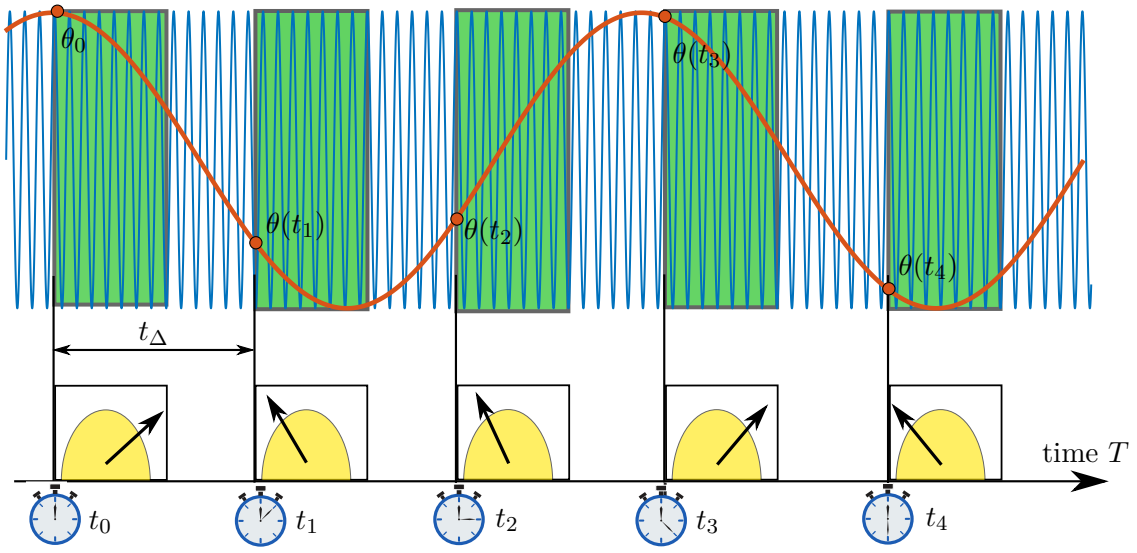

Figure 7.2: The Qdyne principle. Using phase-sensitive measurements (green boxes), an oscillating field (blue line) with the frequency ν is examined. By sampling with a fixed sampling rate ($1/t_\Delta$), the evolution of the signal phase (orange line) can be recorded.

t_Δ to generate a Moiré pattern in order to further specify m (compare section 9.5). It follows:

$$\theta(t) = 2\pi\nu t + \theta_0 = 2\pi(\nu_{\mathrm{LO}} - \nu)t + \theta_0, \tag{7.4}$$

where the full derivation can be found in appendix A.3.6. In figure 7.2 the working principle is sketched for a sinusoidal field (blue line). For an arbitrary signal phase θ_0 a first phase-sensitive measurement is performed at $t_0 = 0$ (green rectangle on the far left). The resulting sensor response is recorded and for a precisely known moment of time $t_1 = t_\Delta$ the next measurement is performed. If t_Δ is not a multiple of the signal period, the phase of the signal changes $\theta(t_1) \neq \theta_0$ and thus the measurement of the sensor results in a different outcome. If this is repeated with a fixed sampling time $t_n = n \cdot t_\Delta$, the phase of the signal for the nth measurement evolves according to equation (7.4) as:

$$\theta(t_n) = 2\pi(\nu_{LO} - \nu)nt_\Delta + \theta_0 = 2\pi\delta_{\mathrm{b}}nt_\Delta + \theta_0, \tag{7.5}$$

where δ_{b} is the beating frequency ($\delta_{\mathrm{b}} = \nu_{\mathrm{LO}} - \nu$). Thus, $\theta(t_n)$ increases linearly with the repetition number n and the sampling rate can be adjusted by tailoring t_Δ. Because every measurement of $\theta(t)$ takes some time, it is not possible to choose t_Δ arbitrarily, especially since overheads due to initialisation and readout of the sensor qubit have to be taken into account. As for traditional heterodyne detection the frequency of the measurement signal (orange line) is down-converted to δ_{b}. The goal of Qdyne is to estimate δ_{b}.

As long as a measurement has no back-effect on the signal, it can be repeated for an arbitrary time. Since consecutive measurements are correlated, a prolongation of the acquisition time leads to more precise results. Especially the frequency resolution is only limited by the accuracy of adjusting t_Δ, and in particular, not by the T_2-time of the quantum sensor. Qdyne is also different to 'lock-in' techniques, since it requires no feedback to lock the probe to the signal phase [172]. It is important to note that the beating frequency δ_b can only be determined up to a sign ambiguity, which for example can be lifted by performing a second experiment with an altered t_Δ.

7.1.3 Experimental realisation with nitrogen-vacancy centres

All experiments were performed on a standard home-built confocal microscope with 532 nm laser excitation (appendix A.1.2). The spin-dependent fluorescence was measured with an avalanche photodiode (APD) and recorded using a time-tagged single photon counting card (FastComTec MCS6A) with sub-nanosecond time resolution. Synchronisation between the pulser (Tektronix AWG70001A) and the photon counter, which is essential for a correct assignment of the outcomes to the respective measurements, is realised by a TTL-pulse. Resonant microwaves used to coherently drive the sensor qubit were generated by the same arbitrary waveform generator with 20 ps timing resolution. All test signals were generated by crystal quartz oscillator stabilised signal generators.

An example for the analysis protocol is sketched in figure 7.3. The time-tagged single photon counting card records every detected photon with a timestamp (here in units of bins), as sketched in figure 7.3(a). The data was post-processed by discarding all background photons recorded outside of the readout window and by summing up all photons detected in a single run. This results in a photon time trace array with each entry corresponding to the number of detected photons in the respective iteration. Due to the low detection efficiency, during most of the readouts no photon was detected and as a consequence several thousand iterations are required (compare section 3.3). Single-shot readout could be used to improve the information per readout, albeit with the disadvantage of having a greatly reduced sampling rate (see section 9.4.1 for a more in depth discussion). In order to obtain the beating frequency δ_b, discrete Fourier transform or other suitable analysis techniques, as maximum likelihood estimation, can be applied (figure 7.3(b)). The special advantages of Fast Fourier transform (FFT) algorithms are that they are suited for multi-frequency signals, also yield an estimate of the signal amplitudes and that the computational costs are relatively small. However, it has been recently reported that Bayesian inference models for signal processing can further improve the signal analysis under certain circumstances [226].

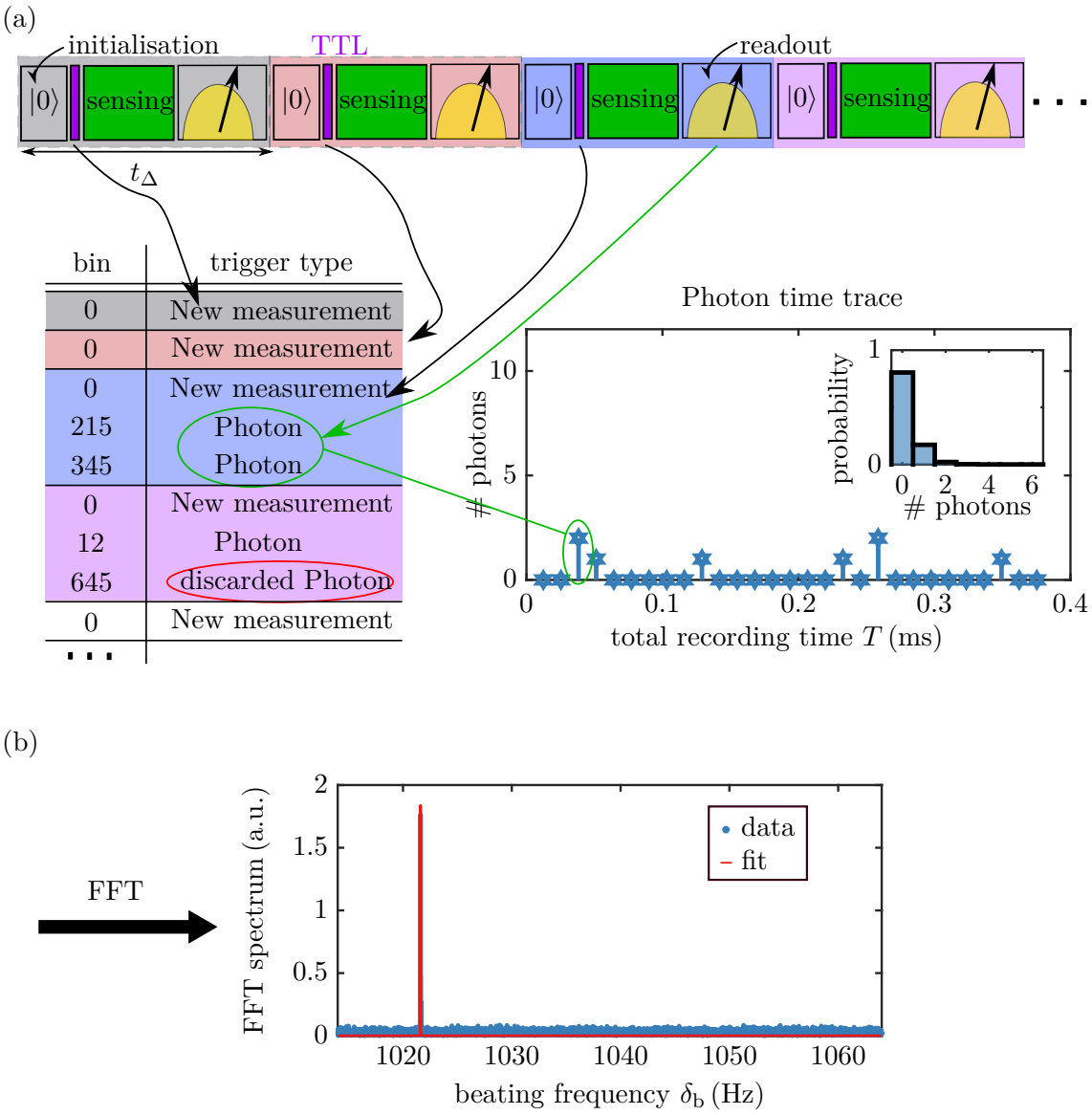

Figure 7.3: Recording and analysis principle of a Qdyne measurement. (a) TTL-pulses and photons are recorded with a timestamp (here in units of bins) and post-processing compromises discarding photons which are recorded outside of the detection window (red circle). The resulting 1D-array contains the number of detected photons for every measurement repetition, which are mostly zero due to the low detection efficiency (inset). (b) By performing a discrete Fourier transform, the beating frequency δ_b can be obtained. The height of the observed peak corresponds to the signal amplitude. Modified with permission from [153].

7.2 Quantum heterodyne detection based on dynamical decoupling

Dynamical decoupling (DD) can be used to measure signals with frequency components in the range of several kHz up to a few tens of MHz, as discussed in section 4.3. This section contains results which have been published in [153] and [226].

7.2.1 Derivation of the population formula

The signal Hamiltonian of an oscillating signal in z-direction with a single frequency ν has the form:

$$\mathcal{H}(t) = \frac{\hbar\Omega}{2} \sin\left(2\pi\nu t + \theta\right)\hat{\sigma}_z, \tag{7.6}$$

where Ω is the coupling strength between sensor and signal and $\hat{\sigma}_z$ is the respective Pauli matrix. If brought into a coherent superposition state, the sensor qubit accumulates a relative phase ϕ between both eigenstates during the interaction with $\mathcal{H}(t)$ and the DD sequence. If the temporal spacing between the π-pulses is close to $1/(2\nu)$, ϕ depends on the signal phase θ as (compare equation (4.23) for $\omega_\Delta \to 0$):

$$\phi = \frac{2\Omega T_{\mathrm{int}}}{\pi} \cos(\theta), \tag{7.7}$$

where T_{int} is the coherent interaction time between sensor and signal. For traditional DD spectroscopy, either the signal phase θ is locked to maximise the signal accumulation or the result is an average over many realisations with arbitrary phases, as for example discussed for nanoscale NMR in section 5.2. For Qdyne, however, it is essential that ϕ depends on θ, which allows one to use DD for phase sensitive measurements. The sensor phase ϕ for each measurement is then given by equations 7.4 and 7.7:

$$\phi = \frac{2\Omega T_{\mathrm{int}}}{\pi} \cos(2\pi\delta_{\mathrm{b}} t + \theta_0), \tag{7.8}$$

where θ_0 again corresponds to the signal phase at time $t = 0$. The amplitude of this sinusoidal dependency is proportional to the coupling Ω and the interaction time $T_{\mathrm{int}} \leq T_2$. Usually a final $\pi/2$-pulse is used to transfer ϕ into a population difference, before performing a projective measurement. The probability to find the sensor state in $|0\rangle$ then reads:

$$P_0 = \frac{1}{2} + \frac{1}{2} \cos\left(\gamma - \phi\right), \tag{7.9}$$

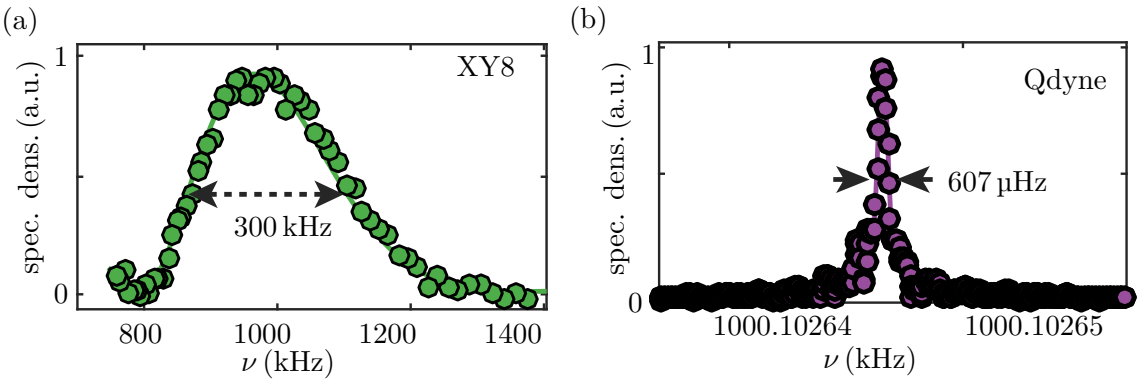

Figure 7.4: Comparison between Qdyne and traditional DD spectroscopy. (a) Spectrum obtained using traditional DD spectroscopy. The linewidth is about 300 kHz and limited by the inverse of the interaction time. (b) The FWHM of the Qdyne spectrum is 607 µHz and only restricted by the stability of the local oscillator. Modified with permission from [153].

where γ is the angle between initialisation and readout basis. For $\gamma = \pi/2$ and small ϕ, it follows [153]:

$$P_0 = \frac{1}{2} + \frac{\Omega T_{\text{int}}}{\pi} \cos(2\pi\delta_{\text{b}} t + \theta_0). \tag{7.10}$$

7.2.2 Proof of principle

In order to demonstrate these findings experimentally, Qdyne was used to measure a 880 nT magnetic field oscillating close to $\nu = 1$ MHz. For this purpose, XY8-1 sequences with a π-pulse spacing of 500 ns were applied. The numbers of recorded photons of every individual readout were stored separately and in the end the frequency was obtained using Fourier analysis (see section 7.1.3). The repetition rate of the individual measurements was $1/t_\Delta = 1/(9\,\mu\text{s})$.

The result is compared to traditional DD spectroscopy, where the spacing between the π-pulses in the XY8-1 sequences was adjusted sequentially. For every of the 50 data point more than 10^6 repetitions were averaged in order to collect enough information. In figure 7.4 the spectra obtained with Qdyne and DD after a total recording time of $T = 5000$ s are shown. Taking the different scaling of the frequency axes into account, the disparity of the linewidths is immense. The Qdyne spectrum has a full width at half maximum (FWHM) of just 607 µHz [153]. In principle a FWHM which scales as $1/T$ is expected, which means 200 µHz for the 5000 s recording time. However, the stability of the local oscillator itself eventually limits the reachable resolution (see next section for a more in depth discussion).

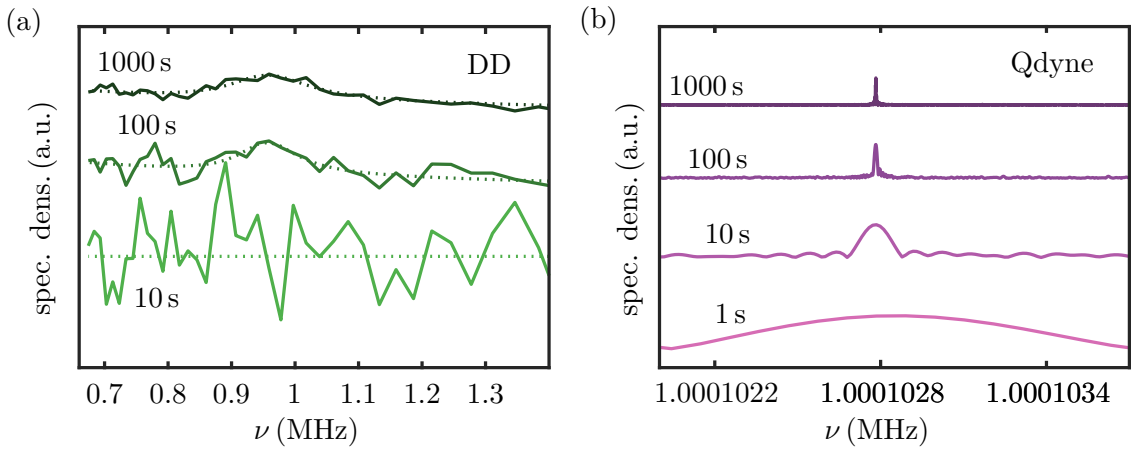

Figure 7.5: Qdyne and traditional DD spectra as a function of time. (a) Traditional DD spectrum recorded with 50 points. After 10 s there is no visible signal and it takes about 100 s to find a broad peak. Although the spectrum gets less noisy, increasing the total recording time does not change the linewidth. The dotted lines correspond to Lorentzian fits to the data. (b) Qdyne spectrum for different recording times. Even after 1 s a clear peak in the data (no smoothing) is visible and the linewidth is much smaller than for DD (note the different scaling of the frequency axis). By increasing the recording duration, the linewidth further reduces. Modified with permission from [153].

The linewidth of the DD spectrum is given by the inverse of the interaction time T_{int}, amounts about 300 kHz and also would not improve when recording for a longer duration. This is in more detail analysed in the next section.

7.2.3 In depth analysis of Qdyne

In the following, further important properties that can be used to classify spectroscopic techniques as resolution, precision and signal-to-noise ratio (SNR) and their dependency on the recording time T are analysed. In a different experimental run, we measured a magnetic field oscillating close to $\nu = 1\,\text{MHz}$ using the Qdyne technique for in total 5000 s. In a subsequent experiment, we used traditional DD spectroscopy to measure an identical signal for the same duration. By storing the result of every repetition individually, it is possible to reconstruct spectra for almost arbitrary recording durations T (up to 5000 s). For $T = 10\,\text{s}$, $T = 100\,\text{s}$ and $T = 1000\,\text{s}$, the DD spectra composed of 50 points are plotted in figure 7.5(a). In order to improve the overview, parts of the data are offset and Lorentzian fits are added (dotted lines). After $T = 10\,\text{s}$, no signal is detectable due to the large noise. It takes almost 10 times longer to find a small peak centred around 1 MHz. Extending the recording duration to $T = 1000\,\text{s}$ further reduces the noise, but does not alter the linewidth.

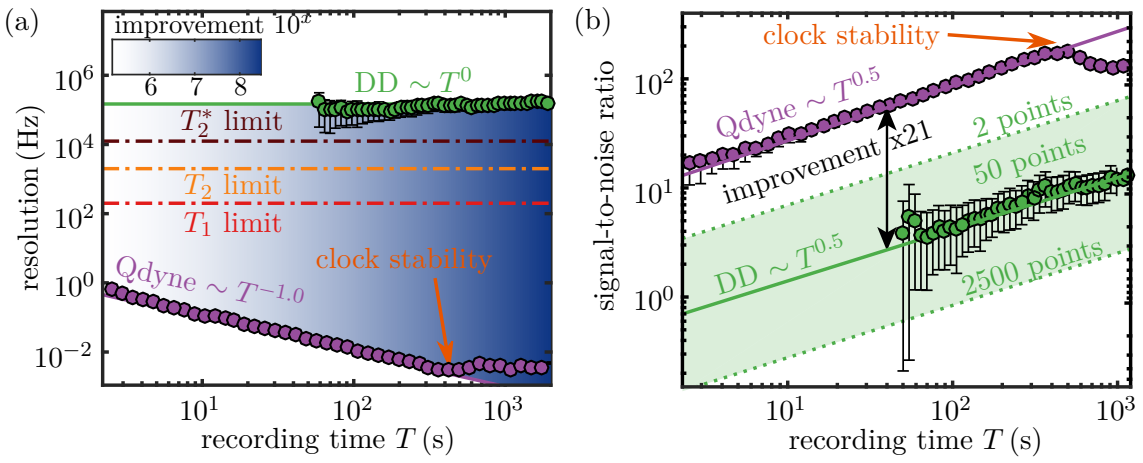

Figure 7.6: Resolution and SNR of Qdyne and DD spectra. (a) The resolution, which corresponds to the FWHM value, is independent of the total measurement time in the case of DD. It is given as the inverse of the interaction time and would finally be limited by the T_2 coherence time. On the other hand, the FWHM in the Qdyne spectrum reduces linearly with T. It is eventually limited by the stability of the local oscillator clock. (b) Signal-to-noise ratio as a function of recording duration for Qdyne and DD spectroscopy. Both techniques show a $T^{0.5}$-scaling, characteristic for photon shot noise limited measurements. However, there is a clear offset in favour of the Qdyne spectrum. The main reason is that for DD different frequency components (here 50) have to be samples individually, which leads to a large temporal overhead. Modified with permission from [153].

The Qdyne spectra for the same T are plotted in figure 7.5(b), again using offsets to improve the overview. Even after $T = 1\,\mathrm{s}$ it is already possible to find a clear peak with a width of about 1 Hz and increasing T further reduces the FWHM. The apparent differences including linewidth, SNR and precision are discussed in more detail in the following. In order to extract these parameters, we used least-square fits with Lorentzian lineshape.

Resolution

The resolution, which here corresponds to the FWHM, of the Qdyne and traditional DD spectra is plotted in figure 7.6(a) as a function of the total recording time T. As expected, the linewidth for DD spectroscopy is given by the inverse of the interaction time T_{int} and does not improve when T is increased. Although, the full coherence of the quantum sensor is not utilised here, T_{int} is eventually limited by the T_2 time (about 300 µs for the used NV centre). Even the inverse of the T_1 relaxation time, which is usually about an order of magnitude longer, is much larger than the width of the 1 Hz line observed with Qdyne spectroscopy after $T = 1\,\mathrm{s}$. The resolution further improves as T^{-1} and we measure a linewidth of 20 mHz after $T = 50\,\mathrm{s}$ and 2.7 mHz for $T = 500\,\mathrm{s}$. The latter is

slightly greater than the expected $1/T$ behaviour, which might be due to instability of the used clock.

The resolution of the Qdyne method is finally limited by the stability of the local oscillator clock, which is about 500 s for the presented experiment. As described above, a clock is used to adjust the time t_Δ between adjacent measurements and is typically generated by a crystal oscillator operating at a certain frequency. Since no oscillator perfectly generates the specified frequency, there are always some deviations, which limit the performance.

Signal-to-noise ratio

The signal-to-noise ratio (SNR) is obtained as the amplitude of the Lorentzian fit divided by the standard deviation of the experimental data with respect to this fit (compare supplemental material of [153]). From the data shown in figure 7.6(b), it is clear that the SNR is superior for Qdyne. Although the SNR improves as $T^{1/2}$ with both techniques, as expected for photon shot noise limited measurements, we observe an offset corresponding to a 21-fold improvement in favour of Qdyne. This is equivalent to a 441-fold speed up in measurement time (due to the $T^{1/2}$ scaling). As soon as T approaches the stability limit of the local oscillator clock, the SNR does not improve anymore for Qdyne.

There are two main reasons for this enhanced SNR. Probably most important is that with Qdyne all spectral components in a given bandwidth are sampled simultaneously (see section 7.2.5), whereas with traditional DD spectroscopy individual frequency components have to be recorded individually and in succession. For our experiments, we used 50 points and consequently for every point only a fiftieth of the total time can be spent. Increasing the number of data points N_{data} results in a more noisy result and a worse SNR (scaling as $N_{\mathrm{data}}^{-1/2}$), which is exemplarily indicated with the green dotted lines in figure 7.6(b) for 2 and 2500 points. The second reason is that the readout basis can be adapted with Qdyne, which is especially relevant for weak signals. For traditional DD spectroscopy, if the result is an average of realisations recorded with varying signal phases, the readout basis should match with the initialisation basis, since otherwise parts of the measurement signal might average out.

Precision

Finally, the precision as a function of T is compared for Qdyne and traditional DD spectroscopy in figure 7.7. Here, we refer to precision $\Delta\nu$ as the uncertainty of estimating the value of the frequency ν. Although this is closely related to the resolution, which represents the linewidth of the peak in the spectrum, the precision is given by the accuracy to

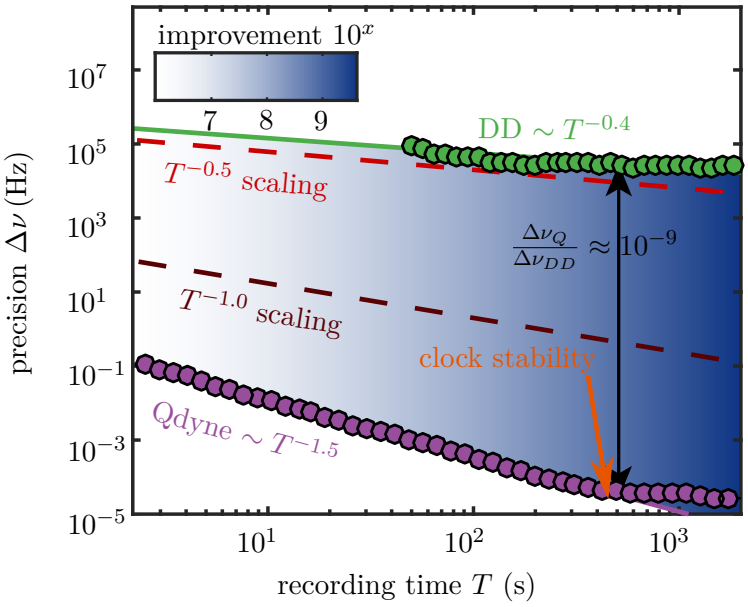

Figure 7.7: Frequency precision for Qdyne and dynamical decoupling spectroscopy. For DD the precision, which is here defined as the uncertainty to estimate the frequency, improves close to the expected $T^{-0.5}$ scaling. With Qdyne the estimate improves as $T^{-1.5}$ up to the stability of the local oscillator clock. Further recording leads to an improvement close to $T^{-0.5}$. The maximal relative enhancement compared to DD is about 9 order of magnitude. Modified with permission from [153].

locate the peak maximum. Here, we used least-square fits with Lorentzian lineshape to estimate these values for both techniques. The precision is then extracted using the fit accuracy for 95 % confidence intervals.

For traditional DD spectroscopy, this uncertainty reduces as $T^{-0.4}$. Since the noise on every data point is photon shot noise limited, one would expect a $T^{-0.5}$ scaling. Taking further small noise sources into account, as for example that the lineshape is not perfectly Lorentzian, the observed behaviour is within the expected range. In contrast, the frequency estimate with Qdyne improves as $T^{-3/2}$ [153] up to about 500 seconds. The frequency sensitivity, here defined as $\eta_\nu = \Delta\nu\sqrt{T}$, reads $\eta_\nu = 0.37/T\,(\sqrt{\text{Hz}})^{-1}$ in this range.

Even for longer times we observe an improvement, however with a reduced $T^{-1/2}$ behaviour. The final precision after 5000 s is about 26 µHz, which is eleven orders or magnitude below the 1 MHz signal frequency [153]. The precision of frequency estimation depends linearly upon SNR and linewidth. As the former scales as $1/\sqrt{T}$ and the latter as T^{-1}, the combination of both leads to the observed $T^{-3/2}$ scaling. A detailed theoretical analysis would exceed the scope of this thesis and can be found in the supplementary material

of [153]. Excluding temporal overheads due to initialisation and readout, the combination of reduced linewidth and improved SNR yields the following precision for Qdyne [153]:

$$\Delta\nu^{\mathrm{Q}} = \frac{1}{\Omega T\sqrt{TT_2}}, \tag{7.11}$$

which is valid as long as the local oscillator T_{LO} and the signal remain stable. For comparison, the precision for DD spectroscopy is given by [153]:

$$\Delta\nu^{\mathrm{DD}} = \frac{1}{\Omega T_2\sqrt{TT_2}}, \tag{7.12}$$

where it is assumed that every data point contributes equally to the precision. Since this is generally not the case, the true precision is usually poorer. The results obtained for Qdyne and traditional DD spectroscopy are very similar and only differ due to the decreased linewidth [153]:

$$\frac{\Delta\nu^{\mathrm{DD}}}{\Delta\nu^{\mathrm{Q}}} = \frac{T}{T_2}. \tag{7.13}$$

However, the ratio T/T_2 can be very large and we find a maximum of about 10^9 in the presented experiments. Thus, by storing the result of every readout onto a computer hard drive, the signal can be reconstructed over arbitrarily long periods T, and the fragility of the quantum sensor can be overcome.

Compared to techniques relying on a quantum memory, where phase information is stored on an additional, long-living qubit and lengthy waiting times are applied before continuing with the next measurement, the advantage is that the signal is continuously sampled. By using a quantum memory the precision reads [153]:

$$\Delta\nu^{\mathrm{M}} = \frac{1}{\Omega T_2\sqrt{TT_{\mathrm{M}}}}, \tag{7.14}$$

where T_{M} refers to the coherence time of the memory qubit. The comparison with Qdyne yields [153]:

$$\frac{\Delta\nu^{\mathrm{M}}}{\Delta\nu^{\mathrm{Q}}} = \frac{T}{\sqrt{T_{\mathrm{M}}T_2}}. \tag{7.15}$$

For $T > T_{\mathrm{LO}}$, the formula for the precision of Qdyne changes slightly [153]:

$$\Delta\nu^{\mathrm{Q}} = \frac{1}{\Omega T_{\mathrm{LO}}\sqrt{TT_2}}, \tag{7.16}$$

and $\Delta\nu^{\mathrm{Q}}$ scales as $T^{-1/2}$ with the total recording time agreeing with the experimental observations. Under the assumption that $T_{\mathrm{LO}} \gg T_{\mathrm{M}} \gg T_2$, Qdyne allows to obtain much

more precise estimates. Furthermore, Qdyne works without the need of an additional memory qubit and complex and/or lengthy quantum operations.

Since the Heisenberg limit usually scales as T^{-1}, these results seem astonishing. However, the usual Heisenberg limit considers amplitude estimation and, as it is shown in more detail in chapter 8 and in [202, 240, 241], the Heisenberg limit for frequency precision is given by T^{-2} as long as the probe is coherent.

7.2.4 Multiple frequency fields

Many interesting fields have several frequency components. Then the task of spectroscopy is to estimate the amplitude and frequency of each component, or at least their differences. For instance in NMR this is important to identify chemical structures. The signal Hamiltonian of a field with two frequencies is:

$$\mathcal{H} = \frac{\hbar\Omega_1}{2}\sin\left(2\pi\nu_1 t + \theta_1\right)\hat{\sigma}_z + \frac{\hbar\Omega_2}{2}\sin\left(2\pi\nu_2 t + \theta_2\right)\hat{\sigma}_z = \mathcal{H}_1 + \mathcal{H}_2. \tag{7.17}$$

Since $\mathcal{H}_1$ and $\mathcal{H}_2$ commute, their interaction on the quantum sensor can be evaluated separately. Following equation (7.8), the sensor phase reads:

$$\phi = \frac{2\Omega_1 T_{\text{int}}}{\pi}\cos(2\pi\delta_{\text{b}1}t + \theta_1) + \frac{2\Omega_2 T_{\text{int}}}{\pi}\cos(2\pi\delta_{\text{b}2}t + \theta_2), \tag{7.18}$$

where $\delta_{\text{b}1,2} = |\nu_{\text{LO}} - \nu_{1,2}|$ and $\theta_{1,2}$ are the respective signal phases at $t = 0$. The sensor phase ϕ is a linear combination of two oscillating functions and a Fourier transform should reveal both components. This can analogously be extended for an arbitrary number N_ν of frequencies and then ϕ reads:

$$\phi = \frac{2T_{\text{int}}}{\pi}\sum_{n=1}^{N\nu}\Omega_n\cos\left(2\pi\delta_{\text{b}n}t + \theta_n\right). \tag{7.19}$$

We exemplarily test these findings by recording a signal with three frequency components using the Qdyne technique for 180 s. The signal was artificially generated by combining the output of three independent signal generators. The differences of the individual frequencies, namely 25 Hz and 22 Hz, were chosen to be much smaller than the resolution of the traditional DD spectroscopy (about 250 kHz in this case). The relevant part of the spectrum obtained by Fourier transforming the recorded time trace is shown in figure 7.8(a).

As expected, all three frequencies can be discriminated with ease. The 7 mHz linewidth of each individual peak almost corresponds to the 180 s total measurement time and would in principle allow to distinguish frequency components with differences of just a few mil-

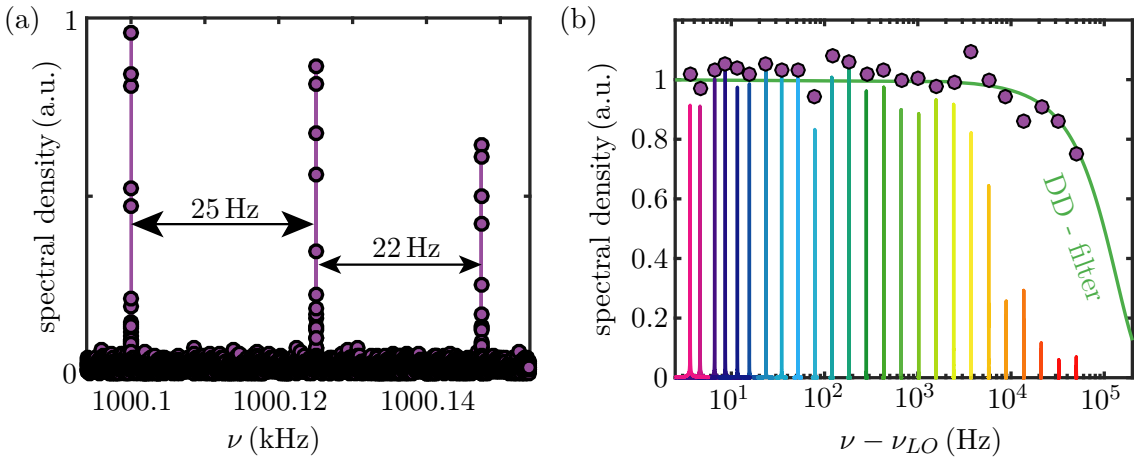

Figure 7.8: Spectroscopy of a signal with multiple frequencies and spectral bandwidth. (a) Qdyne spectrum of a signal with three frequencies. Although the individual frequencies differ only by a few hertz, they can be easily resolved. (b) Frequency bandwidth of the Qdyne technique. For traditional DD spectroscopy the bandwidth is given by the filter function of the protocol (green solid line). A variety of normalised spectra recorded with the Qdyne technique at different beating frequencies $\delta_\mathrm{b} = |\nu_\mathrm{LO} - \nu|$ are added in different colours. For larger δ_b the amplitudes of the peaks are smaller than expected. For the purple points the amplitude under the peaks is used as a measure instead (discussion see text). Modified with permission from [153].

lihertz. As a consequence, the Qdyne technique is especially suitable for multi-chromatic signals since all spectral components in a given bandwidth (see section 7.2.5) are sampled simultaneously.

7.2.5 Bandwidth of Qdyne spectroscopy

Another important measure for a spectroscopic technique is its bandwidth, defined as the accessible range of frequencies which can be detected without changing the protocol parameters. Since DD is used to make the quantum sensor sensitive to oscillating fields, only frequency components, which can be measured with the respective DD protocol are recordable with Qdyne.

The bandwidth of a DD sequence is given by its filter function, which is in more detail described in section 4.3. These spectral filters depend on the spacing τ between the π-pulses and the total interaction time T_int. They are peaked at the resonance condition $\nu_0 = 1/(2\tau)$ and their FWHM is given by the inverse of T_int. Thus, the filter sets the range of accessible frequencies, as well as the sensitivity for the respective components.

In order to examine these considerations, we used the XY8-1 sequence to perform Qdyne spectroscopy on signals oscillating close to $\nu = 1\,\mathrm{MHz}$. The spacing between the individual π-pulses was adjusted to 500 ns, which corresponds to a resonance frequency of exactly

$\nu_0 = 1\,\mathrm{MHz}$. We further tailored the temporal overhead due to initialisation and readout such that the local oscillator frequency was $\nu_{\mathrm{LO}} = 1\,\mathrm{MHz}$ as well. We then step-by-step changed the frequency ν of the signal and recorded a Qdyne spectrum for 100 s, respectively. The results are plotted in figure 7.8(b) together with the DD filter function.

For small $\delta_{\mathrm{b}} = |\nu_{\mathrm{LO}} - \nu|$, the amplitudes of the Fourier transform peaks follow the expected behaviour. However, if δ_{b} gets larger than 10 kHz, the height of the peaks is smaller than anticipated. If we instead use the area under the peaks as a measure, the expected trend is recovered (purple points). Thus, the peaks broaden for large δ_{b}, which is not well understood yet [153].

By adjusting T_{int}, the bandwidth of the Qdyne technique can be tuned and the smaller the interaction time is, the larger is the bandwidth. However, a lowering of T_{int} is also accompanied with a decrease in amplitude sensitivity, since the interaction period between sensor and signal is reduced. Thus, there is an inherent trade-off between bandwidth and sensitivity.

Finally, it should be noted that the minimal beating frequency δ_{b}, which can be obtain when performing FFT is given by $1/T$.

7.2.6 Nanoscale NMR with Qdyne

In the previous sections the resolution enhancement of Qdyne over traditional DD spectroscopy has been demonstrated. However, the high magnetic field sensitivity and spatial resolution of the quantum sensor have not been fully made use of. One highly interesting application is nuclear magnetic resonance (NMR) on the nanoscale, as discussed in chapter 5. Although the sensitivity of a single NV centre is sufficient for these experiments, the frequency resolution is rather poor when using traditional DD spectroscopy.

We applied Qdyne with the XY8-4 sequence to record the ^{1}H spectrum of a polybutene oil sample placed on top of the diamond (compare figure 5.3, diamond described in appendix A.1.5). For a single NV centre located $(5.4 \pm 0.2)\,\mathrm{nm}$ below the diamond surface, the main part of the signal arises from on the order of 10^4 proton spins. This small sample size is below the detection limit of traditional NMR spectrometers. Due to overheads for initialisation and readout, the time spacing t_Δ between individual measurements was about 18.3 µs. The resulting spectrum after recording for about 7 hours in a 23 mT bias field is plotted in figure 7.9(a).

Although the spectrum shows a clear signal, the FWHM is still about 2 kHz. The outliers below 985 kHz correspond to very small beating frequencies and are probably due to fluctuations in the experimental setup. The reason for the broad line is the short coherence of the NMR signal itself. Since the oil is highly viscous with a diffusion coefficient

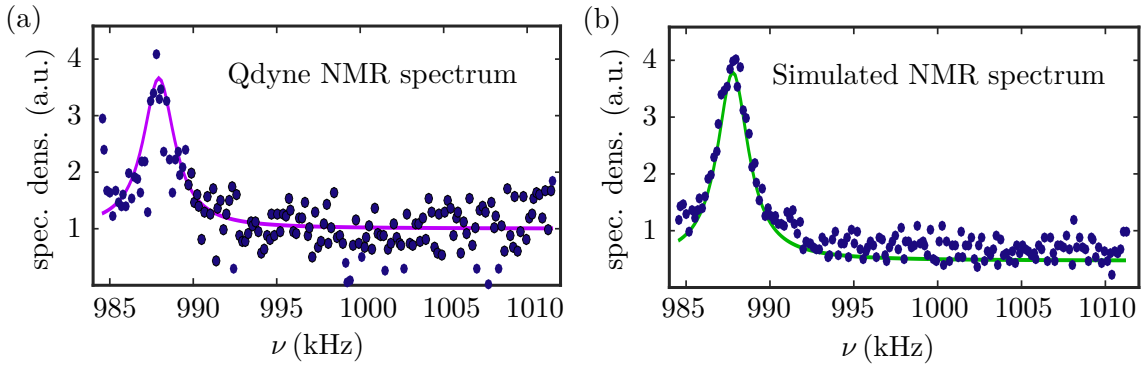

Figure 7.9: Nanoscale NMR using Qdyne. (a) Experimentally obtained NMR spectrum of ^{1}H spins in polybutene using the Qdyne technique. The linewidth of the peak is limited by the coherence of the NMR signal. (b) Simulated spectrum for the same measurement parameters. The solid lines are Lorentzian fits. Modified with permission from [153].

of about $10^{-15}\,\mathrm{m}^2/\mathrm{s}$ at ambient conditions, proton spin-spin interactions lead to relaxation within a timescale between 0.01 and 0.1 ms. Also molecular diffusion and instabilities in the bias magnetic field could increase the FWHM.

This assumption is backed-up by a rigorous atomistic simulation. By modeling $7 \cdot 10^4$ diffusing ^{1}H-spins inside of a 6 nm by 12 nm by 12 nm volume interacting with the NV centre an nanoscale NMR experiment can be emulated. The working principle and assumptions for these calculations are in more detail discussed in the supplementary material of [153]. The spectrum obtained using the same parameters as in the experimental realisation is displayed in figure 7.9(b).

Thermal polarisation

Although the results above demonstrate detection of NMR signals from nanoscale samples using the Qdyne technique, diffusion and spin-spin interactions limit the coherence time of the signal and thus the achievable spectral resolution. Furthermore, averaging is not possible due to the stochastic nature and random phase of the dominating statistical polarisation. Classical NMR, instead, relies on the thermal polarisation M_z of the nuclear target spins, which is uniform for the entire sample, and thus even fast diffusion does not play a role. This motivates a modified protocol, which is in more detail discussed in [226]. The idea is to extract the influence of the thermal signal by averaging out the impact of the statistical polarisation. This is possible, because the signal phase of the thermal polarisation can be controlled via a $\pi/2$-pulse, which rotates the orientation of M_z into the $x-y-$plane. Although stochastical polarisation is dominant, it reduces as $1/\sqrt{N}$ when

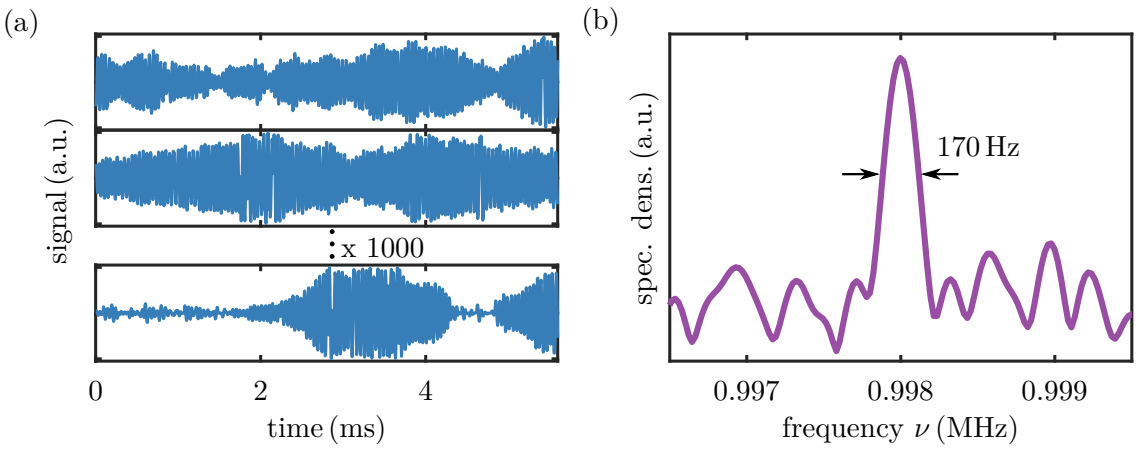

Figure 7.10: Qdyne spectroscopy using thermal polarisation. (a) Taking statistical and thermal polarisation into account, NMR signals were simulated and sampled (with a rate of 5 MHz). A single NV centre and the Qdyne principle were used to measure 1000 of these signals in succession. (b) Averaging over the individual outcomes and taking the Fourier transform reveals a peak and its linewidth is limited by the 5.6 ms length of each simulated signal.

averaging N repetitions due to the random amplitudes and phases, while M_z is identical for all iterations.

In order to demonstrate the working principle, NMR signals oscillating close to 1 MHz were simulated and applied to a single NV centre using an arbitrary waveform generator and a copper wire as antenna. The signals compromise both, a large stochastical contribution affected by a diffusion coefficient of $1 \cdot 10^{-12}\,\mathrm{m}^2/\mathrm{s}$ and a tiny thermal signal ($\langle M_z \rangle = 0.1\,\%$). These amplitudes are equivalent to the strength of a typical real NMR signal for an NV centre located about 6.2 nm below the diamond surface and example signals are shown in figure 7.10(a). The first signal was recorded using 1000 measurements (each 5.6 µs) and the Qdyne principle. After that a new NMR signal was simulated (same parameters) and measured as described above. We repeated this procedure until 1000 different simulated signals were recorded, and averaged the individual measurement outcomes. Taking the FFT, the resulting spectrum, displayed in figure 7.10(b), shows a clear peak with a linewidth of about 170 Hz, which is just limited by the 5.6 ms length of each simulated signal. The diffusion bounded linewidth would be more than 10 kHz in this case.

Although the principle is working, the signal is proportional to the thermal polarisation M_z, which is very small on the nanoscale, especially at lower magnetic fields. This requires recording for many hours in order to average out the impact of statistical polarisation and to gather enough statistic for a representative SNR. In order to decrease the measurement time, one option is to use an ensemble of NV centres. Since the thermal polarisation is

uniform across the entire sample and the stochastical one is not, simultaneously measuring N quasi identical NV centres has the same effect as averaging over N repetitions with a single NV centre. An experimental demonstration including chemical shift and J-coupling resolution was successfully realised in [154]. Using ensembles, however, downgrades the nanoscale spatial resolution to $\sim \mathrm{mm}^3$. Another idea to improve the thermal polarisation is to hyperpolarise the sample. Conveniently, it has been demonstrated that NV centres are outreaching polarisation sources for nuclear spin hyperpolarisation [109,242–245]. The idea is to use NV centres for both, first polarising target nuclear spins and then detecting the magnified signal. These results path the way for a quantum diamond spectrometer for nanoscale NMR and EPR spectroscopy [246].

7.2.7 Conclusion

The presented experiments show that quantum heterodyne detection can be used to perform magnetic field spectroscopy with very high SNR, resolution and precision. In particular, the frequency resolution is not limited by the rather short T_2 coherence time of the quantum sensor, but can be extended up to the stability of an external clock. Dynamical decoupling was used to make the individual measurement results dependent on the phase of the signal of interest and thereby create correlations between subsequent measurements. Since no further technical demands or complex protocols are required, as for approaches relying on quantum memories, Qdyne is usable for a wide range of applications. By comparing it to traditional dynamical decoupling spectroscopy we were able to improve the frequency resolution by eight orders of magnitude and the precision, which scales as $T^{-3/2}$, by nine orders of magnitude. We demonstrated that Qdyne has the potential to be used in nanoscale NMR, where good frequency resolutions are particularly important, for example for molecular structure determination. However, the short coherence time of the signal itself still remains a problem.

At the same time as these results were published, another group reported a similar work [221]. Shortly afterwards, NMR experiments with chemical shift resolution were reported with ensembles of NV centres [154]. Recently, it has been shown that the principle can also be used to measure the frequency of single spins [164,247].

8 Quantum frequency discrimination

When a single coherent quantum probe is intended to be used for detecting a NMR signal, the optimal strategy depends on the problem. Especially, if a certain amount of information is already available, recording a full spectrum might not be the best solution. An example for this is a diagnostics test, which could be realised by using the sensor to examine a sample that contains one of two types of molecules. The detected frequency distribution indicates which molecule is present and this, for example, can be used to find out if a certain chemical reaction has occurred. If the NMR data of both molecules are available, the task is to discriminate between two known frequencies or frequency distributions in the NMR signal. Although recording a full spectrum is still a solution to this problem, the available information would not be used entirely. In particular, when using a quantum sensor as a probe, there is a different strategy that is optimal for such a quantum-enabled diagnostics problem, which is discussed in this chapter.

The precise problem is sketched in figure 8.1. It is a special case of a general decision problem studied by [249] and related hypothesis testing frameworks [250]. A time dependent signal oscillates with one of two possible frequency distributions and the task is to find the correct option.

A particularly salient question is which strategy minimises the measurement time necessary to decide between both alternatives. When applying a suitable discrimination method, both frequency distributions will lead to different measurement results and as long as this difference is larger than the readout noise, a discrimination is possible. In a classical scenario, usually a single measurement is sufficient, for example through improving the signal-to-noise ratio by enhancing the recording duration. Because of quantum projection noise due to the stochastical nature of quantum mechanical readouts, quantum statistics usually requires that a measurement has to be repeated many times and averaged to obtain detailed information.

In the following, a quantum mechanical measurement scheme, which minimises the probability for making an incorrect decision, is introduced. The idea is to drive the sensor to an eigenstate and then such 'yes-no' type experiments in principle allow discrimination using just a single measurement. In general, the scheme is applicable to arbitrary frequency distributions, but for the sake of simplicity we first concentrate on the simplest case of just

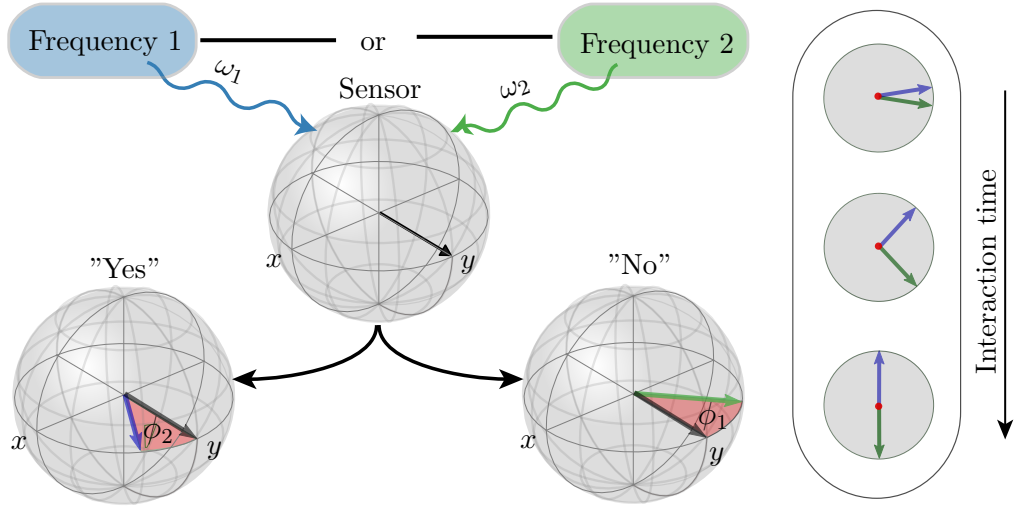

Figure 8.1: Frequency discrimination problem. A quantum sensor is used to measure a field of interest, which is composed of either frequency distribution ω_1 or ω_2. During the interaction a phase ϕ is acquired which depends on the field and the applied control. After a time T_{int}, the sensor is readout and a decision for either ω_1 or ω_2 has to be made. Modified from [248], licensed under CC BY 4.0, http://creativecommons.org/licenses/by/4.0/.

two frequencies ω_1 and ω_2, before discussing a more complex example. We use single NV centres to experimentally realise the described protocol and extensively discuss traditional and single-shot readout with relating to the discrimination problem. Parts of the results presented in this section are published in [248].

8.1 Theoretical derivation

The signal Hamiltonian of an oscillating field with a single frequency ω is:

$$\mathcal{H}(\omega)/\hbar = \Omega \sin(\omega t + \theta)\hat{\sigma}_z = H(t)\hat{\sigma}_z, \tag{8.1}$$

where Ω describes the coupling to the sensor, θ is the signal phase and $\hat{\sigma}_z$ is the Pauli spin operator. For this problem, it is known that ω can only be one of two possible alternatives – ω_1 or ω_2 – and the task is to find the correct option as quickly as possible.

The idea is to tailor the evolution of the quantum sensor in a way, that the final state under the presence of ω_1 is orthogonal to the one under ω_2. In Ramsey-type protocols, the sensor acquires a quantum phase ϕ, which is mapped to a population difference before readout. Orthogonality can be achieved, when the difference $\phi_\Delta = \phi(\omega_1) - \phi(\omega_2)$ is π. Then, spin projection noise can be eliminated completely and, if other noise sources are negligible, a single measurement is in principle sufficient to discriminate between ω_1 and

ω_2. As shown in [202] and section 4.5.1, the evolution of ϕ_Δ is limited by the maximal $\lambda_{\max}$ and minimal eigenvalues $\lambda_{\min}$ of $\mathcal{H}_\Delta/\hbar = (\mathcal{H}(\omega_1) - \mathcal{H}(\omega_2))/\hbar$:

$$\frac{\mathrm{d}\phi_\Delta}{\mathrm{d}t} \leq \lambda_{\max}(t) - \lambda_{\min}(t). \tag{8.2}$$

In order to minimise the required time to achieve orthogonality:

$$\phi_\Delta = \int_0^{t_{\mathrm{opt}}} \frac{\mathrm{d}\phi_\Delta}{\mathrm{d}t}\mathrm{d}t = \int_0^{t_{\mathrm{opt}}} (\lambda_{\max}(t) - \lambda_{\min}(t))\ \mathrm{d}t = \pi, \tag{8.3}$$

has to be solved. For the discrimination problem, it is:

$$\lambda_{\max} = -\lambda_{\min} = \Omega(\sin(\omega_1 t + \theta) - \sin(\omega_2 t + \theta)), \tag{8.4}$$

and thus it follows:

$$\phi_\Delta = \int_0^{t_{\mathrm{opt}}} 4\Omega \left|\sin\left(\frac{\omega_2 - \omega_1}{2}t\right)\cos\left(\frac{\omega_1 + \omega_2}{2}t + \theta\right)\right| \mathrm{d}t = \pi. \tag{8.5}$$

Assuming $\omega_\Delta = |\omega_2 - \omega_1| \ll \frac{1}{t_{\mathrm{opt}}}$ and $(\omega_1 + \omega_2)/2 \gg \frac{1}{t_{\mathrm{opt}}}$ yields:

$$\phi_\Delta = \frac{2}{\pi}\Omega\omega_\Delta t_{\mathrm{opt}}^2 = \pi, \tag{8.6}$$

and the optimal time is given by [248]:

$$t_{\mathrm{opt}} = \frac{\pi}{\sqrt{2\Omega\omega_\Delta}}. \tag{8.7}$$

Interestingly, ϕ_Δ depends quadratically on t_{opt} – a special characteristic of frequency measurements [153, 241]. This time can be significantly shorter than the Fourier limit given by $t = 1/\omega_\Delta$.

The protocol, that obtains this limit is sketched in figure 8.2. A sequence of equally spaced π-pulses is used as a control field and the crucial point is the timing of these π-pulses. The idea is to apply them close to the nodes of the signal, exactly whenever $H_\Delta = H(\omega_1) - H(\omega_2)$ changes sign, which means, that the spacing between the individual π-pulses should be [248]:

$$\tau = \frac{2\pi}{\omega_1 + \omega_2}. \tag{8.8}$$

This control ensures that the sensor phase evolves as [248]:

$$\phi(\omega_1) \ = 2\int_0^{T_{\mathrm{int}}} \frac{2\Omega}{\pi}\sin\left(\frac{\omega_\Delta}{2}t' + \theta\right)\mathrm{d}t' \ = -\phi(\omega_2), \tag{8.9}$$

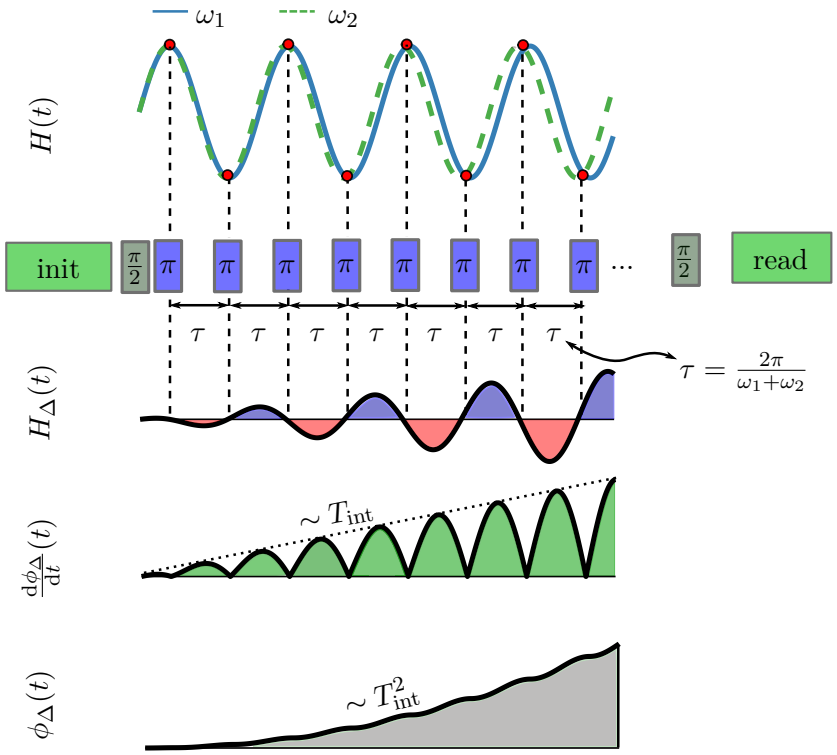

Figure 8.2: Protocol for quantum frequency discrimination. The idea is to apply a train of equally spaced π-pulses whenever $H_\Delta(t)$ ($\mathcal{H}_\Delta = \hbar H_\Delta(t)\hat{\sigma}_z$) changes sign. This type of control ensures that ϕ_Δ grows monotonically. Since the envelope of $\mathrm{d}\phi_\Delta/\mathrm{d}t$ increases linearly with T_{int}, ϕ_Δ scales as T_{int}^2. Modified from [248], licensed under CC BY 4.0, http://creativecommons.org/licenses/by/4.0/.

and thus, ϕ increases with the same rate for ω_1 and ω_2, but with opposing sign. After integration and assuming $\omega_\Delta T_{\text{int}} \ll 1$, it follows [248]:

$$\phi(\omega_1) = -\phi(\omega_2) = \frac{\Omega}{\pi}\left(\omega_\Delta T_{\text{int}}^2 \cdot \cos(\theta) + 4T_{\text{int}} \cdot \sin(\theta)\right). \tag{8.10}$$

For $\theta = 0$ (at the start of the interaction period), $\phi_\Delta = \phi(\omega_1) - \phi(\omega_2)$ yields the same result as equation (8.6). After t_{opt}, $\phi_\Delta = \pi$ and by choosing the appropriate readout basis the sensor populates different eigenstates for ω_1 and ω_2.

For very small Ω or ω_Δ, the coherence time of the senor may be smaller than t_{opt}. Nevertheless, the described protocol still remains optimal for this case, which is proven and in more detail discussed in the supplementary information of [248].

8.2 Experimental demonstration

In order to demonstrate these theoretical findings, single NV centres inside the SIL diamond described in appendix A.1.5 were used. We first ignore the impact of measurement noise and use the traditional method to readout the spin state (see section 3.3). A signal generator was used to generate equally strong signals with frequencies $\omega_1 = 2\pi \cdot 999\,\mathrm{kHz}$ and $\omega_2 = 2\pi \cdot 1001\,\mathrm{kHz}$. These frequencies represent the signals to discriminate. After initialisation into $|0\rangle$ and a $\pi/2$-pulse, we used XY8-sequences with an equidistant spacing of $\tau = 500\,\mathrm{ns}$ following the findings from above. During the evolution, the sensor accumulates a phase ϕ, which is mapped into a population difference by a second $\pi/2$-pulse such that the probability to read out $|0\rangle$ is:

$$P_0 = \sin^2\left(\frac{\pi}{4} - \frac{\phi}{2}\right) = \frac{1}{2} - \frac{1}{2}\sin(\phi). \tag{8.11}$$

By tailoring the number of π-pulses, we measured P_0 for different interaction times T_{int} and the results are shown in figure 8.3(a). The difference $P_0(\omega_1) - P_0(\omega_2)$ initially increase up to t_{opt}, where $P_0(\omega_1) - P_0(\omega_2) = 1$ and the sensor states for ω_1 and ω_2 are orthogonal. The individual phases $\phi(\omega_1)$ and $\phi(\omega_2)$, which are obtained using equation (8.11), are plotted in figure 8.3(b). As expected, $\phi(\omega_1)$ and $\phi(\omega_2)$ increase with the same rate but with opposing signs up to t_{opt}, where $\phi_\Delta = \pi$. The quadratic increase of ϕ_Δ with the interaction time T_{int} can be seen in the logarithmic plot in figure 8.3(c).

Optimal time as a function of amplitude and frequency

According to equation (8.7), the time t_{opt} required to achieve $\phi_\Delta = \pi$ depends on the frequency difference $\omega_\Delta = \omega_1 - \omega_2$ and the field strength $B_1 = 2\Omega/\tilde{\gamma}_{\mathrm{NV}}$, where $\tilde{\gamma}_{\mathrm{NV}}$ is the gyromagnetic ratio of the NV centre's electron spin. In order to experimentally demonstrate this theoretical finding, the NV population was measured for several different B_1 and ω_Δ as a function of interaction time and t_{opt} was extracted, respectively.

First, $B_1 \approx 1.35\,\mu\mathrm{T}$ was fixed and ω_Δ was changed after every measurement. The result is shown in figure 8.3(d). The solid green line corresponds to the expectation according to equation (8.7) and fits very well to the experimentally recorded data. The errorbars are obtained using the standard deviation of several independent repetitions.

In the same way the dependency on B_1 is demonstrated in figure 8.3(e). For a fixed $\omega_\Delta = 2\pi \cdot 2\,\mathrm{kHz}$ the resulting t_{opt}, shown as blue points, mostly fit very well to the theoretical expectation according to equation (8.7) (blue solid line). The slight differences for small B_1 are due to the long t_{opt} for which the approximation $\omega_\Delta t_{\mathrm{opt}} \ll 1$ is not longer valid.

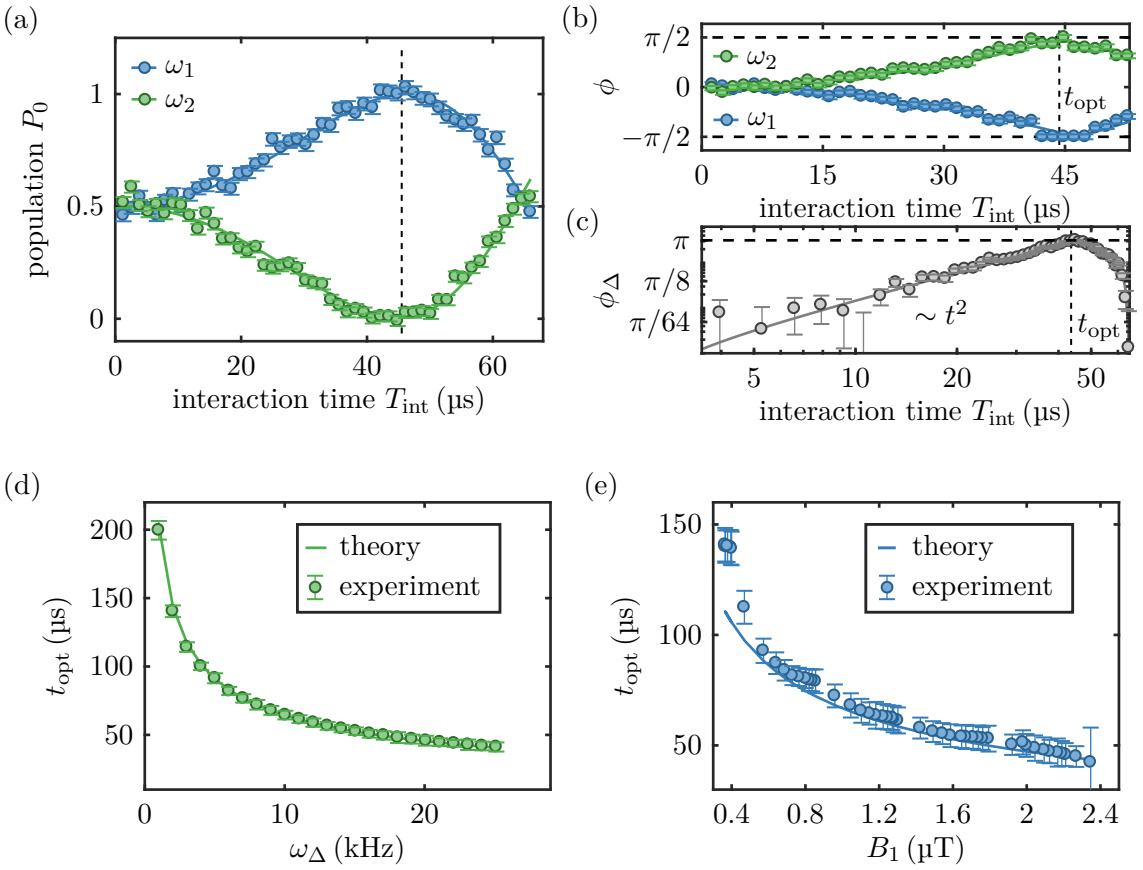

Figure 8.3: Experimental demonstration of the discrimination principle. (a) Evolution of the sensor population P_0 for $\omega_1 = 2\pi \cdot 999\,\text{kHz}$ and $\omega_2 = 2\pi \cdot 1001\,\text{kHz}$ as a function of interaction time T_{int}. The difference $\Delta P_0 = P_0(\omega_1) - P_0(\omega_2)$ increases up to t_{opt}, where $\Delta P_0 = 1$. From this point, prolonging the interaction time reduces ΔP_0 and is thus counterproductive. (b) Acquired sensor phases $\phi(\omega_1)$ and $\phi(\omega_2)$ as a function of T_{int}. Both, $\phi(\omega_1)$ and $\phi(\omega_2)$, increase with the same rate but with opposing signs. (c) Their difference $\phi_\Delta = |\phi(\omega_1) - \phi(\omega_2)|$ scales as T_{int}^2. (d) Dependency of the required time t_{opt} to achieve $\phi_\Delta = \pi$ on the frequency difference ω_Δ and (e) the magnetic field strength B_1. All solid lines correspond to the theoretical expectations according to equations 8.6, 8.7 and 8.11. Modified from [248], licensed under CC BY 4.0, http://creativecommons.org/licenses/by/4.0/.

8.3 Quantum discrimination for complex frequency distributions

For many possible applications, interesting signals have multiple frequency components with various amplitudes. For these more general cases, where the task is to discriminate between two arbitrary frequency distributions f_1 and f_2, the optimal control is nevertheless based on the same principles. By interacting with the signal of interest, the sensor acquires a phase ϕ and for $\phi_\Delta = \phi_1 - \phi_2$ the speed bound given by equation (8.2) still applies. The associated protocol requires π-pulses whenever $H_\Delta = H_1 - H_2$ changes sign, where [248]

$$\mathcal{H}_{1,2}(t)/\hbar = \int_0^\infty f_{1,2} \sin(\omega t) \mathrm{d}\omega \, \hat{\sigma}_z = H_{1,2}(t)\hat{\sigma}_z, \tag{8.12}$$

is the signal Hamiltonian for f_1 or f_2.

In figure 8.4 an illustrative example for NMR detection is given, which is especially relevant since the initial phase of a thermally polarised sample is defined by the applied $\pi/2$-pulse. The ^{13}C-NMR spectra of ethanol (C_2H_6O) and 2-propanol (C_3H_8O) represent f_1 and f_2 in this case and each consist of two peaks with different amplitudes (figure 8.4(a)).

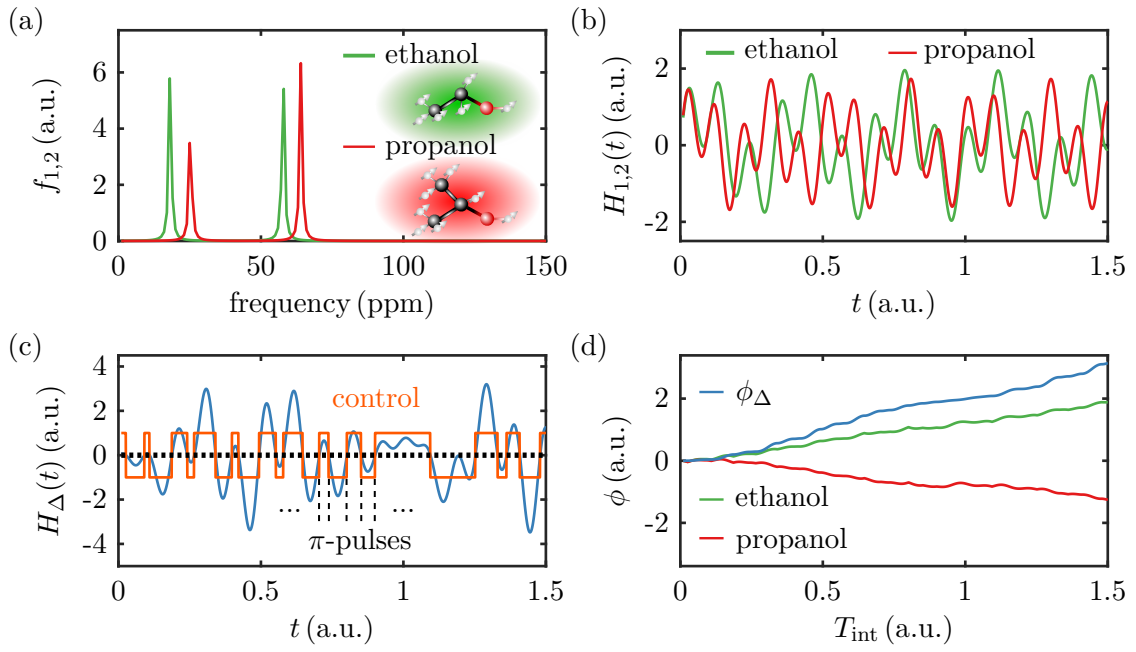

Figure 8.4: Discrimination for complex frequency distributions. (a) The ^{13}C-NMR of ethanol (C_2H_6O, index 1) and 2-propanol (C_3H_8O, index 2) (values from [223]). (b) NMR signals $H_{1,2}$ of both molecules as a function of time. (c) Signal difference (blue) and optimal control (orange). (d) Evolution of the sensor phases $\phi_{1,2}$ during interaction and the difference $\phi_\Delta = \phi_1 - \phi_2$. Modified from [248], licensed under CC BY 4.0, http://creativecommons.org/licenses/by/4.0/.

As shown in figure 8.4(b), the associated NMR signals are clearly different for both molecules. Their difference $H_\Delta(t) = H_1(t) - H_2(t)$ is shown in figure 8.4(c) (blue line) and the control π-pulses should be applied whenever $H_\Delta(t)$ changes sign. Although the values of the acquired phases $\phi_1(t)$ and $\phi_2(t)$ are different, the signs are still opposing and the applied control ensures that ϕ_Δ increases monotonically.

8.4 Discussion of different readout strategies

Above, optimal frequency estimation using a single quantum sensor has been discussed – however, up to now only in consideration of the eventually limiting quantum projection noise. When performing a real-world measurement, other noise sources influence the probability to decide on the correct frequency. For example, every quantum sensor interacts with environmental noise which relaxes the quantum state into its thermal equilibrium (compare section 4.5.4). Furthermore, errors can enter through a non-perfect initialisation fidelity. Finally, the classical noise added during the readout has to be considered.

In the following, the influences of the latter two are examined in more detail for two optical readout strategies. The influences of relaxation are neglected since the relevant interaction times are here much shorter than the T_2 coherence time.

When a single NV centre is readout optically, photons are the measurement quantity. Intuitively, the signal-to-noise ratio (SNR) improves if more photons are recorded. This can be achieved by either increasing the number of fluorescent sensors (figure 8.5(a)) or by collecting more fluorescence from a single sensor (figure 8.5(b)). Classically, both options yield equivalent sensitivity, as long as the final intensity is the same.

For a quantum sensor, however, these two strategies can lead to significantly different results. Especially when the collection efficiency is sufficient to readout the state of the sensor, quantum projection noise (QPN) rather than photon shot noise (PSN) dominates the sensitivity. Depending on the application, the two strategies may have different requirements with respect to complexity and needed resources. In the following, it is shown that ensemble averaging (strategy 1) yields at least as good performance as single-shot readout (SSR) (strategy 2) when benchmarked against the number of detected photons, whereas SSR has certain advantages when measurement time or number of measurements are taken into account.

We use single NV centres to experimentally realise both strategies. The experiments were performed on a home-build confocal microscope and controlled by the Qudi software suite (appendix A.1.4 and [236]). In order to lift the degeneracy of the $m_s = \pm 1$ spin states and use the $m_s = 0$ and $m_s = -1$ states as an effective qubit, all measurements

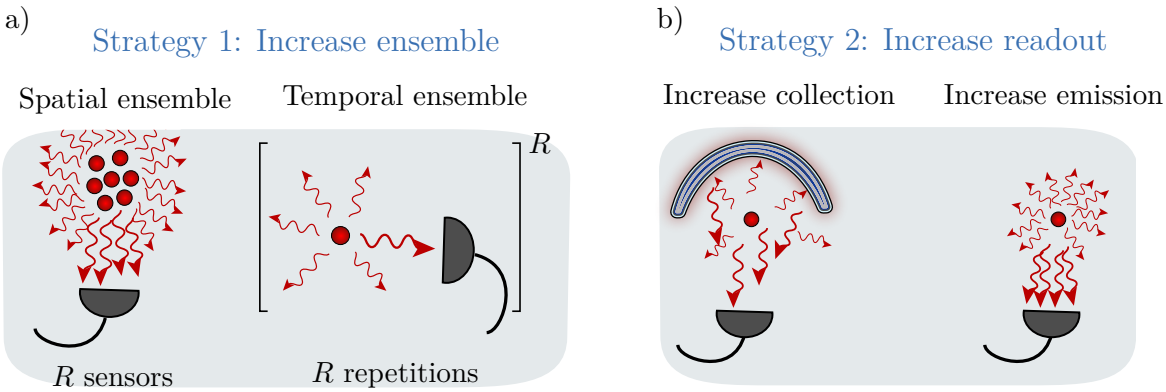

Figure 8.5: Strategies to improve the sensitivity of a fluorescent sensor. The sensitivity of a fluorescent atomic sensor is determined by the signal and the noise associated with the detected photons and can be improved by recording more photons. (a) One option is to increase the number of sensors either by using more identical sensors (spatial ensemble) or by repetitively measuring a single sensor (temporal ensemble). (b) A second strategy is to enhance the number of collected photons. Possible options include improving the collection efficiency or increasing the emission.

were performed under a bias magnetic field of about $B_0 \approx 40\,\mathrm{mT}$ aligned along the NV centre symmetry axis.

8.4.1 Strategy 1 – Ensemble averaging

Strategy 1 can in principle be realised in two ways and the first option is using multiple identical sensors. Since here the experiments are limited to single NV centres, we repetitively measured the same one (temporal ensemble) using the traditional readout method (compare section 3.3). The corresponding quantum wire diagram is sketched in figure 8.6(a).

In figure 8.6(b), a typical time-trace for 75 individual measurements is shown (readout window about 500 ns). Due to the low detection efficiency, photons are recorded only in a small percentage of experiments and the probability for detecting more than one photon is tiny. As the histograms in figure 8.6(c) show, the number of recorded photons N_{ph} follows Poissonian statistics with averaged photon numbers of $c_0 \approx 0.085$ for $|0\rangle$ and $c_1 \approx 0.071$ for $|1\rangle$. This difference is much too small for a reliable assignment and thus hardly any information about the sensor state can be obtained within a single measurement. The usual principle is to combine all photons collected in R_{ens} repetitions, whereby the quantum nature of the NV centre electron spin is obscured since the result is already an average over many repetitions.

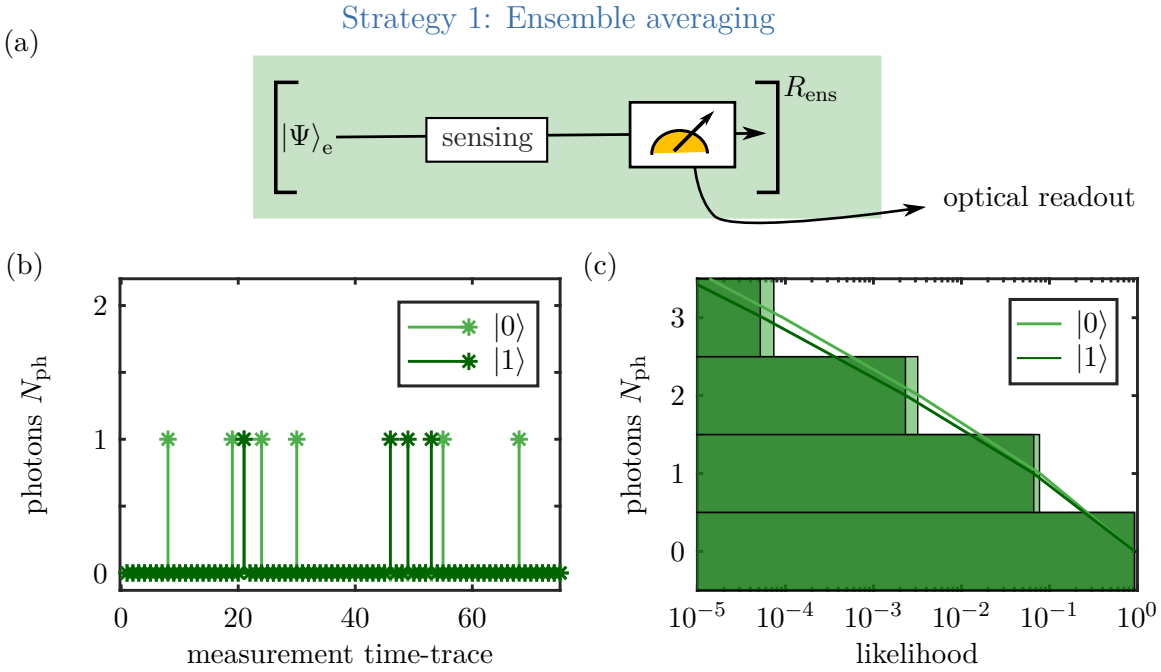

Figure 8.6: Quantum wire diagram for ensemble averaging and photon statistics. (a) Ensemble averaging can be realised by repetitively performing the cycle consisting of initialisation, sensing period and readout. (b) Number of recorded photons as a function of the measurement repetition for the states $|0\rangle$ and $|1\rangle$. (c) The histograms obtained from about $4 \cdot 10^6$ individual measurements are well fitted by Poisson distributions (solid lines) with averaged photon numbers $c_0 = 0.085$ for $|0\rangle$ and $c_1 = 0.071$ for $|1\rangle$. Modified from [248], licensed under CC BY 4.0, http://creativecommons.org/licenses/by/4.0/.

Contribution of photon shot noise and quantum projection noise

For an optical readout of a quantum sensor the two main noise contributions are usually PSN and QPN. Since the expected number of recorded photons $\mathcal{N} = \langle N_{ph} \rangle$ after R_{ens} readouts relates to the sensor population P_0 as:

$$\mathcal{N} = R_{ens} \cdot [c_0 P_0 + c_1(1 - P_0)] = R_{ens} \cdot [(c_0 - c_1)P_0 + c_1], \tag{8.13}$$

where c_0 and c_1 are the number of photons collected from the $|0\rangle$ and $|1\rangle$ states within a single readout, the PSN contribution reads:

$$\delta_{PSN} = \sqrt{\mathcal{N}} = \sqrt{R_{ens} \cdot [c_0 P_0 + c_1(1 - P_0)]}. \tag{8.14}$$

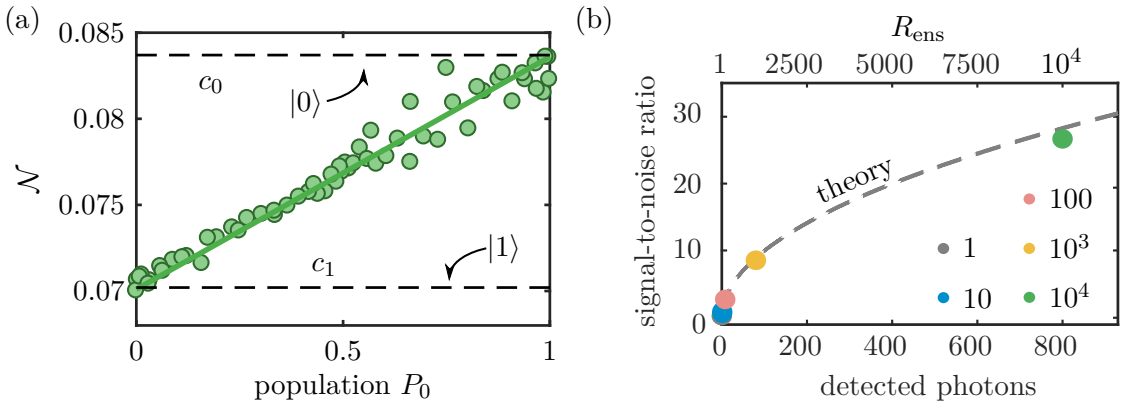

Figure 8.7: Expected number of photons and noise for ensemble averaging. (a) Averaged number of detected photons $\mathcal{N}$ per readout over sensor population P_0. There is a linear dependency with parameters $c_0 \approx 0.085$ and $c_1 \approx 0.071$. Modified from [248], licensed under [251]. (b) Since $\mathcal{N}$ grows linearly with the number of iterations R_{ens} and photon shot noise increases only as $\sqrt{\mathcal{N}}$, the signal-to-noise ratio scales as $\sqrt{R_{\mathrm{ens}}}$. The coloured points are obtained from experimental data for different R_{ens}.

The influences of imperfect initialisation can be included in c_0 and c_1. The QPN contribution is given by:

$$\delta_{\mathrm{QPN}} = (c_0 - c_1)\sqrt{R_{\mathrm{ens}} \cdot P_0(1 - P_0)} \tag{8.15}$$

where the factor $(c_0 - c_1)$ corresponds to the photon difference between both states and is added to improve the comparability of both noise types. For the total noise it follows [4]:

$$\delta_{\mathrm{total}} = \sqrt{\delta_{\mathrm{PSN}}^2 + \delta_{\mathrm{QPN}}^2}. \tag{8.16}$$

As figure 8.7(a) shows, we find the expected linear dependency between $\mathcal{N}$ and P_0 and $c_0 \approx 0.085$ and $c_1 \approx 0.071$ for our experiments. Using these numbers, it follows that PSN dominates with a contribution larger than 99 % for $P_0 = 0.5$. This is independent of the total number of detected photons, as further averaging reduces both PSN and QPN equally. The resulting signal to noise improves as $\sqrt{\mathcal{N}}$ (or $\sqrt{R_{\mathrm{ens}}}$), which is shown in figure 8.7(b).

Experimental realisation

In order to experimentally analyse frequency discrimination, every measurement was repeated $1 \cdot 10^6 - 4 \cdot 10^6$ times for both frequencies and the result of every repetition was stored individually. This allows to freely distribute these individual realisations into en-

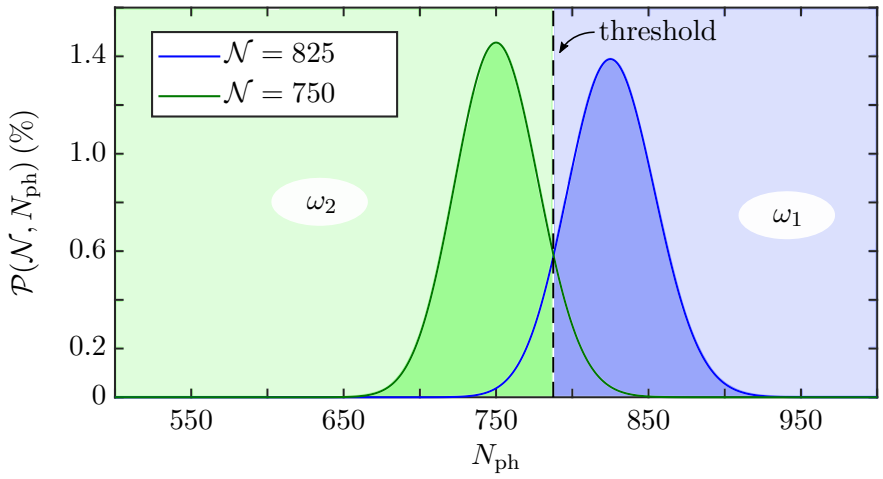

Figure 8.8: Decision criterion for frequency discrimination. For this example the expected number of collected photons is $\mathcal{N} = 825$ for ω_1 and $\mathcal{N} = 750$ for ω_2. The resulting Poisson distributions – blue line for ω_1 and green line for ω_2 – represent the likelihood to measure a certain number of photons N_{ph}. In the blue shaded sector the likelihood for ω_1 is larger and in the green shaded the opposite is true. The decision threshold is thus chosen as the intersection of both distributions and their overlap is a measure for the error probability.

sembles. For example, $R_{\mathrm{ens}} = 10^4$ measurements were randomly combined to data sets each corresponding to $\mathcal{N} \approx 800$.

Discrimination error

Under the assumption that the correct frequency is unknown, a decision for either ω_1 or ω_2 is made for every set. The intuitive decision criterion is to choose the frequency for which the found N_{ph} is more probable. The probability to detect a certain number of photons N_{ph} is given by the respective Poisson distribution:

$$\mathcal{P}(\mathcal{N}, N_{\mathrm{ph}}) = \frac{\mathcal{N}^{N_{\mathrm{ph}}}}{N_{\mathrm{ph}}!} \cdot \exp\left(-\mathcal{N}\right), \tag{8.17}$$

where $\mathcal{N}$ is a function of the frequency. As sketched in figure 8.8, the decision threshold is then the intersection point of both distributions and since N_{ph} is a discrete number, the threshold photon counts N_{thres} is here defined as:

$$\begin{aligned} &\mathcal{P}\left(\mathcal{N}(\omega_2), N_{\mathrm{ph}}\right) \geq \mathcal{P}\left(\mathcal{N}(\omega_1), N_{\mathrm{ph}}\right) \quad \text{for all} \quad N_{\mathrm{ph}} \leq N_{\mathrm{thres}}, \\ &\mathcal{P}\left(\mathcal{N}(\omega_2), N_{\mathrm{ph}}\right) < \mathcal{P}\left(\mathcal{N}(\omega_2), N_{\mathrm{ph}}\right) \quad \text{for all} \quad N_{\mathrm{ph}} > N_{\mathrm{thres}}. \end{aligned} \tag{8.18}$$

After having made a decision for every set, we extract the error probability as the ratio of incorrect assignments compared to the total number of decisions. The theoretically expected error probability is given by (assuming that both frequencies are equally likely):

$$U = 1 - 0.5 \cdot (C_1 + C_2), \tag{8.19}$$

where C_1 is the probability for a correct decision when ω_1 is present:

$$C_1 = \sum_{n=N_{\text{thres}}+1}^{R_{\text{ens}}} \mathcal{P}(\mathcal{N}, n), \tag{8.20}$$

and C_2 is the counterpart for ω_2:

$$C_2 = \sum_{n=0}^{N_{\text{thres}}} \mathcal{P}(\mathcal{N}, n). \tag{8.21}$$

8.4.2 Strategy 2 – Single-shot readout

For strategy 2 we used a weakly coupled ^{13}C nuclear spin as an additional memory to indirectly increase the fluorescence for every individual readout. If the perpendicular hyperfine coupling $A_\perp$ between NV centre and memory is small, flip-flops processes are efficiently suppressed, even during the readout of the electronic state [252, 253]. Here, the suitable hyperfine coupling parameters ($A_\parallel \approx 50\,\text{kHz}$ and $A_\perp \approx 1.4\,\text{kHz}$, diamond described in appendix A.1.5) led to memory lifetimes on the order of several seconds for moderate fields around 27 mT. The idea is to map the NV population onto this memory qubit. After an initial readout, the memory state is efficiently preserved and can be readout via a quantum-non-demolition measurement [238, 254–256].

The principle is sketched in figure 8.9(a). As for ensemble averaging, the sensor qubit is initialised and acquires the measurement information by interacting with the field of interest. Before the first readout of the NV centre, however, the sensor and the memory are entangled by using a selective radio frequency pulse (controlled-not (CNOT) gate). As sketched in figure 8.9(b), this pulse (RF1) only flips the nuclear spin state if the NV centre is in $|0\rangle$ [248]:

$$(\alpha\,|0\rangle + \beta\,|1\rangle) \otimes |\uparrow\rangle \xrightarrow{\text{RF1}} \alpha\,|0\downarrow\rangle + \beta\,|1\uparrow\rangle \tag{8.22a}$$

$$(\alpha\,|0\rangle + \beta\,|1\rangle) \otimes |\downarrow\rangle \xrightarrow{\text{RF1}} \alpha\,|0\uparrow\rangle + \beta\,|1\downarrow\rangle\,. \tag{8.22b}$$

The transitions frequencies for RF1 and RF2 are different due to the parallel hyperfine coupling $A_\parallel$ between electron spin and nuclear spin, as shown in figure 8.9(c). In order to

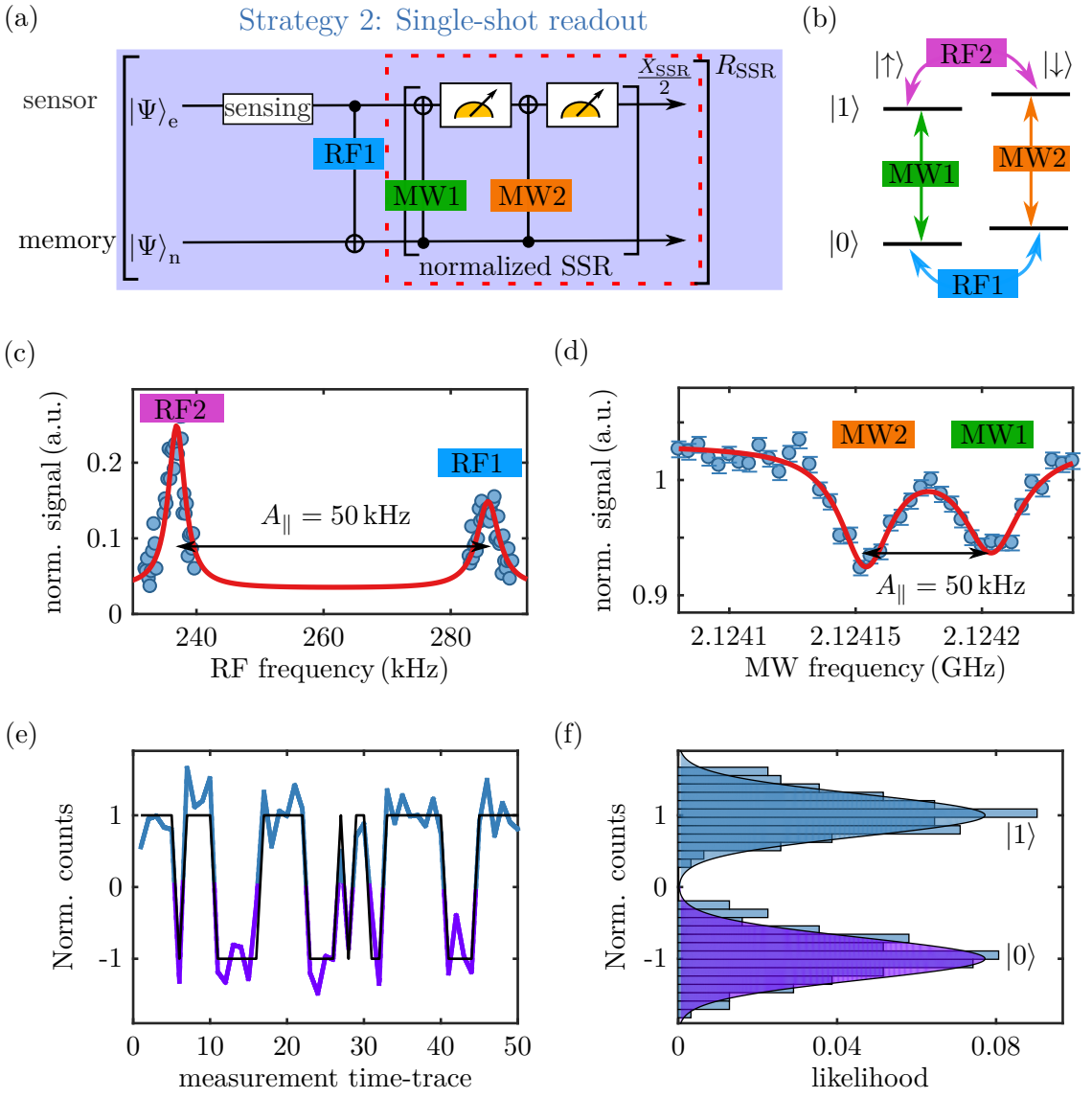

Figure 8.9: Protocol and photon statistics for single-shot readout. (a) Using selective π-pulses (coloured boxes), the sensor state can be mapped onto a memory qubit, which can be readout with a SSR technique. A more detailed description is in the text. (b) Energy levels of the sensor (states $|0\rangle$ and $|1\rangle$) memory (states $|\uparrow\rangle$) and $|\downarrow\rangle$ system and corresponding transitions. (c) Nuclear resonance experiment showing that the resonance frequencies for RF1 and RF2 differ by $A_\parallel$. The red line corresponds to a Lorentzian fit to the data. (d) Pulsed ODMR experiment demonstrating that the resonance frequencies for MW1 and MW2 differ by $A_\parallel$. The red line corresponds to a Lorentzian fit to the data. (e) The normalised count trace follows two-step Bernoulli statistics. (f) The corresponding histogram comprises two Poisson distributions – one for each qubit state. Modified from [248], licensed under CC BY 4.0, http://creativecommons.org/licenses/by/4.0/.

avoid simultaneous driving of both transitions the Rabi frequency of an selective pulse Ω needs to be much smaller than $2\pi \cdot A_{\parallel}$ (compare equation (2.30)). Alternatively, Ω can be chosen such that the generalised Rabi frequency for the unintended transition results in a 2π-rotation, which leads to the condition $\Omega/(2\pi) = A_{\parallel}/\sqrt{3}$.

The readout then projects both qubits into corresponding eigenstates. While the spin of the NV centre is populated into the $m_s = 0$ state due to the optical pumping, the state of the memory is only weakly perturbed. This allows to repetitively map its state back onto the electron spin (here X_{SSR} times) and in this way measure the nuclear spin state with a high fidelity in a single-shot readout (SSR).

In order to mitigate slow fluctuations, for example due to an unstable laser power, a normalised scheme was applied. The idea is to use two microwave CNOT gates (MW1 and MW2), which flip the electron spin depending on the nuclear state – MW1 if the nuclear spin is in $|\uparrow\rangle$ and MW2 for $|\downarrow\rangle$. As shown in figure 8.9(d), the resonance frequencies for MW1 and MW2 are also separated by $A_{\parallel}$. If MW1 flips the electron spin to $|1\rangle$, the detected fluorescence during the subsequent laser pulse is low, whereas MW2 would lead to no flip and high fluorescence [248]:

$$|0\rangle \otimes |\uparrow\rangle \xrightarrow{\mathrm{MW1}} |1\uparrow\rangle \Rightarrow \text{low fluorescence} \xrightarrow{\text{laser read}} |0\rangle \otimes |\uparrow\rangle\,, \tag{8.23a}$$

$$|0\rangle \otimes |\uparrow\rangle \xrightarrow{\mathrm{MW2}} |0\uparrow\rangle \Rightarrow \text{high fluorescence} \xrightarrow{\text{laser read}} |0\rangle \otimes |\uparrow\rangle\,, \tag{8.23b}$$

and vice versa. After summing up all photons in the X_{SSR} repetitions, the normalised signal is given by [248]:

$$PL_{\mathrm{norm}} = \frac{PL_1 - PL_2}{PL_1 + PL_2}, \tag{8.24}$$

where PL_1 and PL_2 are the total numbers of collected photons during the first and second readout pulses. In order to digitise the normalised count data, the negative data was assigned to the $|\uparrow\rangle$ state and the positive data to the $|\downarrow\rangle$ state. Since the nuclear spin is flipped if the NV centre's state is $|0\rangle$, the spin flip probability of the nucleus corresponds to the population P_0 of the NV centre. In our experiment, the durations of the RF1 pulses were about 100 µs and the lengths of MW1 and MW2 pulses around 17 µs.

In figure 8.9(e) a typical time-trace showing quantum jumps is presented. It represents a step function closely following Bernoulli statistic. The corresponding histogram, shown in figure 8.9(f), reveals two Poisson distributions and the fidelity for state assignment is limited by their overlap. As long as the readout time does not exceed the memory lifetime, the larger the number of collected photons, the lower is the overlap between the two distributions and the higher is the assignment fidelity. QPN, however, is not reduced.

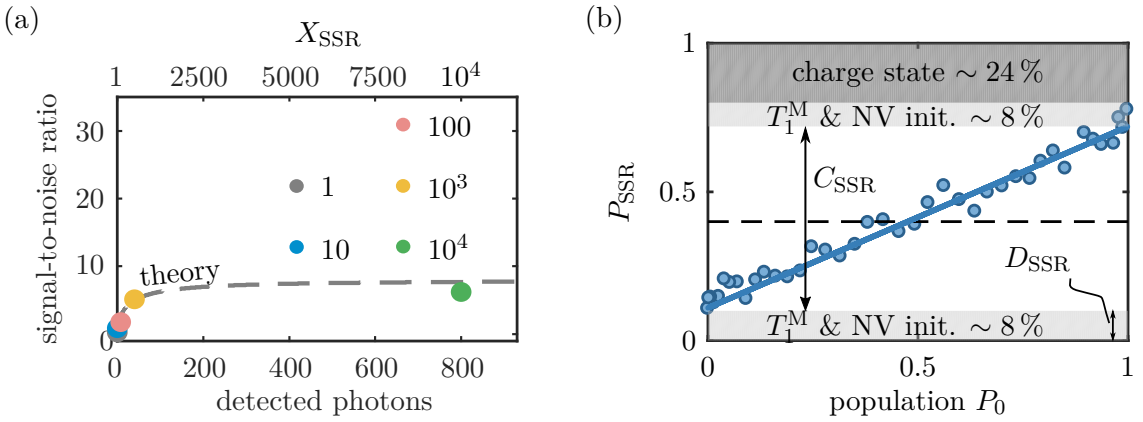

Figure 8.10: Signal-to-noise ratio and flip probability for single-shot readout. (b) The signal-to-noise ratio depends on the fidelity of assignment. It strongly increases for low photon numbers yielding a highly improving SNR. If the fidelity approaches unity the SNR saturates. (b) Flip rate P_{SSR} as a function of the sensor population P_0, which should be identical for an ideal measurement. Due to charge state conversion processes, the non-perfect initialisation fidelity of the NV centre and the limited lifetime of the memory spin T_1^M the contrast is reduced. Subfigure (b) is modified from [248], licensed under CC BY 4.0, http://creativecommons.org/licenses/by/4.0/.

Contribution of photon shot noise and quantum projection noise

For SSR the PSN contribution reads:

$$\delta_{PSN} = \sqrt{X_{SSR} \cdot [c_0 P_0 + c_1(1 - P_0)]}, \tag{8.25}$$

where X_{SSR} is the number of repetitive readouts. The QPN contribution is given by:

$$\delta_{QPN} = (c_0 - c_1) X_{SSR} \sqrt{P_0(1 - P_0)}. \tag{8.26}$$

For $X_{SSR} = 10^4$ readouts of the nuclear spin from which ~ 800 photons are detected, quantum projection noise contributes 86 % to the overall readout noise (for $P_0 = 0.5$).

The SNR as a function of the number of detected photons is plotted in figure 8.10(a). While the averaged photon count still grows linearly with the number of SSR repetitions, the SNR increases only for a small range before it saturates. For low photon numbers, the fidelity of assignment strongly increases yielding a highly improved SNR. However, the information content of the measurement is limited to a single bit. Thus, if the assignment fidelity is already very high (close to 90 % for $X_{SSR} = 10^3$), collecting further photons does not longer particularly impact the SNR since the dominating QPN does not improve.

The comparison of figure 8.7(b) and figure 8.10(a) suggests that due to the superior SNR, ensemble averaging always performs better than a single SSR measurement. However,

this is not strictly the case and SSR provides certain advantages, which are discussed in section 8.4.3.

Experimental realisation

The experimental analysis is very similar to the one used for ensemble averaging. Every measurement was repeated about 2000 times for both frequencies and the individual results were randomly combined if necessary. Assuming that the correct frequency is unknown, a decision for either ω_1 or ω_2 is made for every set.

Discrimination error

Instead of using Poisson distributions to compute the decision threshold, here binomial distributions are taken:

$$\mathcal{B}(p_i, R_{\mathrm{SSR}}, n) = \begin{pmatrix} R_{\mathrm{SSR}} \\ n \end{pmatrix} p_i^n (1-p_i)^{R_{\mathrm{SSR}}-n}, \tag{8.27}$$

where n is the number of nuclear spin flips in R_{SSR} tries and p_i is the flip probability for ω_i.

The decision threshold N_{thres} is the intersection point of the distributions for ω_1 and ω_2. After having made a decision for every set, the error probability corresponds to the ratio of incorrect assignments compared to the total number of decisions.

The theoretical expectation for the error probability is calculated as before, with the only difference, that again binomial distributions are used [248]:

$$U = 1 - 0.5 \cdot \Big(\underbrace{\sum_{n=N_{\mathrm{thres}}+1}^{R_{\mathrm{SSR}}} \mathcal{B}(p_1, R_{\mathrm{SSR}}, n)}_{C_1} + \underbrace{\sum_{n=0}^{N_{\mathrm{thres}}} \mathcal{B}(p_2, R_{\mathrm{SSR}}, n)}_{C_2} \Big), \tag{8.28}$$

where C_1 and C_2 are the probabilities for a correct decision when ω_1 and ω_2 are present.

Limitations of the single-shot readout

For an ideal SSR the flip rate P_{SSR} of the ^{13}C memory spin should correspond to the probability to find the NV centre in $|0\rangle$. NV centres can, however, lose an electron under illumination and become neutrally charged. These charge state conversion processes have to be considered, since in its neutral charge state, which is present about $20-30\,\%$ of the time under green illumination, the NV centre is insensitive [105, 257]. This is in more detail discussed in appendix A.3.7. Further limitations include the not perfect initialisation

fidelity of the NV centre itself (maximal about 92 % [105]) and statistical flips of the ^{13}C spin due to its non-infinite lifetime.

In order to quantify these limitations, we used a simple Rabi fringe recorded using SSR to extract P_{SSR} as a function of P_0, which is plotted in figure 8.10(b). Although we find the expected linear dependency there are unequal margins on top and the bottom. Whilst the margin at the bottom is about 10 % and is dominated by the imperfect initialisation of the NV centre into $m_{\mathrm{s}} = 0$ and the finite lifetime of the memory, the additional contribution due to the charge state conversion processes ($\sim 20\,\%$) becomes evident for the top margin. The resulting flip probability of the memory P_{SSR} as a function of the NV population P_0 can be expressed as:

$$P_{\mathrm{SSR}} = C_{\mathrm{SSR}} \cdot P_0 + D_{\mathrm{SSR}}, \tag{8.29}$$

where $C_{\mathrm{SSR}} \approx 0.61$ and $D_{\mathrm{SSR}} \approx 0.11$ for our experiments [248].

8.4.3 Performance for quantum frequency discrimination

In the following, quantum frequency discrimination is experimentally analysed for the two discussed readout strategies.

Noise as a function of sensor population

One clear difference between QPN and PSN is that QPN depends on the sensor population P_0. In order to show this, we recorded P_0 as a function of coherent interaction time (as shown in figure 8.3) for both strategies, using the discrimination protocol (same parameters as in section 8.2) We then repeated the measurement multiple times and looked at fluctuations in the measurement result. From these data sets, the standard deviation was computed for both cases and the results are plotted in figure 8.11. The solid lines correspond to the theoretical expectations according to (compare equation (8.14)):

$$\delta_{\mathrm{PSN}} = \sqrt{R_{\mathrm{ens}}\mathcal{N}}, \tag{8.30}$$

for ensemble averaging and (compare equation (8.26)):

$$\delta_{\mathrm{SSR}} = (c_0 - c_1) X_{\mathrm{SSR}} \sqrt{P_0(1 - P_0)}, \tag{8.31}$$

for SSR.

As expected, the PSN dominated ensemble averaging is almost independent of P_0, whereas the standard deviation obtained with SSR follows the expected $\sqrt{P_{\mathrm{SSR}}(1 - P_{\mathrm{SSR}})}$ dependency. QPN is maximal for $T_{\mathrm{int}} = 0$ and reduces until $t_{\mathrm{opt}} = 44\,\mu\mathrm{s}$, where the sensor

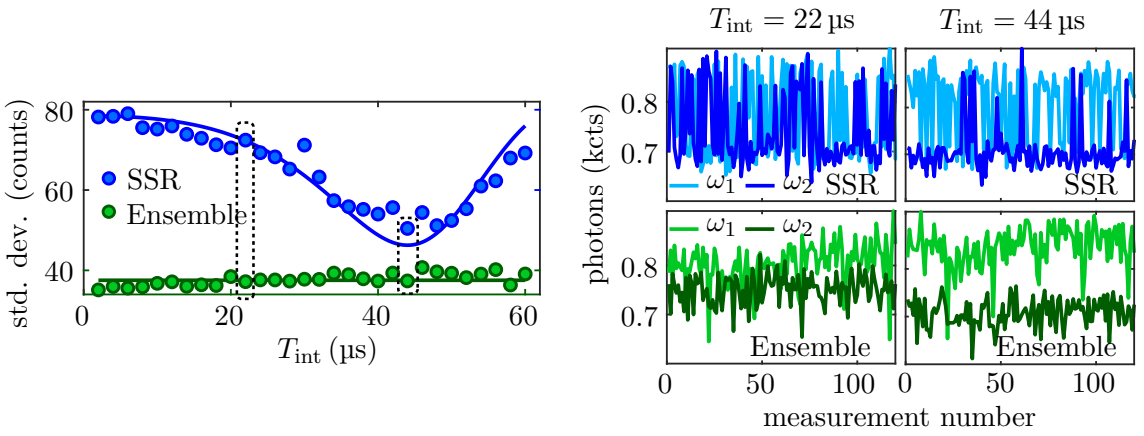

Figure 8.11: Readout noise as a function of interaction time. The standard deviation for SSR is dominated by QPN. Since QPN is a function of the senor population P_0, it changes for different interaction times. It is maximal for $P_0 = 0.5$ and it is minimal if P_0 approaches either zero or one. On the contrary, the standard deviation for ensemble averaging is almost independent of P_0. On the right side the measurement time-traces for two different interaction time $T_{\mathrm{int}} = 22\,\mu s$ and $T_{\mathrm{int}} = 44\,\mu s$ are shown. While for SSR the fluctuations clearly reduce (top panel), the average standard deviation remains unchanged for ensemble averaging (bottom panel). Modified from [248], licensed under CC BY 4.0, http://creativecommons.org/licenses/by/4.0/.

is in one of its eigenstates and QPN would reduce to zero for a perfect SSR. Due to the above discussed limitations, QPN does not vanish completely in our experiments.

Error probability over interaction time

In figure 8.12(a) the probability for an incorrect frequency assignment is plotted for 800 recorded photons with both readout strategies. Although the discrimination error reduces for both methods with increasing coherent interaction time, there is a clear difference in the performance. For ensemble averaging, the discrimination error mainly depends on the overlap between the Poisson distributions of the detected photons for ω_1 and ω_2. Since their centres drift apart, if $\Delta P_0 = P_0(\omega_1) - P_0(\omega_2)$ increases, the overlap reduces with increasing interaction time and reaches a minimum when $\Delta P_0 = 1$. The additional contribution from QPN for the SSR results in a greater error probability and approaches zero only if $\phi_\Delta = \pi$, where the probability for an incorrect assignment of both methods should in theory coincide. Due to the limitations discussed above, we observe an increased error likelihood for SSR. The solid lines correspond to theoretical expectations according to equations 8.19 and 8.28. Assuming an ideal SSR, we obtain the red solid line in figure 8.12(a) and retrieve this equivalence.

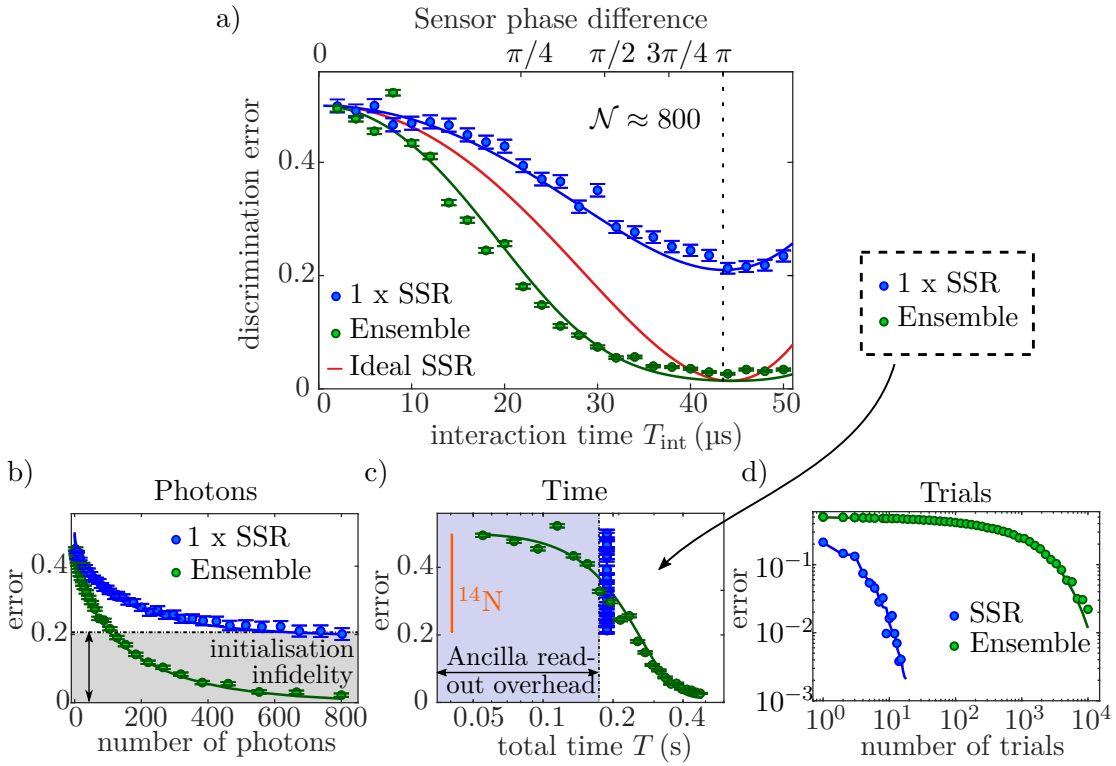

Figure 8.12: Experimental frequency discrimination for both strategies. (a) Probability for an incorrect assignment as a function of coherent interaction time. In order to have the same number of photons $\mathcal{N} = 800$, one SSR with $X_{\mathrm{SSR}} = 10^4$ and about 10^4 ensemble averages are compared. Ensemble averaging performs better due to absence of quantum projection noise. (b) Due to the limited initialisation fidelity of the memory qubit, the error probability is limited to about 0.2 for a single SSR. (c) Since the photon acquisition rate depends on different mechanisms for both strategies, the error probability as a function of the total measurement time requires further discussion (see text). (d) When considering only the number of trials, SSR clearly outperforms ensemble averaging. All solid lines are theoretical expectations according to equations 8.19 and 8.28. Modified from [248], licensed under CC BY 4.0, http://creativecommons.org/licenses/by/4.0/.

In the following, the discrimination error as a function of number of recorded photons, total measurement time and number of trials is analysed in more detail for a fixed interaction time of 44 µs (corresponds to $\phi_\Delta = \pi$, black dotted line in figure 8.12(a)).

Error probability as a function of number of photons

First, we concentrate on the dependency of the error probability on the number of detected photons for both methods. In order to tune this number, R_{ens} and X_{SSR} were adapted. The results are plotted in figure 8.12(b). Here, the effect of imperfect initialisation on the discrimination error can be clearly seen. For $\phi_\Delta = \pi$, QPN vanishes and thus each photon should convey the same information, irrespective of whether using ensemble averaging or

the SSR method. The solid lines correspond to the theoretical expectations according to the equations 8.19 and 8.28. We find that the error probability obtained for SSR saturates around 20 %, which is due to the imperfect initialisation fidelity and thus cannot be further enhanced – even when recording more photons. In this case, only enhancing the initialisation fidelity, for example by applying charge state detection techniques [257] can bridge the gap between the error probabilities for the two readout strategies.

Error probability as a function of measurement time

Another very important resource is the total time T – including all the measurement overheads – needed for recording. For ensemble averaging each additional repetition requires another sensing period and thus the measurement time is proportional to the interaction duration T_{int} – plus an offset due to initialisation (t_{init}) and readout (t_{read}):

$$T_{\mathrm{ens}} = R_{\mathrm{ens}} \left(t_{\mathrm{init}} + T_{\mathrm{int}} + t_{\mathrm{read}} \right), \tag{8.32}$$

where $t_{\mathrm{init}} + t_{\mathrm{read}} \approx 1.5\,\mu\mathrm{s}$ for our experiments. SSR only requires one period of coherent interaction and most of the overheads arise from initialisation and readout of the memory:

$$T_{\mathrm{SSR}} = t_{\mathrm{init}}^{\mathrm{anc}} + T_{\mathrm{int}} + X_{\mathrm{SSR}} \cdot t_{\mathrm{read}}^{\mathrm{anc}}, \tag{8.33}$$

where $t_{\mathrm{init}}^{\mathrm{anc}} \approx 100\,\mu\mathrm{s}$ and $t_{\mathrm{read}}^{\mathrm{anc}} \approx 17\,\mu\mathrm{s}$ for our experiments. Thus, for $X_{\mathrm{SSR}} > 10$ most of temporal overheads is due to the repetitive readout.

The error as a function of T required for different T_{int} is plotted in figure 8.12(c). For ensemble averaging $R_{\mathrm{ens}} = 10^4$ was used and for SSR $R_{\mathrm{SSR}} = 1$ and $X_{\mathrm{SSR}} = 10^4$ in order to collect the same number of photons. The solid lines correspond to the expectation according to equations 8.19 and 8.28, where T_{int} is replace by T_{ens} and T_{SSR}.

For ensemble averaging the reduction of the discrimination error has the same shape as in figure 8.12(a) and for the optimal interaction time $T \approx 0.45\,\mathrm{s}$ are required. In contrast, the total recording time T is almost independent of T_{int} for SSR and the data points are all densely located close to $T = 0.17\,\mathrm{s}$. If the interaction time exceeds the time needed for one mapping operation (here 17 µs), it is less costly to collect an additional photon for SSR and the discrimination error reduces faster. The duration of the mapping is limited by the coupling between sensor and memory qubit. By using a more strongly coupled ancilla, the temporal overheads for SSR can be reduced. For NV centres the intrinsic ^{14}N nucleus allows CNOT gates on the order of 0.5 µs and the potential advantage is indicated by the orange line in figure 8.12(c). The discrimination error for multiple SSR experiments and the consequences of a reduced X_{SSR} are further discussed in [248].

Error probability as a function of number of trials

Finally, we compare the error probability as a function of the number of coherent interaction periods n for each strategy (figure 8.12(d)). This is relevant, if the sample degrades or is contaminated when measured and thus many interrogations are not possible. High confidence for a single interrogation can only be obtained with SSR, which thus performs significantly better. We find an exponential reduction of the probability to decide for the incorrect frequency as the number of tries is increased, however for the ensemble averaging with a much slower convergence. For small n the theoretically expected error can be computed numerically using equations 8.19 and 8.28 (solid lines in figure 8.12(d)). As a result, the error probability after eight measurements is reduced by approximately a factor of 10 compared to a single measurement for SSR. Further increasing to 15 measurements yields an about 100-fold reduction. Beyond that we found no incorrect decisions for any experimentally obtained subset anymore. Theoretically, the error probability approaches 10^{-3} and thus cannot be faithfully interrogated with the available data. For ensemble averaging almost $n = 10^4$ tries are required to reduce the discrimination error below 10 %.

8.5 Conclusion

A quantum mechanical detection scheme, optimised for discrimination of two frequency distributions, is introduced. The idea is based on driving the sensor state, depending on the present distribution, into one of two orthogonal bases. The sensor phase increases quadratically with coherent interaction time and the required time can be shorter than the Fourier limit. Neglecting further noise sources, this scheme in principle allows error-free discrimination after a single coherent interaction period. Taking additionally the photon shot noise related to the optical readout of a single NV centre into account, the performance of two strategies – ensemble averaging and single-shot readout – are compared with respect to the discrimination problem. It is shown that quantum mechanical projective measurements produce different measurement uncertainties to photon shot noise dominated measurements, which coincide only when the quantum projection noise is removed. As in more detail discussed in [248], the findings in this chapter can also be used to optimise frequency estimation protocols based on a single quantum coherent probe.

The presented results could find application in construction of diagnostic tests based on single quantum sensors and are especially useful for NMR, for which frequency distributions are usually well-known and the signal phase can be controlled [154,226]. If faced with a decision on how to allocate finite resources to construct better sensors, the presented results are relevant – in particular for nanoscale sensors based on single quantum spins.

9 Quantum spectrum analysis

Spectrum analysis is one of the most important tasks for the wide range of applications, for which periodic signals of magnetic, electrical, optical, acoustic or other nature are relevant. Spectra contain an enormous amount of information and for example allow to reconstruct any signal of interest. Therefore, high accuracy is essential for high informative value and correct result interpretation. Quantum sensors have certain advantages compared to classical devices and are indispensable if quantum effects or spatial resolution become important, as for nanoscale NMR [22, 23].

Thus, exploring the possibilities of using a quantum probe for spectrum analysis is highly interesting [155, 258]. The findings in chapter 7 show that the quantum heterodyne (Qdyne) principle is very similar to classical heterodyne detection, which is the basis of many present spectrum analysers. Although the Qdyne principle slightly differs from its classical analogue, it keeps the most important properties, namely down-conversion of high frequency signals to the detector bandwidth, sensor coherence independent resolution, and simultaneous detection of frequency, amplitude and phase.

While in chapter 7 the main focus is on the idea, the working principle and the improved frequency resolution, in the following the possibility of applying the Qdyne principle to spectrum analysis is discussed in more detail. In section 9.1 a measurement sequence is introduced, which is fundamentally different from dynamical decoupling and increases the maximal detectable frequency for NV centres to more than 100 GHz while maintaining the Hz to sub-mHz precision. After experimentally demonstrating the working principle in section 9.2, a magnetic AC field is characterised by estimating its amplitude, frequency and phase in section 9.3. Options to improve the sensitivity are discussed in section 9.4, before finally the dynamic and spectral bandwidth are analysed in section 9.5. Although the experimental realisations are based on single NV centres in diamond, the results are in principle applicable to other quantum platforms. Parts of the results presented in this chapter are accepted for publication [259].

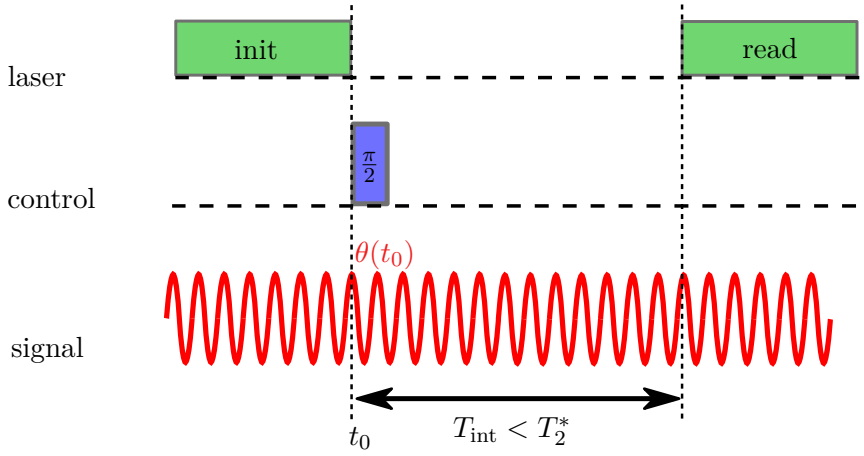

Figure 9.1: Sketch of measurement sequence. After initialisation of the sensor qubit, an optimally instantaneous control $\pi/2$-pulse around a fixed axis is applied. During the interaction with the signal the state further evolves, which can be depicted as another rotation on the Bloch sphere, for which the rotation axis depends on the signal phase $\theta(t_0)$ at time t_0 (compare section 9.1.2).

9.1 Measurement sequence and theoretical analysis

Measurement sequences which are sensitive to the phase of the signal of interest are the fundamental building block of the Qdyne principle (compare section 7.1). The idea introduced here is to show that the final sensor state when interacting with a near-resonant field can be tailored to depend not only on the strength and the frequency of this field but also on its phase θ. In section 2.5 it is shown, that a control signal resonant to the splitting of two sensor levels can be used to perform unitary rotations on the Bloch sphere and the rotation axis is determined by θ.

Analogously, an unknown oscillating field can initiate rotations if its frequency is near-resonant. It was recently shown, that this principle allows for nanoscale NMR experiments [260]. However, without further control, a measurement of the sensor population would be independent of θ due to the circular symmetry of the Bloch sphere. In the following, it is theoretically derived and experimentally shown that the application of an additional $\pi/2$-pulse with known phase, as sketched in figure 9.1, allows to break this symmetry.

As a result, repetitive measurements of this type can be correlated to record the temporal dependency of $\theta(T)$ with the total measurement time T and thereby find the signal frequency. By tailoring the sensor levels, the resonance condition can be adjusted. For NV centres, for example, the splitting of the spin levels depends on the external bias field, and 3.5 T corresponds to about 100 GHz [261, 262]. The interaction duration, however, is limited by the T_2^*-time.

9.1.1 Derivation of the population formula

The aim is to measure an oscillating field with coupling Ω and frequency ν, close to the transition frequency of the sensor ν_0. The corresponding Hamiltonian is:

$$\mathcal{H}(t) = \frac{h\nu_0}{2}\hat{\sigma}_z + \hbar\Omega \sin(2\pi\nu t + \theta)\hat{\sigma}_x. \tag{9.1}$$

Assuming that the frequency of the signal is almost resonant ($\nu \approx \nu_0$) and going into the rotating frame with respect to ν, $\mathcal{H}(t)$ reads after applying the rotating wave approximation (compare appendix A.3.1):

$$\mathcal{H}_{\text{int}}(t) = \frac{\hbar}{2}\begin{pmatrix} -2\pi\nu_\Delta & \Omega e^{-i\theta} \\ \Omega e^{i\theta} & 2\pi\nu_\Delta \end{pmatrix}, \tag{9.2}$$

where $\nu_\Delta = \nu - \nu_0$. In the following, it is for the moment assumed that $\nu_\Delta \ll \Omega/(2\pi)$ and thus can be neglected. Then $\mathcal{H}_{\text{int}}$ simplifies to:

$$\mathcal{H}_{\text{int}}(t) = \frac{\hbar\Omega}{2}\left(\cos(\theta)\hat{\sigma}_x + \sin(\theta)\hat{\sigma}_y\right), \tag{9.3}$$

and thus the time evolution is governed by:

$$\mathcal{U}_{\text{int}} = \exp\left(-i\frac{\Omega \cdot T_{\text{int}}}{2}\left(\cos(\theta)\hat{\sigma}_x + \sin(\theta)\hat{\sigma}_y\right)\right), \tag{9.4}$$

where T_{int} is the duration the sensor interacts with the signal of interest. This operator describes a rotation on the Bloch sphere by an angle proportional to $\Omega \cdot T_{\text{int}}$ around an axis in the $x-y-$plane defined by θ (compare section 2.5).

After initialising the quantum probe into one of its eigenstates we use a control $\pi/2$-pulse to bring it into a coherent superposition state and let it interact with the signal. The time evolution operator of the $\pi/2$-pulse is given by:

$$\mathcal{U}_{\pi/2}(t) = \frac{1}{\sqrt{2}}\begin{pmatrix} 1 & -\sin(\theta_{\pi/2}) - i\cos(\theta_{\pi/2}) \\ \sin(\theta_{\pi/2}) - i\cos(\theta_{\pi/2}) & 1 \end{pmatrix}, \tag{9.5}$$

where $\theta_{\pi/2}$ defines the angle of the $\pi/2$-rotation. If the quantum system is for example initialised in $|0\rangle$, we find after the combined time evolution $\mathcal{U} = \mathcal{U}_{\text{int}}\mathcal{U}_{\pi/2}$, the following probability $P_0 = |\langle 0|\mathcal{U}|0\rangle|^2$ to readout $|0\rangle$:

$$P_0 = \frac{1}{2}[1 - \sin(\Omega T_{\text{int}})\cos(\theta - \theta_{\pi/2})]. \tag{9.6}$$

Thus, P_0 has a sinusoidal dependency on θ. The amplitude of this oscillation is proportional to $\sin(\Omega T_{\text{int}})$ (see section 9.5 for a more in depth discussion). By using that the time evolution of $\theta(T)$ as a function of the total recording time T is $\theta(T) = 2\pi\nu T + \theta(T=0)$, it follows:

$$P_0(T) = \frac{1}{2}[1 - \sin(\Omega T_{\text{int}}) \cos\Big(2\pi\nu T + \theta(T=0) - \theta_{\pi/2}(T)\Big)]. \tag{9.7}$$

In the case the phase of the $\pi/2$-pulse is fixed in the rotating frame of the sensor qubit, meaning it evolves as $\theta_{\pi/2}(T) = 2\pi\nu_0 T + \theta_{\pi/2}(T=0)$ in the laboratory frame, it is:

$$P_0(T) = \frac{1}{2}[1 - \sin(\Omega T_{\text{int}}) \cos(2\pi\nu_\Delta T + \theta_0)], \tag{9.8}$$

where the initial phase is $\theta_0 = \theta(T=0) - \theta_{\pi/2}(T=0)$ and the detection frequency reads $\nu_\Delta = |\nu - \nu_0|$.

If the phase of the $\pi/2$-pulse is fixed in the laboratory frame ($\theta_{\pi/2}(T) = \theta_{\pi/2}(T=0)$), usually many signal periods are within T_{int} and a local oscillator frequency ν_{LO} identical to the one introduced in section 7.1.2 can be defined. Then, it follows:

$$P_0(T) = \frac{1}{2}[1 - \sin(\Omega T_{\text{int}}) \cos(2\pi(\nu_{\text{LO}} - \nu)T + \theta_0)]. \tag{9.9}$$

In principle, it is also possible to perform the control $\pi/2$-pulse after the interaction period, which is discussed in more detail in appendix A.3.6.

9.1.2 Illustrative explanation

After the rather mathematical description of the principle, in the following a more illustrative explanation on the Bloch sphere is given. The idea is to initialise the quantum sensor into the $|0\rangle$ state and then use an optimally instantaneous $\pi/2$-pulse.

As sketched in figure 9.2(a), in which this axis corresponds to the x-axis ($\theta_{\pi/2} = \pi$), the state vector of the qubit results on the y-axis through this rotation. During the interaction with the signal of interest, another rotation is performed, for example another $\pi/2$-rotation, and the rotation axis is defined by the signal phase θ.

If $\theta = \pi$, the rotational axes of the initial $\pi/2$-pulse and the $\pi/2$-rotation caused by the signal are identical and thus an effective π-rotation is performed and the final state is $|1\rangle$, as shown in figure 9.2(c). If $\theta = \pi/2$, the rotational axes are perpendicular and the signal effectively performs no rotation. The final state is then an equally populated superposition state. For any other θ, the probability of measuring $|0\rangle$ is given by equation (9.6). For three different rotation angles ($\Theta \in \{\pi/3, \pi/2, 2\pi/3\}$) the final states are shown for a variety of $\theta \in [0, 2\pi)$ in figure 9.2(b).

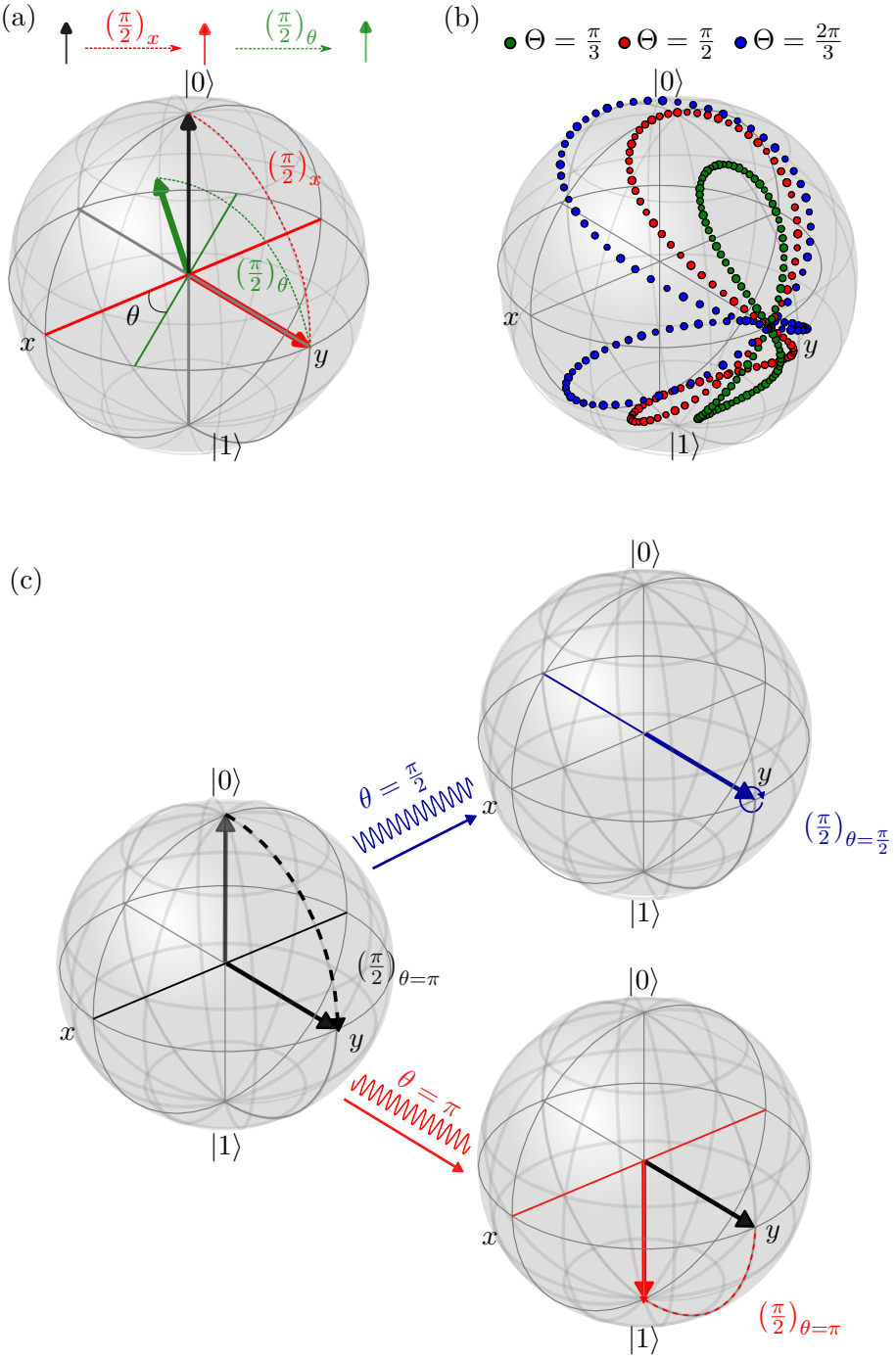

Figure 9.2: Illustration of the state evolution on the Bloch sphere. (a) After initialisation of the qubit into $|0\rangle$, a control $\pi/2$-pulse around a fixed axis (here x-axis) is applied. During the interaction with the signal another rotation (here $\pi/2$) is performed and the rotation axis depends on the signal phase θ. (b) The final states for various $\theta \in [0, 2\pi)$ with a spacing of $\Delta\theta = \pi/50$ are plotted for three different rotation angles Θ. For $\Theta = \pi/2$ the measurement contrast is maximal. (c) Evolution of the sensor state on the Bloch sphere for $\theta = \pi$ and $\theta = \pi/2$ ($\Theta = \pi/2$).

9.1.3 Non-negligible frequency detuning

In the case that ν_Δ is not negligible, the analysis is more complicated. For reasons of overview, the derivation is only briefly outlined and the full derivation can be found in [259]. Based on equation (9.2), the time evolution during the interaction with the signal is described by:

$$\mathcal{U}_{\text{int}} = \cos\left(\frac{\Omega_\text{R} T_\text{int}}{2}\right) \mathbb{1} - i \sin\left(\frac{\Omega_\text{R} T_\text{int}}{2}\right) \begin{pmatrix} -\frac{2\pi\nu_\Delta}{\Omega_\text{R}} & \frac{\Omega}{\Omega_\text{R}} e^{-i\theta} \\ \frac{\Omega}{\Omega_\text{R}} e^{i\theta} & \frac{2\pi\nu_\Delta}{\Omega_\text{R}} \end{pmatrix}, \tag{9.10}$$

where Ω_R is the generalised Rabi frequency (compare equation (2.31)):

$$\Omega_\text{R} = \sqrt{\Omega^2 + (2\pi\nu_\Delta)^2}. \tag{9.11}$$

Setting $\theta_\Delta = \theta - \theta_{\pi/2}$, the final population reads [259]:

$$P_0 = \frac{1}{2}\left[1 + \frac{4\pi\nu_\Delta\Omega}{\Omega_\text{R}^2} \sin\left(\frac{\Omega_\text{R} T_\text{int}}{2}\right)^2 \sin(\theta_\Delta) - \frac{\Omega}{\Omega_\text{R}} \sin(\Omega_\text{R} T_\text{int}) \cos(\theta_\Delta)\right], \tag{9.12}$$

and also oscillates with the phase of the signal θ. For $2\pi\nu_\Delta \ll \Omega$ it follows $\Omega_\text{R} \approx \Omega$ and equation (9.6) is recovered.

9.2 Experimental demonstration of the principle

For the experimental realisations, single NV centres in a 99.9999 % ^{12}C purified diamond (more detailed description in appendix A.1.5) were used as quantum probes. An AWG (Tektronics AWG70001A) performed the timing of the laser pulses and generated the control $\pi/2$-pulses.

9.2.1 Population as a function of the signal phase

We start our experimental analysis by measuring P_0 as a function of the signal phase θ with the aim to validate equation (9.6). As sketched in figure 9.3(a), another AWG (Tektronics AWG70001A) generated the sensing signal in order to have precise control over θ. For synchronisation of both devices TTL-triggers were used.

The strength of the $\nu \approx 1.5\,\text{GHz}$ signal resonant to the $m_\text{s} = 0$ and $m_\text{s} = -1$ sub-states was adjusted such that a $\pi/2$-rotation is performed during the interaction duration T_int. The detection frequency was chosen to be very small so that the signal phase changed by only about 0.10° for consecutive measurements. In order to cover a range larger than 2π, 5000 phase sensitive measurements were preformed in a row. We repeated this procedure

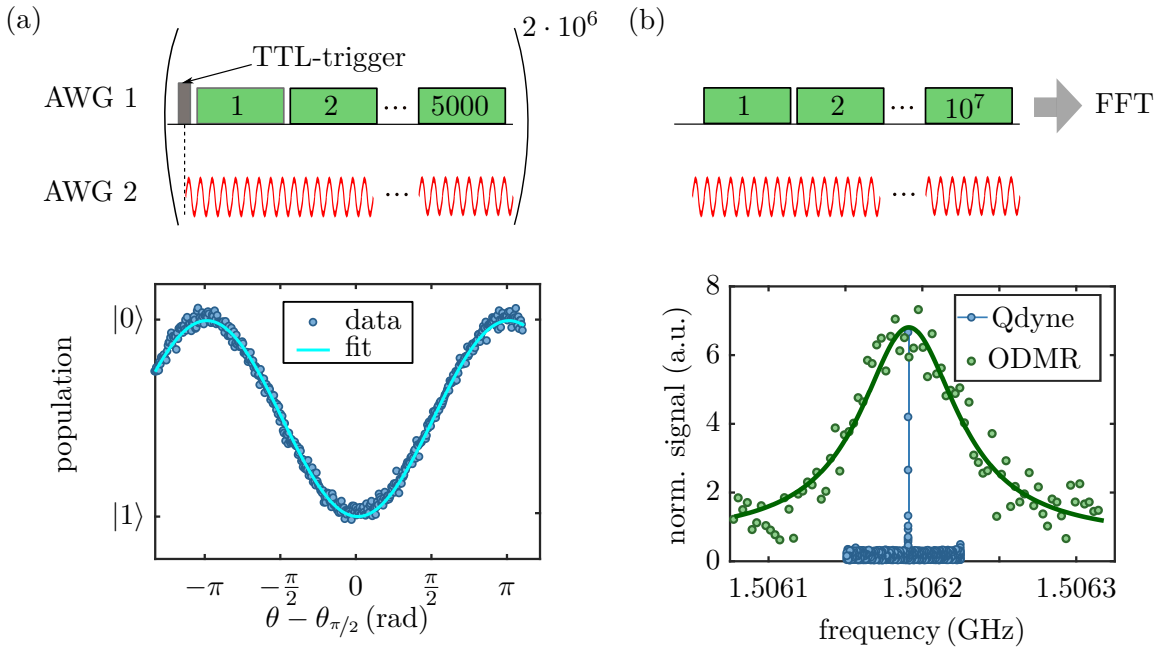

Figure 9.3: Experimental demonstration of the principle. (a) Sensor population as a function of signal phase θ. One arbitrary waveform generator (AWG1) is used to perform the control sequences (green boxes) sketched in figure 9.1 and a second AWG (AWG2) generates the signal (red line), which is probed with 5000 measurements per iteration. Synchronisation of both devices via a TTL-trigger pulse in the very beginning of every of the $2 \cdot 10^6$ repetitions, allows to sum up the individual results. A fit (light blue line) to the measured states verifies the expected sinusoidal behaviour. (b) Spectrum obtained by performing a FFT over the outcome of 10^7 measurements (blue data). It is compared to a sequentially recorded ODMR-like spectrum (green data, Lorentzian fit added).

about $2 \cdot 10^6$ times. Since both AWG were synchronised, $\theta(T)$ was identical for every iteration and thus averaging is possible. After summing up all the photons recorded during the $2 \cdot 10^6$ iterations, the plot in figure 9.3(a) was obtained (only every tenth data point is plotted for reasons of overview). As expected, P_0 has a sinusoidal dependency on θ. The light blue line represents a fit according to equation (9.6) through the data.

9.2.2 Frequency spectrum

Next, we use these phase-sensitive measurements to obtain a spectrum by applying the Qdyne principle. For a magnetic field oscillating close to 1.5 GHz and generated by an independent signal generator, we used 10^7 times the technique sketched in figure 9.1. The data recording and the analysis follow the description in section 7.1.3 and the obtained FFT of the data recorded in about 120 s is shown in figure 9.3(b). There is a clear peak at the expected frequency with a width of just about 15 mHz, which corresponds to the eleventh fractional digit of the 1.5 GHz signal frequency.

Traditionally, spectroscopy in the gigahertz range can also be performed with the ODMR technique described in section 4.1. By successively shifting the qubit levels, different frequency components are sampled and a spectrum can be obtained. Instead of changing these levels, an equivalent spectrum was recorded by changing the frequency of a test signal. The result is also added to figure 9.3(b) including a Lorentzian fit (green data). The width of the line obtained hereby is given by the inverse of the interaction time, which would be eventually limited by the T_2^*-time of the quantum sensor. For the measured NV centre, $1/T_2^* \approx 100\,\mathrm{kHz}$, which is about seven orders of magnitude larger than the linewidth obtained with Qdyne after 120 s.

9.2.3 Signals with multiple spectral components

The evolution of the quantum state for a signal with a single frequency under the introduced protocol is extensively discussed in section 9.1. However, a field of interest might have multiple frequency components. In the following this case is examined in more detail. The Hamiltonian of a signal with N spectral components can be written as:

$$\mathcal{H} = \frac{h\nu_0}{2}\hat{\sigma}_z + \sum_{n=1}^{N}\left[\hbar\Omega_n \sin\left(2\pi\nu_n + \theta_n\right)\hat{\sigma}_x\right], \tag{9.13}$$

where Ω_n, ν_n and θ_n are the respective coupling strengths, frequencies and phases. In the rotating frame with respect to the resonance frequency ν_0 of the sensor $\mathcal{H}_{\mathrm{int}}$ reads:

$$\mathcal{H}_{\mathrm{int}}(t) = \frac{\hbar}{2}\begin{pmatrix} 0 & \sum_{n=1}^{N}\Omega_n \mathrm{e}^{-i(2\pi\nu_{\Delta,n}t+\theta_n)} \\ \sum_{n=1}^{N}\Omega_n \mathrm{e}^{i(2\pi\nu_{\Delta,n}t+\theta_n)} & 0 \end{pmatrix}, \tag{9.14}$$

where $\nu_{\Delta,n} = \nu_n - \nu_0$. Finding an analytical solution is very challenging due to the explicit time-dependency of this Hamiltonian. Therefore, the assumption $\forall\nu_{\Delta,n} \ll \forall\Omega_n/(2\pi)$ is applied, which especially makes $\mathcal{H}_{\mathrm{int}}$ time-independent:

$$\mathcal{H}_{\mathrm{int}} = \sum_{n=1}^{N}\left[\frac{\hbar\Omega_n}{2}\left(\cos\left(\theta_n\right)\hat{\sigma}_x + \sin\left(\theta_n\right)\hat{\sigma}_y\right)\right]. \tag{9.15}$$

Reordering all terms with respect to $\hat{\sigma}_x$ and $\hat{\sigma}_y$ yields:

$$\mathcal{H}_{\mathrm{int}} = \sum_{n=1}^{N}\left[\frac{\hbar\Omega_n}{2}\cos\left(\theta_n\right)\right]\hat{\sigma}_x + \sum_{n=1}^{N}\left[\frac{\hbar\Omega_n}{2}\sin\left(\theta_n\right)\right]\hat{\sigma}_y = \frac{1}{2}\left(\Omega_x\hat{\sigma}_x + \Omega_y\hat{\sigma}_y\right), \tag{9.16}$$

where $\Omega_x = \sum_{n=1}^{N}\left[\hbar\Omega_n\cos\left(\theta_n\right)\right]$ and $\Omega_y = \sum_{n=1}^{N}\left[\hbar\Omega_n\sin\left(\theta_n\right)\right]$ is defined.

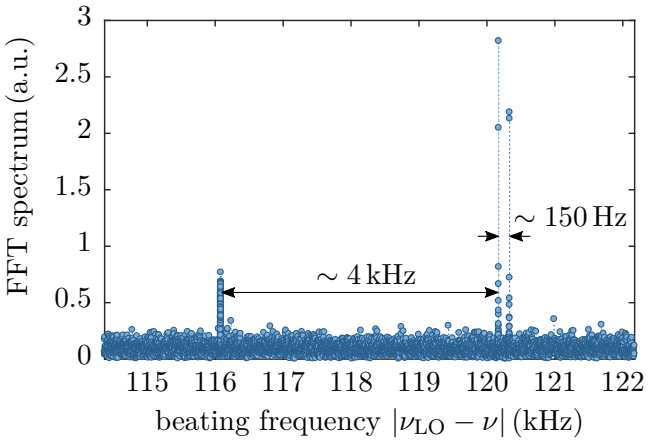

Figure 9.4: Spectroscopy of a magnetic field with three frequency components. All three frequencies are revealed in the FFT spectrum. For reasons of overview only the relevant part of the spectrum is shown. Adapted with permission from [259]. Copyright 2021 by the American Physical Society.

This Hamiltonian describes a single rotation on the Bloch sphere with rotation angle and axis depending on Ω_x and Ω_y. If the sensor is initialised in $|0\rangle$, the probability P_0 to finally measure $|0\rangle$ reads:

$$P_0 = \frac{1}{2} - \frac{1}{2\Omega_\mathrm{e}} \left[\Omega_y \cos\left(\theta_{\pi/2}\right) - \Omega_x \sin\left(\theta_{\pi/2}\right)\right] \sin\left(\Omega_\mathrm{e} T_\mathrm{int}\right), \tag{9.17}$$

where

$$\Omega_\mathrm{e}^2 = \Omega_x^2 + \Omega_y^2. \tag{9.18}$$

Thus, P_0 is a sum of sinusoidal functions and all frequency components should be revealed when performing a FFT. In order to show these findings experimentally, we combined the output of three independent signal generators, each generating a signal with slightly different frequency. The resulting FFT is plotted in figure 9.4. As expected, all three frequency components are revealed in the spectrum. If the assumption $\forall\nu_{\Delta,n} \ll \forall\Omega_n/(2\pi)$ does not hold, $\mathcal{H}_\mathrm{int}$ is time-dependent and further analysis is required.

9.2.4 Interactions during initialisation and readout

Unlike signals recorded with DD, for which the sensor population only changes if the control sequence is applied, a resonant field alters the sensor state on its own. This might be a problem, since these unwanted interactions can reduce the initialisation and readout fidelity and thus negatively influence the measurement performance.

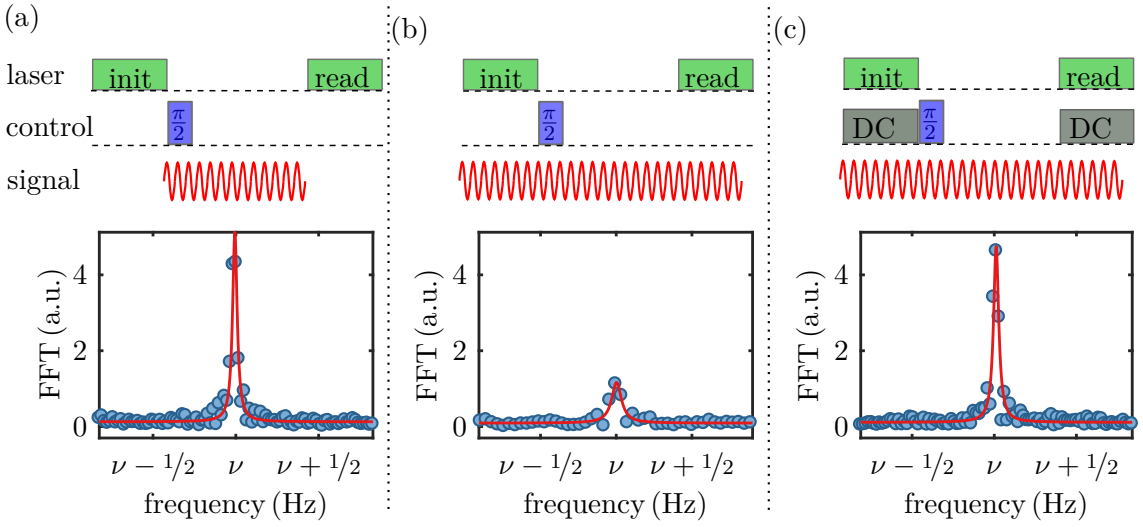

Figure 9.5: Spectra recorded under different readout and initialisation conditions. (a) Qdyne spectrum, when the signal was turned off during initialisation and readout period. (b) Fourier spectrum, when recording a continuous signal. The interactions with the qubit during initialisation and readout reduce the measurement contrast. (c) This loss of sensitivity can be recovered by shifting the energy levels of the qubit by applying an additional DC field during initialisation and readout period. Adapted with permission from [259]. Copyright 2021 by the American Physical Society.

For an artificial test signal the interaction time can be controlled, for example using switches. However, in a real-world application switching the signal on and off by request is usually not possible. In order to examine the influences, Qdyne spectra were recorded for two different scenarios. In the first scenario, the signal was turned off during initialisation and readout, whereas for the second scenario, an identical signal was continuously turned on. The results are plotted in figure 9.5(a) and 9.5(b). As expected, the heights of the observed FFT peaks differ. The peak obtained, after recording the pulsed signal, is about four times higher. Since the SNR scales as square root of the total measurement time, this corresponds to an about 16 times longer recording duration.

The idea to solve this problem is to apply a DC magnetic field during the initialisation and readout period. This DC magnetic field shifts the qubit levels and if strong enough detunes them and the signal out of resonance. Then the quantum probe is insensitive to this signal during the time this additional DC magnetic field is applied. Experimentally, we realised the DC field by sending a DC current through the same copper wire which was used for the remaining control pulses. By using a fast switch we were able to turn it on and off within less than 20 ns. To experimentally demonstrate the working principle, a current which shifted the energy difference of our qubit levels by approximately 3 MHz, as shown in figure 9.6, was applied. This shift was enough to eliminate the interaction

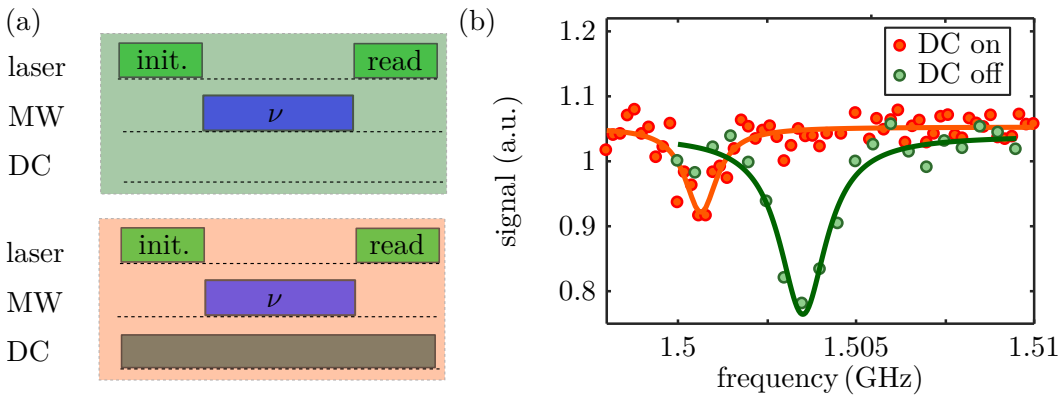

Figure 9.6: Shifting the resonance frequency using a DC current. (a) Sequences of a traditional pulsed ODMR measurement (top panel) and a pulsed ODMR measurement with an additional magnetic field generated by a DC current (bottom panel). (b) The DC field shifts the qubit levels by about 3 MHz compared to the unperturbed spectrum (green data). Solid lines are Lorentzian fits to the data.

between sensor and signal almost completely. The resulting FFT spectrum is plotted in figure 9.5(c). We observe about the same contrast as for the pulsed signal.

9.3 Signal reconstruction

In time-domain, a periodic signal can be described as a sum over all its components:

$$B(t) = \sum_n B_n \sin\left(2\pi\nu_n t + \theta_n\right), \tag{9.19}$$

where B_n are the amplitude, ν_n the frequency and θ_n the phase parameters. The task for reconstructing a signal of interest, is to find these parameters. While many other techniques are limited to estimate either the frequency or the amplitude [263, 264], and often only work well if the other parameters are known precisely, the advantage of Qdyne is that a Fourier spectrum of the signal can be obtained. Analysing and interpretation of a FFT is a fundamental and well-studied problem and in the following the basics are briefly summarised and exemplified for our experimental data. For this purpose a magnetic field oscillating with a single frequency at $\nu = 1.510\,82\,\mathrm{GHz}$ was recorded by performing a measurement every 3.38 µs. The interaction time was $T_{\mathrm{int}} = 1.4\,\mu\mathrm{s}$ and the remaining time is due to overheads.

Amplitude estimation

The amplitude spectrum can be obtained by computing the absolute value of the complex discrete Fourier transform $\mathcal{F}(\nu)$:

$$|\mathcal{F}(\nu)| = \sqrt{\mathrm{Re}(\mathcal{F}(\nu))^2 + \mathrm{Im}(\mathcal{F}(\nu))^2}. \tag{9.20}$$

For our data, as shown in the amplitude spectrum after 2 s in figure 9.7(a), there is only one peak in $|\mathcal{F}(\nu)|$. The height of the peak is a measure for the strength of the magnetic field and for conversion, we used a calibration signal with very precisely known field strength.

One problem with the discrete nature of the recording is that the obtained spectrum is discrete as well. The discretisation depends on the sample rate and the total number of sampling points. Thus, it is not unlikely that the actual frequency is in between two frequency points of the FFT spectrum. In order to obtain a continuous spectrum, several surrounding bins and a suitable function can be used for interpolation [265, 266]. For our analysis, all amplitude spectra were fitted using Lorentzian functions in order to obtain the respective parameters. Their uncertainties (correspond to the error bars) were estimated using 95 % confidence intervals. For the test signal, the estimated field strength B_1 is plotted for different total recording times T in figure 9.7(c). The uncertainty ΔB_1 in estimating B_1 as a function of T is plotted in figure 9.7(d). As expected, ΔB_1 reduces as $\sqrt{T}$ since the SNR improves as $\sqrt{T}$. After a total recording time of $T = 120\,\mathrm{s}$ we

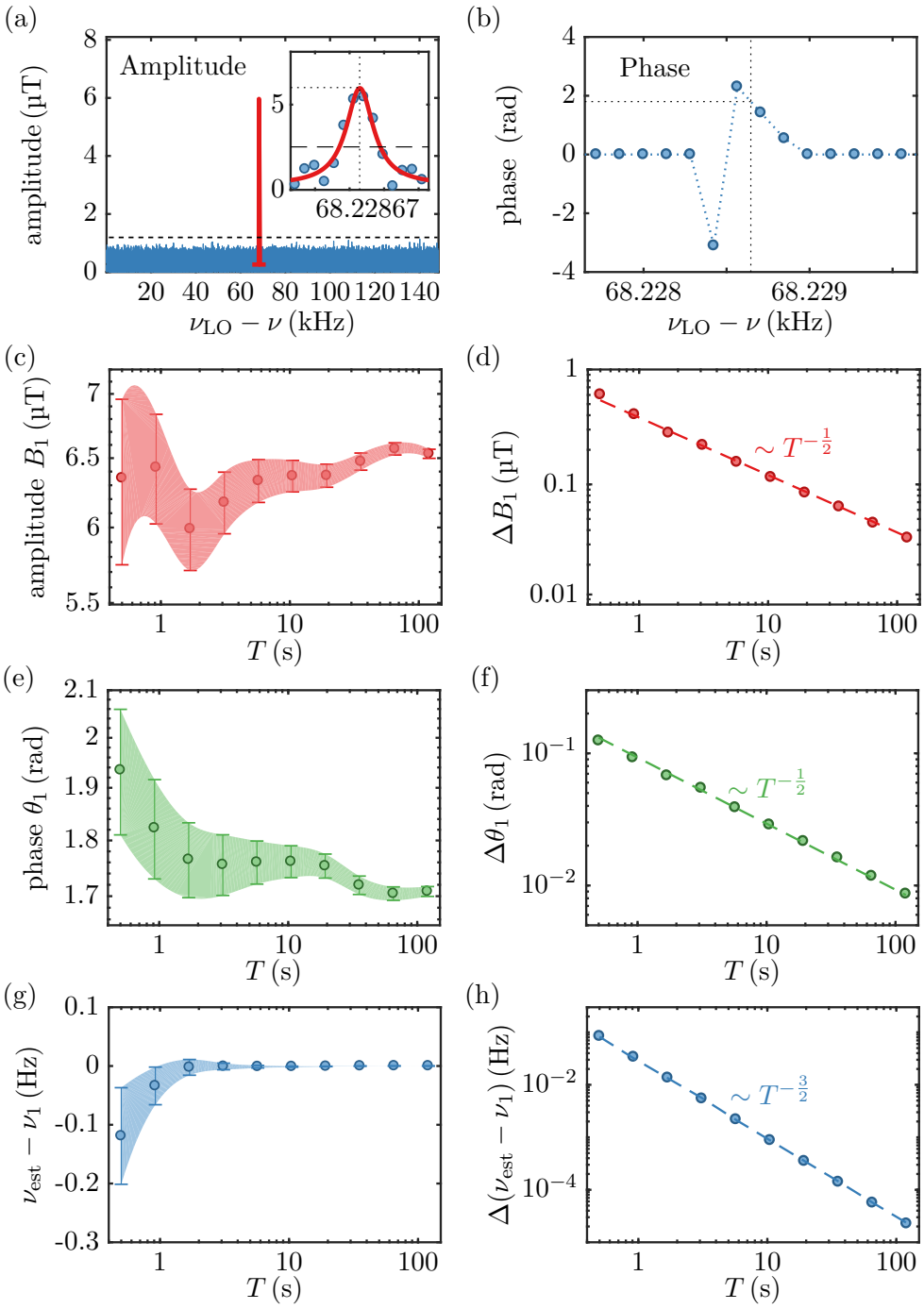

Figure 9.7: Experimental determination of the signal parameters. Amplitude (a) and phase spectrum (b) obtained from the complex FFT. Estimate of the signal amplitude B_1 in (c), signal phase θ_1 in (e) and deviation of the estimate frequency ν_{est} from the signal frequency ν_1 in (g) as a function of total recording time T. While the uncertainties for amplitude estimation ΔB_1 in (d) and phase estimation $\Delta\theta_1$ in (f) reduce as $\sqrt{T}$, the uncertainty $\Delta(\nu_{est} - \nu_1)$ in (h) decreases as $T^{-1.5}$. Adapted with permission from [259]. Copyright 2021 by the American Physical Society.

were able to reduce ΔB_1 to about 30 nT. This corresponds to an amplitude sensitivity of $\eta_B \approx 330\,\mathrm{nT}/\sqrt{\mathrm{Hz}}$.

Frequency estimation

To estimate the frequency, the same amplitude spectrum and Lorentzian fits can be used to find the position of the peak maximum ν_{est}. The obtained deviation from the real signal frequency ν_1 is plotted in figure 9.7(g). The difference quickly decays and the uncertainty, again obtained finding the 95 % confidence intervals, reduces as $T^{-1.5}$ to about 23 µHz for $T = 120\,\mathrm{s}$ (see figure 9.7(h)). The reasons are the same as the ones extensively discussed in section 7.2.3.

Phase estimation

The phase spectrum is given by the argument of the complex FFT:

$$\measuredangle\mathcal{F} = \mathrm{arctan2}\left(\frac{\mathrm{Im}(\mathcal{F})}{\mathrm{Re}(\mathcal{F})}\right), \tag{9.21}$$

where arctan2 takes into account that the traditional arctangent returns only values in the $[-\pi/2, \pi/2]$ interval.

Since equation (9.21) depends on the ratio of imaginary and real part, even points with a tiny absolute value can have a significant contribution. Ignoring all the points below the threshold indicated by the dashed line in the inset of figure 9.7(a), the phase spectrum after $T = 2\,\mathrm{s}$ is shown in figure 9.7(b). By using a linear interpolation to extract the signal phase θ_1, our estimate is plotted as a function of the total recording time T in figure 9.7(e). The uncertainty $\Delta\theta$, which is displayed in figure 9.7(f), was obtained using 95 % confidence intervals and reduces as $\sqrt{T}$ due to the improved SNR. After $T = 120\,\mathrm{s}$ we were able to estimate the phase down to $\Delta\theta_1 = 0.49°$. The resulting phase sensitivity reads $\eta_\theta = \Delta\theta_1\sqrt{T} \approx 5.4\,°/\sqrt{\mathrm{Hz}}$. One should note that for a detuned signal the estimated phase might be different from the real signal phase, which is in more detail discussed in [259].

9.4 Improving the sensitivity

In the following, two techniques to improve the amplitude estimation are discussed. First, the possibility to perform single-shot readout (SSR) is examined and second, a decoupling technique is used to extend the interaction time.

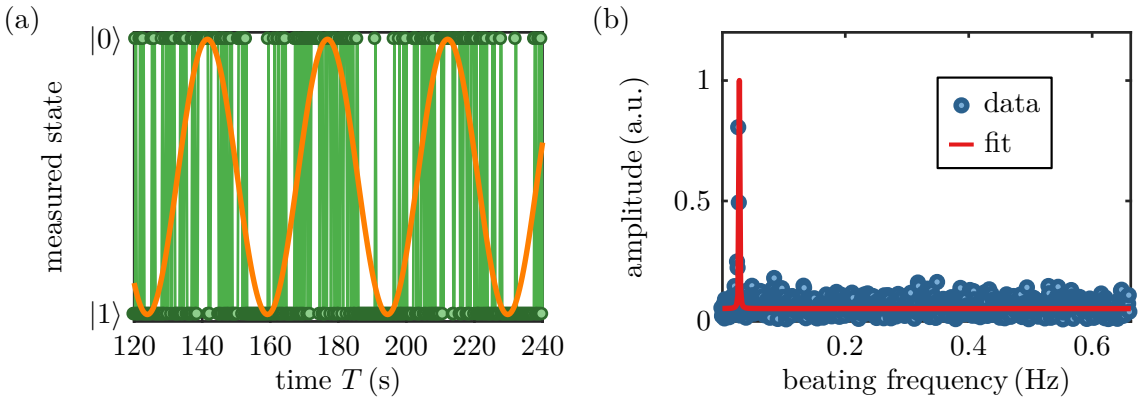

Figure 9.8: Time trace and FFT for Qdyne recorded with SSR. (a) Segment of a time trace recorded via a Qdyne-type measurement using SSR. The distribution of data points is probabilistically either $|0\rangle$ or $|1\rangle$ depending on the final sensor state. There a many quantum jumps if $P_0 \approx 0.5$ and only a few of $P_0 \approx 0$ or $P_0 \approx 1$. The bias towards recording $|1\rangle$ is due to charge state conversion processes. A sinusoidal fit to the data is added as orange line. (b) Spectrum obtained via FFT of the full time trace. The red line is a Lorentzian fit to the data.

9.4.1 Qdyne spectroscopy using single-shot readout

One option to improve the SNR is to reduce the measurement noise. As discussed in section 8.4.2, SSR uses quantum non-demolition measurements to practically eliminate the photon shot noise (PSN) due to the optical readout. Then only the fundamentally limiting quantum projection noise (QPN) remains. The cost is a highly increased readout time.

Prove of principle

In order to perform SSR, the same NV centre, ^{13}C nuclear memory and protocol as described in section 8.4.2 were used. Under an external magnetic bias field of around 420 mT aligned along the symmetry axis of the NV centre, an artificial signal oscillating close to $\nu \approx 1.692$ GHz was recorded for 720 s using Qdyne and SSR ($X_{\mathrm{SSR}} = 6500$).

The individual outcomes are displayed as function of the recording time T in figure 9.8(a). For reasons of overview only a part of the full data is presented. This time trace is fundamentally different from the traditional readout (compare figure 7.3). Instead of recording mostly zero or one photons, many photons are recorded and, if the recording duration is long enough, every measurement outcome can be assigned to a certain state (compare figure 8.9(a)).

Then, the beating associated to the Qdyne technique is more obviously imprinted in the time trace. If the final sensor population is close to $P_0 \approx 1$, it is highly probable to

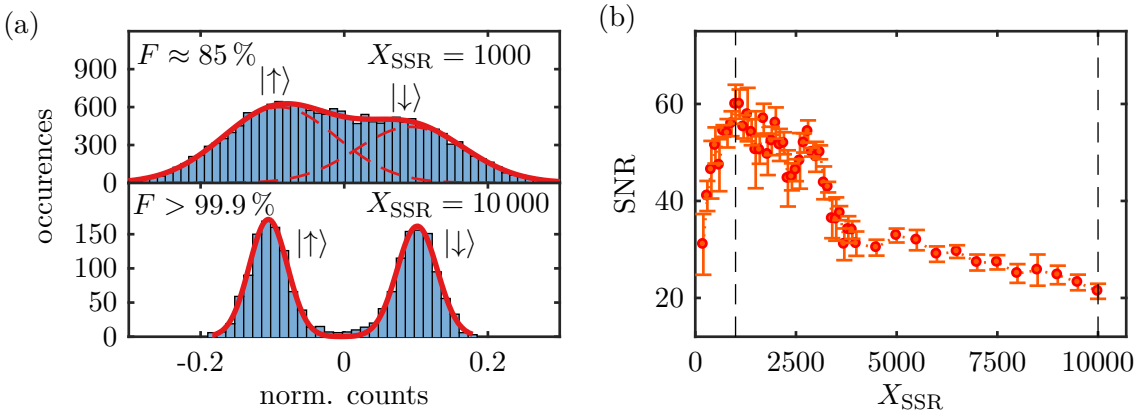

Figure 9.9: SNR in dependence of the number of repetitive readouts. (a) Upper panel: Histogram for $X_{\mathrm{SSR}} = 1000$, lower panel: Histogram for $X_{\mathrm{SSR}} = 10\,000$. The fidelity F of state assignment depends on the overlap of both distributions. Gaussian fits are added to the data (red lines). (b) SNR as a function of X_{SSR}. For this experiment, the SNR is highest for $X_{\mathrm{SSR}} \approx 1000$.

measure state $|0\rangle$. On the contrary, if the final state is $P_0 \approx 0$, mostly $|1\rangle$ is measured. Both outcomes are equally probable for $P_0 \approx 0.5$ and there are a lot of quantum jumps between consecutive measurements. There is a bias towards recording $|1\rangle$ in our experiments, which is due to charge state conversion processes between NV^- and NV^0 [257] (see section 8.4.2 for a more detailed discussion). A sinusoidal fit (orange line) reveals the same beating frequency of about 28 mHz as the FFT of the full data set ($T = 720\,\mathrm{s}$), shown in figure 9.8(b).

Sensitivity as a function of the SSR readout duration

A free parameter is the number of repetitive readouts X_{SSR} per SSR, which should be chosen such that the resulting SNR is maximal. After every SSR measurement the number of detected photons needs to be assigned to a state. The fidelity of this assignment is limited by PSN and depends on X_{SSR} as shown in figure 9.9(a). For example, the readout fidelity is around 85 % for $X_{\mathrm{SSR}} \approx 1000$, while it is $> 99.9\,\%$ for $X_{\mathrm{SSR}} \approx 10\,000$. Although the fidelity increases with X_{SSR}, the overall SNR can be reduced due to the extended time required for every readout (compare equation (8.33)). Thus, a compromise between those two opposing scalings has to be found. In order to experimentally examine the optimal X_{SSR} for our case, Qdyne spectra for various X_{SSR} were recorded ($T_{\mathrm{total}} = 720\,\mathrm{s}$). For statistical reasons every measurement was repeated four times. From the obtained FFT spectra, the SNR of each spectrum was obtained. The averaged SNR data are shown in figure 9.9(b) and the errorbars correspond to the standard deviation.

As expected, for very small X_{SSR} the fidelity of assignment is poor and the SNR strongly increases with X_{SSR}. At some point, however, the improved readout fidelity is compensated by the elevated measurement time and the SNR decreases slowly. We find an optimal point at around $X_{\mathrm{SSR}} \approx 1000$. This number of course depends on the exact setup parameters and might differ for a different setting.

Comparison of SSR and traditional readout

In order to compare the performance between SSR and traditional readout, a similar signal was recorded once with each technique. Including the overhead for initialisation and readout we could perform a measurement approximately every 4 µs using the traditional readout. Due to the increased readout duration ($X_{\mathrm{SSR}} = 1000$) one SSR measurement could be achieved only every 0.04 s. This corresponds to an about 10^4 times lower sampling rate, however, partially compensated by obtaining much more meaningful data.

While we find SNR ≈ 100 for the traditional readout after $T = 100\,\mathrm{s}$, we obtain only SNR ≈ 25 after $T = 720\,\mathrm{s}$ for SSR. Taking the typical $\sqrt{T}$-scaling into account this corresponds to a 11-fold reduction of the sensitivity. However, SSR becomes more effective if the interaction time T_{int} is increased. While the sampling rate for the SSR mainly depends on the readout duration and is almost independent of the interaction time, the sampling rate for the traditional readout reduces almost linearly if T_{int} increases. By prolonging the interaction time or decreasing the SSR readout duration, for example by using a more strongly coupled memory, the performance difference becomes smaller and at some point SSR can be superior.

9.4.2 Enhanced sensitivity through decoupling

If the two levels of the qubit are used to measure a weak resonant field, the time of coherent interaction T_{int} is usually limited by the T_2^*-dephasing time. As a consequence, the accuracy of estimating the amplitude is restricted by T_2^*, which for NV centres is usually just a few microseconds. Although the problem with the low frequency resolution can be solved applying the Qdyne technique, the precision for amplitude estimation, which improves as $\sqrt{T_{\mathrm{int}}}$ [4], is still unchanged. Recently, it has been shown that it is possible to extend T_{int} for these problems [263, 264]. The idea is to decouple the sensor from time-independent and slowly fluctuating noise while maintaining its sensitivity for the field of interest. The decoupling techniques can be based on both continuous driving [263] or pulsed dynamical decoupling [264]. In the following, it is examined if these protocols are adaptable to the Qdyne principle, for which it is important that the outcome of a

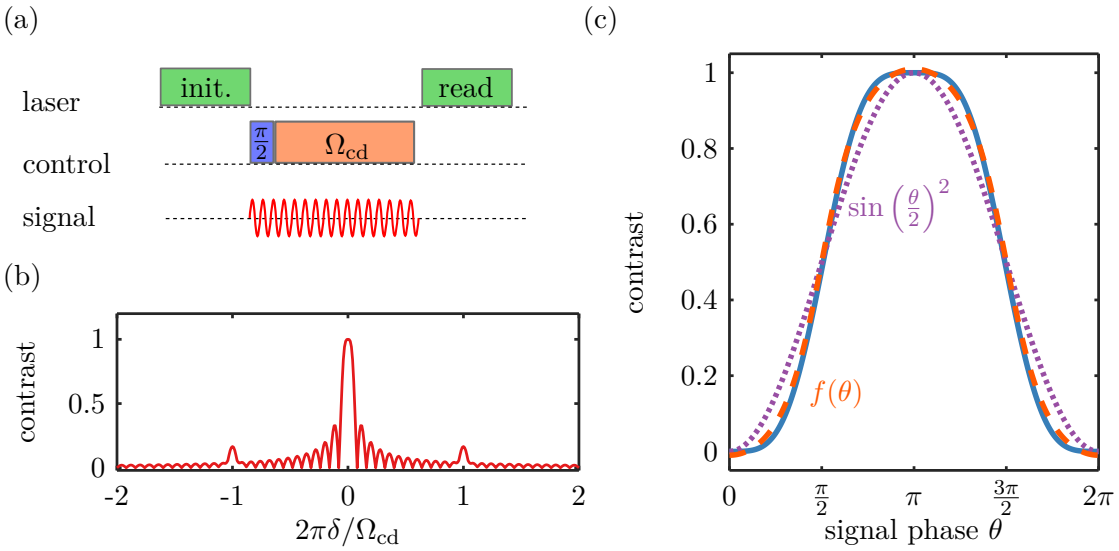

Figure 9.10: Principles of Qdyne based on decoupling through coherent driving. (a) Sketch of pulse sequence. (b) Simulated contrast as function of detuning δ. There are three resonance lines representing a Mollow triplet. (c) Simulated contrast as a function of the signal phase θ for $\delta = 0$ (blue solid line). The dependency is almost sinusoidal (purple dotted line), and can be well approximated by $f(\theta) = \sqrt{\left(\frac{2}{\pi}\right)^3} \arctan\left(-\frac{\pi}{2}\cos(\theta)\right) + \frac{1}{2}$ (orange dashed line, empirically found).

measurement depends on the signal phase. We concentrate on the continuous driving case, but the findings in principle also apply to the DD version.

Principle

The protocol, which is sketched in figure 9.10(a), is very similar to the technique used in [263]. After initialisation and a $\pi/2$-pulse, a resonant continuous driving field with coupling strength Ω_{cd} and with the same phase as the $\pi/2$-pulse is used to decouple the sensor from environmental noise. Unlike in [263], there is no final $\pi/2$-pulse before the readout. The reason for this modification is that in [263] the protocol was tailored to be independent of the signal phase θ. Then averaging over multiple iterations does not require phase locking. However, this behaviour is in contrast to the Qdyne principle.

If the interaction time is chosen appropriately, namely $\Omega_{cd} \cdot T_{int} = n \cdot 2\pi$ $(n \in \mathbb{N})$, the sensor is driven to return precisely to its starting state. The measurement contrast as a function of the signal frequency detuning $\delta = \nu - \nu_{driv}$ was simulated numerically. For this simulation the driving field was chosen to be 20 times stronger than the signal. The result in figure 9.10(b) shows that there are three resonance lines – a large one centred

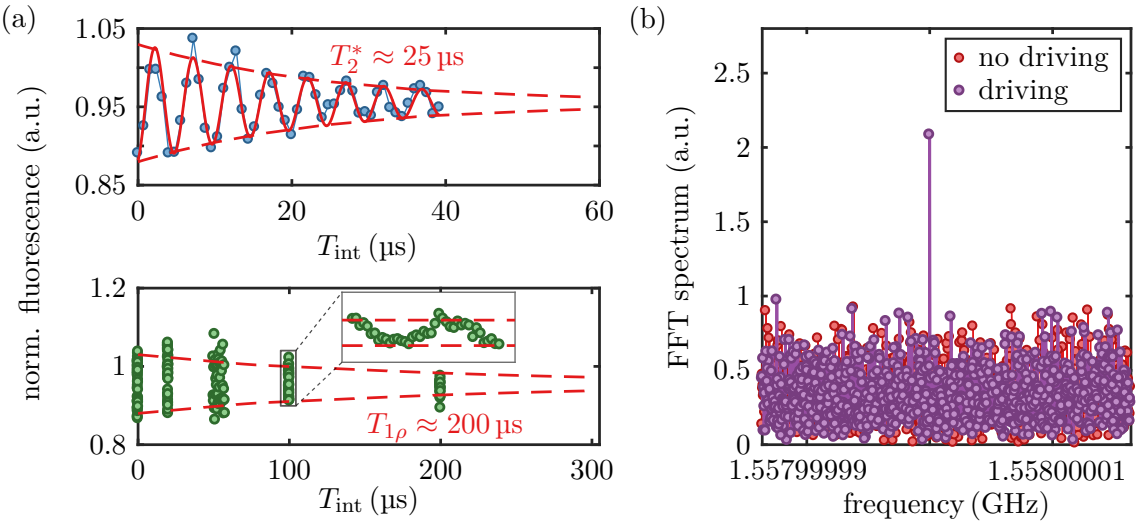

Figure 9.11: Qdyne based on decoupling through coherent driving. (a) The decay of a Ramsey type experiment reveals the T_2^* dephasing time of the sensor (upper panel). The interaction time can be prolonged to the much longer spin locking time $T_{1\rho}$ using a strong driving field. As shown in the lower panel, Rabi oscillations with a reasonable contrast are still observable after $T_{\text{int}} = 100\,\mu s$. (b) For an interaction time of $T_{\text{int}} = 100\,\mu s$, the Qdyne experiment with coherent driving (purple data) shows a clear peak at the signal frequency in contrast to the one without driving (red data).

around $\delta = 0$ and two smaller ones centred around $\delta = \pm\Omega_{\text{cd}}/(2\pi)$ – which represent a Mollow triplet [267]. The linewidths are proportional to the inverse of T_{int}.

For this protocol the measurement outcome depends on θ, which is shown in figure 9.10(c) for $\delta = 0$. Although the phase dependency is not perfectly sinusoidal, in the following, we concentrate on this central peak since the sensitivity is highest.

All conclusions here are based on simulations and finding analytical expressions remains an open task. Also, applying two driving fields to further decouple the sensor from noise in the first driving field as realised in [263] might be interesting.

Experimental realisation

We start our analysis by showing that we can indeed increase the interaction time T_{int} using this kind of decoupling. Therefore, we first use basic Ramsey interferometry to probe the T_2^* decay time (compare section 4.5.4). The result is presented in the upper panel of figure 9.11(a). From the decaying oscillations, $T_2^* \approx 25\,\mu s$ can be obtained. We compare this result to the decay of the Rabi oscillations caused by a strong driving field with $\Omega_{\text{cd}} = 2\pi \cdot 3.75\,\text{MHz}$ (lower panel figure 9.11(a)). Oscillations with a reasonable contrast are still detectable after interaction times exceeding $100\,\mu s$, since the sensor is decoupled from low frequency noise sources (decay time $T_{1\rho} \approx 200\,\mu s$).

Finally, we focus on using this enhanced coherence time to perform Qdyne spectroscopy with a higher amplitude sensitivity. The same 36 nT signal with frequency $\nu = 1.558\,\mathrm{GHz}$ was measured using the Qdyne techniques with (same $\Omega_{\mathrm{cd}} = 2\pi \cdot 3.75\,\mathrm{MHz}$) and without decoupling for $T = 30\,\mathrm{s}$ and $T_{\mathrm{int}} \approx 100\,\mu\mathrm{s}$. The relevant parts of the obtained spectra are displayed in figure 9.11(b). As expected, for the Qdyne experiment measured without decoupling (red data), there is no signal in the FFT spectrum. In contrast, there is a clear peak in the spectrum of the Qdyne realisation with coherent driving (purple data). For the presented data, we find a sensitivity of about $16\,\mathrm{nT}/\sqrt{\mathrm{Hz}}$.

9.5 Bandwidth of the quantum spectrum analyser

Other important properties of a spectrum analyser are the spectral and dynamic bandwidths, which define the ranges of frequencies and amplitudes that can be measured unambiguously within a single experiment.

9.5.1 Dynamic bandwidth

The dynamic bandwidth determines which field amplitudes can be resolved unambiguously. As shown above, the coupling Ω of the signal to the quantum sensor defines the angle of rotation $\Theta = \Omega \cdot T_{\mathrm{int}}$. If $2\pi(\nu - \nu_0) \ll \Omega$, the obtained peak height C in the FFT spectrum scales as (compare equation (9.6)):

$$C \sim |\sin(\Omega T_{\mathrm{int}})| = |\sin(\Theta)|. \tag{9.22}$$

Due to the periodicity in equation (9.22), the following Θ yield the same C:

$$\Theta = \frac{\pi}{2} \pm \delta_\Phi + n \cdot \pi, \tag{9.23}$$

where $\delta_\Phi \in [0, \pi/2]$ and $n \in \mathbb{N}$.

For example, a $\pi/2$-rotation and a $3\pi/2$-rotation or any other half integer of π entail the same C. Thus, only if the rotation angle Θ is known within $\pi/2$, it can be identified uniquely.

This can be experimentally observed by performing Qdyne spectroscopy for a variety of Θ. In order to change Θ, we recorded the same signal ($\Omega \approx 2\pi \cdot 0.5\,\mathrm{MHz}$) for various T_{int}. The obtained peak heights in the resulting FFT spectra are plotted in figure 9.12(a), together with the theoretical curve according to equation (9.22) (red solid line). As expected, there are several T_{int} for which C is identical.

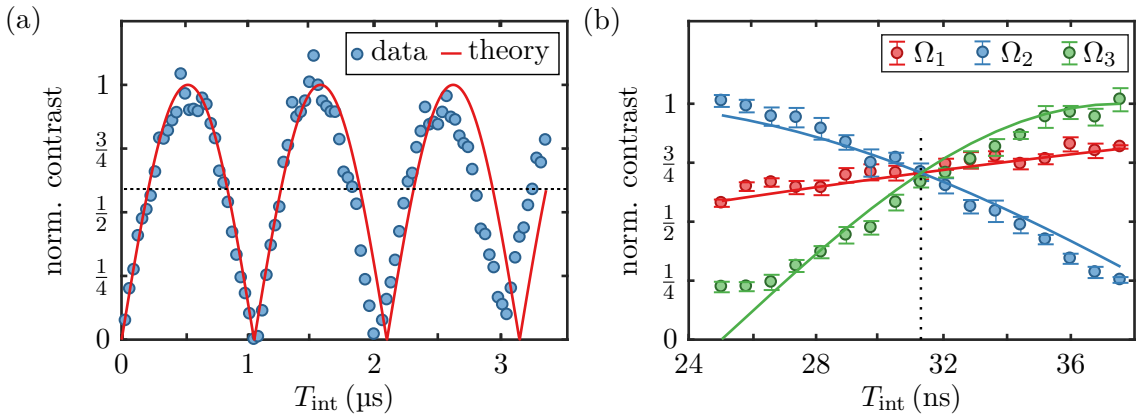

Figure 9.12: Dynamic bandwidth of the spectrum analyser. (a) Normalised contrast as a function of the interaction time T_{int}. As indicated by the black dotted line, there are several T_{int} which lead to the same rotation angle Θ. (b) For different coupling strength, the contrast is plotted as a function of T_{int}. Although Ω_n differs, the measurement outcome for $T_{\mathrm{int}} = 31.3\,\mathrm{ns}$ is identical. For both subfigures, the solid lines are computed as $|\sin(\Theta)|$ and the measurement data are normalised accordingly. The deviations for large T_{int} are due to drifts in the experimental setup. Adapted with permission from [259]. Copyright 2021 by the American Physical Society.

In order to increase the dynamic bandwidth, further measurements can be performed. The idea is to modify the interaction time $T'_{\mathrm{int}} = T_{\mathrm{int}} + t_\delta$ by a relatively small amount t_δ and the modified rotation angle Θ' is [259]:

$$\Theta' = \Theta + \Omega \cdot t_\delta = \Theta + \delta\Theta. \tag{9.24}$$

Then, Ω can be determined unambiguously for all $\delta\Theta = \Omega \cdot t_\delta < \pi/2$ [259]. Choosing t_δ small increases the dynamic bandwidth by a lot. However, it becomes more difficult to resolve the smaller $\delta\Theta$ and thus, longer total recording times might be required.

We experimentally verify these findings by performing experiments for three signals with different strengths ($\Omega_1 = 2\pi \cdot 4\,\mathrm{MHz}$, $\Omega_2 = 2\pi \cdot 12\,\mathrm{MHz}$, $\Omega_3 = 2\pi \cdot 20\,\mathrm{MHz}$). As shown in figure 9.12(b), all three magnetic fields have the same contrast for an interaction time of $T_{\mathrm{int}} = 31.3\,\mathrm{ns}$. By changing T_{int} this degeneracy can be lifted.

9.5.2 Spectral bandwidth

For the introduced protocol, the signal frequency ν has to correspond to the splitting of the qubit levels ($h\nu_0$). For a small detuning $\nu_\Delta = \nu - \nu_0$, there is still an interaction, albeit with a reduced performance (filter function compare equation (9.12)).

The dependency of the peak amplitudes in the FFT spectra on ν_Δ is experimentally investigated by sequentially measuring signals with different frequencies (same strength

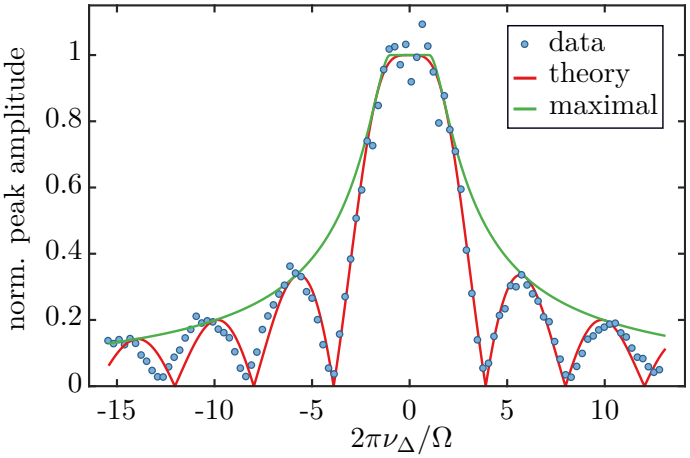

Figure 9.13: Spectral bandwidth of the spectrum analyser. Peak amplitudes in the FFT spectra as a function of the detuning $\nu_\Delta = \nu - \nu_0$ between transition frequency of the qubit ν_0 and signal frequency ν. The recorded data (blue dots) fit well with the theoretical expectations according to equation (9.12) (red line) and equation (9.25) (green line). The small deviations for large $|\nu_\Delta|$ are probably due to drifts of the bias magnetic field. Adapted with permission from [259]. Copyright 2021 by the American Physical Society.

$\Omega \cdot T_{\text{int}} = \pi/2$). The normalised peak amplitudes, obtained after recording for a few seconds respectively, are presented as a function of ν_Δ in figure 9.13.

The presented data represent the spectral filter of the used technique. As expected, the amplitude is highest when $\nu_\Delta \approx 0$ and reduces if $|\nu_\Delta|$ increases. The rotation angle Θ is determined by the generalised Rabi frequency Ω_{R} (compare equation (9.11)). Since Ω_{R} is larger than Ω, a rotation by more than $\Theta > \pi/2$ is performed if the interaction time T_{int} is fixed. If $|2\pi\nu_\Delta| = \sqrt{15}\Omega \approx 3.87\Omega$, Ω_{R} is four times larger than Ω and thus instead of a $\pi/2$-rotation a full 2π-rotation is performed. This is equivalent to not rotating at all and the contrast vanishes. The same is true for $2\pi|\nu_\Delta| = \sqrt{63}\Omega$ or more general $2\pi|\nu_\Delta| = \sqrt{(4 \cdot n)^2 - 1} \cdot \Omega$, where 2 or n full rotations are performed. Between these minima, there are maxima, albeit with a reduced contrast compared to $\nu_\Delta = 0$. For reasons explained below, $\Omega_{\text{R}} \cdot T_{\text{int}} = \pi$ at these points.

In figure 9.13 the expected contrast according to equation (9.12) is added as a red line. The data points fit well to the expectations. The small deviations for large $|\nu_\Delta|$ are probably due to drifts of the bias magnetic field during the experiments, which shift ν_0. The width of the central peak scales as $1/T_{\text{int}}$ and for the FWHM we empirically find $\nu_{\text{FWHM}} \approx 1.36/T_{\text{int}}$, if $\Omega T_{\text{int}} = \pi/2$ is fixed.

As Ω_{R} determines the rotation angle, the interaction time T_{int} which maximises the measurement contrast C is a function of ν_Δ. In order to find this optimal time and the resulting contrast, one can compute the maximal and the minimal value of equation (9.12)

as a function of the signal phase θ. For reasons of overview, only the result is presented here, and the full derivation can be found in [259]. We find that the maximal contrast is given by [259]:

$$C \sim \begin{cases} 1 & \text{for } 2\pi\,|\nu_\Delta| \leq \Omega, \\ \frac{4\pi|\nu_\Delta|\Omega}{\Omega_\mathrm{R}^2} & \text{for } 2\pi\,|\nu_\Delta| > \Omega, \end{cases} \tag{9.25}$$

for the following interaction times [259]:

$$T_\mathrm{int} = \begin{cases} \frac{2}{\Omega_\mathrm{R}} \arcsin\left(\frac{\Omega_\mathrm{R}}{\sqrt{2}\Omega}\right) & \text{for } 2\pi\,|\nu_\Delta| \leq \Omega, \\ \frac{\pi}{\Omega_\mathrm{R}} & \text{for } 2\pi\,|\nu_\Delta| > \Omega. \end{cases} \tag{9.26}$$

Thus, as long as $2\pi\,|\nu_\Delta| \leq \Omega$, it is always possible to obtain $C \sim 1$ if relaxation can be neglected. The required interaction time corresponds to an effective $\pi/2$-pulse, meaning that half of the population is transferred. Since this is not possible for $2\pi\,|\nu_\Delta| > \Omega$ anymore (since $\Omega^2/\Omega_\mathrm{R}^2 < 0.5$), the optimal C is achieved, when the effective rotation angle is the largest, which happens for $\Omega_\mathrm{R} \cdot T_\mathrm{int} = \pi$. This result is also included in figure 9.13 as a green solid line and fits well to the other data.

Spectral bandwidth taking measurement overheads into account

In section 7.1 the local oscillator frequency is defined as $\nu_\mathrm{LO} = m/t_\Delta$, where $m \in \mathbb{N}$ minimises $|t_\Delta - m/\nu|$ and t_Δ is the time between consecutive measurements. At first sight, this definition seems impractical since ν is the parameter which should be estimated and thus, the value of m is ambiguous. In general, the following signal frequencies:

$$\nu_{m,\pm} = \frac{m}{t_\Delta} \pm \nu_\delta, \tag{9.27}$$

yield the same beating frequency $\delta_\mathrm{b} = \nu_\delta$, where ν_δ is any frequency within $\nu_\delta \in [0, \frac{1}{2t_\Delta}]$. Thus, there is a $1/t_\Delta$ periodicity and a sign ambiguity in ν_δ. However, the used measurement sequence is usually only sensitive for a small range of frequencies, which is usually limited by T_int^{-1} (see previous section). Thus, as long as measurement overheads are negligible ($t_\Delta \approx T_\mathrm{int}$), only a single m yields $\nu_{m,\pm}$ which are within this range. If overheads for initialisation and readout become relevant ($t_\Delta \gg T_\mathrm{int}$), many choices for m are possible. In this case the spectral bandwidth can be increased by performing another measurement with modified $t'_\Delta = t_\Delta + t_\delta$. Then, the beating frequency changes to [259]:

$$\delta'_\mathrm{b} = \left|\delta_\mathrm{b} \pm \frac{m \cdot t_\delta}{t_\Delta(t_\Delta + t_\delta)}\right| = |\delta_\mathrm{b} \pm \delta_1|\,, \tag{9.28}$$

and as long as $\delta_1 < \min(\delta_\mathrm{b}, \frac{1}{2t_\Delta} - \delta_\mathrm{b})$, it is possible to determine m unambiguously.

In this and the previous section, it was shown that both the dynamic and the spectral bandwidth can be increased by performing an additional measurement. If the parameters are chosen conveniently, both improvements can be realised at the same time.

9.6 Conclusion

In this chapter the idea of a spectrum analyser based on a quantum sensor is presented and extensively discussed. We used single NV centres to simultaneously measure the amplitude, frequency and phase of a signal and thus all parameters that are required for signal reconstruction. For this purpose, we applied the Qdyne principle together with a phase-sensitive technique, which in principle enables spectroscopy up to more than 100 GHz and showed how to analyse the obtained FFT spectra. In particular, we were able to show mHz frequency estimation for a 1.5 GHz field, which corresponds to estimation of the frequency at the eleventh fractional digit. We introduce methods to improve the sensitivity and analyse the impact of dynamical decoupling on the sensitivity both numerically and experimentally. Important properties as the spectral and dynamic bandwidths are analysed and possibilities to extend these values are discussed. Although we used single NV centres in diamond, the principles are transferable to most other quantum sensing platforms. The ideas and findings presented here may find further application for nano-circuits as used for communication purposes or high field nanoscale NMR.

10 Conclusion and Outlook

10.1 Conclusion

Quantum spectroscopy and in particular magnetometry with single negatively charged nitrogen-vacancy (NV) centres in diamond are highly relevant and promising research topics and the main focus of this thesis. One of the most exciting applications is nuclear magnetic resonance (NMR) spectroscopy on the nanoscale. Quantum sensors are required to improve the sensitivity and spatial resolution of classical NMR spectrometers. The underlying mechanisms for detecting external nuclear spins with single NV centres located just a few nanometre below the diamond surface using pulsed dynamical decoupling (DD) spectroscopy were explained. The experimentally performed demonstrations show that it is possible to discriminate between different nuclear isotopes.

One big problem of pulsed DD protocols are spurious responses due to the finite length of the applied control pulses. They distort the measurement outcome and can lead to incorrect signal assignment. Here, a measurement technique based on randomisation of control pulse phases was introduced. Suppression of spurious harmonics for both NMR signals and classical AC magnetometry was successfully demonstrated. Furthermore, mitigation of pulse imperfections, for example due to a non-optimal pulse amplitude, is improved when using the randomisation protocol.

A further problem with traditional DD based spectroscopy is the low spectral resolution in the kHz-range, which is due to the limited coherence time of the NV centre's electron spin. Here, a spectroscopic technique, called quantum heterodyne (Qdyne) detection was introduced, and an eight orders of magnitude improved resolution down to 607 µHz was demonstrated. By taking advantage of a stable external clock, it is possible to correlate subsequent phase-sensitive measurements. This results in a resolution which is only limited by the stability of this clock. Sampling all spectral components in a given bandwidth simultaneously yields an improved SNR and is especially convenient when measuring a signal with multiple spectral components. This was demonstrated by detecting a magnetic field with three frequencies separated by only a few Hz. Furthermore, application of the Qdyne principle for nanoscale NMR was shown. The linewidth, however, was still limited

by the coherence time of the signal itself. Possible options to solve this problem, for example by using thermal instead of statistical polarisation, were discussed.

Moreover, quantum frequency discrimination was discussed. The optimal strategies when the task is to discriminate between two known frequency distributions were experimentally realised. By removing quantum projection noise, discrimination of two frequencies separated by just 2 kHz within a single coherent 44 µs interaction period was shown. Taking additional readout noise into account, two strategies – ensemble averaging and single-shot readout – were discussed and experimentally realised. It was demonstrated that every strategy has certain advantages and the optimal technique depends on the precise conditions and available resources.

In the last experimental chapter, the possible application of NV centres together with the Qdyne technique for quantum spectrum analysis was examined. A detection scheme was introduced, which allows NV centres to interact with fields of interest in the range of several kHz up to more than 100 GHz by adjusting an external bias field. The performance of the quantum spectrum analyser for signal reconstruction was analysed, including a discussion about the dynamic and spectral bandwidths. By applying continuous driving, decoupling from environmental noise was realised which showed an improved sensitivity.

10.2 Outlook

Although quantum metrology is relatively young, it is a particularly fascinating and promising research area. The variety of advantages, as for example the high spatial resolution, offer great potential for novel applications and technologies. A wide range of scientific research areas, including single-molecule microscopy [268] and nanoscale NMR [269], would profit from the benefits.

Recently, adaptive protocols attracted a lot of attention [105, 270, 271]. In combination with a suitable real-time feedback control, for example based on machine or Hamiltonian learning [272–276], the first experimental realisation showed that it is possible to surpass the standard measurement limit scaling [277–279]. Especially for NV centres, where usually fluorescence photons are the measurement quantity, advanced data analysis [226, 229] and deep learning approaches [280] have the potential to further improve the measurement performance.

Recent findings, as new reported sensing techniques [281], the realisation of quantum error correction [238, 282, 283] or the combination with atomic force microscopy [150, 284, 285] prove that the limits and capabilities are still by far not reached. Also, NV centre based sensors will benefit from progress on the engineering side – either by improving the

properties of NV centres, as positioning [286] or coherence time [287,288], or by enhancing the amount of detected photons by nanostructuring [122,127] or improved optics.

Furthermore, quantum sensors are required for characterisation in most other quantum technologies. Against this background, it is very probable, that they will have an important role in the development of new technologies and find application in both high-end-applications and everyday devices.

Appendix

A Appendix

A.1 Setup

In this section the most important components of the experimental setup, which is sketched in figure A.1, are discussed. Thereafter, the used diamond samples are shortly introduced and finally, three different methods to align the magnetic bias field are presented.

A.1.1 Microwave setup

Using microwave (MW) and radio frequency (RF) fields, it is possible to manipulate the spin states of the NV centre's electron spin and nearby nuclear spins (see section 2.5). Since the durations of the required MW pulses usually need to be on the order of just a few tens of nanoseconds and the protocols can be very complex, high temporal resolution and good control over the form of the fields are required.

Because of that, an arbitrary waveform generator (AWG) (Tektronix AWG70001A) was used to realise all protocols. An AWG can in principle generate arbitrary output signals, enabling free control over frequencies, amplitudes and phases – within certain hardware limitations. The adjustable sampling rate, up to 50 GSamples/s, allows to adjust pulse lengths and interaction periods with a timing resolution down to 20 ps and to generate signals in the range of DC up to about 20 GHz. In order to suppress harmonics and further undesired spectral components suitable filters were used. For the highest sampling rate the AWG memory allows to play waveforms with a duration up to about 320 ms and by reducing the sampling rate, even longer sequences are possible.

The output voltage is limited to a maximal peak-to-peak voltage of 500 mV with a resolution of about 2 mV. Since the durations of control pulses are proportional to the amplitudes of the MW and RF fields, the signals were amplified. The outputs of both amplifiers (AR-60S1G4A and AR-75A250A) were combined using a suitable devices (PRO-TRI 174/350-520/760-N or Wainwright WDK7+6-DC-1000/1430-6000-60S3) and guided to a printed circuit board (PCB), onto which the diamond sample is glued. A thin copper wire (Goodfellow CU005171), soldered over the diamond surface, with a thickness of just 20 nm, is used as an antenna. The transmitted current is ended using a 50 Ω termination.

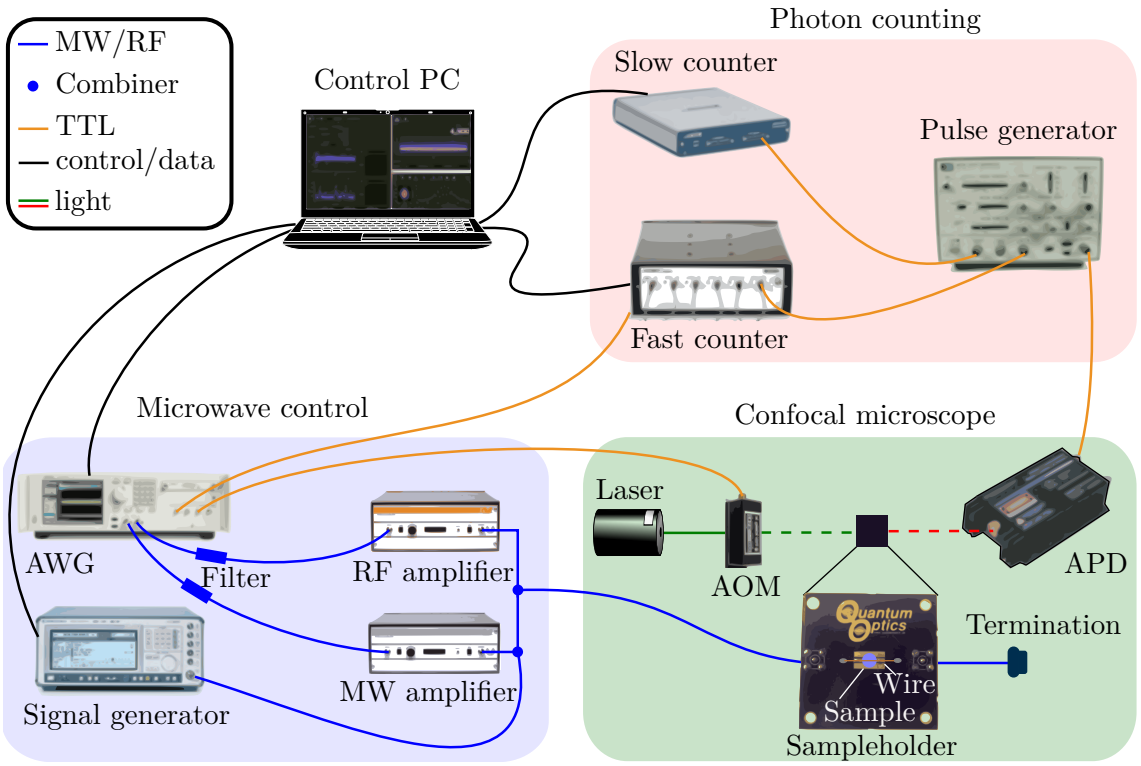

Figure A.1: Schematic overview of the experimental setup. The most important components of the experimental setup are here divided into four parts: microwave control (appendix A.1.1), confocal microscope (appendix A.1.2), photon counting (appendix A.1.3) and control PC (appendix A.1.4). The sketch is by far not complete, and only the most important connections were added.

Besides the analogous one, the AWG has two digital outputs. The first one can trigger the acousto-optic modulator (AOM), which is used to control the laser excitation (compare appendix A.1.2), and the other digital channel is connected to the photon counting device and ensures synchronisation (see appendix A.1.3).

Other signal generators (Gigatronics 2520B and/or Rohde & Schwarz SMIQ06B) can be optionally integrated to output continuous wave (cw) signals, which can be used as test signals or for cw experiments as ODMR (see section 4.1). Using a combiner, the same wire can be used as antenna.

A.1.2 Confocal microscope

The atomic size of single NV centres requires high spatial resolution in order to find and address these defects. For this purpose, a homebuilt confocal setup [289, 290] was used for all experiments presented in this thesis. A schematic sketch with the most important components is shown in figure A.2.

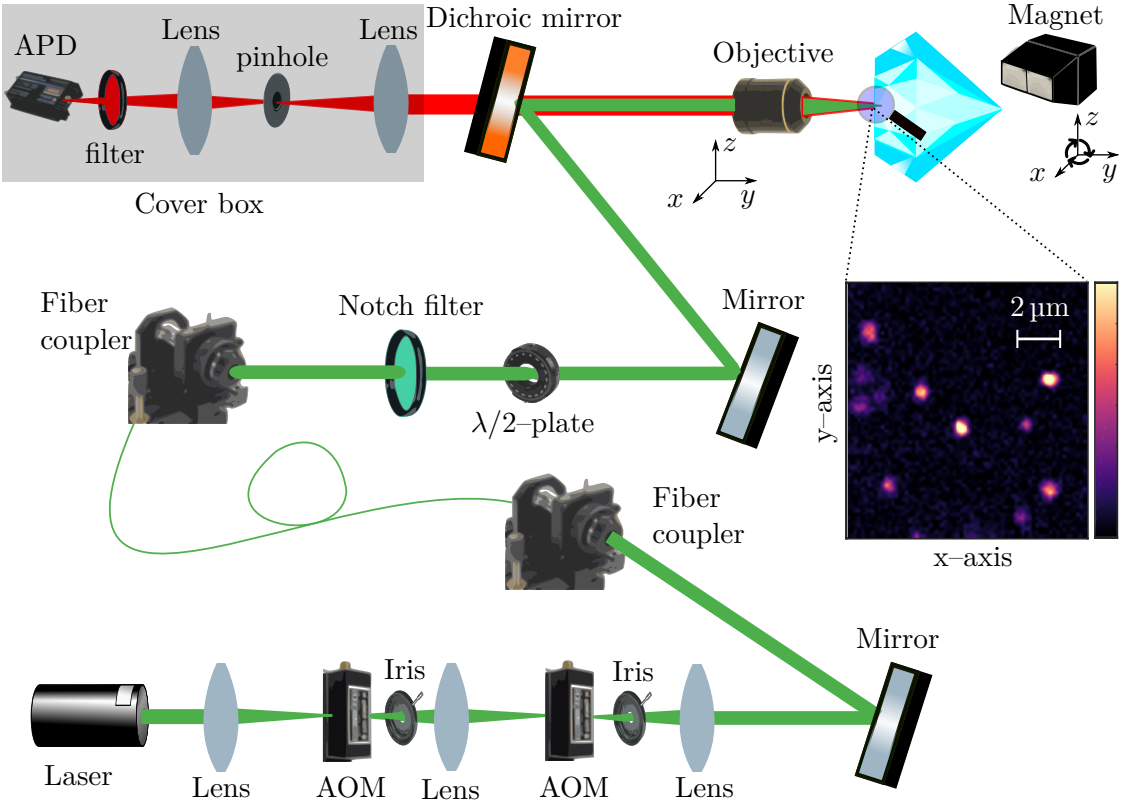

Figure A.2: Schematic overview of the confocal microscope. A green laser is coupled into a movable objective, which can be scanned over the diamond surface in steps of typically 10 nm to 1 µm. A pinhole ensures that only the red-shifted fluorescence coming from the confocal volume reaches the avalanche photodiode (APD). Single NV centres appear as a bright spot in the confocal image here. A more detailed description of all parts is in the text.

A frequency doubled Nd:YAG laser (Laser Quantum gem 532) produces a monochromatic and coherent beam of collimated and linearly polarised light with a wavelength of 532 nm. Since this laser is operating in cw mode, the laser light needs to be chopped in order to generate the pulses required for the experiments. For this purpose, the beam is focused onto an acousto-optic modulator (AOM) (Crystal Technology 3200-146) using a convex lens. An AOM is a transparent crystal that uses the acousto-optic effect to change certain properties, as spatial direction, intensity, frequency, phase and polarisation, of the light passing through it. Here, mainly the deflection due to Bragg diffraction is important and by isolating the first order using an iris, the transmittance can be turned on and off within rise times of a few tens of nanoseconds. As the extinction ratio is limited to about 1:1000, a second AOM was used for most experiments, since laser leakage leads to undesired excitation of NV centres during interaction periods.

The chopped laser pulses are collimated by another lens and directed onto a fibre coupler. The single-mode fibre has two main purposes. First, it restores the Gaussian TEM_{00} mode, which might have got distorted by the AOMs. Furthermore, the fibre decouples the above described part of the confocal setup from the part described in the following. So, if adjustments or fine-tunings are required in either part, the other part does not have to be adapted.

The outcoupled light is directed onto a notch filter (Chroma Technology HQ530/30M), which removes any other spectral components, for example originating from fluorescence of the fibre. In order to optimise the absorption of the NV centre, the polarisation of the laser light should be preferably parallel to the dipole axes of the NV centre in order to maximise the transition dipole moment. For this purpose, the laser polarisation can be adapted by a $\lambda/2$-plate (Thorlabs WPH10M-532). The light is further directed onto a dichroic mirror (Thorlabs DMLP567L), which mainly reflects light below 550 nm, while spectral components above 584 nm are efficiently transmitted. The reflected light is directed to an objective (Olympus UPLSAPO60XO or Olympus MPLFLN100X), which is positioned on a piezostage (NPoint NPXY200Z25A) with a scan range of 200 µm × 200 µm × 25 µm and an accuracy of 0.5 nm. In this way positioning and scanning of the objective, which focuses the laser light onto the diamond sample, is possible.

The diamond is placed on a PCB sample holder (see figure A.1), which is screwed onto another stage which allows coarse 3D-positioning with an accuracy of about 1 µm.

In order to apply a magnetic bias field, a permanent magnet, consisting of neodymium, is attached to a 3D-positioning stage (Physik Instrumente M-521). For further control over the direction of the field, an additional rotation stage (Zaber T-RS60A) is implemented. Three different methods to align this bias field are introduced in appendix A.1.6.

The light emitted from the NV centres is collected by the same objective and passed onto the dichroic filter, which transmits the red-shifted fluorescence. Thereafter, it is focused onto a pinhole (Thorlabs PS25, 25 µm diameter) to ensure that mainly light emitted from the confocal volume passes to the detector. For shielding purposes, this part of the setup is covered by an additional box. A 645 nm highpass filter (Chroma Technology HQ645LP) is used to exclude reflections from the excitation beam, fluorescence from the NV^0 charge state (ZPL at 575 nm) and the diamond Raman lines ($\tilde{\nu} = 1332\,\mathrm{cm}^{-1}$, i.e. 573 nm first order and 620 nm second order for 532 nm excitation). The remaining fluorescence is focused onto an avalanche photodiode (APD) (Excelitas Technologies SPCMAQRH-15) with single-photon sensitivity by another lens.

The confocal volume depends on the properties of the objective, the laser wavelength λ and the diffraction index n of the immersion medium. The resolution of an ideal confocal

microscope (with an infinitely small pinhole) in the full width at half maximum sense is given by [290]:

$$\Delta x = \frac{0.37\lambda}{NA}, \tag{A.1}$$

$$\Delta z = \frac{0.64\lambda}{n - \sqrt{n^2 - NA^2}}, \tag{A.2}$$

where NA is the numerical aperture of the objective. In a real-world realisation the finite size of the pinhole has to be taken into account [290]. Depending on the diamond sample different objectives and immersion media were used, which are in more detail discussed in appendix A.1.5.

In order to obtain a multi-dimensional image, the position of the objective is scanned in small steps, typically between 10 nm and 1 µm. By recording the PL, it is possible to construct an image as shown on the right side of figure A.2.

A.1.3 Photon counting

Whenever the APD detects a photon, it outputs a TTL-pulse. Theses signals need to be recorded and in the case of measurements with laser pulses, where the readout window is usually not longer than 500 ns, a high timing resolution is required. For this task a multiple-event time digitiser (Fast ComTec MCS6A) was used as a fast counter. This device records every TTL-signal with a time stamp and a timing resolution of down to 0.2 ns. The collected data is transferred and stored on the control PC, where it is further analysed.

If the fluorescence for cw laser excitation should be recorded, for example to create an confocal image, a lower timing resolution is sufficient. For this purpose a multi-function data acquisition device (National Instruments PCIe-6323) was used as a slow counter and the recorded signal was sent to the PC as well. The analogue outputs of the same device were employed to control the piezostage, which enables scanning of the objective in the confocal microscope.

In order to operated both the fast and slow counter simultaneously, a pulse generator (Hewlett-Packard 8012B) was used to create two identical copies of the APD output.

A.1.4 Control PC and measurement software

For controlling the experiment, command and parameter input and data visualisation a PC was used. The necessity of all the hardware devices operating together in a coordinated fashion requires a reliable control software. Therefore, for most experiments relevant for this thesis, the Qudi software suite was used. Qudi is a general, modular, multi-operating

system suite which is written in Python 3 [236]. The science modules can be categorised into three domains. The logic modules control and coordinate a given experiment, pass input parameters and evaluate measurement data. The graphical user interface (GUI) modules allow parameter input, data visualisation and offer a convenient way to interact with the logic modules. Finally, different experimental hardware usually differ widely in their command structure, sometimes even when manufactured from the same company. For this purpose, the hardware modules are responsible for 'translating' the commands coming from the logic modules into the language of the used hardware. This intuitive design simplifies the addition of new hardware devices or the implementation of new measurement protocols. Using Qudi and a suitable script, it is possible to perform a complex experiment, including setting up numerous hardware devices, controlling the measurement, evaluation of the results and saving the data, by a simple touch of a button.

A.1.5 Overview of examined diamond samples

In the following, the diamonds used for the experiments presented in this thesis are shortly introduced. All these samples were regularly boiled in a 1:1:1 tri-acid mixture (H_2SO_4:HNO_3:$HClO_4$) for several hours at $130 - 180\,°C$ in order to remove graphitic and organic residuals from the surface. Besides for the solid immersion lens sample, an oil objective (Olympus UPLSAPO60XO) and immersion oil (Fluka Analytical 10976) were used for all experiments.

Solid immersion lens sample

For some experiments which are presented in this thesis an all diamond solid immersion lens (SIL) provided by Element 6[1] was used. In order to integrate NV centres the backside was overgrown with a 100 nm thick diamond layer of 99.999 % isotopically enriched ^{12}C using the plasma enhanced chemical vapour deposition (CVD) method with parameters similar to the ones in [291]. As the radius of the hemisphere is 0.5 mm and no other objective with a sufficient large working distance was available, an air objective (Olympus MPLFLN100X) and no immersion medium were used for this diamond.

Single-shot readout sample

All experiments, for which a ^{13}C spin was used as quantum memory to enable single-shot readout (SSR) measurements, were preformed using a flat diamond with a CVD grown surface layer. The reduced abundance of ^{13}C isotopes down to 0.1 % ensures relative long dephasing times, while the probability to find a ^{13}C nuclei coupling to one of the

[1] www.e6.com

NV centres, which were incorporated during the growth, is still relatively large. In fact, all results were obtained with the same NV – ^{13}C pair, which stands out due to its suitable hyperfine coupling parameters (parallel and perpendicular hyperfine couplings: $A_{\parallel} \approx 50\,\mathrm{kHz}$ and $A_{\perp} \approx 1.4\,\mathrm{kHz}$). The NV centre is located well below the diamond surface (about 4 µm) and has a relatively long dephasing time $T_2^* \approx 50\,\mu\mathrm{s}$.

Nanoscale NMR sample

This diamond was used for most experiments with the aim to detect a nanoscale NMR signal (sections 5.2 and 7.2.6). Shallow NV centres were generated by implanting $^{15}N^+$ ions with a $3 \cdot 10^8\,\mathrm{ions/cm^2}$ dose for implantation energies of 2.5 and 5 keV into a 99.999 % ^{12}C isotopically enriched CVD grown diamond with (100) surface orientation, provided by Element 6. After subsequent annealing, NV centres formed primarily in a depth between 2 and 15 nm.

Nanoscale NMR sample II

For the nanoscale NMR experiments which show that randomisation of pulse phases can suppress spurious harmonics (chapter 6), a different sample with natural abundance of ^{13}C isotopes was required. This diamond was implanted with $^{15}N^+$ ions with an energy of 1.5 keV and a dose of $2 \cdot 10^9\,\mathrm{ions/cm^2}$. Shallow NV centres with a depth of around $(5 \pm 1)\,\mathrm{nm}$ formed during the 3 h subsequent annealing in vacuum at 1000 °C.

A.1.6 Magnetic field alignment

All experiments presented in this thesis were performed under an external magnetic bias field aligned parallel to the symmetry axes of the measured NV centres. The bias field was primarily used to split the degenerate $m_s = -1$ and $m_s = +1$ spin states. A misaligned field leads to a reduction of both, fluorescence and readout contrast, and has further negative influences onto the measurement performance. In the following, three different strategies to align this external field are shortly introduced.

Magnetic field alignment by fluorescence optimisation

The dependency of the fluorescence on the orientation of the magnetic field $\vec{B}$ can be used to align it. If $\vec{B}$ has a component perpendicular to the symmetry axis of the NV centre, here characterised by the misalignment angle ζ sketched in figure A.3(a), the spin quantum numbers m_s are not eigenstates of the system anymore, but the eigenstates are rather an incoherent mixture of all m_s. This reduces the probability to be in the bright

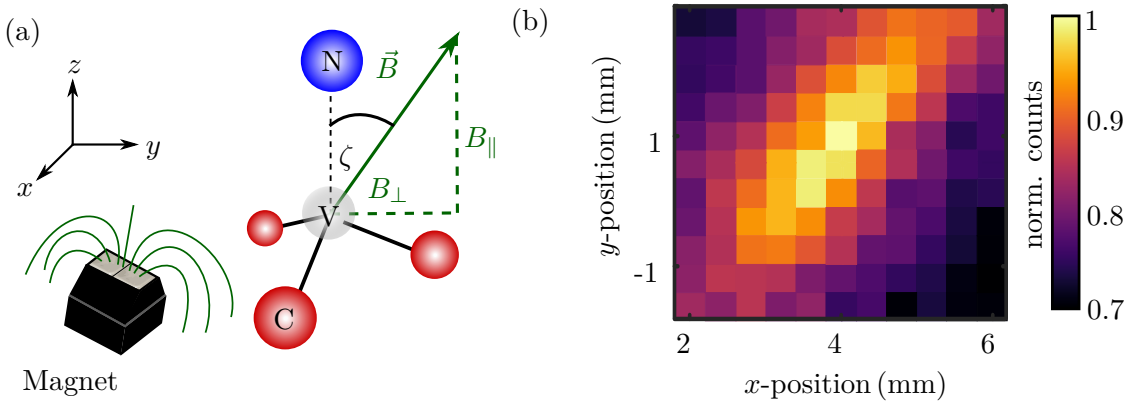

Figure A.3: Magnetic field alignment by fluorescence optimisation. (a) The misalignment can be described by the angle ζ between magnetic field vector $\vec{B}$ and symmetry axis of the NV centre (corresponds to the z-axis here). (b) Experimental demonstration of the working principle. For different magnet positions, which correspond to different orientations of $\vec{B}$, the fluorescence is measured. As expected, the number of recorded photons decreases if the alignment is poor.

$m_s = 0$ state and thus the fluorescence decreases [292]. If ζ is small, the combination of ZFS and Zeeman interaction is usually much larger than the perpendicular component and the effect of spin mixing is small. However, close to the ground and excited state level anti-crossing (LAC) around 51 mT and 102 mT, the $m_s = -1$ and $m_s = 0$ spin states are energetically almost degenerate and even a small perpendicular magnetic field component becomes important [292].

The alignment principle is rather simple. By scanning the above described permanent magnet different magnetic field orientations can be probed. An example is shown in figure A.3(b) for a magnetic bias field close to 50 mT. For this experiment, fluorescence was collected for 5 s at every position. The number of detected photons depends on the magnetic field orientation and reduces by more than 30 % if the alignment is poor. The accuracy depends on the stability of the fluorescence, which is for example influenced by laser fluctuations. Close to a LAC, an alignment better than $\zeta < 1°$ can be achieved.

Magnetic field alignment via transition frequencies optimisation

Besides mixing of the spin states, a magnetic field perpendicular to the symmetry axis of the NV centre also influences the relative locations of the energy levels. If strain fields and hyperfine coupling terms are omitted, the simplified NV Hamiltonian reads:

$$\mathcal{H}/h = D\hat{S}_z^2 + \gamma_{\mathrm{NV}} \underbrace{B\cos(\zeta)}_{B_{\parallel}} \hat{S}_z + \gamma_{\mathrm{NV}} \underbrace{B\sin(\zeta)}_{B_{\perp}} \hat{S}_x, \tag{A.3}$$

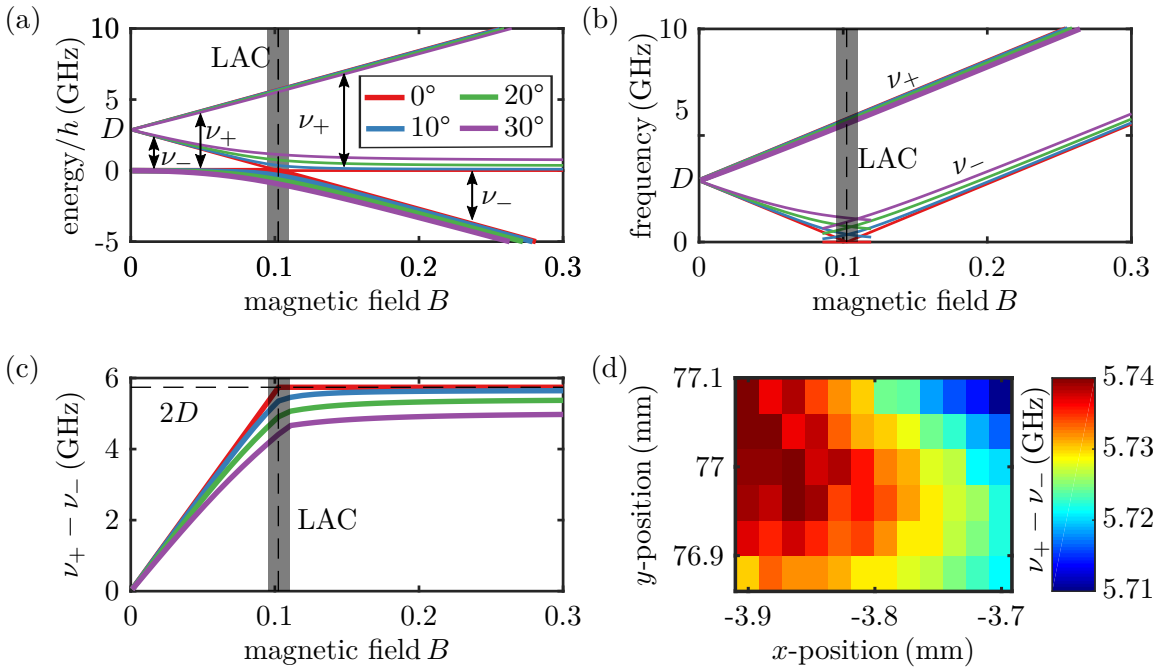

Figure A.4: Magnetic field alignment by transition frequencies optimisation. (a) Eigenvalues of the Hamiltonian described by equation (A.3) as a function of the magnetic field B for different misalignment angles ζ (in legend). (b) The corresponding transition frequencies ν_+ and ν_- depend on ζ. The behaviour close to the level anti-crossing (LAC) is approximated, and is more complex in reality, especially since any hyperfine couplings are omitted here [293]. (c) Difference of the two transition frequencies as a function of B. (d) Experimental demonstration of the working principle. By scanning the position of a permanent magnet different orientations of the magnetic field are probed.

where $D = 2.87\,\mathrm{GHz}$ is the ZFS, B the magnetic field strength, and ζ the angle between the symmetry axis of the NV centre and the direction of the magnetic field as defined in figure A.3(a). Due to the cylindrical symmetry, it is sufficient to consider a perpendicular field $B_\perp$ pointing only in x-direction. Without any misalignment ($\zeta = 0$), $m_\mathrm{s} = +1$ and $m_\mathrm{s} = -1$ are eigenstates and their energies split symmetrically and linearly with B. Computing the eigenvalues of equation (A.3), however, shows that the splitting of the levels becomes asymmetric for $\zeta > 0$, which is depicted in figure A.4(a). This changes the transition frequencies ν_+ and ν_-, as shown in figure A.4(b). Especially, after the ground state level anti-crossing (LAC) at $B_\mathrm{LAC} \approx 102\,\mathrm{mT}$, where the difference $\nu_{\pm,\Delta} = \nu_+ - \nu_-$ is exactly twice the ZFS for a perfectly aligned field, the changes become apparent, as depicted in figure A.4(c). Thus, $\nu_{\pm,\Delta}$ is a measure for the magnetic field alignment.

In order to demonstrate this, the permanent magnet was scanned at a magnetic bias field of around 200 mT, so well above B_LAC. For every position both transition frequencies ν_+ and ν_- were measured using the ODMR technique (see section 4.1) and the result is

shown in figure A.4(d) . If $\nu_+ - \nu_- = 2D = 5.74\,\mathrm{GHz}$, the magnetic field should be very well aligned. The accuracy of this magnetic field alignment technique depends on the precision of the transition frequencies measurements. At 200 mT, an uncertainty of 1 MHz in estimating ν_+ and $\nu-$ corresponds to about 1° accuracy. If the bias field is smaller than B_{LAC}, $\Delta\nu_\pm$ is still maximal for $\zeta = 0$ and it is $\nu_+ + \nu_- = 2D$.

Magnetic field alignment by nuclear spin lifetime optimisation

The third alignment technique requires an additional nuclear spin and for NV centres the inherent nitrogen spin or a nearby ^{13}C spin are typical options. Although, there usually is a large mismatch between the energy difference of the electronic and nuclear spin states, flip-flop processes between both spin species are possible [92, 145, 294]. The rate depends on the perpendicular component of the hyperfine coupling, which is usually even higher in the excited state [85]. Transverse magnetic fields can speed up the flip-flop rates and thus, the nuclear spin lifetime is a measure for the magnetic field alignment.

One possible protocol to probe the lifetime of a nuclear spin is sketched in figure A.5(a) and consists of two parts. First, the nuclear spin, with states $|\uparrow\rangle$ and $|\downarrow\rangle$, is polarised. Here a series of controlled-not (CNOT) gates is used, after initialising the NV centre into $|0\rangle$ by a laser pulse:

$$|0\rangle \otimes (|\uparrow\rangle + |\downarrow\rangle) \xrightarrow{\mathrm{MW}} |0\uparrow\rangle + |1\downarrow\rangle \xrightarrow{\mathrm{RF}} (|0\rangle + |1\rangle) \otimes |\uparrow\rangle \xrightarrow{\mathrm{init.}} |0\uparrow\rangle\,. \tag{A.4}$$

The first CNOT gate (MW) is a selective microwave π-pulse which flips the electron spin only if the nuclear spin is in the $|\downarrow\rangle$ state. The second CNOT gate (RF) flips the nuclear spin only if the NV centre in the $|1\rangle$ state. As a consequence, the nuclear spin state is initialised into the $|\uparrow\rangle$ state.

The second part of the protocol measures the decay of the nuclear spin polarisation. The simple sequence of the same MW-CNOT gate and optical readout of the NV centre's state, which also initialises it into $|0\rangle$ again, is repeated R times. As long as the nuclear spin state has not flipped, the detected fluorescence stays high. The relaxation rate R_{relax} depends on the degree of magnetic field alignment, as shown for the example curves in figure A.5(c), measured for the inherent ^{15}N spin. Although ζ differs only by about 1° for both cases, R_{relax} deviates by about a factor of 4. In order to gather enough statistics, initialisation and readout are repeated many time. This example data corresponds to the coloured squares in figure A.5(d), for which the magnet was scanned as described in the two previous sections. The accuracy of the alignment can be well below $\zeta < 1°$, especially at higher magnetic bias fields. Another option to probe the nuclear spin lifetime is the single-shot readout technique discussed in section 8.4.2 and [254].

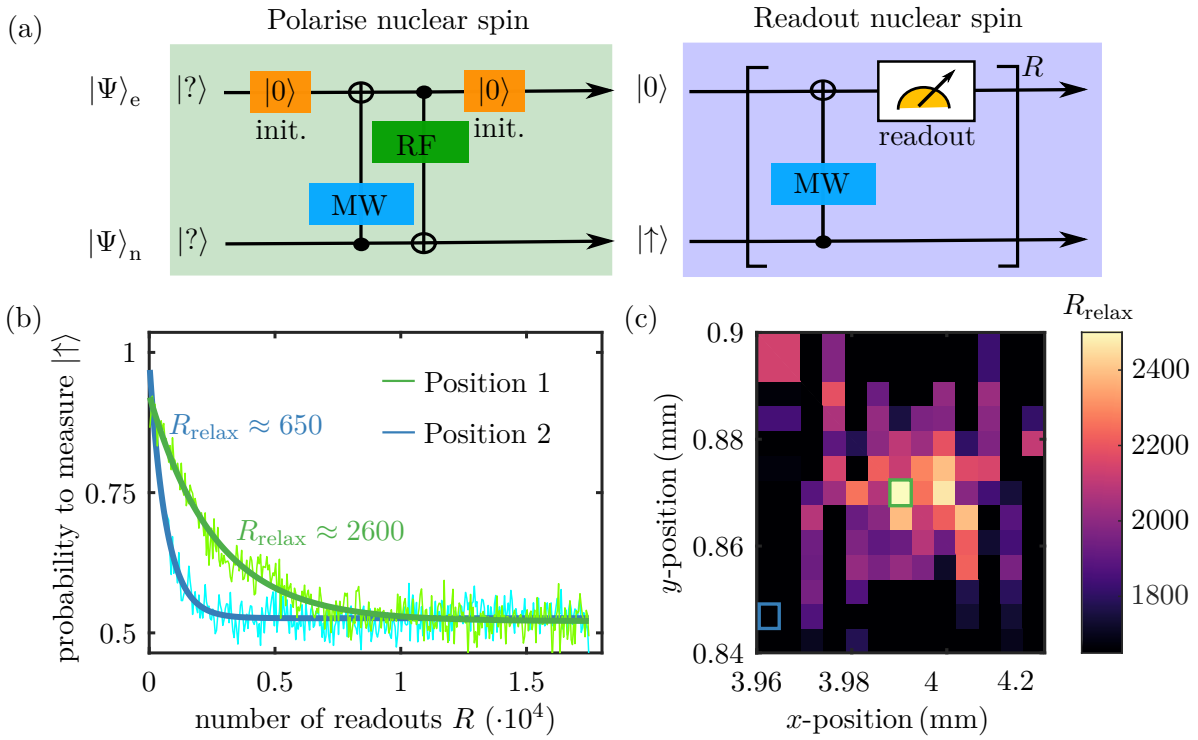

Figure A.5: Magnetic field alignment by nuclear spin lifetime optimisation. (a) Possible protocol to measure the nuclear spin lifetime. Using the NV centre and two CNOT gates (light blue and dark green boxes), the nuclear spin can be initialised. Thereafter, its spin state is probed R times. (b) Polarisation decay as a function of the readout number R. The decay constant R_{relax} depends on the alignment of the magnetic field. (c) In order to find the optimal magnet position, the nuclear spin lifetime is measured for different magnet positions, which correspond to different orientations of the bias field.

A.2 Diamond synthesis and nitrogen-vacancy centre creation

For sensing purposes ultrapure diamonds and NV centres with long coherence times are essential. In the following, techniques to create such diamonds and NV centres are shortly introduced.

Diamond synthesis

Due to their extraordinary properties diamonds become more and more interesting for research and industry. Natural diamonds are formed in the mantle of the earth, where the required conditions for a phase transition are met. However, the number of natural diamonds is limited which leads to high purchasing costs. Also, for scientific purposes

diamonds with special properties are better suited. Since the middle of the 20th century different methods for diamond synthesis were developed.

The idea of the high pressure high temperature (HPHT) method is to generated conditions, for which the diamond synthesis occurs naturally. For this purpose, a carbon melt is heated up to temperatures exceeding 2000 K and pressures up to about 10 GPa are applied [295]. Under such conditions – similar to the ones in the earth mantle – a phase transition to diamond occurs. Adding metals such as iron, cobalt or nickel can help to catalyse the reaction and reduce pressure and temperature requirements [296, 297]. Since normally a large number of impurities are included, most diamonds produced by this technique are crystals of type Ib [297]. Using very clean carbon melts and elements that bind impurities, it is possible to obtain IIa type diamonds [297].

As the name implies, chemical vapour deposition (CVD) is based on chemical reactions in the gas-phase which lead to a deposition of diamond onto the surface of a substrate. The substrate is placed in an evacuated growth chamber and a gas mixture of hydrogen and a hydrocarbon, typically methane, is added. In order to enable the chemical reaction energy needs to be fed into the system. Usually microwaves are used to heat up the gas mixture until a plasma forms. Hydrogen atoms then terminate the dangling carbon bonds on the surface of the substrate. It also splits up the hydrocarbons to reactive carbon-containing radicals such as CH_2. These radicals can bond to the surface of the substrate either as graphite or diamond. Since hydrogen etches graphite much quicker than diamond, diamond remains and starts to deposit layer-by-layer on the surface. One of the main advantages of the CVD method is that impurities can only be incorporated if they are in the gas mixture. If the reaction chamber is well designed impurities are mainly due to contamination of the source gases, which can be very pure. In this way, it is possible to grow type IIa diamonds with very low impurity ratios. Additionally, by using isotopically enriched hydrocarbons the amount of ^{12}C and ^{13}C isotopes in the diamond can be controlled. Recently, the creation of 99.999 % ^{12}C enriched samples was reported [298]. More detailed information about the CVD process can be found in [297, 299].

Creation of NV centres

Due to the naturally high nitrogen and vacancy content, NV centres usually exist in every diamond. The probably simplest way to increase their number is to heat up the diamond above 600 °C. At these temperatures vacancies become mobile and diffuse through the diamond lattice [55, 300]. If they reach nitrogen atoms, NV centres, which are immobile up to higher temperatures, are formed. For scientific purposes it is desirable to have control over the position, the density or other properties. For example, the interaction

usually reduces with the sensor-sample-distance and thus the NV centre should be as close as possible to the sample. In order to generate additional NV centres the two best-known methods are nitrogen ion implantation [301–303] and doping during the CVD growth [304].

For implantation, atomic or molecular nitrogen is ionised and accelerated towards the surface of the diamond by an electrical potential. Inside the diamond the nitrogen ions are scattered several times and knock out carbon atoms. After losing their energy this way, they finally stop somewhere in the diamond lattice. Subsequent annealing mobilises the created vacancies and increases the NV centre yield. Ion implantation is a convenient technique to control the spatial distribution of NV centres. By tuning the energy of the nitrogen ions the penetration depth can be adjusted. For example energies of a few keV lead to shallow NV centres with a depth in the lower nm range [302, 305]. Also SRIM (Stopping and Range of Ions in Matter) simulations can help to predict the penetration depth distributions of implanted nitrogen [306]. By focusing the ion beam or using lithography the axial distribution can be restricted [307]. The implantation dose can be tuned by controlling the implantation fluence. Important for application in industry, implementation on a millimetre-scale device using traditional semiconductor fabrication techniques has recently been demonstrated [308].

The second method relies on the incorporation of nitrogen during the growth process. Due to the controlled and rather slow growth, the CVD method is usually most suitable. The depth and concentration of the nitrogen atoms can be controlled by adjusting the nitrogen gas inlet. Adding nitrogen just for a short time results in a thin layer of NV centres, which is often referred to as δ-doping [291, 309]. It is also possible to create NV centres with a preferential orientation [288]. Additional radiation by electrons or carbon can increase the number of vacancies and thus the number of NV centres, but also introduces lattice damage, which can negatively influence the properties of the NV centres [310, 311]. Although the lateral nitrogen location is statistically distributed in the CVD layer, ^{12}C implantation in combination with a mask with nanoscale apertures allows to achieve 3D localisation of NV centres within a volume of $(\approx 180\,\mathrm{nm})^3$ [304].

For both methods the nitrogen isotope forming the NV centre can be controlled. In order to ensure that the NV centre of interest is intentionally created, ^{15}N is usually used due to its low natural abundance of 0.37 % [312].

A.3 Mathematical derivations

A.3.1 Time evolution and rotating reference frame

Time evolution operator

In section 2.1, the time evolution operator $\mathcal{U}(t_1, t_0)$ is introduced as a way to describe the temporal evolution of a closed system:

$$|\Psi(t_1)\rangle = \mathcal{U}(t_1, t_0)\,|\Psi(t_0)\rangle\,. \tag{A.5}$$

In the following, this is analysed in more detail. The time evolution operator has to fulfill the time-dependent Schrödinger equation:

$$i\hbar\frac{\partial}{\partial t}\,|\Psi(t)\rangle = \mathcal{H}(t)\,|\Psi(t)\rangle\,. \tag{A.6}$$

Inserting equation (A.5) into equation (A.6) and using that $|\Psi(t_0)\rangle$ is not explicitly time-dependent, it follows:

$$i\hbar\frac{\partial}{\partial t}\mathcal{U}(t_1, t_0) = \mathcal{H}(t)\mathcal{U}(t_1, t_0). \tag{A.7}$$

Solving equation (A.7) is in general not straightforward. Only if either the Hamiltonian $\mathcal{H}$ is time-independent or the operators $\mathcal{H}$ that correspond to different moments of time commute, $\mathcal{U}(t_1, t_0)$ is given by:

$$\mathcal{U}(t_1, t_0) = \exp\left(-\frac{i}{\hbar}\int_{t_0}^{t_1}\mathcal{H}(t')\mathrm{d}t'\right). \tag{A.8}$$

Most Hamiltonians which are relevant for this thesis fulfill either of these requirements and thus the respective time-evolution operators are described by equation (A.8). As an example, the Hamiltonian of a two level system without further interaction is given by:

$$\mathcal{H}_0 = \frac{\hbar\omega_0}{2}\hat{\sigma}_z, \tag{A.9}$$

where ω_0 is the resonance frequency of the system and the time-evolution operator reads:

$$\mathcal{U}(t, 0) = \exp\left(-i\frac{\omega_0 t}{2}\hat{\sigma}_z\right). \tag{A.10}$$

Quantum system in its rotating frame

In order to transfer a quantum system into a different interaction picture, both its Hamiltonian $\mathcal{H}(t)$ and its state $|\Psi(t)\rangle$ have to be adapted. The transferred state vector can be defined as:

$$|\Lambda(t)\rangle \equiv \mathcal{R}\,|\Psi(t)\rangle\,, \tag{A.11}$$

where $\mathcal{R}$ is an unitary operator, which is defined below. After rewriting equation (A.11) as $\mathcal{R}^\dagger\,|\Lambda(t)\rangle = |\Psi(t)\rangle$ and inserting into the time-dependent Schrödinger equation (equation (A.6)), it follows:

$$\begin{aligned} i\hbar\frac{\partial}{\partial t}(\mathcal{R}^\dagger\,|\Lambda(t)\rangle) &= \mathcal{H}\mathcal{R}^\dagger\,|\Lambda(t)\rangle \\ i\hbar\left(\frac{\partial\mathcal{R}^\dagger}{\partial t}\,|\Lambda(t)\rangle + \mathcal{R}^\dagger\frac{\partial}{\partial t}\,|\Lambda(t)\rangle\right) &= \mathcal{H}\mathcal{R}^\dagger\,|\Lambda(t)\rangle\,. \end{aligned} \tag{A.12}$$

By multiplying $\mathcal{R}$ from the left side, it is:

$$i\hbar\left(\mathcal{R}\frac{\partial\mathcal{R}^\dagger}{\partial t}\,|\Lambda(t)\rangle + \frac{\partial}{\partial t}\,|\Lambda(t)\rangle\right) = \mathcal{R}H\mathcal{R}^\dagger\,|\Lambda(t)\rangle\,, \tag{A.13}$$

and reordering the terms yields:

$$i\hbar\frac{\partial}{\partial t}\,|\Lambda(t)\rangle = \left(\mathcal{R}H\mathcal{R}^\dagger - i\hbar\mathcal{R}\frac{\partial\mathcal{R}^\dagger}{\partial t}\right)|\Lambda(t)\rangle\,. \tag{A.14}$$

By comparing with the Schrödinger equation for $|\Lambda(t)\rangle$, it follows for the Hamiltonian in the interaction picture:

$$\mathcal{H}_{\text{int}}(t) = \mathcal{R}\mathcal{H}\mathcal{R}^\dagger - i\hbar\mathcal{R}\frac{\partial\mathcal{R}^\dagger}{\partial t}. \tag{A.15}$$

The form of $\mathcal{R}$ depends on the problem. Since the idea is to move into the rotating reference frame of the unperturbed quantum system whose evolution is given by equation (A.10), a convenient choice is:

$$\mathcal{R} = \exp\left(i\frac{\omega_0 t}{2}\hat{\sigma}_z\right). \tag{A.16}$$

To illustrate the working principle, in the following $\mathcal{H}_0$ (compare equation (A.9)) is transformed from the laboratory frame into the system's rotating frame:

$$\mathcal{H}_0^{\text{int}} = \mathrm{e}^{\frac{i}{2}\omega_0 t\hat{\sigma}_z}\frac{\hbar\omega_0}{2}\hat{\sigma}_z\mathrm{e}^{-\frac{i}{2}\omega_0 t\hat{\sigma}_z} - i\hbar\cdot\mathrm{e}^{\frac{i}{2}\omega_0 t\hat{\sigma}_z}\left(\frac{\partial}{\partial t}\mathrm{e}^{-\frac{i}{2}\omega_0 t\hat{\sigma}_z}\right), \tag{A.17}$$

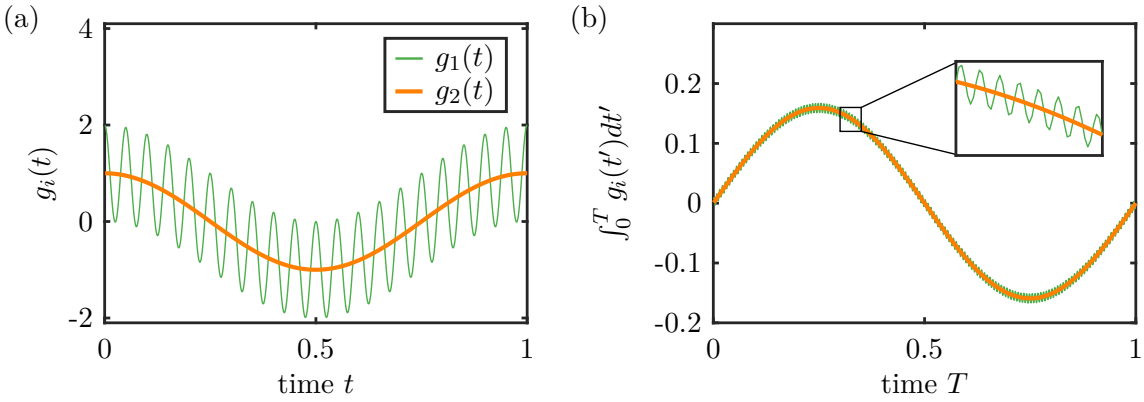

Figure A.6: Effects of fast rotating terms. (a) Comparison of the two functions $g_1(t)$ and $g_2(t)$ given by $g_1(t) = \cos(\omega_1 t) + \cos(\omega_2 t)$ (green line) and $g_2(t) = \cos(\omega_2 t)$ (orange line) with $\omega_1 = 20 \cdot \omega_2$. Both functions differ by the characteristic beating of $g_1(t)$. (b) Integral of $g_1(t)$ and $g_2(t)$ as a function of time T. Since the difference is only marginal, the quickly oscillating term can be neglected.

and since $\hat{\sigma}_z$ commutes with itself:

$$\mathcal{H}_0^{\text{int}} = \frac{\hbar\omega_0}{2}\hat{\sigma}_z \; + i\hbar \cdot e^{\frac{i}{2}\omega_0 t\hat{\sigma}_z}\left(\frac{i\omega_0}{2}\hat{\sigma}_z\right)e^{-\frac{i}{2}\omega_0 t\hat{\sigma}_z} = 0. \tag{A.18}$$

As expected, without external perturbations the quantum state stays stationary.

Effect of fast rotating terms

The rotating wave approximation (RWA) plays an important role in quantum mechanics. The idea is that fast oscillating terms in an effective Hamiltonian can be neglected. This can be seen by considering a function consisting of an oscillating term:

$$f(t) = \cos(\omega_1 t). \tag{A.19}$$

If $T \gg 1/\omega_1$, the integral over $f(t)$ reads:

$$\int_0^T f(t')\mathrm{d}t' = \frac{\sin(\omega_1 T)}{\omega_1} \approx 0, \tag{A.20}$$

since $|\sin(x)| \leq |1|$ for all $x \in \mathbb{R}$. An illustrative example is given in figure A.6 for the function:

$$g(t) = \cos(\omega_1 t) + \cos(\omega_2 t), \tag{A.21}$$

with $\omega_1 = 20 \cdot \omega_2$. For a timescale corresponding to ω_2, only the slow oscillating term in

equation (A.21) is relevant for the integral:

$$\int_0^T g(t')\mathrm{d}t' \approx \frac{\sin(\omega_2 T)}{\omega_2} = \int_0^T \cos(\omega_2 t)\mathrm{d}t'. \tag{A.22}$$

Thus, one can often neglect the effect of the terms in the Hamiltonian, which oscillate much faster than the relevant time scale.

Rotating wave approximation

If a two-level quantum system interacts with a near-resonant field with frequency ω_1 the Hamiltonian reads:

$$\mathcal{H} = \underbrace{\frac{\hbar\omega_0}{2}\hat{\sigma}_z}_{\mathcal{H}_0} + \underbrace{\hbar\Omega\cos(\omega_1 t + \theta_1)\hat{\sigma}_x}_{\mathcal{H}_1}, \tag{A.23}$$

where Ω combines the signal amplitude and the coupling to the quantum system, σ_j are the respective Pauli matrices and θ_1 is the signal phase. Since $\mathcal{H}_0$ vanishes when transformed into the rotating frame (see above), it follows:

$$\mathcal{H}_\mathrm{int} = \mathrm{e}^{i\frac{\omega_0 t}{2}\hat{\sigma}_z}\mathcal{H}_1\mathrm{e}^{-i\frac{\omega_0 t}{2}\hat{\sigma}_z}. \tag{A.24}$$

For simplicity of presentation, the substitutions $Z = \omega_0 t/2$ and $X = \omega_1 t + \theta_1$ are introduced:

$$\mathcal{H}_\mathrm{int} = e^{iZ\hat{\sigma}_z}\left[\hbar\Omega\cos(X)\hat{\sigma}_x\right]e^{-iZ\hat{\sigma}_z}. \tag{A.25}$$

After rewriting the matrix exponent as:

$$\mathrm{e}^{iZ\hat{\sigma}_z} = \cos(Z)\mathbb{1} + i\sin(Z)\hat{\sigma}_z, \tag{A.26}$$

where $\mathbb{1}$ is the identity matrix, it follows:

$$\mathcal{H}_\mathrm{int} = \left[\cos(Z)\mathbb{1} + i\sin(Z)\hat{\sigma}_z\right]\hbar\Omega\cos(X)\hat{\sigma}_x\left[\cos(Z)\mathbb{1} - i\sin(Z)\hat{\sigma}_z\right]. \tag{A.27}$$

After expansion of the products and using $\sigma_\mathrm{j}\sigma_\mathrm{m} = \epsilon_\mathrm{jmn}i\sigma_n$, $\mathcal{H}_\mathrm{int}$ reads:

$$\mathcal{H}_\mathrm{int} = \hbar\Omega\cos(X)\left[\cos(2Z)\hat{\sigma}_x - \sin(2Z)\hat{\sigma}_y\right]. \tag{A.28}$$

Assuming $|\omega_0 + \omega_1| \gg |\Omega|$, the rotating wave approximation can be applied and it follows ($\omega_\Delta = \omega_0 - \omega_1$):

$$\mathcal{H}_\mathrm{int} = \frac{\hbar\Omega}{2}\begin{pmatrix} 0 & \mathrm{e}^{-i(\omega_\Delta t+\theta_1)} \\ \mathrm{e}^{i(\omega_\Delta t+\theta_1)} & 0 \end{pmatrix}. \tag{A.29}$$

If $\omega_\Delta \approx 0$, $\mathcal{H}_{\text{int}}$ simplifies to:

$$\mathcal{H}_{\text{int}} = \frac{\hbar\Omega}{2}\left[\cos(\theta_1)\hat{\sigma}_x + \sin(\theta_1)\hat{\sigma}_y\right]. \tag{A.30}$$

The time evolution operator is then according to equation (A.8):

$$\mathcal{U}(t,0) = \exp\left(-i\frac{\Omega t}{2}\left[\cos(\theta_1)\hat{\sigma}_x + \sin(\theta_1)\hat{\sigma}_y\right]\right). \tag{A.31}$$

A.3.2 Fisher information for binomial and Poisson distributions

The importance of the Fisher information (FI) for parameter estimation is highlighted in section 4.5.1. In the following, the FI of the two most important distributions in this thesis are derived.

Fisher information for Bernoulli trial

If any further readout noise can be neglected, a quantum sensing experiment using a qubit is a Bernoulli trial. If P_0 is the probability to readout $|0\rangle$, the probability for measuring n times $|0\rangle$ in N tries is given by the binomial distribution:

$$\mathcal{B}(n|P_0,N) = \binom{N}{n} P_0^n (1-P_0)^{N-n}. \tag{A.32}$$

The corresponding FI reads according to equation (4.24):

$$\begin{aligned} I(\omega) &= \sum_{n\in\mathcal{X}} \left[\frac{1}{\mathcal{B}(n|P_0,N)^2}\left(\frac{n\mathcal{B}(n|P_0,N)}{P_0} - \frac{(N-n)\mathcal{B}(n|P_0,N)}{(1-P_0)}\right)^2 \left(\frac{\partial P_0}{\partial\omega}\right)^2 \mathcal{B}(n|P_0,N)\right] = \\ &= \frac{1}{(P_0(1-P_0))^2}\cdot\left(\frac{\partial P_0}{\partial\omega}\right)^2 \sum_{n\in\mathcal{X}}\left[(n-NP_0)^2\mathcal{B}(n|P_0,N)\right], \end{aligned} \tag{A.33}$$

where $\mathcal{X}$ is the set of all possible outcomes and ω the parameter to be estimated. Since $N\cdot P_0$ is the expectation value and $\sum_{x\in\mathcal{X}}\left[(x-NP_0)^2\mathcal{B}(n|P_0,N))\right]$ is the definition of the variance, which for the binomial distribution is given by $N\cdot P_0(1-P_0)$, it follows:

$$I(\omega) = \frac{N}{P_0(1-P_0)}\left(\frac{\partial P_0}{\partial\omega}\right)^2. \tag{A.34}$$

Fisher information for Poisson distributions

The discrete nature of photons can be modelled by the Poisson distribution:

$$\mathcal{P}(N_{\mathrm{ph}}|\mathcal{N}) = \frac{\mathcal{N}^{N_{\mathrm{ph}}}}{N_{\mathrm{ph}}!}\mathrm{e}^{-\mathcal{N}}, \tag{A.35}$$

which describes the probability to find N_{ph} photons in a measurement for which $\mathcal{N}$ photons are expected. According to equation (4.24), the FI reads:

$$\begin{aligned} I(\omega) &= \sum_{N_{\mathrm{ph}}\in\mathcal{X}} \left[\frac{1}{\mathcal{P}(N_{\mathrm{ph}}|\mathcal{N})^2} \left(\frac{N_{\mathrm{ph}} \cdot \mathcal{P}(N_{\mathrm{ph}}|\mathcal{N})}{\mathcal{N}} - \mathcal{P}(N_{\mathrm{ph}}|\mathcal{N}) \right)^2 \left(\frac{\partial \mathcal{N}}{\partial \omega} \right)^2 \mathcal{P}(N_{\mathrm{ph}}|\mathcal{N}) \right] = \\ &= \frac{1}{\mathcal{N}^2} \cdot \left(\frac{\partial \mathcal{N}}{\partial \omega} \right)^2 \sum_{N_{\mathrm{ph}}\in\mathcal{X}} \left[(N_{\mathrm{ph}} - \mathcal{N})^2 \mathcal{P}(N_{\mathrm{ph}}|\mathcal{N}) \right]. \end{aligned} \tag{A.36}$$

As $\sum_{N_{\mathrm{ph}}\in\mathcal{X}} \left[(N_{\mathrm{ph}} - \mathcal{N})^2 \mathcal{P}(N_{\mathrm{ph}}|\mathcal{N}) \right]$ is the variance, which is given by $\mathcal{N}$ for the Poisson distribution, the Fisher information reads:

$$I(\omega) = \frac{1}{\mathcal{N}} \left(\frac{\partial \mathcal{N}}{\partial \omega} \right)^2. \tag{A.37}$$

A.3.3 Sensitivity of ODMR spectroscopy

As discussed in section 4.5, the precision of a measurement is given by the sensor response and the readout noise. Regarding NV centre ODMR (compare section 4.1), the noise is dominated by PSN and the slope of the spectrum yields the sensor response. Although the exact line-shape depends on a variety of parameters, as the environmental noise, the dips in an ODMR spectrum can usually be reasonably reproduced by a Lorentzian function $\mathcal{I}(\nu)$:

$$\mathcal{I}(\nu) = \mathcal{I}_0 \left(1 - \frac{C \left(\frac{1}{2}\Gamma \right)^2}{(\nu - \nu_0)^2 + \left(\frac{1}{2}\Gamma \right)^2} \right), \tag{A.38}$$

where $\mathcal{I}_0$ is the number of collected photons in the off-resonant case, ν_0 is the resonance frequency, $C = (\mathcal{I}_0 - \mathcal{I}(\nu_0))/\mathcal{I}_0$ is the contrast, and Γ is the full width at half maximum (FWHM). Since PSN is almost independent of the readout intensity, the most sensitive point is where the sensor response to a change of the measurement parameter is maximal – or in other words, where the slope $(\partial\mathcal{I}/\partial\nu)$ is highest, as sketched in figure A.7. Then is follows:

$$\left| \left(\frac{\partial \mathcal{I}(\nu)}{\partial \nu} \right) \right|_{\mathrm{max}} = \frac{3\sqrt{3} C \mathcal{I}_0}{4\Gamma}, \tag{A.39}$$

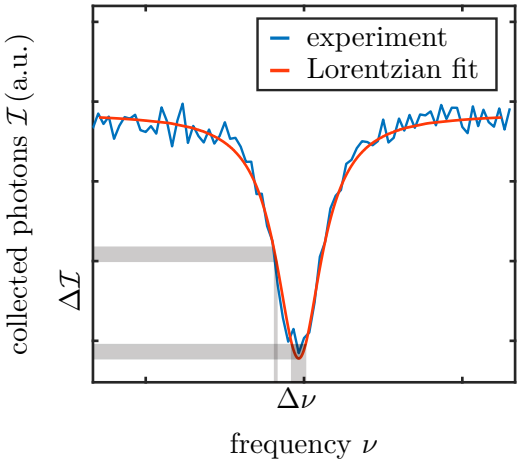

Figure A.7: Precision of ODMR spectroscopy. The frequency uncertainty $\Delta\nu$ depends on the uncertainty of the signal $\Delta\mathcal{I}$ and the sensor response, given by the slope. Usually the best estimate can be achieved when measuring at the point with the highest slope.

and the resulting sensitivity reads (compare section 4.5.3):

$$\eta_{\mathrm{ODMR}} = \frac{4}{3\sqrt{3}} \frac{\Gamma}{\gamma_{\mathrm{NV}} C} \frac{\sqrt{\mathcal{I}_{\mathrm{max}}}}{\mathcal{I}_0}, \tag{A.40}$$

where $\mathcal{I}_{\mathrm{max}} = \mathcal{I}_0(1 - 3C/4)$ are the number of recorded photons at the maximal slope. The sensitivity depends on the width of the resonance line Γ, which is a function of the laser power, the microwave amplitude and the T_2^*-time [313].

A.3.4 Precision and dynamic range for Ramsey interferometry

In section 4.2 the Ramsey protocol is introduced. In the following the achievable precision and dynamic range are discussed in more detail.

Precision of Ramsey interferometry

Since the precision depends on the noise of the measurement, the type of noise is important. In the edge case that only QPN limits the precision, the uncertainty ΔB for estimating an unknown magnetic field B aligned parallel to the symmetry axis of the NV centre is given by (compare equation (4.29)):

$$\Delta B = \min \left(\frac{\sqrt{P_0(1 - P_0)}}{N} \left| \frac{\partial P_0}{\partial B} \right|^{-1} \right), \tag{A.41}$$

where N is the number of repetitions. The population typically follows (compare equation (4.7)):

$$P_0 = \frac{1}{2} - \frac{1}{2}\cos\left(\tilde{\gamma}_{\mathrm{NV}} B T_{\mathrm{int}}\right), \tag{A.42}$$

where T_{int} is the coherent interaction time. It follows:

$$\Delta B = \min\left(\frac{\sqrt{1-\cos^2\left(\tilde{\gamma}_{\mathrm{NV}} B T_{\mathrm{int}}\right)}}{\sqrt{N}\left|\sin\left(\tilde{\gamma}_{\mathrm{NV}} B T_{\mathrm{int}}\right)\right|\tilde{\gamma}_{\mathrm{NV}} T_{\mathrm{int}}}\right) = \frac{1}{\tilde{\gamma}_{\mathrm{NV}} T_{\mathrm{int}}\sqrt{N}}. \tag{A.43}$$

The precision improves linearly with the interaction time and as $\sqrt{N}$. Taking the total time $T = N T_{\mathrm{int}}$ into account it follows for the sensitivity (neglecting measurement overheads):

$$\eta = \frac{1}{\tilde{\gamma}_{\mathrm{NV}}\sqrt{T_{\mathrm{int}}}}. \tag{A.44}$$

For the traditional readout of NV centres the noise is dominated by photon shot noise and the uncertainty follows (compare equation (4.33)):

$$\Delta B = \min\left(\sqrt{\mathcal{N}}\left|\frac{\partial \mathcal{N}}{\partial B}\right|^{-1}\right), \tag{A.45}$$

where $\mathcal{N}$ is the number of photons expected to record within N repetitions:

$$\mathcal{N} = (\mathcal{I}_0 - \mathcal{I}_1)P_0 + \mathcal{I}_1, \tag{A.46}$$

and $\mathcal{I}_0$ and $\mathcal{I}_0$ are the expected number of photons for the states $|0\rangle$ and $|1\rangle$ (compare equation (3.13)). It follows:

$$\Delta B = \min\left(\frac{\sqrt{\mathcal{N}}}{0.5(\mathcal{I}_0 - \mathcal{I}_1)\left|\sin\left(\tilde{\gamma}_{\mathrm{NV}} B T_{\mathrm{int}}\right)\right|\tilde{\gamma}_{\mathrm{NV}} T_{\mathrm{int}}}\right). \tag{A.47}$$

The lowest uncertainty is usually achieved if $\left|\sin\left(\tilde{\gamma}_{\mathrm{NV}} B T_{\mathrm{int}}\right)\right| \approx 1$, which corresponds to the points of the highest slope in the Ramsey fringes as exemplified in figure A.8. As a consequence, $P_0 \approx 0.5$ and $\mathcal{N} \approx 0.5 \cdot (\mathcal{I}_0 + \mathcal{I}_1)$ and it follows:

$$\Delta B \approx \frac{\sqrt{0.5(\mathcal{I}_0 + \mathcal{I}_1)}}{0.5(\mathcal{I}_0 - \mathcal{I}_1)\tilde{\gamma}_{\mathrm{NV}} T_{\mathrm{int}}} = \frac{1}{C\sqrt{\mathcal{N}}\tilde{\gamma}_{\mathrm{NV}} T_{\mathrm{int}}}, \tag{A.48}$$

where the contrast is here defined as $C = (\mathcal{I}_0 - \mathcal{I}_1)/(\mathcal{I}_0 + \mathcal{I}_0)$. The sensitivity then reads (neglecting measurement overheads):

$$\eta \approx \frac{1}{\tilde{\gamma}_{\mathrm{NV}} C\sqrt{\mathcal{N}_{\sin} T_{\mathrm{int}}}}, \tag{A.49}$$

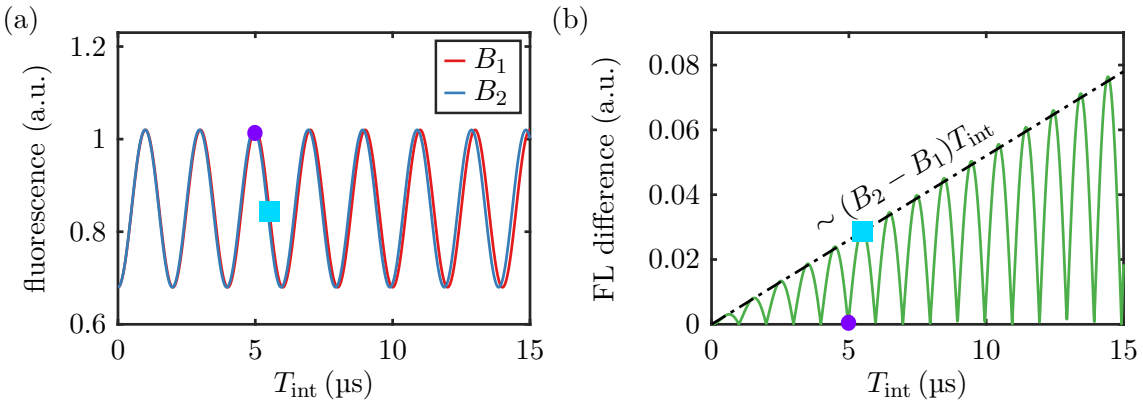

Figure A.8: Precision of Ramsey interferometry. (a) Simulated Ramsey fringes for two similar magnetic fields B_1 and B_2. (b) The fluorescence (FL) difference almost vanishes close to the signal anti-nodes (e.g. violet circle) and is largest at the points of maximum slope (e.g. light blue square). The envelop increases proportional to the interaction time T_{int}.

where $\mathcal{N}_{\mathrm{sin}} = \mathcal{N}/N$ is the number of photons expected to be detected during a single readout.

In principle T_{int} should be extended as far as possible. Due to magnetic fluctuations in the environment the quantum state relaxes (compare section 4.5.4) and the contrast reduces with increasing T_{int} as shown in figure A.9. The optimal coherent interaction time is usually close to half the T_2^*-time [4] if measurement overheads can be neglected, and approaches T_2^* if these overheads are comparable or larger than the interaction time.

Dynamic range of Ramsey interferometry

Another important property is the accessible field range. Due to phase wrapping the problem is that sinusoidal functions are bijective only in the interval $\phi \in [0, \pi)$. For example, the measurement outcome is the same if $\phi(= \tilde{\gamma}_{\mathrm{NV}} B T_{\mathrm{int}})$ is $\pi/2$ or $5\pi/2$. As a consequence, a prior knowledge is necessary for an unambiguous determination. When recording at the point with highest slope, the magnetic field range is given by $B \in [-B_\Delta, B_\Delta)$, where $B_\Delta = \frac{\pi}{2\tilde{\gamma}_{\mathrm{NV}} T_{\mathrm{int}}}$ [314].

A longer T_{int} leads to a higher precision, but a reduced accessible field range. Different strategies to overcome this issue have been developed and experimentally tested. The basic idea is to start with a small T_{int} in order to have a high field range and then step-by-step change T_{int} to improve the measurement precision [314]. Recently it has been shown that adaptive measurements based on machine learning can reach a sensitivity of $60\,\mathrm{nTs}^{1/2}$ taking initialisation, readout and computational overheads into account [279].

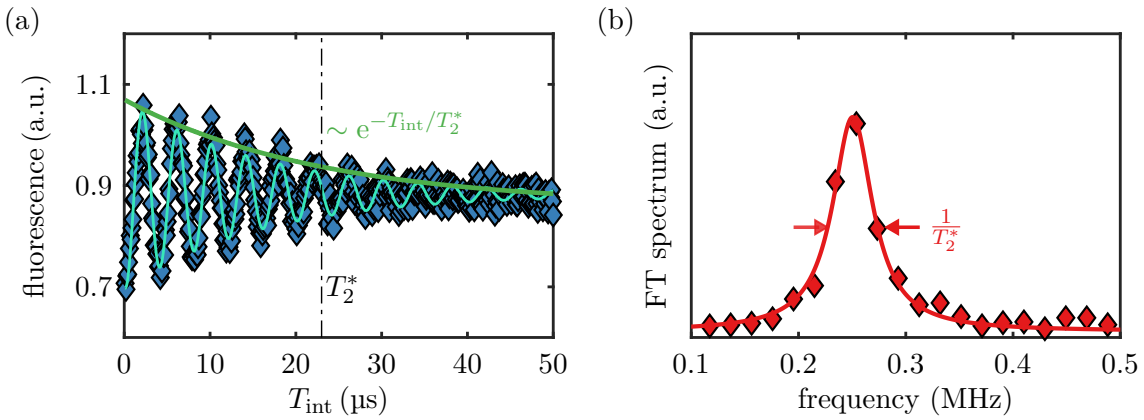

Figure A.9: Limits of Ramsey interferometry. (a) Due to fluctuations in the environment or interaction with magnetic noise, the oscillation decays with the T_2^* dephasing time. The solid light green line correspond to an exponentially decaying sinusoidal fit. (b) Fourier transform (FT) spectrum. The dephasing limits the linewidth and thus the precision of the measurement outcome. The solid line corresponds to a Lorentzian fit to the data.

A.3.5 Derivation of the spectral filter for dynamical decoupling

In section 4.3.2 the spectral filter for dynamical decoupling (DD) is discussed. In the following, equation (4.15) is derived in more detail. The Fourier transform of the function describing the π-pulses $F(t)$ reads:

$$\mathcal{F}(\omega) = \int_{-\infty}^{\infty} F(t') e^{i\omega t'} dt', \tag{A.50}$$

where $F(t)$ is a stepwise function and changes its sign after every π-pulse (compare equation (4.13)):

$$\mathcal{F}(\omega) = \int_{t_0}^{t_0+\tau} e^{i\omega t'} dt' - \int_{t_0+\tau}^{t_0+2\tau} e^{i\omega t'} dt' + \int_{t_0+2\tau}^{t_0+3\tau} e^{i\omega t'} dt' - .... \int_{t_0+(N_\pi-1)\tau}^{t_0+N_\pi\tau} e^{i\omega t'} dt', \tag{A.51}$$

where τ is the spacing between π-pulses and t_0 a temporal offset. Integration and inserting the boundary parameters yields:

$$\mathcal{F}(\omega) = \frac{1}{i\omega}\left[e^{i\omega(t_0+\tau)} - e^{i\omega t_0} - e^{i\omega(t_0+2\tau)} + e^{i\omega(t_0+\tau)} + ... + (-1)^{N_\pi} e^{i\omega(t_0+(N_\pi-1)\tau)}\right]. \tag{A.52}$$

It follows:

$$\mathcal{F}(\omega) \approx \frac{2}{i\omega}\left[\sum_{n=0}^{N_\pi} (-1)^n e^{i\omega n\tau}\right]. \tag{A.53}$$

A.3.6 Additional information concerning Qdyne

Detection frequency in Qdyne

In section 7.1 it has been shown that the detection frequency $\delta_\mathrm{b} = |\nu_\mathrm{LO} - \nu|$ for the quantum heterodyne (Qdyne) technique is given by the difference between local oscillator frequency ν_LO and signal frequency ν (compare equation (7.4)). In the following, this is derived in more detail. The time-dependent phase $\theta(t)$ of an oscillating field with frequency ν can be written as:

$$\theta(t) = 2\pi\nu t + \theta_0. \tag{A.54}$$

For Qdyne this phase is measured in intervals of t_Δ and by setting $\theta_0 = 0$ for simplicity, it follows for the nth measurement:

$$\theta(n) = 2\pi\nu n t_\Delta. \tag{A.55}$$

By rewriting t_Δ as the closest multiple of the signal period $T_\mathrm{p} = 1/\nu$ plus the remaining time δ_t, it follows:

$$\theta(n) = 2\pi\nu n(mT_\mathrm{p} + \delta_t), \tag{A.56}$$

where m is an integer number. Since $\nu \cdot T_\mathrm{p} = 1$, it is $m \cdot n \cdot \nu \cdot T_\mathrm{p} = 1$ and it follows:

$$\begin{aligned}
\theta(n) &= 2\pi\nu n\delta_t = 2\pi\nu n\frac{\nu_\mathrm{LO} - \nu}{\nu_\mathrm{LO} - \nu}\delta_t \\
&= 2\pi\nu n\frac{\nu_\mathrm{LO} - \nu}{\frac{m}{t_\Delta} - \frac{1}{T_\mathrm{p}}}\delta_t = 2\pi\nu n\frac{\nu_\mathrm{LO} - \nu}{\frac{mT_\mathrm{p} - t_\Delta}{t_\Delta T_\mathrm{p}}}\delta_t \\
&= 2\pi(\nu_\mathrm{LO} - \nu) \cdot nt_\Delta \cdot \nu T_\mathrm{p} \cdot \frac{\delta_t}{mT_\mathrm{p} - t_\Delta}.
\end{aligned} \tag{A.57}$$

By using that $\nu \cdot T_\mathrm{p} = 1$ and $\delta_t = mT_\mathrm{p} - t_\Delta$, it follows:

$$\theta(n) = 2\pi(\nu_\mathrm{LO} - \nu)n \cdot t_\Delta = 2\pi(\nu_\mathrm{LO} - \nu)t. \tag{A.58}$$

After adding θ_0 again, the equality of equations A.54 and A.58 is shown.

Timing of the control pulse in Qdyne

For the technique described in chapter 9, a control $\pi/2$-pulse around a fixed axis in the beginning of the sequence is used. However, this $\pi/2$-control may be performed at the end of the sequence as well. In order to illustrate this, the state evolution for this case is sketched in figure A.10. For this purpose, the same rotation angles Θ and the same signal phases θ are used as for figure 9.2. Although, the final states are in principle different

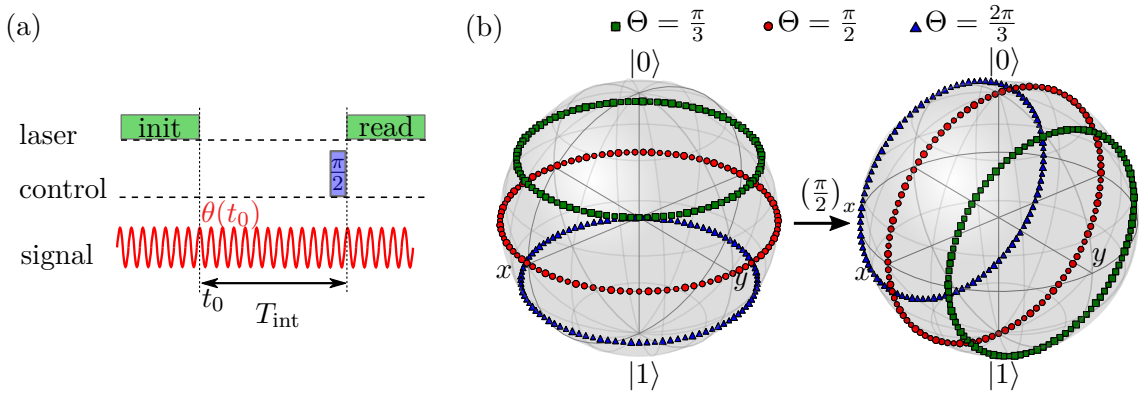

Figure A.10: Alternative Qdyne sequence and corresponding state evolution. (a) Measurement sequence when the control $\pi/2$-pulse is applied right before the readout. (b) On the left side the quantum states after the interaction period with the signal, but before the $\pi/2$-pulse are shown for a variety of signal phases $\theta \in [0, 2\pi)$ and three rotation angles Θ. After applying the $\pi/2$-pulse, here around the x-axis, the final states depicted on the right side are obtained.

from the case when the $\pi/2$-pulse is applied in the beginning, the measurement outcomes are the same, since only the projection onto the z-axis is relevant.

Alternative decoupling sequence

In section 9.4.2, it is shown that a driving field can be used to decouple the sensor and thereby extend the interaction time. In order to apply the Qdyne principle the measurement outcomes are still required to dependent on the signal phase θ. In the main part this was shown for the central peak. Using the modified protocol sketched in figure A.11, it is also possible to use the other two transitions. The simulations (see section 9.4.2 for more details) in figure A.11(b) and (c) verify the working principle. In this case the measurement contrast dependency on θ is sinusoidal.

A.3.7 Charge state of the nitrogen-vacancy centre

As shortly discussed in sections 3.1.3, 3.3 and 8.4.2, the NV centre can be in different charge states and in particular, optical illumination can induce interconversions between the negative NV^- and the neutral NV^0 states [80, 81]. For the NV^- to NV^0 conversion, it is reported that the physical principle involves a two photon process in which one photon excites the NV centre and the second photon transfers the electron to the conduction band [105, 315]. The back conversion is also a two step process, which is in more detail discussed in [316]. In the following, a simple technique, applicable to identify the current

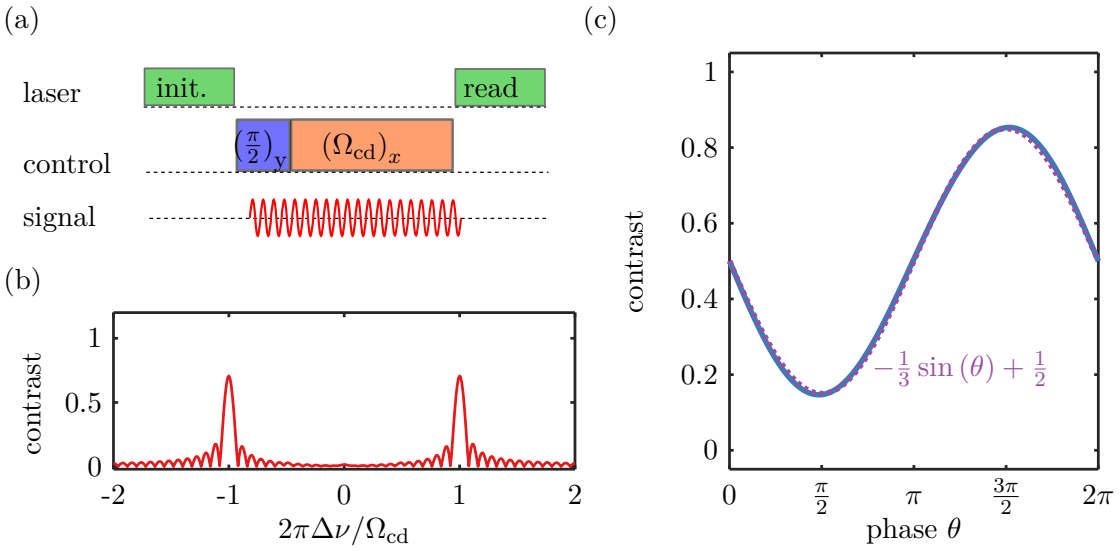

Figure A.11: Modified version for Qdyne based on coherent decoupling. (a) Sketch of pulse sequence. (b) Simulated measurement contrast as function of detuning $\Delta\nu$. The middle line vanishes for this protocol. (c) Simulated measurement contrast as a function of the signal phase θ (blue solid line), which is identical for both peaks. The dependency is sinusoidal (purple dotted line).

charge state, is shortly introduced and it is shown that for laser pulses typically used for this thesis it is about three times more probable to find the NV^- state.

The idea to discriminate both charge states is to use a light source with a wavelength between the zero phonon lines of NV^- (637 nm) and NV^0 (575 nm). Assuming just single photon processes, only the NV^- state is excited in this case and as a consequence, fluorescence is only emitted if the NV centre is in this state [257]. The measurement sequence is sketched in figure A.12(a). As usual, a green laser pulse (532 nm) with a duration of a few microseconds is used to initialise the NV centre. After a short idle time ($\sim 1\,\mu s$) a much longer orange laser pulse (duration about 5 ms) with a wavelength of 594 nm is used to readout the charge state. Since the conversion rate scales quadratically with the illumination intensity, it is important to choose the laser power low in order to prevent conversion to the NV^0 state [316].

Just the fluorescence photons collected during the illumination with the orange laser pulse are recorded and in order to collect sufficient statistics this simple sequence was repeated about $1.4 \cdot 10^4$ times. The resulting histogram is plotted in figure A.12(b) and is a combination of two distributions corresponding to the fluorescence of the NV^- and NV^0 states. The histogram is fitted using the sum of two Poisson distributions and by computing the respective areas the probability to be in either charge state can be estimated. For

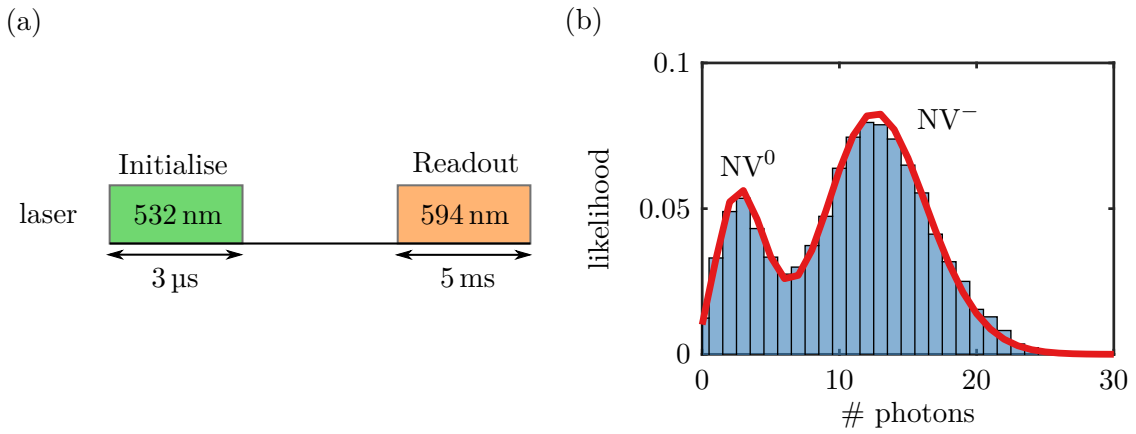

Figure A.12: Probabilities to find the NV centre in the NV$^-$ and NV^0 states. (a) Pulse sequence for measuring the charge state of an NV centre. (b) Histogram of recorded fluorescence photons during illumination with the orange laser pulse. The red solid line corresponds to a fit consisting of the sum of two Poissonian distributions.

the presented experimental result, it can be found that the probability for the NV$^-$ state is about 75 % and for the NV^0 state about 25 %.

More details about the conversion processes and the dependency on the laser power and wavelength can be found in [257, 316].

Abbreviations

AC alternating current

AOM acousto-optic modulator

APD avalanche photodiode

AWG arbitrary waveform generator

CNOT controlled-not

CVD chemical vapour deposition

cw continuous wave

DC direct current

DD dynamical decoupling

EPR electron paramagnetic resonance

FFT Fast Fourier transform

FI Fisher information

FID free induction decay

FWHM full width at half maximum

GUI graphical user interface

HPHT high pressure high temperature

ISC intersystem crossing

LAC level anti-crossing

MRI magnetic resonance imaging

MW microwave

NMR nuclear magnetic resonance

NV nitrogen-vacancy

ODMR optically detected magnetic resonance

PCB printed circuit board

PL photoluminescence

ppm parts per million

PSN photon shot noise

Qdyne quantum heterodyne

QPN quantum projection noise

qubit quantum bit

RF radio frequency

RWA rotating wave approximation

SIL solid immersion lens

SNR signal-to-noise ratio

SSR single-shot readout

TTL transistor-transistor-logic

ZFS zero field splitting

ZPL zero phonon line

Symbols

$\mathcal{B}$ binomial distribution

c_0 expected number of photons for state $|0\rangle$ within a single readout

c_1 expected number of photons for state $|1\rangle$ within a single readout

E_0 energy difference between the levels of the qubit

$h = 6.626\,069 \cdot 10^{-34}\,\mathrm{J\,s}$, Planck constant

$\hbar = h/(2\pi) = 1.054\,571\,817 \cdot 10^{-34}\,\mathrm{J\,s}$, reduced Planck constant

I Fisher information

$k_B = 1.380\,649 \cdot 10^{-23}\,\mathrm{J/K}$, Boltzmann constant

m_s electron spin quantum number

N_ph number of detected photons

N_π number of π-pulses in a dynamical decoupling sequence

N_thres threshold photon count for frequency discrimination

$\mathcal{N}$ number of photons expected to detect

$\mathcal{N}_\mathsf{sin}$ expected number of detected photons in a single readout

P_0 sensor population, probability to readout $|0\rangle$

P_SSR flip probability of the nuclear memory spin

$\mathcal{P}$ Poisson distribution

R_ens number of repetitions for the ensemble average

R_{SSR} number of repetitions for the SSR average

$\hat{S}_x$ x-component of the spin vector

$\hat{S}_y$ y-component of the spin vector

$\hat{S}_z$ z-component of the spin vector

T_{int} coherent interaction time

T total recording time

T_{sin} total time for a single measurement including all temporal overheads

T_1 life time

T_2 coherence time

T_2^* dephasing time

t_Δ time between consecutive Qdyne measurements

t_{opt} optimal coherent interaction time for frequency discrimination

X_{SSR} number of repetitive readouts for one single-shot readout

δ_{b} beating frequency in a Qdyne measurement

$\gamma_{\mathsf{NV}} \approx 28.03\,\mathrm{GHz/T}$, gyromagnetic ratio of the NV centre

$\tilde{\gamma}_{\mathsf{NV}} = 2\pi \cdot \gamma_{\mathrm{NV}}$, gyromagnetic ratio of the NV centre in units of rad/(sT)

γ_n gyromagnetic ratio of a nuclear spin

γ angle between initialisation and readout basis

$\mu_0 = 4\pi \cdot 10^7\,\mathrm{N/A^2}$, vacuum permeability

ν_L Larmor frequency

ν_{LO} local oscillator frequency

ν_0 transition frequency of the qubit in units of Hertz

$\omega_0 = E_0/\hbar$, angular transition frequency of the qubit in units of radian per second

Ω coupling strength, also Rabi frequency

Ω_{cd} coupling strength of coherent driving field

Ω_{R} generalised Rabi frequency

$|\Psi\rangle$ quantum state

ϕ quantum phase of the sensor qubit, azimuthal angle in the Bloch sphere

$\hat{\sigma}_x = \begin{pmatrix} 0 & 1 \\ 1 & 0 \end{pmatrix}$, Pauli x-matrix

$\hat{\sigma}_y = \begin{pmatrix} 0 & -i \\ i & 0 \end{pmatrix}$, Pauli y-matrix

$\hat{\sigma}_z = \begin{pmatrix} 1 & 0 \\ 0 & -1 \end{pmatrix}$, Pauli z-matrix

$\mathbb{1} = \begin{pmatrix} 1 & 0 \\ 0 & 1 \end{pmatrix}$ or $\begin{pmatrix} 1 & 0 & 0 \\ 0 & 1 & 0 \\ 0 & 0 & 1 \end{pmatrix}$, identity matrix

ϑ polar angle in the Bloch sphere

Θ rotation angle on the Bloch sphere

θ phase of an oscillating signal

$\theta_{\pi/2}$ phase of a $\pi/2$-pulse

ζ angle of magnetic field misalignment

List of Figures

2.1 Qubit as two-level system and presented in the Bloch sphere 8
2.2 Binomial distribution and standard deviation 12
2.3 Laboratory and rotating frame 14
2.4 Coherent control of a qubit 16
2.5 Application of $\pi/2$-pulses around different axes 17
2.6 Rotation about the z-axis 18
2.7 Steps in a typical quantum sensing measurement 19

3.1 Publications relating to NV centres 21
3.2 Discrete energy levels in solid state systems 23
3.3 Photography of different types of diamond 25
3.4 The nitrogen-vacancy centre in diamond 26
3.5 The nitrogen-vacancy centre as a spin qubit 27
3.6 Level scheme of the NV centre's electronic spin in the ground state 31
3.7 Initialisation of the NV centre's electronic spin by optical pumping 33
3.8 Relaxation dynamics and fluorescence properties of the NV centre 35
3.9 Fluorescence for different spin states as a function of time 36
3.10 Optimal readout duration for NV centres 37
3.11 Fluorescence for differently shaped diamonds 39
3.12 Coherent control of the NV centre 43

4.1 Principle of the ODMR technique 46
4.2 Principle of pulsed ODMR 47
4.3 Scheme and experimental examples for Ramsey interferometry 49
4.4 Principle of a pulsed DD sequence 51
4.5 Principle of sensing AC fields using DD 52
4.6 DD control in time and frequency space 53
4.7 Performance of DD as a function of pulse spacing and signal phase 55
4.8 Principle of the XY8-sequence 56
4.9 Experimental determination of the T_2^*- and T_2-times for a NV centre 61
4.10 Experimental determination of the T_1-time for a NV centre 63

5.1 Size comparison between classical and nanoscale NMR 68
5.2 Interpretation of an NMR spectrum 71
5.3 Nanoscale nuclear magnetic resonance setup 74
5.4 Simulated nanoscale NMR signal 75
5.5 Experimental nanoscale NMR 76
5.6 Deconvolution of the measurement signal 77

6.1 Basic unit for pulsed dynamical decoupling 82
6.2 Principle of phase randomisation for dynamical decoupling 83
6.3 Simulated quantum spectroscopy with the XY8 sequence 84
6.4 Experimental suppression of spurious harmonics by phase randomisation . . 87
6.5 Experimental detection of proton spins using the randomised XY8 sequence 88
6.6 Quantum spectroscopy with the randomised XY8 sequence 90
6.7 Enhancement of robustness with phase randomisation 92
6.8 Enhanced phase robustness with the randomisation protocol 93

7.1 Limited resolution of dynamical decoupling spectroscopy 96
7.2 The Qdyne principle 98
7.3 Recording and analysis principle of a Qdyne measurement 100
7.4 Comparison between Qdyne and traditional DD spectroscopy 102
7.5 Qdyne and traditional DD spectra as a function of time 103
7.6 Resolution and SNR of Qdyne and DD spectra 104
7.7 Frequency precision for Qdyne and dynamical decoupling spectroscopy . . . 106
7.8 Spectroscopy of a signal with multiple frequencies and spectral bandwidth . 109
7.9 Nanoscale NMR using Qdyne 111
7.10 Qdyne spectroscopy using thermal polarisation 112

8.1 Frequency discrimination problem 116
8.2 Protocol for quantum frequency discrimination 118
8.3 Experimental demonstration of the discrimination principle 120
8.4 Discrimination for complex frequency distributions 121
8.5 Strategies to improve the sensitivity of a fluorescent sensor 123
8.6 Quantum wire diagram for ensemble averaging and photon statistics 124
8.7 Expected number of photons and noise for ensemble averaging 125
8.8 Decision criterion for frequency discrimination 126
8.9 Protocol and photon statistics for single-shot readout 128
8.10 Signal-to-noise ratio and flip probability for single-shot readout 130
8.11 Readout noise as a function of interaction time 133

8.12 Experimental frequency discrimination for both strategies 134

9.1 Sketch of measurement sequence 138
9.2 Illustration of the state evolution on the Bloch sphere 141
9.3 Experimental demonstration of the principle 143
9.4 Spectroscopy of a magnetic field with three frequency components 145
9.5 Spectra recorded under different readout and initialisation conditions 146
9.6 Shifting the resonance frequency using a DC current 147
9.7 Experimental determination of the signal parameters 149
9.8 Time trace and FFT for Qdyne recorded with SSR 151
9.9 SNR in dependence of the number of repetitive readouts 152
9.10 Principles of Qdyne based on decoupling through coherent driving 154
9.11 Qdyne based on decoupling through coherent driving 155
9.12 Dynamic bandwidth of the spectrum analyser 157
9.13 Spectral bandwidth of the spectrum analyser 158

A.1 Schematic overview of the experimental setup 168
A.2 Schematic overview of the confocal microscope 169
A.3 Magnetic field alignment by fluorescence optimisation 174
A.4 Magnetic field alignment by transition frequencies optimisation 175
A.5 Magnetic field alignment by nuclear spin lifetime optimisation 177
A.6 Effects of fast rotating terms 182
A.7 Precision of ODMR spectroscopy 186
A.8 Precision of Ramsey interferometry 188
A.9 Limits of Ramsey interferometry 189
A.10 Alternative Qdyne sequence and corresponding state evolution 191
A.11 Modified version for Qdyne based on coherent decoupling 192
A.12 Probabilities to find the NV centre in the NV^- and NV^0 states 193

List of Tables

3.1 Types of diamond 24
3.2 Coupling constants for the NV centre 30

5.1 List of some of the most important nuclear isotopes with a spin 69

Bibliography

[1] N. Tyler, *Safe and secure*, Newelectronics magazine **49**, 24 (2016),
URL: http://www.newelectronics.co.uk/article-images/149323/P24-25.pdf

[2] S. A. Bagloee, M. Tavana, M. Asadi, and T. Oliver, *Autonomous vehicles: challenges, opportunities, and future implications for transportation policies*, Journal of Modern Transportation **24**, 284 (2016),
URL: http://dx.doi.org/10.1007/s40534-016-0117-3

[3] B. P. Abbott, et al., *Observation of Gravitational Waves from a Binary Black Hole Merger*, Physical Review Letters **116**, 061102 (2016),
URL: http://dx.doi.org/10.1103/PhysRevLett.116.061102

[4] C. L. Degen, F. Reinhard, and P. Cappellaro, *Quantum sensing*, Reviews of Modern Physics **89**, 035002 (2017),
URL: http://dx.doi.org/10.1103/RevModPhys.89.035002

[5] J. F. Barry, M. J. Turner, J. M. Schloss, D. R. Glenn, Y. Song, M. D. Lukin, H. Park, and R. L. Walsworth, *Optical magnetic detection of single-neuron action potentials using quantum defects in diamond*, Proceedings of the National Academy of Sciences **113**, 14133 (2016),
URL: http://dx.doi.org/10.1073/pnas.1601513113

[6] S. A. Diddams, J. C. Bergquist, S. R. Jefferts, and C. W. Oates, *Standards of Time and Frequency at the Outset of the 21st Century*, Science **306**, 1318 (2004),
URL: http://dx.doi.org/10.1126/science.1102330

[7] F. Riehle, *Frequency Standards: Basics and Applications*, Wiley-VCH, Weinheim, (2004),
URL: http://dx.doi.org/10.1002/3527605991

[8] K. Roth, *NMR-Tomography and -Spectroscopy in Medicine*, Springer, Berlin Heidelberg, (1984),
URL: http://dx.doi.org/10.1007/978-3-642-69741-8

[9] H. H. Mantsch, L. P. Choo-Smith, and R. A. Shaw, *Vibrational spectroscopy and medicine: An alliance in the making*, Vibrational Spectroscopy **30**, 31 (2002),
URL: http://dx.doi.org/10.1016/S0924-2031(02)00036-X

[10] R. Bowtell, *Medical imaging: Colourful future for MRI*, Nature **453**, 993 (2008),
URL: http://dx.doi.org/10.1038/453993a

[11] H. W. Spiess, *NMR Spectroscopy: Pushing the Limits of Sensitivity*, Angewandte Chemie - International Edition **47**, 639 (2008),
URL: http://dx.doi.org/10.1002/anie.200704428

[12] E. Betzig and J. K. Trautman, *Near-Field Optics: Microscopy, Spectroscopy, and Surface Modification Beyond the Diffraction Limit*, Science **257**, 189 (1992),
URL: http://dx.doi.org/10.1126/science.257.5067.189

[13] P. Mansfield, *Snapshot Magnetic Resonance Imaging (Nobel Lecture)*, Angewandte Chemie International Edition **43**, 5456 (2004),
URL: http://dx.doi.org/10.1002/anie.200460078

[14] M. A. Richards, J. A. Scheer, and W. A. Holm, *Principles of Modern Radar: Basic principles*, SciTech Publishing, Raleigh, (2010),
URL: http://dx.doi.org/10.1049/sbra021e

[15] S. Lloyd, M. Mohseni, and P. Rebentrost, *Quantum principal component analysis*, Nature Physics **10**, 631 (2014),
URL: http://dx.doi.org/10.1038/NPHYS3029

[16] L. Reimer, *Scanning Electron Microscopy*, volume 45, Springer, Berlin Heidelberg, (1998),
URL: http://dx.doi.org/10.1007/978-3-540-38967-5

[17] D. B. Williams and C. B. Carter, *Transmission Electron Microscopy: A Textbook for Materials Science*, Springer Science+Business Media, New York, (2009),
URL: http://dx.doi.org/10.1007/978-0-387-76501-3

[18] B. Voigtländer, *Atomic Force Microscopy*, NanoScience and Technology, Springer Nature Switzerland AG, Cham, (2019),
URL: http://dx.doi.org/10.1007/978-3-030-13654-3

[19] Y. Waseda, E. Matsubara, and K. Shinoda, *X-Ray Diffraction Crystallography*, Springer, Berlin Heidelberg, (2011),
URL: http://dx.doi.org/10.1007/978-3-642-16635-8

[20] D. A. Redman, S. Brown, R. H. Sands, and S. C. Rand, *Spin Dynamics and Electronic States of N-V Centers in Diamond by EPR and Four-Wave-Mixing Spectroscopy*, Physical Review Letters **67**, 3420 (1991),
URL: http://dx.doi.org/10.1103/PhysRevLett.67.3420

[21] A. Gruber, A. Dräbenstedt, C. Tietz, L. Fleury, J. Wrachtrup, and C. Von Borczyskowski, *Scanning Confocal Optical Microscopy and Magnetic Resonance on Single Defect Centers*, Science **276**, 2012 (1997),
URL: http://dx.doi.org/10.1126/science.276.5321.2012

[22] T. Staudacher, F. Shi, S. Pezzagna, J. Meijer, J. Du, C. A. Meriles, F. Reinhard, and J. Wrachtrup, *Nuclear magnetic resonance spectroscopy on a (5-nanometer)^3 sample volume*, Science **339**, 561 (2013),
URL: http://dx.doi.org/10.1126/science.1231675

[23] H. J. Mamin, M. Kim, M. H. Sherwood, C. T. Rettner, K. Ohno, D. D. Awschalom, and D. Rugar, *Nanoscale Nuclear Magnetic Resonance with a Nitrogen-Vacancy Spin Sensor.*, Science **339**, 557 (2013),
URL: http://dx.doi.org/10.1126/science.1231540

[24] C. Müller, X. Kong, J.-M. Cai, K. Melentijević, A. Stacey, M. Markham, D. Twitchen, J. Isoya, S. Pezzagna, J. Meijer, J. F. Du, M. B. Plenio, B. Naydenov, L. P. McGuinness, and F. Jelezko, *Nuclear magnetic resonance spectroscopy with single spin sensitivity*, Nature Communications **5**, 4703 (2014),
URL: http://dx.doi.org/10.1038/ncomms5703

[25] A. O. Sushkov, I. Lovchinsky, N. Chisholm, R. L. Walsworth, H. Park, and M. D. Lukin, *Magnetic Resonance Detection of Individual Proton Spins Using Quantum Reporters*, Physical Review Letters **113**, 197601 (2014),
URL: http://dx.doi.org/10.1103/PhysRevLett.113.197601

[26] I. Lovchinsky, A. O. Sushkov, E. Urbach, N. P. De Leon, S. Choi, K. De Greve, R. Evans, R. Gertner, E. Bersin, C. Müller, L. McGuinness, F. Jelezko, R. L. Walsworth, H. Park, and M. D. Lukin, *Nuclear magnetic resonance detection and spectroscopy of single proteins using quantum logic*, Science **351**, 836 (2016),
URL: http://dx.doi.org/10.1126/science.aad8022

[27] T. Staudacher, N. Raatz, S. Pezzagna, J. Meijer, F. Reinhard, C. A. Meriles, and J. Wrachtrup, *Probing molecular dynamics at the nanoscale via an individual paramagnetic centre*, Nature Communications **6**, 8527 (2015),
URL: http://dx.doi.org/10.1038/ncomms9527

[28] M. Loretz, J. M. Boss, T. Rosskopf, H. J. Mamin, D. Rugar, and C. L. Degen, *Spurious Harmonic Response of Multipulse Quantum Sensing Sequences*, Physical Review X **5**, 021009 (2015),
URL: http://dx.doi.org/10.1103/PhysRevX.5.021009

[29] D. P. DiVincenzo, *The Physical Implementation of Quantum Computation*, Fortschritte der Physik **48**, 771 (2000),
URL: http://dx.doi.org/10.1002/1521-3978(200009)48:9/11<771::AID-PROP771>3.0.CO;2-E

[30] J. Johansson, P. Nation, and F. Nori, *QuTiP: An open-source Python framework for the dynamics of open quantum systems*, Computer Physics Communications **183**, 1760 (2012),
URL: http://dx.doi.org/10.1016/j.cpc.2012.02.021

[31] J. Johansson, P. Nation, and F. Nori, *QuTiP 2: A Python framework for the dynamics of open quantum systems*, Computer Physics Communications **184**, 1234 (2013),
URL: http://dx.doi.org/10.1016/j.cpc.2012.11.019

[32] W. H. Zurek, *Decoherence, einselection, and the quantum origins of the classical*, Reviews of Modern Physics **75**, 715 (2003),
URL: http://dx.doi.org/10.1103/RevModPhys.75.715

[33] W. M. Itano, J. C. Bergquist, J. J. Bollinger, J. M. Gilligan, D. J. Heinzen, F. L. Moore, M. G. Raizen, and D. J. Wineland, *Quantum projection noise: Population fluctuations in two-level systems*, Physical Review A **47**, 3554 (1993),
URL: http://dx.doi.org/10.1103/PhysRevA.47.3554

[34] I. I. Rabi, J. R. Zacharias, S. Millman, and P. Kusch, *A New Method of Measuring Nuclear Magnetic Moment*, Physical Review **53**, 318 (1938),
URL: http://dx.doi.org/10.1103/PhysRev.53.318

[35] M. O. Scully and M. S. Zubairy, *Quantum Optics*, Cambridge University Press, Cambridge, (1997),
URL: http://dx.doi.org/10.1017/cbo9780511813993

[36] G. Davies and M. F. Hamer, *Optical studies of the 1.945 eV vibronic band in diamond*, Proceedings of the Royal Society A: Mathematical, Physical and Engineering Sciences **348**, 285 (1976),
URL: http://dx.doi.org/10.1098/rspa.1976.0039

[37] F. Jelezko, I. Popa, A. Gruber, C. Tietz, J. Wrachtrup, A. Nizovtsev, and S. Kilin, *Single spin states in a defect center resolved by optical spectroscopy*, Applied Physics Letters **81**, 2160 (2002),
URL: http://dx.doi.org/10.1063/1.1507838

[38] F. Jelezko and J. Wrachtrup, *Read-out of single spins by optical spectroscopy*, Journal of Physics: Condensed Matter **16**, R1089 (2004),
URL: http://dx.doi.org/10.1088/0953-8984/16/30/R03

[39] F. Jelezko, T. Gaebel, I. Popa, M. Domhan, A. Gruber, and J. Wrachtrup, *Observation of Coherent Oscillation of a Single Nuclear Spin and Realization of a Two-Qubit Conditional Quantum Gate*, Physical Review Letters **93**, 130501 (2004),
URL: http://dx.doi.org/10.1103/PhysRevLett.93.130501

[40] G. Balasubramanian, P. Neumann, D. Twitchen, M. Markham, R. Kolesov, N. Mizuochi, J. Isoya, J. Achard, J. Beck, J. Tissler, V. Jacques, P. R. Hemmer, F. Jelezko, and J. Wrachtrup, *Ultralong spin coherence time in isotopically engineered diamond*, Nature Materials **8**, 383 (2009),
URL: http://dx.doi.org/10.1038/nmat2420

[41] R. Schirhagl, K. Chang, M. Loretz, and C. L. Degen, *Nitrogen-Vacancy Centers in Diamond: Nanoscale Sensors for Physics and Biology*, Annual review of physical chemistry **65**, 83 (2014),
URL: http://dx.doi.org/10.1146/annurev-physchem-040513-103659

[42] L. Rondin, J.-P. Tetienne, T. Hingant, J.-F. Roch, P. Maletinsky, and V. Jacques, *Magnetometry with nitrogen-vacancy defects in diamond*, Reports on progress in physics. Physical Society (Great Britain) **77**, 056503 (2014),
URL: http://dx.doi.org/10.1088/0034-4885/77/5/056503

[43] F. Dolde, H. Fedder, M. W. Doherty, T. Nöbauer, F. Rempp, G. Balasubramanian, T. Wolf, F. Reinhard, L. C. Hollenberg, F. Jelezko, and J. Wrachtrup, *Electric-field sensing using single diamond spins*, Nature Physics **7**, 459 (2011),
URL: http://dx.doi.org/10.1038/nphys1969

[44] F. Dolde, M. W. Doherty, J. Michl, I. Jakobi, B. Naydenov, S. Pezzagna, J. Meijer, P. Neumann, F. Jelezko, N. B. Manson, and J. Wrachtrup, *Nanoscale Detection of a Single Fundamental Charge in Ambient Conditions Using the NV^- Center in Diamond*, Physical Review Letters **112**, 097603 (2014),
URL: http://dx.doi.org/10.1103/PhysRevLett.112.097603

[45] J. Michl, J. Steiner, A. Denisenko, A. Buelau, A. Zimmermann, K. Nakamura, H. Sumiya, S. Onoda, P. Neumann, J. Isoya, and J. Wrachtrup, *Robust and accurate electric field sensing with solid state spin ensembles*, Nano Letters **19**, 4904 (2019), URL: http://dx.doi.org/10.1021/acs.nanolett.9b00900

[46] D. M. Toyli, C. F. de las Casas, D. J. Christle, V. V. Dobrovitski, and D. D. Awschalom, *Fluorescence thermometry enhanced by the quantum coherence of single spins in diamond*, Proceedings of the National Academy of Sciences **110**, 8417 (2013),
URL: http://dx.doi.org/10.1073/pnas.1306825110

[47] G. Kucsko, P. C. Maurer, N. Y. Yao, M. Kubo, H. J. Noh, P. K. Lo, H. Park, and M. D. Lukin, *Nanometre-scale thermometry in a living cell*, Nature **500**, 54 (2013), URL: http://dx.doi.org/10.1038/nature12373

[48] P. Neumann, I. Jakobi, F. Dolde, C. Burk, R. Reuter, G. Waldherr, J. Honert, T. Wolf, A. Brunner, J. H. Shim, D. Suter, H. Sumiya, J. Isoya, and J. Wrachtrup, *High-Precision Nanoscale Temperature Sensing Using Single Defects in Diamond*, Nano Letters **13**, 2738 (2013),
URL: http://dx.doi.org/10.1021/nl401216y

[49] T. Rendler, J. Neburkova, O. Zemek, J. Kotek, A. Zappe, Z. Chu, P. Cigler, and J. Wrachtrup, *Optical imaging of localized chemical events using programmable diamond quantum nanosensors*, Nature Communications **8**, 14701 (2017),
URL: http://dx.doi.org/10.1038/ncomms14701

[50] J. Cai, F. Jelezko, and M. B. Plenio, *Hybrid sensors based on colour centres in diamond and piezoactive layers*, Nature Communications **5**, 4065 (2014),
URL: http://dx.doi.org/10.1038/ncomms5065

[51] M. W. Doherty, V. V. Struzhkin, D. A. Simpson, L. P. McGuinness, Y. Meng, A. Stacey, T. J. Karle, R. J. Hemley, N. B. Manson, L. C. Hollenberg, and S. Prawer, *Electronic Properties and Metrology Applications of the Diamond NV^- Center under Pressure*, Physical Review Letters **112**, 047601 (2014),
URL: http://dx.doi.org/10.1103/PhysRevLett.112.047601

[52] M. S. J. Barson, et al., *Nanomechanical Sensing Using Spins in Diamond*, Nano Letters **17**, 1496 (2017),
URL: http://dx.doi.org/10.1021/acs.nanolett.6b04544

[53] J. M. Taylor, P. Cappellaro, L. Childress, L. Jiang, D. Budker, P. R. Hemmer, A. Yacoby, R. Walsworth, and M. D. Lukin, *High-sensitivity diamond magnetometer with nanoscale resolution*, Nature Physics **4**, 810 (2008),
URL: http://dx.doi.org/10.1038/nphys1075

[54] C. L. Degen, *Scanning magnetic field microscope with a diamond single-spin sensor*, Applied Physics Letters **92**, 243111 (2008),
URL: http://dx.doi.org/10.1063/1.2943282

[55] J. R. Maze, P. L. Stanwix, J. S. Hodges, S. Hong, J. M. Taylor, P. Cappellaro, L. Jiang, M. V. Dutt, E. Togan, A. S. Zibrov, A. Yacoby, R. L. Walsworth, and M. D. Lukin, *Nanoscale magnetic sensing with an individual electronic spin in diamond*, Nature **455**, 644 (2008),
URL: http://dx.doi.org/10.1038/nature07279

[56] G. Popkin, *Quest for qubits*, Science **354**, 1090 (2016),
URL: http://dx.doi.org/10.1126/science.354.6316.1090

[57] M. H. Devoret and R. J. Schoelkopf, *Superconducting Circuits for Quantum Information: An Outlook*, Science **339**, 1169 (2013),
URL: http://dx.doi.org/10.1126/science.1231930

[58] X. Zhang, H.-O. Li, K. Wang, G. Cao, M. Xiao, and G.-P. Guo, *Qubits based on semiconductor quantum dots*, Chinese Physics B **27**, 020305 (2018),
URL: http://dx.doi.org/10.1088/1674-1056/27/2/020305

[59] D. D. Awschalom, L. C. Bassett, A. S. Dzurak, E. L. Hu, and J. R. Petta, *Quantum Spintronics: Engineering and Manipulating Atom-Like Spins in Semiconductors*, Science **339**, 1174 (2013),
URL: http://dx.doi.org/10.1126/science.1231364

[60] C. E. Bradley, J. Randall, M. H. Abobeih, R. C. Berrevoets, M. J. Degen, M. A. Bakker, M. Markham, D. J. Twitchen, and T. H. Taminiau, *A Ten-Qubit Solid-State Spin Register with Quantum Memory up to One Minute*, Physical Review X **9**, 031045 (2019),
URL: http://dx.doi.org/10.1103/PhysRevX.9.031045

[61] J. R. Weber, W. F. Koehl, J. B. Varley, A. Janotti, B. B. Buckley, C. G. Van de Walle, and D. D. Awschalom, *Quantum computing with defects*, Proceedings of the National Academy of Sciences **107**, 8513 (2010),
URL: http://dx.doi.org/10.1073/pnas.1003052107

[62] L. Gordon, J. R. Weber, J. B. Varley, A. Janotti, D. D. Awschalom, and C. G. Van de Walle, *Quantum computing with defects*, MRS Bulletin **38**, 802 (2013), URL: http://dx.doi.org/10.1557/mrs.2013.206

[63] L. Wei, P. K. Kuo, R. L. Thomas, T. R. Anthony, and W. F. Banholzer, *Thermal Conductivity of Isotopically Modified Single Crystal Diamond*, Physical Review Letters **70**, 3764 (1993), URL: http://dx.doi.org/10.1103/PhysRevLett.70.3764

[64] F. Occelli, P. Loubeyre, and R. LeToullec, *Properties of diamond under hydrostatic pressures up to 140 GPa*, Nature Materials **2**, 151 (2003), URL: http://dx.doi.org/10.1038/nmat831

[65] G. Davies and T. Evans, *Graphitization of diamond at zero pressure and at a high pressure*, Proceedings of the Royal Society of London. A. Mathematical and Physical Sciences **328**, 413 (1972), URL: http://dx.doi.org/10.1098/rspa.1972.0086

[66] R. P. Mildren and J. R. Rabeau, *Optical Engineering of Diamond*, Wiley-VCH Verlag GmbH & Co. KGaA, Weinheim, Germany, (2013), URL: http://dx.doi.org/10.1002/9783527648603

[67] I. Aharonovich, S. Castelletto, D. A. Simpson, C. H. Su, A. D. Greentree, and S. Prawer, *Diamond-based single-photon emitters*, Reports on Progress in Physics **74**, 076501 (2011), URL: http://dx.doi.org/10.1088/0034-4885/74/7/076501

[68] A. M. Zaitsev, *Optical Properties of Diamond: A Data Handbook*, Springer, Berlin Heidelberg, (2001), URL: http://dx.doi.org/10.1007/978-3-662-04548-0

[69] L. J. Rogers, K. D. Jahnke, M. W. Doherty, A. Dietrich, L. P. McGuinness, C. Müller, T. Teraji, H. Sumiya, J. Isoya, N. B. Manson, and F. Jelezko, *Electronic structure of the negatively charged silicon-vacancy center in diamond*, Physical Review B **89**, 235101 (2014), URL: http://dx.doi.org/10.1103/PhysRevB.89.235101

[70] L. J. Rogers, K. D. Jahnke, T. Teraji, L. Marseglia, C. Müller, B. Naydenov, H. Schauffert, C. Kranz, J. Isoya, L. P. McGuinness, and F. Jelezko, *Multiple*

intrinsically identical single-photon emitters in the solid state, Nature Communications **5**, 4739 (2014),
URL: http://dx.doi.org/10.1038/ncomms5739

[71] A. Sipahigil, K. D. Jahnke, L. J. Rogers, T. Teraji, J. Isoya, A. S. Zibrov, F. Jelezko, and M. D. Lukin, *Indistinguishable Photons from Separated Silicon-Vacancy Centers in Diamond*, Physical Review Letters **113**, 113602 (2014),
URL: http://dx.doi.org/10.1103/PhysRevLett.113.113602

[72] A. Dietrich, K. D. Jahnke, J. M. Binder, T. Teraji, J. Isoya, L. J. Rogers, and F. Jelezko, *Isotopically varying spectral features of silicon-vacancy in diamond*, New Journal of Physics **16**, 113019 (2014),
URL: http://dx.doi.org/10.1088/1367-2630/16/11/113019

[73] T. Iwasaki, et al., *Germanium-Vacancy Single Color Centers in Diamond*, Scientific Reports **5**, 12882 (2015),
URL: http://dx.doi.org/10.1038/srep12882

[74] P. Siyushev, et al., *Optical and microwave control of germanium-vacancy center spins in diamond*, Physical Review B **96**, 081201 (2017),
URL: http://dx.doi.org/10.1103/PhysRevB.96.081201

[75] T. Iwasaki, Y. Miyamoto, T. Taniguchi, P. Siyushev, M. H. Metsch, F. Jelezko, and M. Hatano, *Tin-Vacancy Quantum Emitters in Diamond*, Physical Review Letters **119**, 253601 (2017),
URL: http://dx.doi.org/10.1103/PhysRevLett.119.253601

[76] P. Deák, B. Aradi, M. Kaviani, T. Frauenheim, and A. Gali, *Formation of NV centers in diamond: A theoretical study based on calculated transitions and migration of nitrogen and vacancy related defects*, Physical Review B **89**, 075203 (2014),
URL: http://dx.doi.org/10.1103/PhysRevB.89.075203

[77] M. W. Doherty, N. B. Manson, P. Delaney, and L. C. L. Hollenberg, *The negatively charged nitrogen-vacancy centre in diamond: the electronic solution*, New Journal of Physics **13**, 025019 (2011),
URL: http://dx.doi.org/10.1088/1367-2630/13/2/025019

[78] M. W. Doherty, N. B. Manson, P. Delaney, F. Jelezko, J. Wrachtrup, and L. C. Hollenberg, *The nitrogen-vacancy colour centre in diamond*, Physics Reports **528**, 1 (2013),
URL: http://dx.doi.org/10.1016/j.physrep.2013.02.001

[79] X.-F. He, N. B. Manson, and P. T. H. Fisk, *Paramagnetic resonance of photoexcited N- V defects in diamond. II. Hyperfine interaction with the ^{14}N nucleus*, Physical Review B **47**, 8816 (1993),
URL: http://dx.doi.org/10.1103/PhysRevB.47.8816

[80] N. B. Manson, J. P. Harrison, and M. J. Sellars, *Nitrogen-vacancy center in diamond: Model of the electronic structure and associated dynamics*, Physical Review B **74**, 104303 (2006),
URL: http://dx.doi.org/10.1103/PhysRevB.74.104303

[81] T. Gaebel, M. Domhan, C. Wittmann, I. Popa, F. Jelezko, J. Rabeau, A. Greentree, S. Prawer, E. Trajkov, P. Hemmer, and J. Wrachtrup, *Photochromism in single nitrogen-vacancy defect in diamond*, Applied Physics B **82**, 243 (2006),
URL: http://dx.doi.org/10.1007/s00340-005-2056-2

[82] M. Pfender, et al., *Protecting a Diamond Quantum Memory by Charge State Control*, Nano Letters **17**, 5931 (2017),
URL: http://dx.doi.org/10.1021/acs.nanolett.7b01796

[83] J. H. Loubser and J. A. Van Wyk, *Electron spin resonance in the study of diamond*, Reports on Progress in Physics **41**, 1201 (1978),
URL: http://dx.doi.org/10.1088/0034-4885/41/8/002

[84] D. Suter and F. Jelezko, *Single-spin magnetic resonance in the nitrogen-vacancy center of diamond*, Progress in Nuclear Magnetic Resonance Spectroscopy **98-99**, 50 (2017),
URL: http://dx.doi.org/10.1016/j.pnmrs.2016.12.001

[85] G. D. Fuchs, V. V. Dobrovitski, R. Hanson, A. Batra, C. D. Weis, T. Schenkel, and D. D. Awschalom, *Excited-state Spectroscopy Using Single Spin Manipulation in Diamond*, Physical Review Letters **101**, 117601 (2008),
URL: http://dx.doi.org/10.1103/PhysRevLett.101.117601

[86] L. J. Rogers, R. L. McMurtrie, M. J. Sellars, and N. B. Manson, *Time-averaging within the excited state of the nitrogen-vacancy centre in diamond*, New Journal of Physics **11**, 063007 (2009),
URL: http://dx.doi.org/10.1088/1367-2630/11/6/063007

[87] K.-M. C. Fu, C. Santori, P. E. Barclay, L. J. Rogers, N. B. Manson, and R. G. Beausoleil, *Observation of the Dynamic Jahn-Teller Effect in the Excited States of*

Nitrogen-Vacancy Centers in Diamond, Physical Review Letters **103**, 256404 (2009), URL: http://dx.doi.org/10.1103/PhysRevLett.103.256404

[88] P. Udvarhelyi, V. O. Shkolnikov, A. Gali, G. Burkard, and A. Pályi, *Spin-strain interaction in nitrogen-vacancy centers in diamond*, Physical Review B **98**, 075201 (2018), URL: http://dx.doi.org/10.1103/PhysRevB.98.075201

[89] V. M. Acosta, A. Jarmola, E. Bauch, and D. Budker, *Optical properties of the nitrogen-vacancy singlet levels in diamond*, Physical Review B **82**, 201202 (2010), URL: http://dx.doi.org/10.1103/PhysRevB.82.201202

[90] M. W. Doherty, F. Dolde, H. Fedder, F. Jelezko, J. Wrachtrup, N. B. Manson, and L. C. L. Hollenberg, *Theory of the ground-state spin of the NV^- center in diamond*, Physical Review B **85**, 205203 (2012), URL: http://dx.doi.org/10.1103/PhysRevB.85.205203

[91] B. Smeltzer, L. Childress, and A. Gali, *^{13}C hyperfine interactions in the nitrogen-vacancy centre in diamond*, New Journal of Physics **13**, 025021 (2011), URL: http://dx.doi.org/10.1088/1367-2630/13/2/025021

[92] A. P. Nizovtsev, S. Y. Kilin, A. L. Pushkarchuk, V. A. Pushkarchuk, S. A. Kuten, O. A. Zhikol, S. Schmitt, T. Unden, and F. Jelezko, *Non-flipping ^{13}C spins near an NV center in diamond: hyperfine and spatial characteristics by density functional theory simulation of the $C_{510}[NV]H_{252}$ cluster*, New Journal of Physics **20**, 023022 (2018), URL: http://dx.doi.org/10.1088/1367-2630/aaa910

[93] K. R. K. Rao and D. Suter, *Characterization of hyperfine interaction between an NV electron spin and a first-shell ^{13}C nuclear spin in diamond*, Physical Review B **94**, 060101 (2016), URL: http://dx.doi.org/10.1103/PhysRevB.94.060101

[94] S. Felton, A. M. Edmonds, M. E. Newton, P. M. Martineau, D. Fisher, D. J. Twitchen, and J. M. Baker, *Hyperfine interaction in the ground state of the negatively charged nitrogen vacancy center in diamond*, Physical Review B **79**, 075203 (2009), URL: http://dx.doi.org/10.1103/PhysRevB.79.075203

[95] M. L. Goldman, M. W. Doherty, A. Sipahigil, N. Y. Yao, S. D. Bennett, N. B. Manson, A. Kubanek, and M. D. Lukin, *State-selective intersystem crossing in*

nitrogen-vacancy centers, Physical Review B **91**, 165201 (2015),
URL: http://dx.doi.org/10.1103/PhysRevB.91.165201

[96] P. Neumann, R. Kolesov, V. Jacques, J. Beck, J. Tisler, A. Batalov, L. Rogers, N. B. Manson, G. Balasubramanian, F. Jelezko, and J. Wrachtrup, *Excited-state spectroscopy of single NV defects in diamond using optically detected magnetic resonance*, New Journal of Physics **11**, 013017 (2009),
URL: http://dx.doi.org/10.1088/1367-2630/11/1/013017

[97] R. Ulbricht, S. Dong, A. Gali, S. Meng, and Z.-H. Loh, *Vibrational relaxation dynamics of the nitrogen-vacancy center in diamond*, Physical Review B **97**, 220302 (2018),
URL: http://dx.doi.org/10.1103/PhysRevB.97.220302

[98] V. M. Huxter, T. A. A. Oliver, D. Budker, and G. R. Fleming, *Vibrational and electronic dynamics of nitrogen-vacancy centres in diamond revealed by two-dimensional ultrafast spectroscopy*, Nature Physics **9**, 744 (2013),
URL: http://dx.doi.org/10.1038/nphys2753

[99] L. J. Rogers, S. Armstrong, M. J. Sellars, and N. B. Manson, *Infrared emission of the NV centre in diamond: Zeeman and uniaxial stress studies*, New Journal of Physics **10**, 103024 (2008),
URL: http://dx.doi.org/10.1088/1367-2630/10/10/103024

[100] L. Robledo, H. Bernien, T. van der Sar, and R. Hanson, *Spin dynamics in the optical cycle of single nitrogen-vacancy centres in diamond*, New Journal of Physics **13**, 025013 (2011),
URL: http://dx.doi.org/10.1088/1367-2630/13/2/025013

[101] J.-P. Tetienne, L. Rondin, P. Spinicelli, M. Chipaux, T. Debuisschert, J.-F. Roch, and V. Jacques, *Magnetic-field-dependent photodynamics of single NV defects in diamond: an application to qualitative all-optical magnetic imaging*, New Journal of Physics **14**, 103033 (2012),
URL: http://dx.doi.org/10.1088/1367-2630/14/10/103033

[102] J. Harrison, M. J. Sellars, and N. B. Manson, *Measurement of the optically induced spin polarisation of N-V centres in diamond*, Diamond and Related Materials **15**, 586 (2006),
URL: http://dx.doi.org/10.1016/j.diamond.2005.12.027

[103] G. D. Fuchs, V. V. Dobrovitski, D. M. Toyli, F. J. Heremans, C. D. Weis, T. Schenkel, and D. D. Awschalom, *Excited-state spin coherence of a single nitrogen-vacancy centre in diamond*, Nature Physics **6**, 668 (2010),
URL: http://dx.doi.org/10.1038/nphys1716

[104] P. Neumann, R. Kolesov, B. Naydenov, J. Beck, F. Rempp, M. Steiner, V. Jacques, G. Balasubramanian, M. L. Markham, D. J. Twitchen, S. Pezzagna, J. Meijer, J. Twamley, F. Jelezko, and J. Wrachtrup, *Quantum register based on coupled electron spins in a room-temperature solid*, Nature Physics **6**, 249 (2010),
URL: http://dx.doi.org/10.1038/nphys1536

[105] G. Waldherr, J. Beck, M. Steiner, P. Neumann, A. Gali, T. Frauenheim, F. Jelezko, and J. Wrachtrup, *Dark States of Single Nitrogen-Vacancy Centers in Diamond Unraveled by Single Shot NMR*, Physical Review Letters **106**, 157601 (2011),
URL: http://dx.doi.org/10.1103/PhysRevLett.106.157601

[106] T. R. Carver and C. P. Slichter, *Polarization of Nuclear Spins in Metals*, Physical Review **92**, 212 (1953),
URL: http://dx.doi.org/10.1103/PhysRev.92.212.2

[107] J. H. Ardenkjaer-Larsen, B. Fridlund, A. Gram, G. Hansson, L. Hansson, M. H. Lerche, R. Servin, M. Thaning, and K. Golman, *Increase in signal-to-noise ratio of > 10,000 times in liquid-state NMR*, Proceedings of the National Academy of Sciences **100**, 10158 (2003),
URL: http://dx.doi.org/10.1073/pnas.1733835100

[108] A. Ajoy, et al., *Orientation-independent room temperature optical ^{13}C hyperpolarization in powdered diamond*, Science Advances **4**, eaar5492 (2018),
URL: http://dx.doi.org/10.1126/sciadv.aar5492

[109] P. Fernández-Acebal, O. Rosolio, J. Scheuer, C. Müller, S. Müller, S. Schmitt, L. P. McGuinness, I. Schwarz, Q. Chen, A. Retzker, B. Naydenov, F. Jelezko, and M. B. Plenio, *Toward Hyperpolarization of Oil Molecules via Single Nitrogen Vacancy Centers in Diamond*, Nano Letters **18**, 1882 (2018),
URL: http://dx.doi.org/10.1021/acs.nanolett.7b05175

[110] D. A. Hopper, R. R. Grote, A. L. Exarhos, and L. C. Bassett, *Near-infrared-assisted charge control and spin readout of the nitrogen-vacancy center in diamond*, Physical Review B **94**, 241201 (2016),
URL: http://dx.doi.org/10.1103/PhysRevB.94.241201

[111] J.-C. Jaskula, B. Shields, E. Bauch, M. Lukin, A. Trifonov, and R. Walsworth, *Improved Quantum Sensing with a Single Solid-State Spin via Spin-to-Charge Conversion*, Physical Review Applied **11**, 064003 (2019),
URL: http://dx.doi.org/10.1103/PhysRevApplied.11.064003

[112] M. Gulka, E. Bourgeois, J. Hruby, P. Siyushev, G. Wachter, F. Aumayr, P. R. Hemmer, A. Gali, F. Jelezko, M. Trupke, and M. Nesladek, *Pulsed Photoelectric Coherent Manipulation and Detection of N-V Center Spins in Diamond*, Physical Review Applied **7**, 044032 (2017),
URL: http://dx.doi.org/10.1103/PhysRevApplied.7.044032

[113] F. M. Hrubesch, G. Braunbeck, M. Stutzmann, F. Reinhard, and M. S. Brandt, *Efficient Electrical Spin Readout of NV^- Centers in Diamond*, Physical Review Letters **118**, 037601 (2017),
URL: http://dx.doi.org/10.1103/PhysRevLett.118.037601

[114] P. Siyushev, M. Nesladek, E. Bourgeois, M. Gulka, J. Hruby, T. Yamamoto, M. Trupke, T. Teraji, J. Isoya, and F. Jelezko, *Photoelectrical imaging and coherent spin-state readout of single nitrogen-vacancy centers in diamond*, Science **363**, 728 (2019),
URL: http://dx.doi.org/10.1126/science.aav2789

[115] L. Robledo, L. Childress, H. Bernien, B. Hensen, P. F. Alkemade, and R. Hanson, *High-fidelity projective read-out of a solid-state spin quantum register*, Nature **477**, 574 (2011),
URL: http://dx.doi.org/10.1038/nature10401

[116] M. S. Blok, C. Bonato, M. L. Markham, D. J. Twitchen, V. V. Dobrovitski, and R. Hanson, *Manipulating a qubit through the backaction of sequential partial measurements and real-time feedback*, Nature Physics **10**, 189 (2014),
URL: http://dx.doi.org/10.1038/nphys2881

[117] J. Cramer, N. Kalb, M. A. Rol, B. Hensen, M. S. Blok, M. Markham, D. J. Twitchen, R. Hanson, and T. H. Taminiau, *Repeated quantum error correction on a continuously encoded qubit by real-time feedback*, Nature Communications **7**, 11526 (2016),
URL: http://dx.doi.org/10.1038/ncomms11526

[118] K. Jensen, N. Leefer, A. Jarmola, Y. Dumeige, V. M. Acosta, P. Kehayias, B. Patton, and D. Budker, *Cavity-Enhanced Room-Temperature Magnetometry Using Absorption by Nitrogen-Vacancy Centers in Diamond*, Physical Review Letters **112**, 160802

(2014),
URL: http://dx.doi.org/10.1103/PhysRevLett.112.160802

[119] D. Hopper, H. Shulevitz, and L. Bassett, *Spin Readout Techniques of the Nitrogen-Vacancy Center in Diamond*, Micromachines **9**, 437 (2018),
URL: http://dx.doi.org/10.3390/mi9090437

[120] A. Batalov, C. Zierl, T. Gaebel, P. Neumann, I.-Y. Chan, G. Balasubramanian, P. R. Hemmer, F. Jelezko, and J. Wrachtrup, *Temporal Coherence of Photons Emitted by Single Nitrogen-Vacancy Defect Centers in Diamond Using Optical Rabi-Oscillations*, Physical Review Letters **100**, 077401 (2008),
URL: http://dx.doi.org/10.1103/PhysRevLett.100.077401

[121] H. Bernien, L. Childress, L. Robledo, M. Markham, D. Twitchen, and R. Hanson, *Two-Photon Quantum Interference from Separate Nitrogen Vacancy Centers in Diamond*, Physical Review Letters **108**, 043604 (2012),
URL: http://dx.doi.org/10.1103/PhysRevLett.108.043604

[122] T. M. Babinec, B. J. Hausmann, M. Khan, Y. Zhang, J. R. Maze, P. R. Hemmer, and M. Lončar, *A diamond nanowire single-photon source*, Nature Nanotechnology **5**, 195 (2010),
URL: http://dx.doi.org/10.1038/nnano.2010.6

[123] S. A. Momenzadeh, R. J. Stöhr, F. F. De Oliveira, A. Brunner, A. Denisenko, S. Yang, F. Reinhard, and J. Wrachtrup, *Nanoengineered diamond waveguide as a robust bright platform for nanomagnetometry using shallow nitrogen vacancy centers*, Nano Letters **15**, 165 (2015),
URL: http://dx.doi.org/10.1021/nl503326t

[124] B. J. M. Hausmann, T. M. Babinec, J. T. Choy, J. S. Hodges, S. Hong, I. Bulu, A. Yacoby, M. D. Lukin, and M. Lončar, *Single-color centers implanted in diamond nanostructures*, New Journal of Physics **13**, 045004 (2011),
URL: http://dx.doi.org/10.1088/1367-2630/13/4/045004

[125] E. Neu, P. Appel, M. Ganzhorn, J. Miguel-Sánchez, M. Lesik, V. Mille, V. Jacques, A. Tallaire, J. Achard, and P. Maletinsky, *Photonic nano-structures on (111)-oriented diamond*, Applied Physics Letters **104**, 153108 (2014),
URL: http://dx.doi.org/10.1063/1.4871580

[126] P. Andrich, B. J. Alemán, J. C. Lee, K. Ohno, C. F. de las Casas, F. J. Heremans, E. L. Hu, and D. D. Awschalom, *Engineered Micro- and Nanoscale Diamonds as*

Mobile Probes for High-Resolution Sensing in Fluid, Nano Letters **14**, 4959 (2014), URL: http://dx.doi.org/10.1021/nl501208s

[127] P. Maletinsky, S. Hong, M. S. Grinolds, B. Hausmann, M. D. Lukin, R. L. Walsworth, M. Loncar, and A. Yacoby, *A robust scanning diamond sensor for nanoscale imaging with single nitrogen-vacancy centres*, Nature Nanotechnology **7**, 320 (2012), URL: http://dx.doi.org/10.1038/nnano.2012.50

[128] D. Riedel, I. Söllner, B. J. Shields, S. Starosielec, P. Appel, E. Neu, P. Maletinsky, and R. J. Warburton, *Deterministic Enhancement of Coherent Photon Generation from a Nitrogen-Vacancy Center in Ultrapure Diamond*, Physical Review X **7**, 031040 (2017), URL: http://dx.doi.org/10.1103/PhysRevX.7.031040

[129] J. P. Hadden, J. P. Harrison, A. C. Stanley-Clarke, L. Marseglia, Y.-L. D. Ho, B. R. Patton, J. L. O'Brien, and J. G. Rarity, *Strongly enhanced photon collection from diamond defect centers under microfabricated integrated solid immersion lenses*, Applied Physics Letters **97**, 241901 (2010), URL: http://dx.doi.org/10.1063/1.3519847

[130] P. Siyushev, F. Kaiser, V. Jacques, I. Gerhardt, S. Bischof, H. Fedder, J. Dodson, M. Markham, D. Twitchen, F. Jelezko, and J. Wrachtrup, *Monolithic diamond optics for single photon detection*, Applied Physics Letters **97**, 241902 (2010), URL: http://dx.doi.org/10.1063/1.3519849

[131] W. Pfaff, B. J. Hensen, H. Bernien, S. B. van Dam, M. S. Blok, T. H. Taminiau, M. J. Tiggelman, R. N. Schouten, M. Markham, D. J. Twitchen, and R. Hanson, *Unconditional quantum teleportation between distant solid-state quantum bits*, Science **345**, 532 (2014), URL: http://dx.doi.org/10.1126/science.1253512

[132] S. Steinert, F. Dolde, P. Neumann, A. Aird, B. Naydenov, G. Balasubramanian, F. Jelezko, and J. Wrachtrup, *High sensitivity magnetic imaging using an array of spins in diamond*, Review of Scientific Instruments **81**, 043705 (2010), URL: http://dx.doi.org/10.1063/1.3385689

[133] E. Van Oort and M. Glasbeek, *Electric-field-induced modulation of spin echoes of N-V centers in diamond*, Chemical Physics Letters **168**, 529 (1990), URL: http://dx.doi.org/10.1016/0009-2614(90)85665-Y

[134] P. Tamarat, T. Gaebel, J. R. Rabeau, M. Khan, A. D. Greentree, H. Wilson, L. C. L. Hollenberg, S. Prawer, P. Hemmer, F. Jelezko, and J. Wrachtrup, *Stark Shift Control of Single Optical Centers in Diamond*, Physical Review Letters **97**, 083002 (2006), URL: http://dx.doi.org/10.1103/PhysRevLett.97.083002

[135] T. Iwasaki, W. Naruki, K. Tahara, T. Makino, H. Kato, M. Ogura, D. Takeuchi, S. Yamasaki, and M. Hatano, *Direct Nanoscale Sensing of the Internal Electric Field in Operating Semiconductor Devices Using Single Electron Spins*, ACS Nano **11**, 1238 (2017), URL: http://dx.doi.org/10.1021/acsnano.6b04460

[136] L. C. Bassett, F. J. Heremans, C. G. Yale, B. B. Buckley, and D. D. Awschalom, *Electrical Tuning of Single Nitrogen-Vacancy Center Optical Transitions Enhanced by Photoinduced Fields*, Physical Review Letters **107**, 266403 (2011), URL: http://dx.doi.org/10.1103/PhysRevLett.107.266403

[137] M. V. Berry, *Quantal Phase Factors Accompanying Adiabatic Changes*, Proceedings of the Royal Society A: Mathematical, Physical and Engineering Sciences **392**, 45 (1984), URL: http://dx.doi.org/10.1098/rspa.1984.0023

[138] M. P. Ledbetter, K. Jensen, R. Fischer, A. Jarmola, and D. Budker, *Gyroscopes based on nitrogen-vacancy centers in diamond*, Physical Review A **86**, 052116 (2012), URL: http://dx.doi.org/10.1103/PhysRevA.86.052116

[139] A. Ajoy and P. Cappellaro, *Stable three-axis nuclear-spin gyroscope in diamond*, Physical Review A **86**, 062104 (2012), URL: http://dx.doi.org/10.1103/PhysRevA.86.062104

[140] D. Maclaurin, M. W. Doherty, L. C. L. Hollenberg, and A. M. Martin, *Measurable Quantum Geometric Phase from a Rotating Single Spin*, Physical Review Letters **108**, 240403 (2012), URL: http://dx.doi.org/10.1103/PhysRevLett.108.240403

[141] F. Jelezko, T. Gaebel, I. Popa, A. Gruber, and J. Wrachtrup, *Observation of Coherent Oscillations in a Single Electron Spin*, Physical Review Letters **92**, 076401 (2004), URL: http://dx.doi.org/10.1103/PhysRevLett.92.076401

[142] C. P. Slichter, *Principles of Magnetic Resonance*, volume 1, Springer, Berlin Heidelberg, (1990),
URL: http://dx.doi.org/10.1007/978-3-662-09441-9

[143] N. F. Ramsey, *A Molecular Beam Resonance Method with Separated Oscillating Fields*, Physical Review **78**, 695 (1950),
URL: http://dx.doi.org/10.1103/PhysRev.78.695

[144] J. R. Maze, A. Dréau, V. Waselowski, H. Duarte, J.-F. Roch, and V. Jacques, *Free induction decay of single spins in diamond*, New Journal of Physics **14**, 103041 (2012),
URL: http://dx.doi.org/10.1088/1367-2630/14/10/103041

[145] V. Jacques, P. Neumann, J. Beck, M. Markham, D. Twitchen, J. Meijer, F. Kaiser, G. Balasubramanian, F. Jelezko, and J. Wrachtrup, *Dynamic Polarization of Single Nuclear Spins by Optical Pumping of Nitrogen-Vacancy Color Centers in Diamond at Room Temperature*, Physical Review Letters **102**, 057403 (2009),
URL: http://dx.doi.org/10.1103/PhysRevLett.102.057403

[146] A. M. Souza, G. A. Álvarez, and D. Suter, *Robust dynamical decoupling*, Philosophical Transactions of the Royal Society A: Mathematical, Physical and Engineering Sciences **370**, 4748 (2012),
URL: http://dx.doi.org/10.1098/rsta.2011.0355

[147] J. Casanova, Z.-Y. Wang, and M. B. Plenio, *Noise-Resilient Quantum Computing with a Nitrogen-Vacancy Center and Nuclear Spins*, Physical Review Letters **117**, 130502 (2016),
URL: http://dx.doi.org/10.1103/PhysRevLett.117.130502

[148] J. Cai, A. Retzker, F. Jelezko, and M. B. Plenio, *A large-scale quantum simulator on a diamond surface at room temperature*, Nature Physics **9**, 168 (2013),
URL: http://dx.doi.org/10.1038/nphys2519

[149] P. C. Humphreys, N. Kalb, J. P. Morits, R. N. Schouten, R. F. Vermeulen, D. J. Twitchen, M. Markham, and R. Hanson, *Deterministic delivery of remote entanglement on a quantum network*, Nature **558**, 268 (2018),
URL: http://dx.doi.org/10.1038/s41586-018-0200-5

[150] D. Rugar, H. J. Mamin, M. H. Sherwood, M. Kim, C. T. Rettner, K. Ohno, and D. D. Awschalom, *Proton magnetic resonance imaging using a nitrogen-vacancy*

spin sensor, Nature Nanotechnology **10**, 120 (2015),
URL: http://dx.doi.org/10.1038/nnano.2014.288

[151] S. J. DeVience, L. M. Pham, I. Lovchinsky, A. O. Sushkov, N. Bar-Gill, C. Belthangady, F. Casola, M. Corbett, H. Zhang, M. Lukin, H. Park, A. Yacoby, and R. L. Walsworth, *Nanoscale NMR spectroscopy and imaging of multiple nuclear species*, Nature Nanotechnology **10**, 129 (2015),
URL: http://dx.doi.org/10.1038/nnano.2014.313

[152] F. Shi, Q. Zhang, P. Wang, H. Sun, J. Wang, X. Rong, M. Chen, C. Ju, F. Reinhard, H. Chen, J. Wrachtrup, J. Wang, and J. Du, *Single-protein spin resonance spectroscopy under ambient conditions*, Science **347**, 1135 (2015),
URL: http://dx.doi.org/10.1126/science.aaa2253

[153] S. Schmitt, et al., *Submillihertz magnetic spectroscopy performed with a nanoscale quantum sensor*, Science **356**, 832 (2017),
URL: http://dx.doi.org/10.1126/science.aam5532

[154] D. R. Glenn, D. B. Bucher, J. Lee, M. D. Lukin, H. Park, and R. L. Walsworth, *High-resolution magnetic resonance spectroscopy using a solid-state spin sensor*, Nature **555**, 351 (2018),
URL: http://dx.doi.org/10.1038/nature25781

[155] T. Rosskopf, J. Zopes, J. M. Boss, and C. L. Degen, *A quantum spectrum analyzer enhanced by a nuclear spin memory*, npj Quantum Inf **3**, 33 (2017),
URL: http://dx.doi.org/10.1038/s41534-017-0030-6

[156] L. M. Pham, S. J. DeVience, F. Casola, I. Lovchinsky, A. O. Sushkov, E. Bersin, J. Lee, E. Urbach, P. Cappellaro, H. Park, A. Yacoby, M. Lukin, and R. L. Walsworth, *NMR technique for determining the depth of shallow nitrogen-vacancy centers in diamond*, Physical Review B **93**, 045425 (2016),
URL: http://dx.doi.org/10.1103/PhysRevB.93.045425

[157] T. H. Taminiau, J. J. T. Wagenaar, T. van der Sar, F. Jelezko, V. V. Dobrovitski, and R. Hanson, *Detection and Control of Individual Nuclear Spins Using a Weakly Coupled Electron Spin*, Physical Review Letters **109**, 137602 (2012),
URL: http://dx.doi.org/10.1103/PhysRevLett.109.137602

[158] S. Kolkowitz, Q. P. Unterreithmeier, S. D. Bennett, and M. D. Lukin, *Sensing Distant Nuclear Spins with a Single Electron Spin*, Physical Review Letters **109**,

137601 (2012),
URL: http://dx.doi.org/10.1103/PhysRevLett.109.137601

[159] N. Zhao, J. Honert, B. Schmid, M. Klas, J. Isoya, M. Markham, D. Twitchen, F. Jelezko, R. B. Liu, H. Fedder, and J. Wrachtrup, *Sensing single remote nuclear spins*, Nature Nanotechnology **7**, 657 (2012),
URL: http://dx.doi.org/10.1038/nnano.2012.152

[160] J. E. Lang, R. B. Liu, and T. S. Monteiro, *Dynamical-Decoupling-Based Quantum Sensing: Floquet Spectroscopy*, Physical Review X **5**, 041016 (2015),
URL: http://dx.doi.org/10.1103/PhysRevX.5.041016

[161] K. Sasaki, K. M. Itoh, and E. Abe, *Determination of the position of a single nuclear spin from free nuclear precessions detected by a solid-state quantum sensor*, Physical Review B **98**, 121405 (2018),
URL: http://dx.doi.org/10.1103/PhysRevB.98.121405

[162] J. Zopes, K. Herb, K. S. Cujia, and C. L. Degen, *Three-Dimensional Nuclear Spin Positioning Using Coherent Radio-Frequency Control*, Physical Review Letters **121**, 170801 (2018),
URL: http://dx.doi.org/10.1103/PhysRevLett.121.170801

[163] J. Zopes, K. S. Cujia, K. Sasaki, J. M. Boss, K. M. Itoh, and C. L. Degen, *Three-dimensional localization spectroscopy of individual nuclear spins with sub-Angstrom resolution*, Nature Communications **9**, 4678 (2018),
URL: http://dx.doi.org/10.1038/s41467-018-07121-0

[164] M. Pfender, P. Wang, H. Sumiya, S. Onoda, W. Yang, D. B. R. Dasari, P. Neumann, X. Y. Pan, J. Isoya, R. B. Liu, and J. Wrachtrup, *High-resolution spectroscopy of single nuclear spins via sequential weak measurements*, Nature Communications **10**, 594 (2019),
URL: http://dx.doi.org/10.1038/s41467-019-08544-z

[165] N. Zhao, J. L. Hu, S. W. Ho, J. T. Wan, and R. B. Liu, *Atomic-scale magnetometry of distant nuclear spin clusters via nitrogen-vacancy spin in diamond*, Nature Nanotechnology **6**, 242 (2011),
URL: http://dx.doi.org/10.1038/nnano.2011.22

[166] F. Shi, X. Kong, P. Wang, F. Kong, N. Zhao, R.-B. Liu, and J. Du, *Sensing and atomic-scale structure analysis of single nuclear-spin clusters in diamond*, Nature

Physics **10**, 21 (2014),
URL: http://dx.doi.org/10.1038/nphys2814

[167] C. A. Ryan, J. S. Hodges, and D. G. Cory, *Robust Decoupling Techniques to Extend Quantum Coherence in Diamond*, Physical Review Letters **105**, 200402 (2010),
URL: http://dx.doi.org/10.1103/PhysRevLett.105.200402

[168] G. de Lange, Z. H. Wang, D. Riste, V. V. Dobrovitski, and R. Hanson, *Universal Dynamical Decoupling of a Single Solid-State Spin from a Spin Bath*, Science **330**, 60 (2010),
URL: http://dx.doi.org/10.1126/science.1192739

[169] B. Naydenov, F. Dolde, L. T. Hall, C. Shin, H. Fedder, L. C. L. Hollenberg, F. Jelezko, and J. Wrachtrup, *Dynamical decoupling of a single-electron spin at room temperature*, Physical Review B **83**, 081201 (2011),
URL: http://dx.doi.org/10.1103/PhysRevB.83.081201

[170] Ł. Cywiński, R. M. Lutchyn, C. P. Nave, and S. Das Sarma, *How to enhance dephasing time in superconducting qubits*, Physical Review B **77**, 174509 (2008),
URL: http://dx.doi.org/10.1103/PhysRevB.77.174509

[171] J. Bylander, S. Gustavsson, F. Yan, F. Yoshihara, K. Harrabi, G. Fitch, D. G. Cory, Y. Nakamura, J.-S. Tsai, and W. D. Oliver, *Noise spectroscopy through dynamical decoupling with a superconducting flux qubit*, Nature Physics **7**, 565 (2011),
URL: http://dx.doi.org/10.1038/nphys1994

[172] S. Kotler, N. Akerman, Y. Glickman, A. Keselman, and R. Ozeri, *Single-ion quantum lock-in amplifier*, Nature **473**, 61 (2011),
URL: http://dx.doi.org/10.1038/nature10010

[173] X. Xu, Z. Wang, C. Duan, P. Huang, P. Wang, Y. Wang, N. Xu, X. Kong, F. Shi, X. Rong, and J. Du, *Coherence-Protected Quantum Gate by Continuous Dynamical Decoupling in Diamond*, Physical Review Letters **109**, 070502 (2012),
URL: http://dx.doi.org/10.1103/PhysRevLett.109.070502

[174] J.-M. Cai, B. Naydenov, R. Pfeiffer, L. P. McGuinness, K. D. Jahnke, F. Jelezko, M. B. Plenio, and A. Retzker, *Robust dynamical decoupling with concatenated continuous driving*, New Journal of Physics **14**, 113023 (2012),
URL: http://dx.doi.org/10.1088/1367-2630/14/11/113023

[175] G. S. Uhrig, *Keeping a Quantum Bit Alive by Optimized π-Pulse Sequences*, Physical Review Letters **98**, 100504 (2007),
URL: http://dx.doi.org/10.1103/PhysRevLett.98.100504

[176] G. S. Uhrig, *Exact results on dynamical decoupling by π pulses in quantum information processes*, New Journal of Physics **10**, 083024 (2008),
URL: http://dx.doi.org/10.1088/1367-2630/10/8/083024

[177] E. Magesan, A. Cooper, H. Yum, and P. Cappellaro, *Reconstructing the profile of time-varying magnetic fields with quantum sensors*, Physical Review A **88**, 032107 (2013),
URL: http://dx.doi.org/10.1103/PhysRevA.88.032107

[178] A. Cooper, E. Magesan, H. N. Yum, and P. Cappellaro, *Time-resolved magnetic sensing with electronic spins in diamond*, Nature Communications **5**, 3141 (2014),
URL: http://dx.doi.org/10.1038/ncomms4141

[179] J. Casanova, Z.-Y. Wang, J. F. Haase, and M. B. Plenio, *Robust dynamical decoupling sequences for individual-nuclear-spin addressing*, Physical Review A **92**, 042304 (2015),
URL: http://dx.doi.org/10.1103/PhysRevA.92.042304

[180] N. Bar-Gill, L. M. Pham, C. Belthangady, D. Le Sage, P. Cappellaro, J. R. Maze, M. D. Lukin, A. Yacoby, and R. Walsworth, *Suppression of spin-bath dynamics for improved coherence of multi-spin-qubit systems*, Nature Communications **3**, 858 (2012),
URL: http://dx.doi.org/10.1038/ncomms1856

[181] F. Dolde, V. Bergholm, Y. Wang, I. Jakobi, B. Naydenov, S. Pezzagna, J. Meijer, F. Jelezko, P. Neumann, T. Schulte-Herbrüggen, J. Biamonte, and J. Wrachtrup, *High-fidelity spin entanglement using optimal control*, Nature Communications **5**, 3371 (2014),
URL: http://dx.doi.org/10.1038/ncomms4371

[182] F. Frank, T. Unden, J. Zoller, R. S. Said, T. Calarco, S. Montangero, B. Naydenov, and F. Jelezko, *Autonomous calibration of single spin qubit operations*, npj Quantum Inf **3**, 48 (2017),
URL: http://dx.doi.org/10.1038/s41534-017-0049-8

[183] A. M. Souza, G. A. Álvarez, and D. Suter, *Robust Dynamical Decoupling for Quantum Computing and Quantum Memory*, Physical Review Letters **106**, 240501

(2011),
URL: http://dx.doi.org/10.1103/PhysRevLett.106.240501

[184] T. Gullion, D. B. Baker, and M. S. Conradi, *New, compensated Carr-Purcell sequences*, Journal of Magnetic Resonance **89**, 479 (1990),
URL: http://dx.doi.org/10.1016/0022-2364(90)90331-3

[185] Z. H. Wang, G. De Lange, D. Ristè, R. Hanson, and V. V. Dobrovitski, *Comparison of dynamical decoupling protocols for a nitrogen-vacancy center in diamond*, Physical Review B - Condensed Matter and Materials Physics **85**, 155204 (2012),
URL: http://dx.doi.org/10.1103/PhysRevB.85.155204

[186] M. A. Ali Ahmed, G. A. Álvarez, and D. Suter, *Robustness of dynamical decoupling sequences*, Physical Review A **87**, 042309 (2013),
URL: http://dx.doi.org/10.1103/PhysRevA.87.042309

[187] J. H. Shim, I. Niemeyer, J. Zhang, and D. Suter, *Robust dynamical decoupling for arbitrary quantum states of a single NV center in diamond*, EPL (Europhysics Letters) **99**, 40004 (2012),
URL: http://dx.doi.org/10.1209/0295-5075/99/40004

[188] D. Farfurnik, A. Jarmola, L. M. Pham, Z.-H. Wang, V. V. Dobrovitski, R. L. Walsworth, D. Budker, and N. Bar-Gill, *Optimizing a dynamical decoupling protocol for solid-state electronic spin ensembles in diamond*, Physical Review B **92**, 060301 (2015),
URL: http://dx.doi.org/10.1103/PhysRevB.92.060301

[189] L. T. Hall, J. H. Cole, C. D. Hill, and L. C. L. Hollenberg, *Sensing of Fluctuating Nanoscale Magnetic Fields Using Nitrogen-Vacancy Centers in Diamond*, Physical Review Letters **103**, 220802 (2009),
URL: http://dx.doi.org/10.1103/PhysRevLett.103.220802

[190] S. Steinert, F. Ziem, L. T. Hall, A. Zappe, M. Schweikert, N. Götz, A. Aird, G. Balasubramanian, L. Hollenberg, and J. Wrachtrup, *Magnetic spin imaging under ambient conditions with sub-cellular resolution*, Nature Communications **4**, 1607 (2013),
URL: http://dx.doi.org/10.1038/ncomms2588

[191] L. T. Hall, C. D. Hill, J. H. Cole, and L. C. L. Hollenberg, *Ultrasensitive diamond magnetometry using optimal dynamic decoupling*, Physical Review B **82**, 045208 (2010),
URL: http://dx.doi.org/10.1103/PhysRevB.82.045208

[192] L. P. McGuinness, L. T. Hall, A. Stacey, D. A. Simpson, C. D. Hill, J. H. Cole, K. Ganesan, B. C. Gibson, S. Prawer, P. Mulvaney, F. Jelezko, J. Wrachtrup, R. E. Scholten, and L. C. L. Hollenberg, *Ambient nanoscale sensing with single spins using quantum decoherence*, New Journal of Physics **15**, 073042 (2013),
URL: http://dx.doi.org/10.1088/1367-2630/15/7/073042

[193] J.-P. Tetienne, T. Hingant, L. Rondin, A. Cavaillès, L. Mayer, G. Dantelle, T. Gacoin, J. Wrachtrup, J.-F. Roch, and V. Jacques, *Spin relaxometry of single nitrogen-vacancy defects in diamond nanocrystals for magnetic noise sensing*, Physical Review B **87**, 235436 (2013),
URL: http://dx.doi.org/10.1103/PhysRevB.87.235436

[194] F. C. Ziem, N. S. Götz, A. Zappe, S. Steinert, and J. Wrachtrup, *Highly Sensitive Detection of Physiological Spins in a Microfluidic Device*, Nano Letters **13**, 4093 (2013),
URL: http://dx.doi.org/10.1021/nl401522a

[195] A. Ermakova, G. Pramanik, J.-M. Cai, G. Algara-Siller, U. Kaiser, T. Weil, Y.-K. Tzeng, H. C. Chang, L. P. McGuinness, M. B. Plenio, B. Naydenov, and F. Jelezko, *Detection of a Few Metallo-Protein Molecules Using Color Centers in Nanodiamonds*, Nano Letters **13**, 3305 (2013),
URL: http://dx.doi.org/10.1021/nl4015233

[196] V. Giovannetti, S. Lloyd, and L. Maccone, *Quantum Metrology*, Physical Review Letters **96**, 010401 (2006),
URL: http://dx.doi.org/10.1103/PhysRevLett.96.010401

[197] R. A. Fisher, *A mathematical Examination of the Methods of determining the Accuracy of Observation by the Mean Error, and by the Mean Square Error*, Monthly Notices of the Royal Astronomical Society **80**, 758 (1920),
URL: http://dx.doi.org/10.1093/mnras/80.8.758

[198] R. A. Fisher, *On the mathematical foundations of theoretical statistics*, Philosophical Transactions of the Royal Society of London. Series A, Containing Papers of a Mathematical or Physical Character **222**, 309 (1922),
URL: http://dx.doi.org/10.1098/rsta.1922.0009

[199] R. A. Fisher, *Theory of Statistical Estimation*, Mathematical Proceedings of the Cambridge Philosophical Society **22**, 700 (1925),
URL: http://dx.doi.org/10.1017/S0305004100009580

[200] H. Cramér, *Mathematical Methods of Statistics*, Princeton, NJ: Princeton University Press, (1946)

[201] C. R. Rao, *Information and the Accuracy Attainable in the Estimation of Statistical Parameters*, Bulletin of the Calcutta Mathematical Society **37**, 81 (1945)

[202] S. Pang and A. N. Jordan, *Optimal adaptive control for quantum metrology with time-dependent Hamiltonians*, Nature Communications **8**, 14695 (2017),
URL: http://dx.doi.org/10.1038/ncomms14695

[203] D. Šafránek, *Simple expression for the quantum Fisher information matrix*, Physical Review A **97**, 042322 (2018),
URL: http://dx.doi.org/10.1103/PhysRevA.97.042322

[204] D. Petz and C. Ghinea, *Introduction to quantum Fisher information*, Quantum Probability and Related Topics **1**, 261 (2011),
URL: http://dx.doi.org/10.1142/9789814338745_0015

[205] Y. Romach, C. Müller, T. Unden, L. J. Rogers, T. Isoda, K. M. Itoh, M. Markham, A. Stacey, J. Meijer, S. Pezzagna, B. Naydenov, L. P. McGuinness, N. Bar-Gill, and F. Jelezko, *Spectroscopy of Surface-Induced Noise Using Shallow Spins in Diamond*, Physical Review Letters **114**, 017601 (2015),
URL: http://dx.doi.org/10.1103/PhysRevLett.114.017601

[206] M. Kim, H. J. Mamin, M. H. Sherwood, K. Ohno, D. D. Awschalom, and D. Rugar, *Decoherence of Near-Surface Nitrogen-Vacancy Centers Due to Electric Field Noise*, Physical Review Letters **115**, 087602 (2015),
URL: http://dx.doi.org/10.1103/PhysRevLett.115.087602

[207] P. Jamonneau, M. Lesik, J. P. Tetienne, I. Alvizu, L. Mayer, A. Dréau, S. Kosen, J.-F. Roch, S. Pezzagna, J. Meijer, T. Teraji, Y. Kubo, P. Bertet, J. R. Maze, and V. Jacques, *Competition between electric field and magnetic field noise in the decoherence of a single spin in diamond*, Physical Review B **93**, 024305 (2016),
URL: http://dx.doi.org/10.1103/PhysRevB.93.024305

[208] N. Bar-Gill, L. Pham, A. Jarmola, D. Budker, and R. Walsworth, *Solid-state electronic spin coherence time approaching one second*, Nature Communications **4**, 1743 (2013),
URL: http://dx.doi.org/10.1038/ncomms2771

[209] A. Jarmola, V. M. Acosta, K. Jensen, S. Chemerisov, and D. Budker, *Temperature- and Magnetic-Field-Dependent Longitudinal Spin Relaxation in Nitrogen-Vacancy*

Ensembles in Diamond, Physical Review Letters **108**, 197601 (2012),
URL: http://dx.doi.org/10.1103/PhysRevLett.108.197601

[210] S. Takahashi, R. Hanson, J. van Tol, M. S. Sherwin, and D. D. Awschalom, *Quenching Spin Decoherence in Diamond through Spin Bath Polarization*, Physical Review Letters **101**, 047601 (2008),
URL: http://dx.doi.org/10.1103/PhysRevLett.101.047601

[211] E. C. Reynhardt, G. L. High, and J. A. van Wyk, *Temperature dependence of spin-spin and spin-lattice relaxation times of paramagnetic nitrogen defects in diamond*, The Journal of Chemical Physics **109**, 8471 (1998),
URL: http://dx.doi.org/10.1063/1.477511

[212] A. Jarmola, A. Berzins, J. Smits, K. Smits, J. Prikulis, F. Gahbauer, R. Ferber, D. Erts, M. Auzinsh, and D. Budker, *Longitudinal spin-relaxation in nitrogen-vacancy centers in electron irradiated diamond*, Applied Physics Letters **107**, 242403 (2015),
URL: http://dx.doi.org/10.1063/1.4937489

[213] P. Atkins and J. de Paula, *Physical Chemistry*, Oxford University Press, Oxford, (2010)

[214] M. Findeisen and S. Berger, *50 and More Essential NMR Experiments: A Detailed Guide*, Wiley-VCH, Weinheim, (2014)

[215] W. R. Nitz and P. Reimer, *Contrast mechanisms in MR imaging*, European Radiology **9**, 1032 (1999),
URL: http://dx.doi.org/10.1007/s003300050789

[216] F. Bloch, *Nuclear Induction*, Physical Review **70**, 460 (1946),
URL: http://dx.doi.org/10.1103/PhysRev.70.460

[217] E. M. Purcell, H. C. Torrey, and R. V. Pound, *Resonance Absorption by Nuclear Magnetic Moments in a Solid*, Physical Review **69**, 37 (1946),
URL: http://dx.doi.org/10.1103/PhysRev.69.37

[218] L. Ciobanu, D. Seeber, and C. Pennington, *3D MR microscopy with resolution 3.7 μm by 3.3 μm by 3.3 μm*, Journal of Magnetic Resonance **158**, 178 (2002),
URL: http://dx.doi.org/10.1016/S1090-7807(02)00071-X

[219] C. L. Degen, M. Poggio, H. J. Mamin, C. T. Rettner, and D. Rugar, *Nanoscale magnetic resonance imaging*, Proceedings of the National Academy of Sciences **106**,

1313 (2009),
URL: http://dx.doi.org/10.1073/pnas.0812068106

[220] G. de Lange, D. Ristè, V. V. Dobrovitski, and R. Hanson, *Single-Spin Magnetometry with Multipulse Sensing Sequences*, Physical Review Letters **106**, 080802 (2011),
URL: http://dx.doi.org/10.1103/PhysRevLett.106.080802

[221] J. M. Boss, K. S. Cujia, J. Zopes, and C. L. Degen, *Quantum sensing with arbitrary frequency resolution*, Science **356**, 837 (2017),
URL: http://dx.doi.org/10.1126/science.aam7009

[222] D. R. Lide, *CRC Handbook of Chemistry and Physics, Internet Version 2005*, CRC Press, Boca Raton, FL, (2005)

[223] DBSWeb : https://sdbs.db.aist.go.jp (National Institute of Advanced Industrial Science and Technology, October 17, 2019),
URL: https://sdbs.db.aist.go.jp

[224] H. J. Mamin, R. Budakian, B. W. Chui, and D. Rugar, *Detection and Manipulation of Statistical Polarization in Small Spin Ensembles*, Physical Review Letters **91**, 207604 (2003),
URL: http://dx.doi.org/10.1103/PhysRevLett.91.207604

[225] H. J. Mamin, T. H. Oosterkamp, M. Poggio, C. L. Degen, C. T. Rettner, and D. Rugar, *Isotope-Selective Detection and Imaging of Organic Nanolayers*, Nano Letters **9**, 3020 (2009),
URL: http://dx.doi.org/10.1021/nl901466p

[226] I. Schwartz, J. Rosskopf, S. Schmitt, B. Tratzmiller, Q. Chen, L. P. McGuinness, F. Jelezko, and M. B. Plenio, *Blueprint for nanoscale NMR*, Scientific Reports **9**, 6938 (2019),
URL: http://dx.doi.org/10.1038/s41598-019-43404-2

[227] D. Cohen, R. Nigmatullin, O. Kenneth, F. Jelezko, M. Khodas, and A. Retzker, *Utilising NV based quantum sensing for velocimetry at the nanoscale*, Scientific Reports **10**, 5298 (2020),
URL: http://dx.doi.org/10.1038/s41598-020-61095-y

[228] X. Kong, A. Stark, J. Du, L. P. McGuinness, and F. Jelezko, *Towards Chemical Structure Resolution with Nanoscale Nuclear Magnetic Resonance Spectroscopy*, Physical Review Applied **4**, 024004 (2015),
URL: http://dx.doi.org/10.1103/PhysRevApplied.4.024004

[229] A. Rotem, T. Gefen, S. Oviedo-Casado, J. Prior, S. Schmitt, Y. Burak, L. Mcguiness, F. Jelezko, and A. Retzker, *Limits on Spectral Resolution Measurements by Quantum Probes*, Physical Review Letters **122**, 060503 (2019),
URL: http://dx.doi.org/10.1103/PhysRevLett.122.060503

[230] N. Aslam, M. Pfender, P. Neumann, R. Reuter, A. Zappe, F. Fávaro de Oliveira, A. Denisenko, H. Sumiya, S. Onoda, J. Isoya, and J. Wrachtrup, *Nanoscale nuclear magnetic resonance with chemical resolution*, Science **357**, 67 (2017),
URL: http://dx.doi.org/10.1126/science.aam8697

[231] G. T. Genov, D. Schraft, N. V. Vitanov, and T. Halfmann, *Arbitrarily Accurate Pulse Sequences for Robust Dynamical Decoupling*, Physical Review Letters **118**, 133202 (2017),
URL: http://dx.doi.org/10.1103/PhysRevLett.118.133202

[232] Z.-Y. Wang, J. E. Lang, S. Schmitt, J. Lang, J. Casanova, L. McGuinness, T. S. Monteiro, F. Jelezko, and M. B. Plenio, *Randomization of Pulse Phases for Unambiguous and Robust Quantum Sensing*, Physical Review Letters **122**, 200403 (2019),
URL: http://dx.doi.org/10.1103/PhysRevLett.122.200403

[233] J. Casanova, Z.-Y. Wang, I. Schwartz, and M. B. Plenio, *Shaped Pulses for Energy-Efficient High-Field NMR at the Nanoscale*, Physical Review Applied **10**, 044072 (2018),
URL: http://dx.doi.org/10.1103/PhysRevApplied.10.044072

[234] J. E. Lang, J. Casanova, Z.-Y. Wang, M. B. Plenio, and T. S. Monteiro, *Enhanced Resolution in Nanoscale NMR via Quantum Sensing with Pulses of Finite Duration*, Physical Review Applied **7**, 054009 (2017),
URL: http://dx.doi.org/10.1103/PhysRevApplied.7.054009

[235] Z. Shu, Z. Zhang, Q. Cao, P. Yang, M. B. Plenio, C. Müller, J. Lang, N. Tomek, B. Naydenov, L. P. McGuinness, F. Jelezko, and J. Cai, *Unambiguous nuclear spin detection using an engineered quantum sensing sequence*, Physical Review A **96**, 051402 (2017),
URL: http://dx.doi.org/10.1103/PhysRevA.96.051402

[236] J. M. Binder, A. Stark, N. Tomek, J. Scheuer, F. Frank, K. D. Jahnke, C. Müller, S. Schmitt, M. H. Metsch, T. Unden, T. Gehring, A. Huck, U. L. Andersen, L. J. Rogers, and F. Jelezko, *Qudi: A modular python suite for experiment control and data processing*, SoftwareX **6**, 85 (2017),
URL: http://dx.doi.org/10.1016/j.softx.2017.02.001

[237] A. Laraoui, F. Dolde, C. Burk, F. Reinhard, J. Wrachtrup, and C. A. Meriles, *High-resolution correlation spectroscopy of ^{13}C spins near a nitrogen-vacancy centre in diamond*, Nature Communications **4**, 1651 (2013),
URL: http://dx.doi.org/10.1038/ncomms2685

[238] T. Unden, P. Balasubramanian, D. Louzon, Y. Vinkler, M. B. Plenio, M. Markham, D. Twitchen, A. Stacey, I. Lovchinsky, A. O. Sushkov, M. D. Lukin, A. Retzker, B. Naydenov, L. P. McGuinness, and F. Jelezko, *Quantum Metrology Enhanced by Repetitive Quantum Error Correction*, Physical Review Letters **116**, 230502 (2016),
URL: http://dx.doi.org/10.1103/PhysRevLett.116.230502

[239] S. Zaiser, T. Rendler, I. Jakobi, T. Wolf, S.-Y. Lee, S. Wagner, V. Bergholm, T. Schulte-Herbrüggen, P. Neumann, and J. Wrachtrup, *Enhancing quantum sensing sensitivity by a quantum memory*, Nature Communications **7**, 12279 (2016),
URL: http://dx.doi.org/10.1038/ncomms12279

[240] T. Gefen, F. Jelezko, and A. Retzker, *Control methods for improved Fisher information with quantum sensing*, Physical Review A **96**, 032310 (2017),
URL: http://dx.doi.org/10.1103/PhysRevA.96.032310

[241] M. Naghiloo, A. N. Jordan, and K. W. Murch, *Achieving Optimal Quantum Acceleration of Frequency Estimation Using Adaptive Coherent Control*, Physical Review Letters **119**, 180801 (2017),
URL: http://dx.doi.org/10.1103/PhysRevLett.119.180801

[242] P. London, J. Scheuer, J.-M. Cai, I. Schwarz, A. Retzker, M. B. Plenio, M. Katagiri, T. Teraji, S. Koizumi, J. Isoya, R. Fischer, L. P. McGuinness, B. Naydenov, and F. Jelezko, *Detecting and Polarizing Nuclear Spins with Double Resonance on a Single Electron Spin*, Physical Review Letters **111**, 067601 (2013),
URL: http://dx.doi.org/10.1103/PhysRevLett.111.067601

[243] J. P. King, K. Jeong, C. C. Vassiliou, C. S. Shin, R. H. Page, C. E. Avalos, H. J. Wang, and A. Pines, *Room-temperature in situ nuclear spin hyperpolarization from optically pumped nitrogen vacancy centres in diamond*, Nature Communications **6**, 8965 (2015),
URL: http://dx.doi.org/10.1038/ncomms9965

[244] J. Scheuer, I. Schwartz, Q. Chen, D. Schulze-Sünninghausen, P. Carl, P. Höfer, A. Retzker, H. Sumiya, J. Isoya, B. Luy, M. B. Plenio, B. Naydenov, and F. Jelezko, *Optically induced dynamic nuclear spin polarisation in diamond*, New Journal of

Physics **18**, 013040 (2016),
URL: http://dx.doi.org/10.1088/1367-2630/18/1/013040

[245] J. Scheuer, I. Schwartz, S. Müller, Q. Chen, I. Dhand, M. B. Plenio, B. Naydenov, and F. Jelezko, *Robust techniques for polarization and detection of nuclear spin ensembles*, Physical Review B **96**, 174436 (2017),
URL: http://dx.doi.org/10.1103/PhysRevB.96.174436

[246] D. B. Bucher, D. P. Aude Craik, M. P. Backlund, M. J. Turner, O. Ben Dor, D. R. Glenn, and R. L. Walsworth, *Quantum diamond spectrometer for nanoscale NMR and ESR spectroscopy*, Nature Protocols **14**, 2707 (2019),
URL: http://dx.doi.org/10.1038/s41596-019-0201-3

[247] K. S. Cujia, J. M. Boss, K. Herb, J. Zopes, and C. L. Degen, *Tracking the precession of single nuclear spins by weak measurements*, Nature **571**, 230 (2019),
URL: http://dx.doi.org/10.1038/s41586-019-1334-9

[248] S. Schmitt, T. Gefen, D. Louzon, C. Osterkamp, N. Staudenmaier, J. Lang, M. Markham, L. P. McGuinness, and F. Jelezko, *Optimal frequency measurements with quantum probes*, npj Quantum Inf **7**, 55 (2021),
URL: http://dx.doi.org/10.1038/s41534-021-00391-5

[249] Y. Aharonov, S. Massar, and S. Popescu, *Measuring energy, estimating Hamiltonians, and the time-energy uncertainty relation*, Physical Review A **66**, 052107 (2002),
URL: http://dx.doi.org/10.1103/PhysRevA.66.052107

[250] C. W. Helstrom, *Quantum detection and estimation theory*, Journal of Statistical Physics **1**, 231 (1969),
URL: http://dx.doi.org/10.1007/BF01007479

[251] Creative Commons Attribution 4.0 International License,
URL: http://creativecommons.org/licenses/by/4.0/

[252] M. V. G. Dutt, L. Childress, L. Jiang, E. Togan, J. Maze, F. Jelezko, A. S. Zibrov, P. R. Hemmer, and M. D. Lukin, *Quantum Register Based on Individual Electronic and Nuclear Spin Qubits in Diamond*, Science **316**, 1312 (2007),
URL: http://dx.doi.org/10.1126/science.1139831

[253] L. Jiang, M. V. G. Dutt, E. Togan, L. Childress, P. Cappellaro, J. M. Taylor, and M. D. Lukin, *Coherence of an Optically Illuminated Single Nuclear Spin Qubit*, Physical Review Letters **100**, 073001 (2008),
URL: http://dx.doi.org/10.1103/PhysRevLett.100.073001

[254] P. Neumann, J. Beck, M. Steiner, F. Rempp, H. Fedder, P. R. Hemmer, J. Wrachtrup, and F. Jelezko, *Single-Shot Readout of a Single Nuclear Spin*, Science **329**, 542 (2010),
URL: http://dx.doi.org/10.1126/science.1189075

[255] P. O. Schmidt, T. Rosenband, C. Langer, W. M. Itano, J. C. Bergquist, and D. J. Wineland, *Spectroscopy Using Quantum Logic*, Science **309**, 749 (2005),
URL: http://dx.doi.org/10.1126/science.1114375

[256] L. Jiang, J. S. Hodges, J. R. Maze, P. Maurer, J. M. Taylor, D. G. Cory, P. R. Hemmer, R. L. Walsworth, A. Yacoby, A. S. Zibrov, and M. D. Lukin, *Repetitive Readout of a Single Electronic Spin via Quantum Logic with Nuclear Spin Ancillae*, Science **326**, 267 (2009),
URL: http://dx.doi.org/10.1126/science.1176496

[257] N. Aslam, G. Waldherr, P. Neumann, F. Jelezko, and J. Wrachtrup, *Photo-induced ionization dynamics of the nitrogen vacancy defect in diamond investigated by single-shot charge state detection*, New Journal of Physics **15**, 013064 (2013),
URL: http://dx.doi.org/10.1088/1367-2630/15/1/013064

[258] M. J. Biercuk, *Quantum measurement: A quantum spectrum analyser*, Nature Physics **7**, 525 (2011),
URL: http://dx.doi.org/10.1038/nphys2005

[259] N. Staudenmaier, S. Schmitt, L. P. McGuinness, and F. Jelezko (2021), *Phase sensitive quantum spectroscopy with high frequency resolution*, Physical Review A, American Physical Society, Forthcoming 2021

[260] J. D. A. Wood, J.-P. Tetienne, D. A. Broadway, L. T. Hall, D. A. Simpson, A. Stacey, and L. C. L. Hollenberg, *Microwave-free nuclear magnetic resonance at molecular scales*, Nature Communications **8**, 15950 (2017),
URL: http://dx.doi.org/10.1038/ncomms15950

[261] N. Aslam, M. Pfender, R. Stöhr, P. Neumann, M. Scheffler, H. Sumiya, H. Abe, S. Onoda, T. Ohshima, J. Isoya, and J. Wrachtrup, *Single spin optically detected magnetic resonance with 60-90 GHz (E-band) microwave resonators*, Review of Scientific Instruments **86**, 064704 (2015),
URL: http://dx.doi.org/10.1063/1.4922664

[262] V. Stepanov, F. H. Cho, C. Abeywardana, and S. Takahashi, *High-frequency and high-field optically detected magnetic resonance of nitrogen-vacancy centers in dia-*

mond, Applied Physics Letters **106**, 063111 (2015),
URL: http://dx.doi.org/10.1063/1.4908528

[263] A. Stark, N. Aharon, T. Unden, D. Louzon, A. Huck, A. Retzker, U. L. Andersen, and F. Jelezko, *Narrow-bandwidth sensing of high-frequency fields with continuous dynamical decoupling*, Nature Communications **8**, 1105 (2017),
URL: http://dx.doi.org/10.1038/s41467-017-01159-2

[264] T. Joas, A. M. Waeber, G. Braunbeck, and F. Reinhard, *Quantum sensing of weak radio-frequency signals by pulsed Mollow absorption spectroscopy*, Nature Communications **8**, 964 (2017),
URL: http://dx.doi.org/10.1038/s41467-017-01158-3

[265] S. M. Ransom, S. S. Eikenberry, and J. Middleditch, *Fourier Techniques for Very Long Astrophysical Time-Series Analysis*, The Astronomical Journal **124**, 1788 (2002),
URL: http://dx.doi.org/10.1086/342285

[266] M. Gasior and J. Gonzalez, *Improving FFT Frequency Measurement Resolution by Parabolic and Gaussian Spectrum Interpolation*, AIP Conference Proceedings **732**, 276 (2004),
URL: http://dx.doi.org/10.1063/1.1831158

[267] B. R. Mollow, *Power Spectrum of Light Scattered by Two-Level Systems*, Physical Review **188**, 1969 (1969),
URL: http://dx.doi.org/10.1103/PhysRev.188.1969

[268] V. S. Perunicic, C. D. Hill, L. T. Hall, and L. C. Hollenberg, *A quantum spin-probe molecular microscope*, Nature Communications **7**, 12667 (2016),
URL: http://dx.doi.org/10.1038/ncomms12667

[269] J. Smits, J. T. Damron, P. Kehayias, A. F. McDowell, N. Mosavian, I. Fescenko, N. Ristoff, A. Laraoui, A. Jarmola, and V. M. Acosta, *Two-dimensional nuclear magnetic resonance spectroscopy with a microfluidic diamond quantum sensor*, Science Advances **5**, eaaw7895 (2019),
URL: http://dx.doi.org/10.1126/sciadv.aaw7895

[270] N. M. Nusran, M. U. Momeen, and M. V. Dutt, *High-dynamic-range magnetometry with a single electronic spin in diamond*, Nature Nanotechnology **7**, 109 (2012),
URL: http://dx.doi.org/10.1038/nnano.2011.225

[271] G. Puentes, G. Waldherr, P. Neumann, G. Balasubramanian, and J. Wrachtrup, *Efficient route to high-bandwidth nanoscale magnetometry using single spins in diamond*, Scientific Reports **4**, 4677 (2015),
URL: http://dx.doi.org/10.1038/srep04677

[272] A. Hentschel and B. C. Sanders, *Machine Learning for Precise Quantum Measurement*, Physical Review Letters **104**, 063603 (2010),
URL: http://dx.doi.org/10.1103/PhysRevLett.104.063603

[273] C. E. Granade, C. Ferrie, N. Wiebe, and D. G. Cory, *Robust online Hamiltonian learning*, New Journal of Physics **14**, 103013 (2012),
URL: http://dx.doi.org/10.1088/1367-2630/14/10/103013

[274] N. Wiebe, C. Granade, C. Ferrie, and D. G. Cory, *Hamiltonian Learning and Certification Using Quantum Resources*, Physical Review Letters **112**, 190501 (2014),
URL: http://dx.doi.org/10.1103/PhysRevLett.112.190501

[275] M. I. Jordan and T. M. Mitchell, *Machine learning: Trends, perspectives, and prospects*, Science **349**, 255 (2015),
URL: http://dx.doi.org/10.1126/science.aaa8415

[276] I. Hincks, C. Granade, and D. G. Cory, *Statistical inference with quantum measurements: methodologies for nitrogen vacancy centers in diamond*, New Journal of Physics **20**, 013022 (2018),
URL: http://dx.doi.org/10.1088/1367-2630/aa9c9f

[277] C. Bonato, M. S. Blok, H. T. Dinani, D. W. Berry, M. L. Markham, D. J. Twitchen, and R. Hanson, *Optimized quantum sensing with a single electron spin using real-time adaptive measurements*, Nature Nanotechnology **11**, 247 (2016),
URL: http://dx.doi.org/10.1038/nnano.2015.261

[278] J. Wang, S. Paesani, R. Santagati, S. Knauer, A. A. Gentile, N. Wiebe, M. Petruzzella, J. L. O'brien, J. G. Rarity, A. Laing, and M. G. Thompson, *Experimental quantum Hamiltonian learning*, Nature Physics **13**, 551 (2017),
URL: http://dx.doi.org/10.1038/nphys4074

[279] R. Santagati, A. A. Gentile, S. Knauer, S. Schmitt, S. Paesani, C. Granade, N. Wiebe, C. Osterkamp, L. P. McGuinness, J. Wang, M. G. Thompson, J. G. Rarity, F. Jelezko, and A. Laing, *Magnetic-Field Learning Using a Single Electronic Spin in Diamond with One-Photon Readout at Room Temperature*, Physical Review

X **9**, 021019 (2019),
URL: http://dx.doi.org/10.1103/PhysRevX.9.021019

[280] N. Aharon, A. Rotem, L. P. McGuinness, F. Jelezko, A. Retzker, and Z. Ringel, *NV center based nano-NMR enhanced by deep learning*, Scientific Reports **9**, 17802 (2019),
URL: http://dx.doi.org/10.1038/s41598-019-54119-9

[281] G. T. Genov, N. Aharon, F. Jelezko, and A. Retzker, *Mixed dynamical decoupling*, Quantum Science and Technology **4**, 035010 (2019),
URL: http://dx.doi.org/10.1088/2058-9565/ab2afd

[282] G. Arrad, Y. Vinkler, D. Aharonov, and A. Retzker, *Increasing Sensing Resolution with Error Correction*, Physical Review Letters **112**, 150801 (2014),
URL: http://dx.doi.org/10.1103/PhysRevLett.112.150801

[283] E. M. Kessler, I. Lovchinsky, A. O. Sushkov, and M. D. Lukin, *Quantum Error Correction for Metrology*, Physical Review Letters **112**, 150802 (2014),
URL: http://dx.doi.org/10.1103/PhysRevLett.112.150802

[284] T. X. Zhou, R. J. Stöhr, and A. Yacoby, *Scanning diamond NV center probes compatible with conventional AFM technology*, Applied Physics Letters **111**, 163106 (2017),
URL: http://dx.doi.org/10.1063/1.4995813

[285] L. Thiel, Z. Wang, M. A. Tschudin, D. Rohner, I. Gutiérrez-Lezama, N. Ubrig, M. Gibertini, E. Giannini, A. F. Morpurgo, and P. Maletinsky, *Probing magnetism in 2D materials at the nanoscale with single-spin microscopy*, Science **364**, 973 (2019),
URL: http://dx.doi.org/10.1126/science.aav6926

[286] F. Fávaro de Oliveira, S. A. Momenzadeh, D. Antonov, J. Scharpf, C. Osterkamp, B. Naydenov, F. Jelezko, A. Denisenko, and J. Wrachtrup, *Toward Optimized Surface δ-Profiles of Nitrogen-Vacancy Centers Activated by Helium Irradiation in Diamond*, Nano Letters **16**, 2228 (2016),
URL: http://dx.doi.org/10.1021/acs.nanolett.5b04511

[287] B. Naydenov, F. Reinhard, A. Lämmle, V. Richter, R. Kalish, U. F. S. D'Haenens-Johansson, M. Newton, F. Jelezko, and J. Wrachtrup, *Increasing the coherence time of single electron spins in diamond by high temperature annealing*, Applied Physics

Letters **97**, 242511 (2010),
URL: http://dx.doi.org/10.1063/1.3527975

[288] C. Osterkamp, M. Mangold, J. Lang, P. Balasubramanian, T. Teraji, B. Naydenov, and F. Jelezko, *Engineering preferentially-aligned nitrogen-vacancy centre ensembles in CVD grown diamond*, Scientific Reports **9**, 5786 (2019),
URL: http://dx.doi.org/10.1038/s41598-019-42314-7

[289] R. H. Webb, *Confocal optical microscopy*, Reports on Progress in Physics **59**, 427 (1996),
URL: http://dx.doi.org/10.1088/0034-4885/59/3/003

[290] B. Amos, G. McConnell, and T. Wilson, *2.2 Confocal Microscopy*, in *Comprehensive Biophysics*, edited by E. H. Egelmann, volume 2, Elsevier, Amsterdam, pp. 3–23, (2012),
URL: http://dx.doi.org/10.1016/B978-0-12-374920-8.00203-4

[291] C. Osterkamp, J. Lang, J. Scharpf, C. Müller, L. P. McGuinness, T. Diemant, R. J. Behm, B. Naydenov, and F. Jelezko, *Stabilizing shallow color centers in diamond created by nitrogen delta-doping using SF_6 plasma treatment*, Applied Physics Letters **106**, 113109 (2015),
URL: http://dx.doi.org/10.1063/1.4915305

[292] R. J. Epstein, F. M. Mendoza, Y. K. Kato, and D. D. Awschalom, *Anisotropic interactions of a single spin and dark-spin spectroscopy in diamond*, Nature Physics **1**, 94 (2005),
URL: http://dx.doi.org/10.1038/nphys141

[293] D. A. Broadway, J. D. Wood, L. T. Hall, A. Stacey, M. Markham, D. A. Simpson, J. P. Tetienne, and L. C. Hollenberg, *Anticrossing Spin Dynamics of Diamond Nitrogen-Vacancy Centers and All-Optical Low-Frequency Magnetometry*, Physical Review Applied **6**, 064001 (2016),
URL: http://dx.doi.org/10.1103/PhysRevApplied.6.064001

[294] L. Childress, M. V. Gurudev Dutt, J. M. Taylor, A. S. Zibrov, F. Jelezko, J. Wrachtrup, P. R. Hemmer, and M. D. Lukin, *Coherent dynamics of coupled electron and nuclear spin qubits in diamond*, Science **314**, 281 (2006),
URL: http://dx.doi.org/10.1126/science.1131871

[295] F. P. Bundy, H. T. Hall, H. M. Strong, and R. H. Wentorf, *Man-Made diamonds*, Nature **176**, 51 (1955),
URL: http://dx.doi.org/10.1038/176051a0

[296] C. M. Sung and M. F. Tai, *Reactivities of Transition Metals with Carbon: Implications to the Mechanism of Diamond Synthesis Under High Pressure*, International Journal of Refractory Metals and Hard Materials **15**, 237 (1997),
URL: http://dx.doi.org/10.1016/S0263-4368(97)00003-6

[297] R. S. Balmer, et al., *Chemical vapour deposition synthetic diamond: materials, technology and applications*, Journal of Physics: Condensed Matter **21**, 364221 (2009),
URL: http://dx.doi.org/10.1088/0953-8984/21/36/364221

[298] M. L. Markham, J. M. Dodson, G. A. Scarsbrook, D. J. Twitchen, G. Balasubramanian, F. Jelezko, and J. Wrachtrup, *CVD diamond for spintronics*, Diamond and Related Materials **20**, 134 (2011),
URL: http://dx.doi.org/10.1016/j.diamond.2010.11.016

[299] M. Schwander and K. Partes, *A review of diamond synthesis by CVD processes*, Diamond and Related Materials **20**, 1287 (2011),
URL: http://dx.doi.org/10.1016/j.diamond.2011.08.005

[300] A. T. Collins and I. Kiflawi, *The annealing of radiation damage in type Ia diamond*, Journal of Physics: Condensed Matter **21**, 364209 (2009),
URL: http://dx.doi.org/10.1088/0953-8984/21/36/364209

[301] S. Pezzagna, D. Rogalla, H.-W. Becker, I. Jakobi, F. Dolde, B. Naydenov, J. Wrachtrup, F. Jelezko, C. Trautmann, and J. Meijer, *Creation of colour centres in diamond by collimated ion-implantation through nano-channels in mica*, physica status solidi (a) **208**, 2017 (2011),
URL: http://dx.doi.org/10.1002/pssa.201100455

[302] A. Haque and S. Sumaiya, *An Overview on the Formation and Processing of Nitrogen-Vacancy Photonic Centers in Diamond by Ion Implantation*, Journal of Manufacturing and Materials Processing **1**, 6 (2017),
URL: http://dx.doi.org/10.3390/jmmp1010006

[303] J. M. Smith, S. A. Meynell, A. C. Bleszynski Jayich, and J. Meijer, *Colour centre generation in diamond for quantum technologies*, Nanophotonics **8**, 1889 (2019),
URL: http://dx.doi.org/10.1515/nanoph-2019-0196

[304] K. Ohno, F. Joseph Heremans, C. F. de las Casas, B. A. Myers, B. J. Alemán, A. C. Bleszynski Jayich, and D. D. Awschalom, *Three-dimensional localization of spins in diamond using ^{12}C implantation*, Applied Physics Letters **105**, 052406 (2014),
URL: http://dx.doi.org/10.1063/1.4890613

[305] B. K. Ofori-Okai, S. Pezzagna, K. Chang, M. Loretz, R. Schirhagl, Y. Tao, B. A. Moores, K. Groot-Berning, J. Meijer, and C. L. Degen, *Spin properties of very shallow nitrogen vacancy defects in diamond*, Physical Review B **86**, 081406 (2012),
URL: http://dx.doi.org/10.1103/PhysRevB.86.081406

[306] J. F. Ziegler, M. D. Ziegler, and J. P. Biersack, *SRIM - The stopping and range of ions in matter (2010)*, Nuclear Instruments and Methods in Physics Research, Section B: Beam Interactions with Materials and Atoms **268**, 1818 (2010),
URL: http://dx.doi.org/10.1016/j.nimb.2010.02.091

[307] R. Fukuda, et al., *Lithographically engineered shallow nitrogen-vacancy centers in diamond for external nuclear spin sensing*, New Journal of Physics **20**, 083029 (2018),
URL: http://dx.doi.org/10.1088/1367-2630/aad997

[308] D. Kim, M. I. Ibrahim, C. Foy, M. E. Trusheim, R. Han, and D. R. Englund, *A CMOS-integrated quantum sensor based on nitrogen-vacancy centres*, Nature Electronics **2**, 284 (2019),
URL: http://dx.doi.org/10.1038/s41928-019-0275-5

[309] K. Ohno, F. Joseph Heremans, L. C. Bassett, B. A. Myers, D. M. Toyli, A. C. Bleszynski Jayich, C. J. Palmstrøm, and D. D. Awschalom, *Engineering shallow spins in diamond with nitrogen delta-doping*, Applied Physics Letters **101**, 082413 (2012),
URL: http://dx.doi.org/10.1063/1.4748280

[310] J. Schwartz, S. Aloni, D. F. Ogletree, and T. Schenkel, *Effects of low-energy electron irradiation on formation of nitrogen-vacancy centers in single-crystal diamond*, New Journal of Physics **14**, 043024 (2012),
URL: http://dx.doi.org/10.1088/1367-2630/14/4/043024

[311] B. Naydenov, V. Richter, J. Beck, M. Steiner, P. Neumann, G. Balasubramanian, J. Achard, F. Jelezko, J. Wrachtrup, and R. Kalish, *Enhanced generation of single optically active spins in diamond by ion implantation*, Applied Physics Letters **96**, 163108 (2010),
URL: http://dx.doi.org/10.1063/1.3409221

[312] K. J. Rosman and P. D. Taylor, *Isotopic compositions of the elements 1997 (Technical Report)*, Pure and Applied Chemistry **70**, 217 (1998), URL: http://dx.doi.org/10.1351/pac199870010217

[313] L. P. McGuinness, *Nanoscale Quantum Sensing Using Nitrogen-Vacancy Centres in Diamond*, PhD thesis, The University of Melbourne, (2012)

[314] G. Waldherr, J. Beck, P. Neumann, R. S. Said, M. Nitsche, M. L. Markham, D. J. Twitchen, J. Twamley, F. Jelezko, and J. Wrachtrup, *High-dynamic-range magnetometry with a single nuclear spin in diamond*, Nature Nanotechnology **7**, 105 (2012), URL: http://dx.doi.org/10.1038/nnano.2011.224

[315] K. Beha, A. Batalov, N. B. Manson, R. Bratschitsch, and A. Leitenstorfer, *Optimum Photoluminescence Excitation and Recharging Cycle of Single Nitrogen-Vacancy Centers in Ultrapure Diamond*, Physical Review Letters **109**, 097404 (2012), URL: http://dx.doi.org/10.1103/PhysRevLett.109.097404

[316] P. Siyushev, H. Pinto, M. Vörös, A. Gali, F. Jelezko, and J. Wrachtrup, *Optically Controlled Switching of the Charge State of a Single Nitrogen-Vacancy Center in Diamond at Cryogenic Temperatures*, Physical Review Letters **110**, 167402 (2013), URL: http://dx.doi.org/10.1103/PhysRevLett.110.167402

Acknowledgements

Here I want to thank the many people without whom this work would not have been possible and that made the last five years of my life such an exceptional and wonderful experience.

First of all, I would like to thank Prof. Fedor Jelezko for having given me the chance to work in his group – the Insitute of Quantum Optics in Ulm – on one of the most exciting topics one can imagine. He always had a sympathetic ear, no matter if there were any questions or problems, and his support and experience were of enormous help.

My special thanks and recognition go to Dr. Liam Paul McGuinness who did an outstanding job in supervising my work as postdoc. His passion for physics is admirable and he did an excellent job always keeping me motivated when experiments went wrong or problems seemed insurmountable. Especially our frequent, long and mostly fruitful discussions were an inspiration. Without his great support this thesis would not have been possible for sure.

Furthermore, I would like to thank Dr. Boris Naydenov who had been an omnipresent contact person for me and a great benefit for the whole institute before he moved to Berlin. There was no question he could not answer and as an expert for both, theory and experiment, I always appreciated his advice.

During the start of my work, my contact person was Christoph Müller, who was always friendly and patient when I had questions about the theory or problems with the setup. I am very grateful for the time he took for helping me while finishing his own thesis.

A successful project in physics is usually a synergy between experiment and theory. Because of that I would like to thank everyone from the theoretical institutes we collaborated with. In particular, Tuvia Gefen, with whom I discussed in countless Skype calls, was very important for the success of the work about Qdyne and frequency discrimination. For the publication about randomisation of pulse phases, my special thanks go to Dr. Zhenyu Wang who introduced me to the idea of the project and who always had time for a discussion when I had questions or problems. Furthermore, I would like to thank Ilai Schwartz, Prof. Martin Plenio and Prof. Alex Retzker for the many fruitful discussions.

The basis of our experiments are good samples. Therefore, I would like to thank Christian Osterkamp, Johannes Lang and Matthew Markham for sample creation and preparation.

Scientific research is no one-man show but based on collaboration. Because of that I want to thank all the people I worked together with inside and outside of the laboratory. Many thanks go to Gerhard Wolff, Felix Stürner and Nicolas Staudenmaier, the Master students that I helped supervising. It was a great pleasure and made me very happy to see their passion when working on common topics.

Of course this acknowledgement is not complete without thanking the best secretary in the world, Maria Heuschmid. Maria is the good soul of the institute and is indispensable when help for processing all of the paper work is required – ranging from hotel reservations to invoices – and thereby being quick and reliable. She is irreplaceable when it comes to organising all the fun group events such as Christmas parties or skiing trips.

No laboratory is permanently functioning without technical support. Therefore, I want to thank Michael Ferner and Manfred Bürzele for always being contactable and very helpful.

Furthermore I would like to thank Liam Paul McGuinness, Christoph Müller, Jochen Scheuer, Christian Osterkamp, Nicolas Staudenmaier, Gerhard Wolff, Genko Genov, Timo Joas and Zhenyu Wang for proofreading. Their useful comments contributed to improve the intelligibility and overall quality of this thesis.

Finally, I am very grateful for everybody who has accompanied me outside my academic life and made my stay in Ulm so enjoyable. Many thanks to all the members of the Institute for Quantum Optics who have integrated me from my first day on and I will gladly look back to the many memorable activities. Especially Christian Osterkamp, Christoph Müller and Jochen Scheuer have become really good friends and I really appreciate our time together. Special thanks go to my girlfriend Anja Seidemann who was always supportive, motivating and sympathetic, and to my family that encouraged me in every situation.

List of Publications

1. *Phase sensitive quantum spectroscopy with high frequency resolution*
   N. Staudenmaier, S. Schmitt, L. P. McGuinness, and F. Jelezko
   Physical Review A, American Physical Society, Forthcoming 2021

2. *Optimal frequency measurements with quantum probes*
   S. Schmitt, T. Gefen, D. Louzon, C. Osterkamp, N. Staudenmaier, J. Lang, M. Markham, A. Retzker, L. P. McGuinness and F. Jelezko
   npj Quantum Inf **7**, 55 (2021)
   URL: http://dx.doi.org/10.1038/s41534-021-00391-5

3. *Online adaptive quantum characterization of a nuclear spin*
   T. Joas, S. Schmitt, R. Santagati, A. A. Gentile, C. Bonato, A. Laing, L. P. McGuinness and F. Jelezko
   npj Quantum Inf **7**, 56 (2021)
   URL: https://dx.doi.org/10.1038/s41534-021-00389-z

4. *Randomisation of Pulse Phases for Unambiguous and Robust Quantum Sensing*
   Z. Wang†, J. E. Lang†, S. Schmitt†, J. Lang, J. Casanova, L. P. McGuinness, T. S. Monteiro, F. Jelezko, and M. B. Plenio
   Physical Review Letters **122**, 200403 (2019)
   URL: http://dx.doi.org/10.1103/PhysRevLett.122.200403

5. *Blueprint for nanoscale NMR*
   I. Schwartz, J. Rosskopf, S. Schmitt, B. Tratzmiller, Q. Chen, L. P. McGuinness, F. Jelezko, and M. B. Plenio
   Scientific Reports **9**, 6938 (2019)
   URL: http://dx.doi.org/10.1038/s41598-019-43404-2

6. *Limits on Spectral Resolution Measurements by Quantum Probes*
   A. Rotem†, T. Gefen†, S. Oviedo-Casado, J. Prior, S. Schmitt, Y. Burak, L. P. McGuinness, F. Jelezko, and A. Retzker
   Physical Review Letters **122**, 060503 (2019)
   URL: http://dx.doi.org/10.1103/PhysRevLett.122.060503

7. *Genauer dank altem Trick*
   S. Schmitt
   Physik in unserer Zeit **49**, 246 (2018)
   URL: http://dx.doi.org/10.1002/piuz.201801510

8. *Magnetic-field-learning using a single electronic spin in diamond with one-photon-readout at room temperature*
   R. Santagati†, A. A. Gentile†, S. Knauer†, S. Schmitt, S. Paesani, C. Granade, N. Wiebe, C. Osterkamp, L. P. McGuinness, J. Wang, M. G. Thompson, J. G. Rarity, F. Jelezko, and A. Laing
   Physical Review X **9**, 21019 (2018)
   URL: http://dx.doi.org/10.1103/physrevx.9.021019

9. *Lithographically engineered shallow nitrogen-vacancy centers in diamond for external nuclear spin sensing*
   R. Fukuda†, P. Balasubramanian†, I. Higashimata, G. Koike, T. Okada, R. Kagami, T. Teraji, S. Onoda, M. Haruyama, K. Yamada, M. Inaba, H. Yamano, F. M. Stürner, S. Schmitt, L. P. McGuinness, F. Jelezko, T. Ohshima, T. Shinada, H. Kawarada, W. Kada, O. Hanaizumi, T. Tanii, and J. Isoya
   New Journal of Physics **20**, 083029 (2018)
   URL: http://dx.doi.org/10.1088/1367-2630/aad997

10. *Toward Hyperpolarization of Oil Molecules via Single Nitrogen Vacancy Centers in Diamond*
    P. Fernández-Acebal, O. Rosolio, J. Scheuer, C. Müller, S. Müller, S. Schmitt, L. P. McGuinness, I. Schwarz, Q. Chen, A. Retzker, B. Naydenov, F. Jelezko, and M. B. Plenio
    Nano Letters **18**, 1882 (2018)
    URL: http://dx.doi.org/10.1021/acs.nanolett.7b05175

11. *Non-flipping ^{13}C spins near an NV center in diamond: hyperfine and spatial characteristics by density functional theory simulation of the $C_{510}[NV]H_{252}$ cluster*
    A. P. Nizovtsev, S. Y. Kilin, A. L. Pushkarchuk, V. A. Pushkarchuk, S. A. Kuten, O. A. Zhikol, S. Schmitt, T. Unden, and F. Jelezko
    New Journal of Physics **20**, 023022 (2018)
    URL: http://dx.doi.org/10.1088/1367-2630/aaa910

12. *Submillihertz magnetic spectroscopy performed with a nanoscale quantum sensor*
    S. Schmitt, T. Gefen, F. M. Stürner, T. Unden, G. Wolff, C. Müller, J. Scheuer,

B. Naydenov, M. Markham, S. Pezzagna, J. Meijer, I. Schwarz, M. Plenio, A. Retzker, L. P. McGuinness, and F. Jelezko
Science **356**, 832 (2017)
URL: http://dx.doi.org/10.1126/science.aam5532

13. *Qudi: A modular python suite for experiment control and data processing*
J. M. Binder, A. Stark, N. Tomek, J. Scheuer, F. Frank, K. D. Jahnke, C. Müller, S. Schmitt, M. H. Metsch, T. Unden, T. Gehring, A. Huck, U. L. Andersen, L. J. Rogers, and F. Jelezko
SoftwareX **6**, 85 (2017)
URL: http://dx.doi.org/10.1016/j.softx.2017.02.001

[†]these authors contributed equally to the work

Parts of this thesis have previously been published in:

- *Submillihertz magnetic spectroscopy performed with a nanoscale quantum sensor*
  S. Schmitt, T. Gefen, F. M. Stürner, T. Unden, G. Wolff, C. Müller, J. Scheuer, B. Naydenov, M. Markham, S. Pezzagna, J. Meijer, I. Schwarz, M. Plenio, A. Retzker, L. P. McGuinness, and F. Jelezko
  Science **356**, 832 (2017)
  Modified with permission of AAAS.
  URL: http://dx.doi.org/10.1126/science.aam5532

- *Blueprint for nanoscale NMR*
  I. Schwartz, J. Rosskopf, S. Schmitt, B. Tratzmiller, Q. Chen, L. P. McGuinness, F. Jelezko, and M. B. Plenio
  Scientific Reports **9**, 6938 (2019)
  URL: http://dx.doi.org/10.1038/s41598-019-43404-2

- *Randomisation of Pulse Phases for Unambiguous and Robust Quantum Sensing*
  Z. Wang†, J. E. Lang†, S. Schmitt†, J. Lang, J. Casanova, L. P. McGuinness, T. S. Monteiro, F. Jelezko, and M. B. Plenio
  Physical Review Letters **122**, 200403 (2019).
  Reprinted with permission. Copyright 2019 by the American Physical Society.
  URL: http://dx.doi.org/10.1103/PhysRevLett.122.200403

- *Optimal frequency measurements with quantum probes*
  S. Schmitt, T. Gefen, D. Louzon, C. Osterkamp, N. Staudenmaier, J. Lang, M. Markham, A. Retzker, L. P. McGuinness and F. Jelezko
  npj Quantum Inf **7**, 55 (2021)
  Licensed under http://creativecommons.org/licenses/by/4.0/
  URL: http://dx.doi.org/10.1038/s41534-021-00391-5

- *Phase sensitive quantum spectroscopy with high frequency resolution*
  N. Staudenmaier, S. Schmitt, L. P. McGuinness, and F. Jelezko
  Physical Review A, American Physical Society, Forthcoming 2021.
  Reprinted with permission. Copyright 2021 by the American Physical Society.

Curriculum Vitae

Curriculum vitae removed for data protection reasons.
Lebenslauf aus Gründen des Datenschutzes entfernt.

Erklärung

Ich versichere hiermit, dass ich die Arbeit selbständig angefertigt habe und keine anderen als die angegebenen Quellen und Hilfsmittel benutzt, sowie die wörtlich oder inhaltlich übernommenen Stellen als solche kenntlich gemacht habe.

Weiterhin erkläre ich, dass die vorliegende Arbeit weder vollständig noch in Auszügen einer anderen Fakultät mit dem Ziel vorgelegt worden ist, einen akademischen Titel zu erwerben. Ich bewerbe mich hiermit erstmalig um den Doktorgrad der Naturwissenschaften der Universität Ulm.

Ulm, den 23. April 2020

Simon Christian Schmitt